

DEVELOPMENT OF 3D METALLIC NANO- STRUCTURES FOR SENSING APPLICATIONS

by

Mohamadreza Najiminaini

M.Sc., Eastern Mediterranean University, 2007
B.Sc., Islamic Azad University, 2005

Thesis Submitted In Partial Fulfillment of the
Requirements for the Degree of
Doctor of Philosophy

in the

School of Engineering Science
Faculty of Applied Sciences

© Mohamadreza Najiminaini 2012

SIMON FRASER UNIVERSITY

Summer 2012

All rights reserved.

However, in accordance with the *Copyright Act of Canada*, this work may be reproduced, without authorization, under the conditions for "Fair Dealing." Therefore, limited reproduction of this work for the purposes of private study, research, criticism, review and news reporting is likely to be in accordance with the law, particularly if cited appropriately.

Approval

Name: Mohamadreza Najiminaini
Degree: Doctor of Philosophy
Title of Thesis: *DEVELOPMENT OF THREE DIMENSIONAL METALLIC NANO-STRUCTURES FOR SENSING APPLICATIONS*

Examining Committee:

Chair: Dr. Shawn Stapleton
Professor, School of Engineering Science

Dr. Bozena Kaminska
Senior Supervisor
Professor, School of Engineering

Dr. Jeffrey J.L. Carson
Supervisor
Assistant Professor, University of Western Ontario

Dr. Carlo Menon
Supervisor
Assistant Professor, School of Engineering

Dr. Karen Kavanagh
Internal Examiner
Professor
Department of Physics

Dr. Alexandre G. Brolo
External Examiner
Associate Professor, Department of Chemistry
University of Victoria

Date Defended/Approved: July 12, 2012

Partial Copyright Licence



The author, whose copyright is declared on the title page of this work, has granted to Simon Fraser University the right to lend this thesis, project or extended essay to users of the Simon Fraser University Library, and to make partial or single copies only for such users or in response to a request from the library of any other university, or other educational institution, on its own behalf or for one of its users.

The author has further granted permission to Simon Fraser University to keep or make a digital copy for use in its circulating collection (currently available to the public at the "Institutional Repository" link of the SFU Library website (www.lib.sfu.ca) at <http://summit/sfu.ca> and, without changing the content, to translate the thesis/project or extended essays, if technically possible, to any medium or format for the purpose of preservation of the digital work.

The author has further agreed that permission for multiple copying of this work for scholarly purposes may be granted by either the author or the Dean of Graduate Studies.

It is understood that copying or publication of this work for financial gain shall not be allowed without the author's written permission.

Permission for public performance, or limited permission for private scholarly use, of any multimedia materials forming part of this work, may have been granted by the author. This information may be found on the separately catalogued multimedia material and in the signed Partial Copyright Licence.

While licensing SFU to permit the above uses, the author retains copyright in the thesis, project or extended essays, including the right to change the work for subsequent purposes, including editing and publishing the work in whole or in part, and licensing other parties, as the author may desire.

The original Partial Copyright Licence attesting to these terms, and signed by this author, may be found in the original bound copy of this work, retained in the Simon Fraser University Archive.

Simon Fraser University Library
Burnaby, British Columbia, Canada

revised Fall 2011

Abstract

The interaction of a light with an array of sub-wavelength holes in a thin metal film has given rise to a unique optical property, the so-called extraordinary optical transmission (EOT). Not only does EOT of a sub-wavelength hole array exceed the incident light on the holes, but also could surpass the diffraction limit of the light and provide an intensified electric field at vicinity of the holes. These phenomena have introduced many new possibilities in the field of photonic applications.

Surface Plasmon Resonance (SPR) sensing is one of the most common applications of a metallic sub-wavelength hole array structure and it results from EOT spectral shifts due to changes in the refractive index of materials on the top or bottom of the structure. In this thesis, novel sub-wavelength hole array structures with a surface plasmon energy matching property between the top and bottom of the structure have been fabricated and tested in a bulk-SPR sensing application. The numerical and experimental results demonstrated improved SPR sensitivities and higher electric field intensity at the edges of the holes at the EOT wavelength for an energy-matched structure compared to a conventional sub-wavelength hole array structure. However, in order to fabricate the novel structure, two systematic studies were performed to elucidate the effects of various geometrical parameters and different composition and thickness of the adhesion layers on the EOT properties of sub-wavelength hole array structures.

Many other applications of a sub-wavelength hole array could potentially benefit from these novel structures due to their enhanced EOT properties over conventional structures.

Keywords: surface plasmon; nano-hole array; extraordinary optical transmission; surface plasmon resonance sensing; nano-fabrication; resonance

Co-Authorship

The thesis includes material from five publications, all of which had contributions from co-authors, as follows:

Chapter 2: M. Najiminaini, F. Vasefi, B. Kaminska, and J. J. L. Carson, "Experimental and numerical analysis on the optical resonance transmission properties of nano-hole arrays," *Opt. Express* 18, 22255-22270 (2010)

Dr. Vasefi aided in a design and fabrication of nano-hole arrays as well as analyzed experimental and numerical results; Dr. Kaminska provided project concept, read and edited the manuscript and provided supervision; Dr. Carson aided in analyzing numerical and experimental results. He also provided fabrication and testing facilities at the University of Western Ontario as well as provided project concept, read and edited the manuscript and provided supervision. I performed a design, fabrication, simulation, and optical characterization of nano-hole arrays. I also analyzed experimental and numerical results and wrote the manuscript.

Chapter 3: M. Najiminaini, F. Vasefi, B. Kaminska, and J. J.L. Carson, "Optical resonance transmission properties of nano-hole arrays in a gold film: effect of adhesion layer," *Opt. Express* 19, 26186-26197 (2011)

Dr. Vasefi aided in analyzing experimental and numerical results, involved on project discussions, and read and edited the manuscript. Dr. Kaminska provided project concept, read and edited the manuscript and provided supervision; Dr. Carson provided project concept, fabrication and testing facilities at the University of Western Ontario, read and edited the manuscript and provided supervision; I designed and fabricated nano-hole arrays on various adhesion layers. I also characterized the fabricated nano-hole arrays using optical transmission microscope, validated experimental results with simulation results, analyzed both simulation and experimental results and wrote the manuscript.

Chapter 4: M. Najiminaini, F. Vasefi, B. Kaminska, and J. J. L. Carson, " Nano-hole array structure with improved surface plasmon energy matching characteristics," Applied Physics Letter 100 (4) (2012)

Dr. Vasefi aided in analyzing experimental and numerical results as well as read and edited the manuscript. Dr. Kaminska provided project concept, read and edited the manuscript and provided supervision. Dr. Carson provided project concept, fabrication and testing facilities at the University of Western Ontario, read and edited the manuscript and provided supervision. I designed and fabricated a novel nano-hole array device with a cavity beneath each nano-hole. I also performed simulation and experiments on the novel nano-hole array device, analyzed both numerical and experimental results, and wrote the manuscript.

Chapter 5: M. Najiminaini, F. Vasefi, B. Kaminska, and J. J. L. Carson, " Effect of Surface Plasmon energy matching on sensing capability of metallic nano-hole arrays," Accepted in Applied Physics Letter (2012).

Dr. Vasefi aided in a design of a novel nano-hole array with a large cavity beneath a nano-hole array area, specifically proposed to use a sacrificial layer between nano-hole array and Pyrex substrate in order to create a controlled cavity depth beneath the nano-hole array; Dr. Kaminska provided project concept, read and edited the manuscript and provided supervision; Dr. Carson provided project concept fabrication and testing facilities at the University of Western Ontario, aided in analyzing experimental results, read and edited the manuscript and provided supervision. I designed and fabricated a novel nano-hole array device with a large cavity. Also, I performed SPR sensing experiments on the novel nano-hole array device, analyzed experimental results, and wrote the manuscript.

Chapter 6: M. Najiminaini, F. Vasefi, B. Kaminska, and J. J. L. Carson, "A three-dimensional plasmonic nanostructure with extraordinary optical transmission," Submitted to Journal of Plasmonics (2012)

Dr. Vasefi was involved on project discussions, read, and edited the manuscript. Dr. Kaminska provided project concept, read and edited the manuscript and provided

supervision; Dr. Carson provided project concept, fabrication and testing facilities at the University of Western Ontario, read and edited the manuscript and provided supervision. I developed, designed and fabricated a novel 3D nanostructure device as well as optically characterized the device, and validated the experimental results with simulation results. I also analyzed both simulation and experimental results and wrote the manuscript.

Dedication

**I would like sincerely to dedicate this thesis
to my beloved family.**

Acknowledgements

I would like to express my sincere thanks to my family for their continuous help, support and encouragement throughout my Ph.D. course. I was very fortunate to have the opportunity to work in the nano-optics field under the supervision of Dr. Bozena Kaminska in my Ph.D. study, and it really opened up many possibilities in my current and future career. Also, I would like to thank Dr. Kaminska for her constant support during my Ph.D. Thank you to my supervisor Dr. Jeffrey J. L. Carson, who taught me many invaluable scientific approaches from starting a scientific project to the completion of the project. It has been an honour to work with Dr. Carson. Without his guidance, patience, and his practical involvement in my research, I would not have been able to fulfill my Ph.D. Thank you to my great friend and mentor Dr. Fartash Vasefi, who introduced me to Dr. Kaminska's and Dr. Carson's research groups and provided me with his unlimited help, support and professional guidance. To Mr. Eldon Ng, you have been a very supportive friend and lab partner and provided me indispensable assistance. Thanks to Dr. Astrid Chamson-Reig and Mr. Yan Zhang for their valuable guidance. Thanks to Dr. Todd Simpson, Dr. Rick Glew, and Mr. Tim Goldhawk for their immeasurable aid in the nano-fabrication facility at Western University. Also, thanks to Dr. Simpson for supervising and training me to use various equipments in the nano-fabrication facility and for your priceless experience and advice. Special acknowledgment to Dr. Ljiljana Trajkovic, Dr. Stephen Campbell, and Dr. François Lagugné-Labarthe for their academic experience and for giving me the opportunity to work in their laboratories. Furthermore, I would like to thank my great friends Vandad Sotoudehnia, Shahrzad Aghasharifianesfahani, Nima Javaheri, Babak Khosravifar, and Masoud Saligheh Rad for giving me constant enthusiasm and encouragement throughout my Ph.D. Thanks to my great friend Mohamad Bakhshashi for his special support. Lastly, I would like to acknowledge the funding agencies MITACS and NSERC for providing the financial support for this project.

Table of Contents

Approval.....	ii
Partial Copyright Licence.....	iii
Abstract.....	iv
Co-Authorship	v
Dedication	viii
Acknowledgements	ix
Table of Contents.....	x
List of Tables.....	xiii
List of Figures.....	xiv
List of Acronyms or Glossary.....	xix
1. Introduction	1
1.1. Overview	1
1.2. Bethe Aperture Theory	2
1.3. Surface Plasmon (SP)	4
1.4. Surface Plasmon excitation	6
1.5. Extraordinary Optical Transmission of sub-wavelength hole arrays	8
1.6. Dependence of EOT on various parameters of the sub-wavelength hole array:.....	10
1.6.1. Materials and geometries.....	11
1.6.2. Illumination angle	13
1.6.3. Fabrication methods.....	17
1.7. Applications of Sub-wavelength hole arrays:	18
1.7.1. Surface Plasmon Resonance (SPR) sensing	18
1.7.2. Surface Enhanced Raman Scattering (SERS)	21
1.7.3. Optical Trapping.....	22
1.7.4. Near-field scanning optical microscopy (NSOM)	22
1.7.5. Optical filters	23
1.7.6. Non-linear Optics	24
1.7.7. Absorption spectroscopy.....	24
1.8. Interpretation and analysis of the literature:	25
1.9. Thesis objective and scope:	27
1.9.1. Research approach.....	27
1.10. References	31
2. Experimental and numerical analysis on the optical resonance transmission properties of nano-hole arrays	38
2.1. Abstract.....	38
2.2. Introduction.....	39
2.3. Methods	41
2.3.1. FDTD simulation of nano-hole arrays.....	41
2.3.2. Electron Beam Lithography (EBL) fabrication methodology.....	44
2.3.3. Optical characterization setup	44
2.3.4. Analysis of the optical transmission spectra	45

2.4.	Results	45
2.4.1.	Experimental observations in Nano-hole array fabrication	45
2.4.2.	Simulation results.....	46
2.4.3.	Experimental results.....	51
2.5.	Discussion.....	57
2.6.	Conclusion	61
2.7.	References.....	61
3.	Optical resonance transmission properties of nano-hole arrays in a gold film: effect of adhesion layer	65
3.1.	Abstract.....	65
3.2.	Introduction.....	66
3.3.	Motivation and objective	68
3.4.	Methods	69
3.4.1.	Electron Beam Lithography (EBL)	69
3.4.2.	Optical characterization setup	72
3.4.3.	FDTD simulation of nano-hole arrays.....	73
3.4.4.	Analysis of the optical transmission spectra	73
3.5.	Results	74
3.6.	Discussion.....	79
3.6.1.	Overall findings	79
3.6.2.	Fabrication of nano-hole arrays.....	80
3.6.3.	Analyses of the experimental and simulation results	81
3.6.4.	Implications of the adhesion layer composition to surface Plasmon sensing	82
3.7.	Conclusions.....	83
3.8.	Acknowledgments	83
3.9.	References.....	84
4.	Nano-hole array structure with improved surface plasmon energy matching characteristics	87
4.1.	Abstract.....	87
4.2.	Introduction.....	88
4.3.	Methods	89
4.4.	Results and discussion.....	91
4.5.	Conclusions.....	95
4.6.	References.....	96
5.	Effect of Surface Plasmon energy matching on the sensing capability of metallic nano-hole arrays	99
5.1.	Abstract.....	99
5.2.	Introduction.....	100
5.3.	Methods	101
5.4.	Results and discussion.....	103
5.5.	Conclusions.....	108
5.6.	References.....	108

6. A three-dimensional plasmonic nanostructure with extraordinary optical transmission.....	111
6.1. Abstract.....	111
6.2. Introduction.....	112
6.3. Methods	113
6.3.1. Finite difference time domain simulation	113
6.3.2. 3D nanostructure fabrication	114
6.3.3. Optical characterization setup	115
6.4. Results	116
6.5. Discussion.....	123
6.6. Conclusions.....	125
6.7. Acknowledgments	125
6.8. References.....	126
7. Summary and future work.....	129
7.1. Overview	129
7.2. Systematic studies.....	129
7.3. Novel plasmonic sub-wavelength structures.....	133
7.4. Some simulation and fabrication constrains.....	140
7.5. Future work	141
7.6. Conclusions.....	143
7.7. References.....	145
Appendices.....	146
Appendix A. Experimental analysis of optical resonance transmission properties of sub-wavelength hole arrays in optically thick metal films.....	147
Appendix B. Effect of adhesion layer on optical resonance transmission properties of nano-hole arrays in an optically thick gold film	157
Appendix C. Surface plasmon resonance sensing using index-matched metallic nano-hole array structures.....	167
Appendix D. Effect of surface plasmon cross-talk on optical properties of closely packed nano-hole arrays	176
Appendix E. Angular domain fluorescence lifetime imaging: a tissue like phantom study	186

List of Tables

Table 2-1. Summary of simulation results related to optical resonance peaks	48
Table 2-2. Summary of experimental results related to optical resonance peaks.....	54
Table 3-1. Summary of the conductive and adhesion layer composition and thickness	70
Table 3-2. Summary of the geometrical parameters of the simulated and fabricated nano-hole arrays	72

List of Figures

Figure 1-1	(a) Schematic of light diffraction through a sub-wavelength aperture perforated in an infinitely thin PEC film. (b) Typical optical transmission spectra through a sub-wavelength aperture in an infinitely thin PEC film. (adapted from [1-8])	3
Figure 1-2	(a) Oscillations of free electrons at the interface between metal and dielectric (b) SP decay length into metal (δm) and dielectric (δd). (adapted from [1-2])	4
Figure 1-3	(a) Electromagnetic propagation length along the surfaces of glass-gold and air-gold interfaces. (b) SP decay length normal to gold/dielectric interface into air, glass, and gold.	6
Figure 1-4	(a) Dispersion curves of SP and light line ($\omega = ckx$), ω_{sp} is a SP frequency. (b) Two-dimensional grating of a square lattice holes: p is the spacing between adjacent holes and a is the width of holes.	7
Figure 1-5	A 2-dimension sub-wavelength hole array in a metal film on a substrate in a square lattice arrangement. p is the spacing between two adjacent holes, a is a width of each hole, K_x wave vector of the light is along the x-axis, and (+1,0), (-1,0), (0, ± 1), (+1,1), and (-1,1) are various (i, j) grating modes.	9
Figure 1-6	Optical transmission of a sub-wavelength hole array as a function of incident angle of illumination for (a) gold and b) silver films. Each spectrum is offset vertically by 0.1% from the preceding spectrum for clarity. The EOTs related to (0, ± 1), (+1, 0), (+1, 1) and (-1,1) SP excitation modes are also indicated.	15
Figure 1-7	Optical characterization setup diagram for two different incident angles of illumination on a sub-wavelength hole array using a) a pinhole and b) an annular diaphragm.	16
Figure 2-1.	(a) Set up and boundary conditions for FDTD simulation of nano-hole array, (b) Electron beam lithography (EBL) for fabrication of nano-hole arrays, (c) SEM of an array of photo-resist nano-pillars, (d) Set up for optical characterization of nano-hole arrays, and (e) SEM of a nano-hole array with the circular nano-holes.	43

Figure 2-2. Optical transmission spectra for nano-hole arrays with various hole shape (square and circular), diameters (150 nm, 200 nm, and 250 nm), and periodicities or P (375 nm, 400 nm, 425 nm, 450 nm, and 475 nm) based on FDTD simulation: (a) circular holes with 150 nm diameter, (b) circular holes with 200 nm diameter, (c) circular holes with 250 nm diameter, (d) square holes with 150 nm length, (e) square holes with 200 nm length, and (f) square holes with 250 nm length. (ag) represents the optical resonance peak from air-gold side. (Pg) represents the optical resonance peak from Pyrex-gold side. 48

Figure 2-3. (1,0) and (1,1) optical resonance analyses of the nano-hole arrays for simulation results (in the graphs legend, D circular hole diameter and L square hole length): (a) (1,0) Pyrex-gold side optical resonance position versus periodicity, (b) (1,0) Pyrex-gold side optical resonance transmission efficiency versus periodicity, (c) (1,0) Pyrex-gold side optical resonance bandwidth versus periodicity, (d) (1,1) Pyrex-gold side optical resonance position versus periodicity, (e) (1,1) Pyrex-gold side optical resonance transmission efficiency versus periodicity, and (f) (1,0) air-gold side optical resonance transmission versus periodicity. 51

Figure 2-4 Optical transmission spectra for nano-hole arrays with various hole shape (square and circular), diameters (150nm, 200nm, and 250nm), and periodicities or P(375nm, 400nm, 425nm, 450nm, and 475nm) in experimental results: (a) circular holes with 150nm diameter, (b) circular holes with 200nm diameter, (c) circular holes with 250nm diameter, (d) square holes with 150nm length, (e) square holes with 200nm length, and (f) square holes with 250nm length. (ag) represents the optical resonance peak from air-gold side. (Pg) represents the optical resonance peak from Pyrex-gold side. 53

Figure 2-5. (1,0) and (1,1) Pyrex-gold side optical resonance analyses of the nano-hole arrays for experimental results (in the graphs legend, D circular hole diameter and L square hole length): (a) (1,0) optical resonance position versus periodicity, (b) (1,0) optical resonance transmission efficiency versus periodicity, (c) (1,0) optical resonance bandwidth versus periodicity, (d) (1,1) optical resonance position versus periodicity, (e) (1,1) optical resonance transmission versus periodicity, and (f) (1,1) optical resonance bandwidth versus periodicity. 56

Figure 3-1. Electron beam lithography (EBL) for fabrication of nano-hole arrays. 71

Figure 3-2. SEM images of a nano-hole array in a 100 nm gold film: (a) angle view, and (b) top view. 71

Figure 3-3. Optical transmission spectra of nano-hole arrays with circular holes, 223 nm in diameter, and 425 nm periodicity in a 100 nm thick gold film for various adhesion layers between gold and Pyrex substrate [5 nm chromium (red curve), 5 nm titanium (blue curve), 10 nm titanium (black curve), etched 10 nm titanium (green curve) and no adhesion layer (purple curve in simulation results)]: (a) simulation results and (b) experimental results. (Pg: Pyrex-gold side). 75

Figure 3-4. The (1,0) optical resonance position versus hole periodicity for nano-hole arrays in a 100 nm gold film with various adhesion layers between the gold and Pyrex substrate [5 nm chromium (red curve), 5 nm titanium (blue curve), etched 10 nm titanium (green curve), and theoretical results (light blue curve in simulation results)]: (a) simulation results and (b) experimental results. 76

Figure 3-5. The spectral transmission modulation ratio for (1,0) resonance peak and its respective minimum versus hole periodicity for nano-hole arrays in a 100 nm gold film with various adhesion layers between gold and Pyrex substrate [5 nm chromium (red curve), 5 nm titanium (blue curve), and etched 10 nm titanium (green curve)]: (a) simulation results and (b) experimental results. 77

Figure 3-6. The (1,0) optical resonance bandwidth versus hole periodicity for nano-hole arrays in a 100 nm gold film with various conductive and adhesion layers between the gold and Pyrex substrate [5 nm chromium (red curve), 5 nm titanium (blue curve), and etched 10 nm titanium (green curve)]: (a) simulation results and (b) experimental results..... 78

Figure 3-7. The spatial distribution of electric field intensity for a xy surface 6 nm above the hole from air-gold side: (a) 5 nm Cr adhesion layer, (b) 5 nm Ti adhesion layer, and (c) etched 10 nm Ti adhesion layer. Spatial distribution of the electric field intensity in the central xz plane of the structure (d) 5 nm Cr adhesion layer, (e) 5 nm Ti adhesion layer, and (f) etched 10 nm Ti adhesion layer. 79

Figure 4-1. (a) A three dimensional schematic view of a NHA with cavities beneath each nano-hole.(b) SEM image of a NHA revealing the cavities (FIB cutting performed in order to observe a cavity beneath each nano-hole)..... 90

Figure 4-2. (a) Schematic of a conventional nano-hole (top) and a nano-hole with cavity (bottom). (b) Spatial distribution of the electric field intensity (log scale) within the nano-hole (xz side view) for a conventional nano-hole (top) and a nano-hole with a cavity (bottom)..... 92

Figure 4-3.	Optical transmission spectra for (a) a conventional NHA and (b) a NHA with cavities when liquids of 1.43, 1.49, and 1.55 refractive index were applied to the top surface. Each NHA had 135 nm circular hole size and 360 nm periodicity.	93
Figure 4-4.	(a) The ratio (η) of the (1,0) resonance peak to (1,0) Wood's Anomaly versus refractive index. (b) Sensitivity [nm/refractive index unit (RIU)] of the (1,0) resonance peak for NHAs of different periodicities. (c) Differential transmission intensity obtained for different refractive index liquids compared to a liquid with a refractive index of 1.58. Measurements were made at 632 nm for the conventional NHA and at 686 nm for the NHA with cavities.	95
Figure 5-1.	(a) A schematic of a NHA in a gold film fabricated on top of sacrificial and substrate layers (top). Also shown is a schematic of a NHA in a gold film where the sacrificial layer has been selectively removed to produce a cavity between the gold film and the substrate (bottom). (b) SEM image (shown at an angle of 54°) of a NHA in a gold film that was FIB milled to reveal the titanium sacrificial layer, the Pyrex substrate, and the presence of a cavity that had a depth of 200 nm (see lower panel).	103
Figure 5-2	(a) Optical transmission spectra of NHAs with 120-nm circular hole size and 400-nm periodicity for 5-nm and 350-nm cavity depths. (b) (1,0) optical resonance position of NHAs versus different cavity depths for NHAs with 120-nm circular hole size and periodicities of 360 nm, 400 nm, and 440 nm.	104
Figure 5-3.	Optical transmission spectra of NHAs with 120-nm circular hole size and 400-nm periodicity collected after a fluid with a refractive index of 1.30 or 1.33 was applied to the free surface. (a) NHA with a 5-nm cavity depth. (b) NHA with a 350-nm cavity depth.....	105
Figure 5-4.	(a) Bulk SPR sensitivity (nm/RIU) (b) Figure of Merit (FOM) for NHAs with 120-nm circular hole size and various periodicities of 360 nm, 400 nm, and 440 nm for 5-nm and 350-nm cavity depths.....	107
Figure 6-1.	(a) A schematic of a NHA in a gold film fabricated on top of sacrificial and substrate layers (top), a schematic of a NHA in a gold film where the sacrificial layer has been etched to form a cavity with uniform depth beneath the NHA (middle), and a schematic of a NHA with nanodisks at the bottom of the cavity (bottom). (b) SEM image (shown at an angle of 54°) of a NHA in a 100-nm gold film that was FIB milled to reveal the titanium sacrificial layer, the Pyrex substrate, and the presence of a 100-nm deep cavity that contained the nanodisks.	115

Figure 6-2 Simulated optical transmission spectra of (a) NHAs with various cavity depths (50 nm, 100 nm, 150 nm, and 200 nm), 140 nm hole diameter and 360 nm periodicity, (b) a nanodisk with 140 nm diameter and 30 nm thickness, and (c) 3D nanostructure containing a NHA in a 100-nm thick gold film (140 nm hole diameter; 360 nm periodicity; cavity depths: 50 nm, 100 nm, 150 nm, or 200 nm; 30-nm thick nanodisks at bottom of the cavity). (d) Visualization of the electric field intensity (xz cross section; LSP coupling resonance wavelength) of a nanohole and a nanodisk for four cavity depths (as indicated at top of each panel; log scale)..... 118

Figure 6-3. (a) Experimental optical transmission spectra of a 3D nanostructure with a NHA in a 100-nm thick gold film with 140 nm hole diameter and 360 nm periodicity for 100 nm and 200 nm cavity depths without nano-disks and (b) with 30-nm thick nano-disks at the bottom of the cavity..... 120

Figure 6-4. (a) Resonance position (LSP coupling between hole and nanodisk) of a perforated 100-nm thick gold film with 360-nm hole periodicity, 50-nm, 75 nm, and 100-nm cavity depth, and 30-nm thick nanodisks at the bottom of the cavity as a function of circular hole and nanodisk diameter taken from simulation (sim) and experimental (exp) results. b) Optical transmission spectra as a function of incident angle of illumination for NHAs with 100-nm hole diameter, 360-nm periodicity, 50-nm cavity depth, and 30-nm thick nanodisks at the bottom of the cavity..... 122

List of Acronyms or Glossary

3D	Three dimensional
BSA	Bovine Serum Albumin
EBL	Electron Beam Lithography
EF	Enhancement Factor
EB_PVD	Electron Beam Physical Vapor Deposition
EOT	Extraordinary Optical Transmission
FDTD	Finite Difference Time Domain
FEP	Fluoropolymer
FIB	Focused Ion Beam
FOM	Figure of Merit
FP	Fabry-Perot
ITO	Indium Thin Oxide
LSP	Localized Surface Plasmon
MUA	11-Mercaptoundecanoic Acid
NA	Numerical Aperture
NHA	Nano-hole Array
NIL	Nano-imprint Lithography
NSOM	Near-field Scanning Optical Microscopy
PBR	Plasmonic Bragg Reflector
PEC	Perfect Electric Conductor
RIU	Refractive Index Unit
SEFS	Surface Enhanced Fluorescence Spectroscopy
SEM	Scanning Electron Microscope
SERS	Surface Enhanced Raman Spectroscopy
SHG	Second Harmonic Generation
SP	Surface Plasmon
SPP	Surface Plasmon Polariton
SPR	Surface Plasmon Resonance
SR	Short Range
SRR	Slit-Ring Resonator

STMR Spectral Transmission Modulation Ratio

1. Introduction

1.1. Overview

Sub-wavelength optics or photonics represents the interaction of light and matter at dimensions smaller than the wavelength of light. The area of sub-wavelength photonics has given a rise to a wide range of novel photonic applications. For example, an array of periodic sub-wavelength apertures perforated in a metal film and metallic sub-wavelength particles have demonstrated unique optical properties, which have not been seen before in larger scale metallic structures in the visible and near infrared ranges [1-1] [1-2]. The occurrence of unexpected optical properties of a sub-wavelength metallic structure is associated with the interaction of light with Surface Plasmon (SP) (so called sub-wavelength plasmonic structure). The unique optical properties of sub-wavelength plasmonic structures have opened up new possibilities for creating and enhancing many photonic applications such as surface enhanced Raman spectroscopy (SERS) and surface plasmon resonance (SPR) sensing [1-3] [1-4]. In this thesis, an array of sub-wavelength apertures in a metal film was studied with respect to the so-called extraordinary optical transmission (EOT), which is not predicted by standard aperture theory [1-5]. The EOT properties of sub-wavelength apertures not only benefits from its high transmission but also provides high localized electric field in vicinity of sub-wavelength apertures [1-6]. These unique characteristics of metallic sub-wavelength apertures could potentially miniaturize photonic devices and overcome diffraction limit of light, which is not achievable with current optical technologies [1-7].

To improve our understanding of the optical properties of a sub-wavelength hole and an array of sub-wavelength holes in a metal film, this chapter includes principles of standard aperture theory, SPs, and SP excitation. Also, it describes previous studies on the dependence of EOT on various parameters of a sub-wavelength hole array in a

metal film, and current applications of plasmonic sub-wavelength holes and sub-wavelength hole arrays. Finally, the objective and scope of the thesis are described to introduce the work performed for chapters 2 through 7.

1.2. Bethe Aperture Theory

An aperture in an optically thick metal film or in a screen is a simple optical element and has a wide variety of uses in optical designs and applications such as near-field scanning optical microscopy and optical imaging. In the twentieth century with the advent of sub-wavelength hole fabrication technology, Bethe theoretically calculated the light transmission through a sub-wavelength round aperture in an infinitely thin perfect electric conductor (PEC) film [1-8]. As shown in Figure 1-1 (a), the scattered light through the sub-wavelength aperture diffracts at the aperture edges. Bethe expressed transmission efficiency of the light through a single sub-wavelength aperture in an infinitely thin PEC film by:

$$\eta_B = 64(kr)^4 / 27\pi^2 \quad 1-1$$

,where $k = 2\pi/\lambda$ is the wave vector of the incident light of wavelength λ and r is the radius of the aperture. As a result, the transmission efficiency drops as $(r/\lambda)^4$, when λ is greater than r and shown in Figure 1-1 (b).

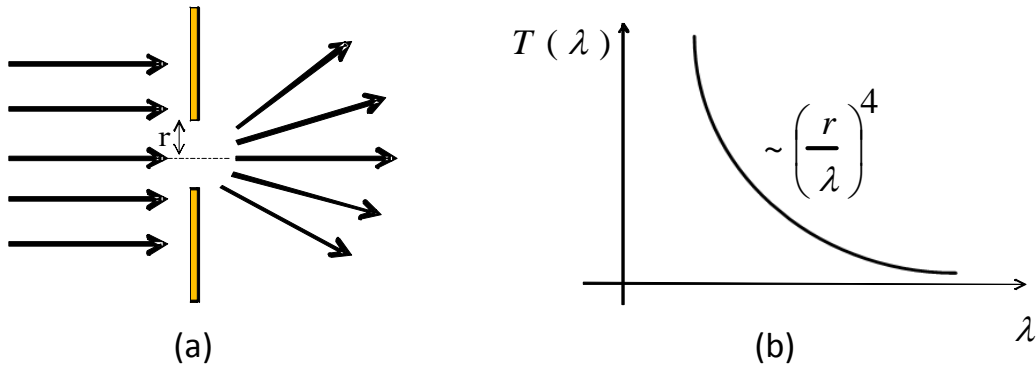


Figure 1-1 (a) Schematic of light diffraction through a sub-wavelength aperture perforated in an infinitely thin PEC film. (b) Typical optical transmission spectra through a sub-wavelength aperture in an infinitely thin PEC film. (adapted from [1-8])

If the real depth of the aperture is considered, the transmission efficiency is attenuated exponentially [1-1]. The exponential decay is related to the fact that the light cannot propagate through the aperture when the wavelength of the light is greater than 2 times the diameter (referred as the cutoff condition) [1-8]. However, the cutoff condition occurs at longer wavelengths when sub-wavelength apertures perforated in real metals are considered [1-1]. It stands to the reason that the light can transfer from propagative to evanescent mode, in the case of real metals. The evanescent mode demonstrates an exponential decay of electromagnetic wave intensity away from interfaces between a metal and a dielectric. Also, the skin depth of metals plays an important role in the penetration depth of the electromagnetic wave into the metal film compared to PEC film [1-2] [1-9].

Experimental measurements revealed the existence of an unexpected enhanced transmission peak in the longer wavelength for a sub-wavelength aperture fabricated in a Ag film, contradicting Bethe aperture theory [1-10]. Bethe aperture theory was formulated for an idealized case and it did not take into account many factors such as surface waves between real metals and dielectrics (i.e. surface Plasmon) [1-1]. The surface waves have a main influence on tunneling the light through the sub-wavelength apertures and generating unexpected optical transmission peaks or resonances.

1.3. Surface Plasmon (SP)

SP is a free-standing electromagnetic wave, due to oscillations of free electrons at the interface between metal and dielectric materials [1-9] [1-11] [1-12]. This results in a strong dependence of SP properties on the dielectric functions of the metal and surrounding dielectric material [1-6] [1-13]. SP waves depend on the roughness of the metal surface, the presence of corrugations, and its periodic metallic structure [1-15]. As shown in Figure 1-2 (a), SP waves exist along the surface of the metal and dielectric materials and are highly localized within the interface area. The SP field intensity drops exponentially into the metal and dielectric materials when it is normal to surface of metal/dielectric interfaces (see Figure 1-2 (b)) [1-9].

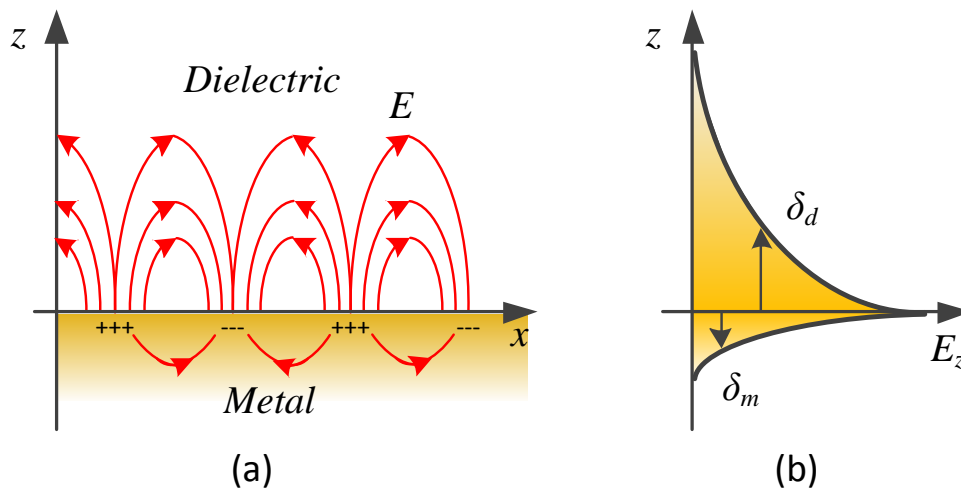


Figure 1-2 (a) Oscillations of free electrons at the interface between metal and dielectric (b) SP decay length into metal (δ_m) and dielectric (δ_d). (adapted from [1-2])

In SP principle, oscillations of free-electrons exist for a metal with a real part of dielectric function less than zero and its magnitude is greater than the dielectric constant of a dielectric material on the metal surface [1-9]. An imaginary part of the dielectric function of a metal causes the attenuation of electromagnetic wave propagating along the surface of a metal and dielectric. Therefore, noble metals (i.e. Ag and Au) have

longer electromagnetic wave propagation lengths along the metal-dielectric surface in optical and near infrared frequencies due to the smaller imaginary part of the dielectric function compared to other metals. The propagation length of the electromagnetic wave along the surface of the metal and dielectric material can be estimated using:

$$L_{sp} = \frac{c}{\omega} \left(\frac{\epsilon'_m + \epsilon_d}{\epsilon'_m \epsilon_d} \right)^{3/2} \frac{(\epsilon'_m)^2}{\epsilon''_m} \quad 1-2$$

,where ϵ'_m and ϵ''_m are the real and imaginary parts of the dielectric function of a metal and ϵ_d is the dielectric constant of a dielectric material. Also, the decay length of the SP propagation normal to the surface of the metal and dielectric and into the metal or dielectric material can be found by:

$$\delta_{sp} = \frac{c}{\omega} \left(\frac{\epsilon'_m + \epsilon_d}{\epsilon_i^2} \right)^{1/2} \quad 1-3$$

where ϵ_i is the dielectric function of the propagation medium (metal or dielectric). For example, the dielectric function of Au from Palik [1-14] was used to calculate and illustrate the electromagnetic propagation length and SP decay length in optical and near-infrared spectrum. The electromagnetic propagation lengths at interfaces of gold-glass and gold-air were calculated using equation (1-2) and shown in Figure 1-3 (a). It is obvious from Figure 1-3 (a) that both propagation lengths along the surfaces increase for longer wavelengths while the propagation length is higher for a gold-air interface compared to a gold-glass interface.

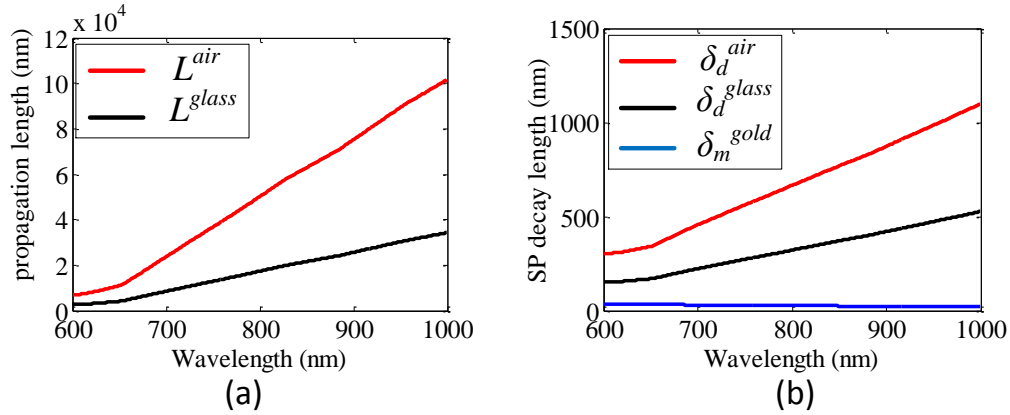


Figure 1-3 (a) *Electromagnetic propagation length along the surfaces of glass-gold and air-gold interfaces.* (b) *SP decay length normal to gold/dielectric interface into air, glass, and gold.*

The SP decay lengths were calculated for gold and away from gold into air and glass dielectrics using equation (1-3) as shown in Figure 1-3 (b). The SP decay length is short for gold and is approximately equivalent to the skin-depth, while the SP decay length for air and glass dielectrics (at the gold interface) is much longer [1-2] [1-9]. The SP decay length increases for air and glass at longer wavelengths. However, the SP decay length for glass is lower than for air at all wavelengths.

1.4. Surface Plasmon excitation

The SPs can be excited using electrons impinging on a metal. However, SP excitation cannot be simply done optically. Light does not excite or couple to SPs on a smooth metal-air interface. This is due to the fact that light momentum is not sufficient to couple to SP. From the conservation of energy, the dispersion relation of SP on a smooth metal film can be expressed by:

$$|\vec{k}_{sp}| = |\vec{k}_0| \sqrt{\frac{\epsilon_m \epsilon_d}{\epsilon_m + \epsilon_d}} \quad 1-4$$

, where ϵ_d and ϵ_m are the dielectric constant of the dielectric, and the dielectric function of metal, respectively, and $\vec{k}_0 = \frac{\omega}{c}$ is the free space wavenumber of the incident excitation photon. The dispersion curves of light and SP are shown in Figure 1-4 (a).

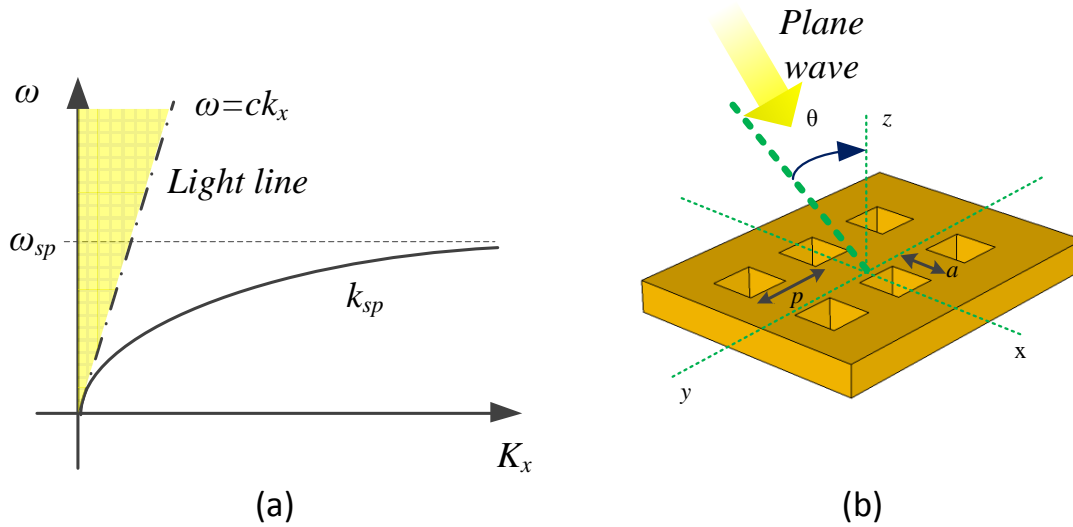


Figure 1-4 (a) Dispersion curves of SP and light line ($\omega = ck_x$), ω_{sp} is a SP frequency. (b) Two-dimensional grating of a square lattice holes: p is the spacing between adjacent holes and a is the width of holes.

The SP curve is located outside the accessible region surrounded by the light line so the light cannot excite SPs at the interface between metal and dielectric. At any specific wavelength, SPs have higher momentum than incident light at the dielectric-metal interface, so features such as prisms, gratings, or surface roughness are necessary to increase the momentum of light to excite SPs [1-2] [1-9]. In the case of a two-dimensional grating in a metal film (e.g. an array of periodic holes in a metal film), light momentum increases due to the grating structure and results in coupling of light to SP. When a plane wave is incident on a grating structure with a square lattice arrangement, the dispersion relation between light and SP on a metallic grating structure can be expressed by:

$$\vec{k}_{sp} = \vec{k}_0 \sin \theta \pm i \vec{u}_x \pm j \vec{u}_y \tag{1-5}$$

,where $\vec{k}_0 \sin \theta$ is the in-plane component of the wave vector of the incident light, $k_0 = \omega/c$ [1-2] [1-5]. \vec{u}_x and \vec{u}_y are the reciprocal lattice wave vectors for a square lattice with $|\vec{u}_x| = |\vec{u}_y| = 2\pi/p$ (p is spacing between adjacent holes), and i and j are integers expressing the scattering mode indices (some examples of i and j are illustrated in Figure 1-5) . Inserting equation (1-4) into equation (1-5) results in the dispersion relation between light and SP, which is formulated as:

$$|\vec{k}_{sp}| = \left[\left(\frac{2\pi}{\lambda} \sin(\theta) + i \frac{2\pi}{p} \right)^2 + \left(j \frac{2\pi}{p} \right)^2 \right]^{1/2} = |\vec{k}_0| \sqrt{\frac{\epsilon_m \epsilon_d}{\epsilon_m + \epsilon_d}} \quad 1-6$$

1.5. Extraordinary Optical Transmission of sub-wavelength hole arrays

Thomas W. Ebbesen discovered that an array of periodic sub-wavelength holes fabricated in an optically thick metal film resulted in extraordinary optical transmission (EOT) phenomena [1-5]. This unique optical property surpasses the diffraction limit of light and is due to excitation of SP waves that exist at the interface of the metal and the dielectric. The excitation of SP occurs due to momentum matching between the SP and the light on account of the periodic arrangement of the sub-wavelength holes [1-5]. This results in the coupling of the light to the SP and evanescent transmission through the sub-wavelength hole array. Finally, the light decouples from SP and radiates to free space. For a normally incident plane wave on an array of periodic sub-wavelength holes (by inserting $\theta = 0$ in equation (1-6)), the wavelengths at which the SP excitation modes can be expressed for a grating or sub-wavelength hole structure with square lattice arrangement by:

$$\lambda_{max} = \frac{p}{\sqrt{i^2 + j^2}} \left(\frac{\epsilon_m \epsilon_d}{\epsilon_d + \epsilon_m} \right)^{1/2} \quad 1-7$$

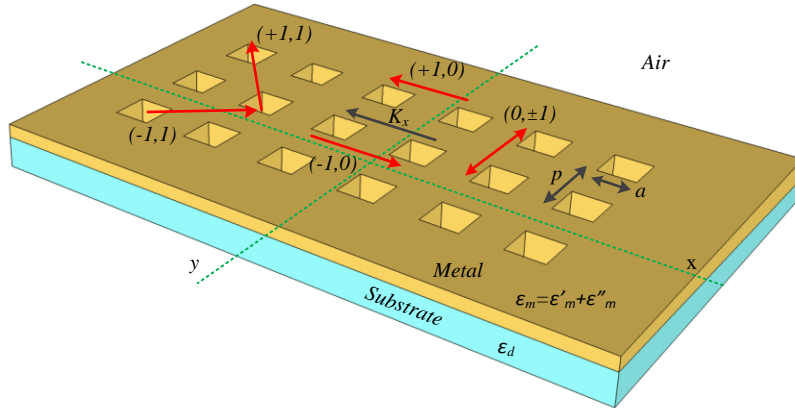


Figure 1-5 A 2-dimension sub-wavelength hole array in a metal film on a substrate in a square lattice arrangement. p is the spacing between two adjacent holes, a is a width of each hole, K_x wave vector of the light is along the x-axis, and $(+1,0)$, $(-1,0)$, $(0,\pm 1)$, $(+1,1)$, and $(-1,1)$ are various (i, j) grating modes.

The equation (1-7) can be used to estimate the EOT positions of sub-wavelength hole arrays for various SP excitation modes (i, j) when incident light is normal to the surface of sub-wavelength hole array [1-5]. Also, the various SP excitation modes depend greatly on a direction of the light wave vector (K_x). For example, when the wave vector of the light (K_x) is along the x-axis, various (i, j) SP excitation modes related to metal/air or metal/substrate interfaces are shown in Figure 1-5. The $(+1,0)$, $(-1,0)$, $(0,\pm 1)$, $(+1,1)$, and $(-1,1)$ are various grating modes, which result in various SP excitation modes from metal/air or metal/substrate sides by the light as shown in Figure 1-5. Also, other grating modes such as $(+2,0)$ and $(-2,0)$ exist, which were not illustrated in Figure 1-5. In this example, the $(\pm 1,0)$ SP excitation modes are parallel to the wave vector of the light (K_x) while the $(0,\pm 1)$ SP excitation mode are perpendicular to the K_x . However, when the light is normal to the surface of the sub-wavelength hole array, the $(\pm 1,0)$ and $(0,\pm 1)$ SP excitation modes result in a spectral overlap in the optical transmission spectra of the structure and a single resonance called $(1,0)$ EOT peak. This is similar for $(+1,1)$, and $(-1,1)$ in the case of light that is normal to the surface of the sub-wavelength hole array.

In a similar way of calculating EOT positions, a transmission minimum (Wood's anomaly) occurs before each EOT at a shorter wavelength. The transmission minimum is due to the diffraction of light by the grating and its propagation in the dielectric. In the case of the transmission minimum, the diffracted wave becomes tangent to the grating and propagates within the dielectric. As a result, the diffracted wave matches the grating periodicity:

$$k_{diff} = \frac{\omega}{c} \sqrt{\epsilon_d} = i \vec{u}_x \pm j \vec{u}_y \quad 1-8$$

,where ϵ_d is dielectric constant of propagation medium. The position of the transmission minimum for a sub-wavelength hole array can be expressed as:

$$\lambda_{min} = \frac{p}{\sqrt{i^2 + j^2}} (\epsilon_d)^{1/2} \quad 1-9$$

1.6. Dependence of EOT on various parameters of the sub-wavelength hole array:

The EOT or resonance properties of sub-wavelength hole arrays can be characterized by the resonance position, resonance transmission efficiency, resonance steepness, resonance bandwidth, and enhanced electric field at the edges of sub-wavelength holes at the resonance wavelengths. All the aforementioned resonance properties of a sub-wavelength hole array play an important role in the efficiency of its applications. However, resonance properties depend greatly on composition of the metal and dielectric materials, various geometrical arrangements of sub-wavelength holes, sub-wavelength hole shapes, and so forth. Many studies have investigated the effect of the geometrical parameters of sub-wavelength hole arrays in various metal films by means of simulation, experiments, and theoretical calculation [1-13], [1-15]-[1-40].

1.6.1. *Materials and geometries*

It has been observed that the optical resonant transmission peaks for sub-wavelength hole arrays in noble metal films such as Au, Ag, and Cu were higher than the other metal films for the same geometrical parameters [1-13]. For arrays in Ni and Cr films, the absorption properties of these metals strongly reduce the resonance transmission efficiency [1-15]. Also, sub-wavelength hole arrays in noble metals demonstrated lower (1,0) resonance bandwidth compared to structures with the same geometrical parameters but fabricated in Ni or Cr metal films [1-15]. This results from the lower absorption of noble metals than the other metal films in the optical and near infrared regime.

SP excitation modes of sub-wavelength hole arrays are dependent on the scattering orders of the holes and dielectric properties of the materials on the top and bottom of the metal [1-6]. The higher refractive index of dielectric materials results in an occurrence of resonance positions at longer wavelengths [1-6]. As a result, the optical resonance peaks related to sub-wavelength hole arrays can be controlled by deposition of materials with a refractive index either below, equal to, or greater than the refractive index of the substrate such as Quartz. Materials with the same dielectric constant in contact with the top and bottom surfaces of the sub-wavelength hole array in the metal film result in the coincidence of the SP resonance energies for SP modes on both surfaces of the metal film [1-6] [1-16]. The optical transmission spectra of a sub-wavelength hole array can be manipulated by changing the refractive index of a liquid material above the array relative to the material in contact with the underside of the array. The matching of SP resonance energies increases the EOT by a factor of 10 or more [1-6] [1-16]. Also, the electric near field intensity in the vicinity of the holes is significantly increased at the resonance wavelengths for the hole array at the SP matching condition [1-6] [1-17]. Furthermore, matching the SP energy of the top and bottom dielectric materials of sub-wavelength hole arrays results in a narrower resonance bandwidth [1-17] [1-18].

The number of holes in a sub-wavelength hole array influence the propagation of electromagnetic waves on metal/dielectric interfaces. A low count of sub-wavelength

holes results in a lower resonance transmission efficiency and wider resonance bandwidth of the sub-wavelength hole array structure [1-19]. However, for an array with a size greater than the electromagnetic propagation length (equation (1-2)) the resonance properties of the structure reach the highest transmission efficiency and narrowest bandwidth. Also, Przybilla et. al. demonstrated that as the number of holes increased from low count to high count (i.e. greater than SP propagation length), the resonance position blue-shifted [1-19].

The transmitted light efficiency at the resonance position of a sub-wavelength hole array can be improved by the use of a plasmonic bragg reflector (PBR) around its structure [1-20] [1-21]. For example, Gordon et. al. demonstrated that a periodic groove or dimple with a half periodicity of the array positioned at the edges of sub-wavelength hole array improved resonance transmission properties of the sub-wavelength hole array [1-21]. This was due to the fact that the PBR induces back reflection of SP waves into the region of the sub-wavelength hole array, resulting in an almost 2-fold enhancement in the resonance transmission efficiency [1-21]. Nevertheless, the resonance bandwidth of this structure with PBR did not change significantly although the resonance transmission efficiency increased.

The enhanced transmission resonance of a sub-wavelength hole array is dependent greatly on the hole size [1-22] [1-23]. The transmission efficiency of a sub-wavelength hole array with square holes at the resonance wavelength increases with size for smaller hole sizes (e.g. hole with an open air fraction less than 20%). Nevertheless, transmission efficiency at the resonance saturates for larger hole sizes [1-22]. The resonance bandwidth of the structure becomes broader for holes with larger square or circular size [1-23], due to an increase in the cut-off wavelength of sub-wavelength holes. The resonance position slightly changes for different hole sizes in case of square and circular holes [1-23].

Another important parameter to be considered is the thickness of metal film. Degiron et. al. demonstrated that sub-wavelength holes fabricated in metal films thinner than 200 nm had a higher transmission efficiency at the resonance position and the resonance transmission efficiency did not change significantly with the metal film

thickness [1-24]. This result was likely due to the SP coupling between the top and bottom surfaces of the sub-wavelength hole array in the metal film. However, for a metal film thicker than 200 nm, the resonance transmission efficiency of the sub-wavelength holes exponentially decayed as the thickness of metal film increased. That is, in the case of uncoupling of the SP from top and bottom of the metal film, the exponential decay of resonance transmission efficiency was experimentally demonstrated [1-24].

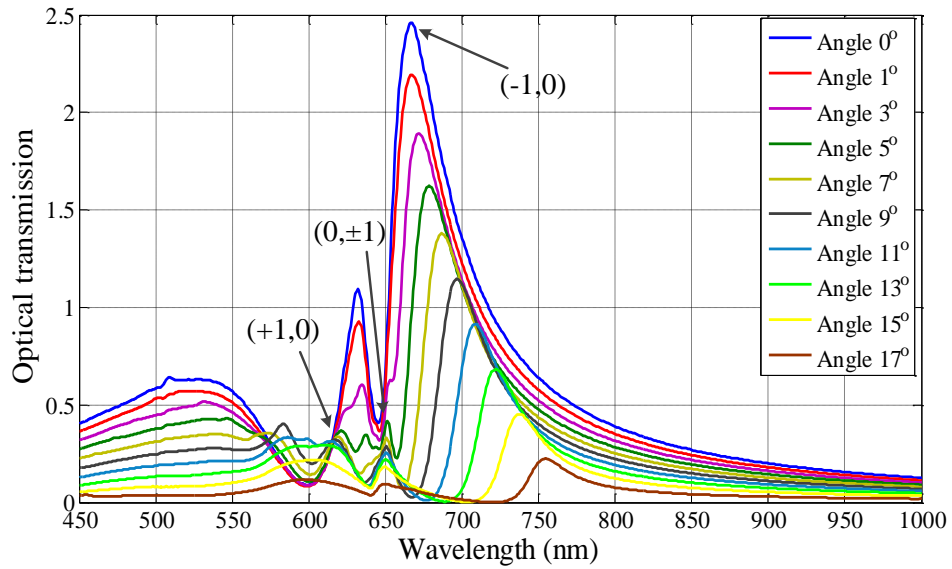
The hole-shape has an influence on the waveguide properties of the hole as well as the scattering of electromagnetic waves on either side of the hole in the metal film. The hole-shape can also be employed to influence the polarization of the electromagnetic wave and intensify the electric near-field [1-25] [1-26]. For example, a sub-wavelength hole with a sharp apex double-hole structure produces a higher electric near-field intensity compared to two holes separated by a short distance [1-25]. A sub-wavelength hole array with rectangular or elliptical holes provides for a strong polarization dependence of the transmission at the resonance position [1-26].

The resonance properties of a sub-wavelength hole array change with respect to arrangement of holes due to modification of light coupling to SP waves [1-27]. For example, it was shown that the resonance position for an array of hexagonally arranged holes occurs at a shorter wavelength than an array with the same periodicity in a square lattice arrangement [1-27]. Moreover, a sub-wavelength hole array with unsymmetrical periodicity (biaxial array) exhibited resonances polarization dependency [1-28]. For a sub-wavelength hole array with a rectangular lattice arrangement, the light polarized along width excites surface waves on width of the array and the light polarized along length of the array excites surface waves on length of the array [1-28]. The resonance of a hole array with a double-hole arrangement had a transmission that depended on linearly polarized light, for which the polarization depended on the orientation of double holes [1-29].

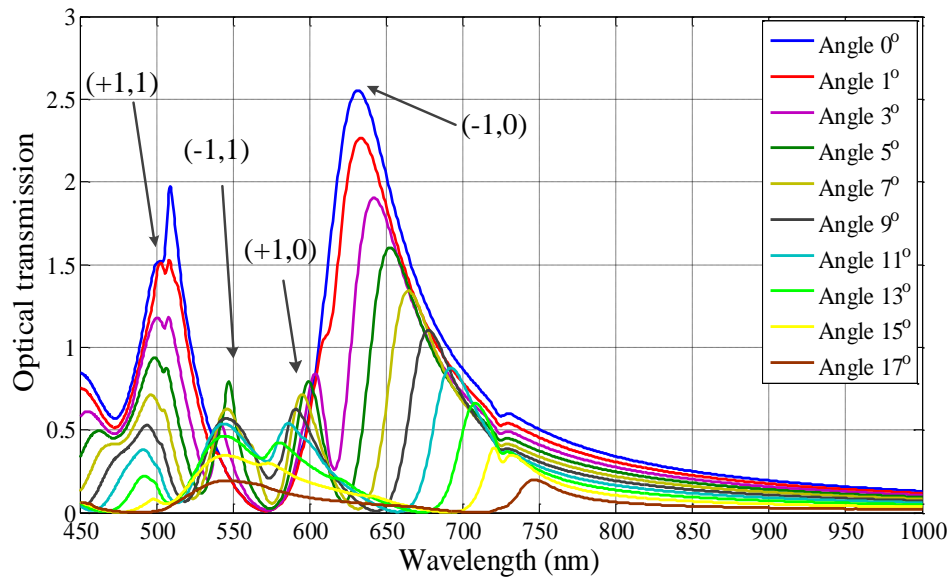
1.6.2. *Illumination angle*

The angle of incident light on a sub-wavelength hole array in a metal film changes its optical transmission properties. The resonance properties of a sub-

wavelength hole array such as its position, bandwidth, and transmission efficiency depend greatly on incident angles of light as shown before [1-30]-[1-32]. It was demonstrated that the resonance bandwidth of the (-1, 0) SP excitation mode varied as the incident angle of light increased [1-30]. Furthermore, an increase in the incident angle of the light blue-shifted or red-shifted resonance positions of a sub-wavelength hole array and the changes in wavelength depended on the SP excitation modes [1-30]-[1-32]. For example, the optical transmission spectra of a sub-wavelength hole array with 200 nm circular holes and 400 nm periodicity in a square lattice arrangement in Au and Ag films were simulated as a function of incident illumination angle and are shown in Figure 1-6 (a) and (b) for the structures in 100 nm Au and 100 nm Ag films, respectively. In the Finite Difference Time Domain (FDTD) simulation model (FDTD solution obtained using a software package from Lumerical Inc.), a plane wave source was used to illuminate a sub-wavelength hole array with an infinite number of holes. As the incident angle of the light was tilted away from the normal, the resonance peak associated with the (-1, 0) SP excitation red-shifted. Also, other resonance peaks related to SP excitation modes such as (0, ±1) and (+1, 0), not normally visible, appeared in the transmission spectra for higher incident angles of illumination. However, they had different behavior than the (-1, 0) SP mode at higher illumination angles. Many other resonance peaks for a sub-wavelength hole array in a silver film appeared at shorter wavelengths and were associated with the (+1, 1) and the (-1, 1) SP excitation modes. The characteristics of gold and its SP properties related to the dielectric material did not provide a strong coupling of the light to SP for wavelengths below 570 nm as well as below the bulk plasma wavelength (500 nm) [1-13] [1-15]. This result was clearly observed in Figure 1-6 (a) since no strong resonances were present below 570 nm for the gold material, while a strong EOT was observed for the silver material at a variety of incident angles of illumination.



(a)



(b)

Figure 1-6 *Optical transmission of a sub-wavelength hole array as a function of incident angle of illumination for (a) gold and (b) silver films. Each spectrum is offset vertically by 0.1% from the preceding spectrum for clarity. The EOTs related to $(0, \pm 1)$, $(+1, 0)$, $(+1, 1)$ and $(-1, 1)$ SP excitation modes are also indicated.*

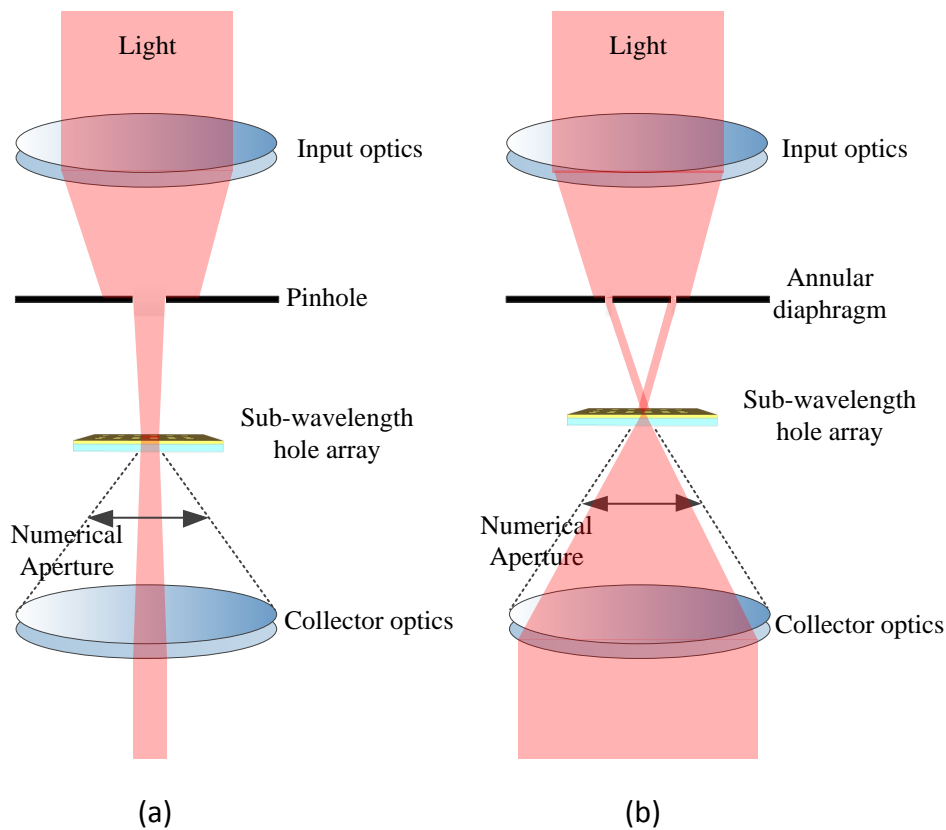


Figure 1-7 *Optical characterization setup diagram for two different incident angles of illumination on a sub-wavelength hole array using a) a pinhole and b) an annular diaphragm*

In optical transmission-based characterization setup for a metallic sub-wavelength hole array (sample) the input optics, diaphragm, and collector optics can be employed in such a way as to illuminate the sample and collect the light transmitted through the sample at various incident angles as shown in Figure 1-7. The various illumination angles result in various SP excitation modes and reveal different optical properties of the sub-wavelength hole array. For example, in Figure 1-7 (a), collimated light was directed on a sub-wavelength hole array by using input optics and a pinhole to select a narrow range of incident angles of light on the sample. A smaller size pinhole

results in a smaller acceptance angle of the incident light on the sample. At the end, the collector optics accepts light transmitted through the sample with a defined angle based on the numerical aperture. In Figure 1-7 (b), an annular diaphragm was used instead of a pinhole and a specific incident angle of the light was selected to illuminate the sample. Then, the transmitted light through the sample was collected by the collector optics, which has an angular acceptance larger than the angular distribution of the incident light for collection of the transmitted light.

1.6.3. Fabrication methods

Fabrication is a key determinant in the control of resonance transmission properties of sub-wavelength hole arrays [1-23], [1-32]-[1-37]. For example, in this thesis, electron beam lithography (EBL) method with a lift-off process was employed to fabricate sub-wavelength hole array structures. The resulting sub-wavelength hole arrays had small edges around each hole in the structure due to the lift-off process of this fabrication method. As a result, the light transmitted through the structure at resonance wavelength decayed and showed a wider bandwidth due to absorption of the light by the edges around each hole [1-23]. This effect becomes negligible when the sub-wavelength holes are fabricated with a lift-free process and EBL and results in higher transmission at resonance with a narrower bandwidth [1-32]. Other fabrication methods such as focused ion beam (FIB) and nano-imprint lithography (NIL) for fabrication of sub-wavelength hole arrays have some deficiency and benefit in EOT properties of these structures [1-33] [1-34]. For instance, in FIB milling, a fabricated hole in a metal film does not have the same area at different depths of the film presenting a funnel-shape or V-shape [1-33]. This results in a more variable optical transmission of the structure compared to the structure fabricated with other methods. In addition to the aforementioned fabrication methods, interference lithography and phase-shifting lithography have been used to fabricate large sub-wavelength hole array structures [1-35] [1-36]. In addition, sub-wavelength polystyrene spheres in a hexagonal arrangement have been used as a mask to fabricate sub-wavelength hole arrays at a large scale [1-37].

In order to fabricate a sub-wavelength hole array, some fabrication methods require additional layers such as adhesion and conductive layers depending on the material selection and fabrication methods. It is well-known that sub-wavelength hole arrays fabricated in a gold film on a Pyrex substrate require an adhesion layer such as indium thin oxide (ITO), Cr, or Ti [1-23]. Although a thin layer of these materials can be employed in the fabrication process, they have a significant influence on the resonance transmission properties of the structure [1-38]. For example, a sub-wavelength hole array fabricated in a gold film on a Cr adhesion layer has a weak resonance transmission related to SP excitation from metal-glass side due to high absorption properties (ohmic loss) of the Cr material. Another study showed improvement of resonance transmission properties of a single sub-wavelength hole in a gold film for enhancing fluorescence signals when a TiO₂ adhesion layer between gold and glass was used [1-39].

Surface roughness of the metal is dependent on the deposition method, accuracy of the deposition machine, and the grain size of the metal. The metal surface roughness influences the resonance transmission properties of a sub-wavelength hole array since SP propagation change with respect to surface structure [1-40]. As a result, a metal film with a rough surface could cause SP energy absorption, lower electromagnetic propagation, and lower transmission efficiency at the resonance peak. Surface roughness also enhances the local electric field near the film surface, although this has been shown to depend greatly on the grain size of the metal [1-41].

1.7. Applications of Sub-wavelength hole arrays:

1.7.1. *Surface Plasmon Resonance (SPR) sensing*

In SPR sensing applications, the optical and physical characteristics of sub-wavelength hole arrays enable device miniaturization, integration into microfluidic structures, and multiplexed analysis in contrast to the conventional Kretschmann configuration and colloidal nano-particles [1-4] [1-6]. Sub-wavelength hole arrays with various geometrical parameters can be fabricated on a single substrate, which can

provide various optical responses from different sub-wavelength hole arrays for a specific analyte [1-42] [1-44].

In SPR sensing, changes in the refractive index of the material at the top or bottom of the sub-wavelength hole array in a metal film results in a measureable change in the resonance transmission properties [1-6] [1-17] [1-18]. For example, a higher refractive index of the dielectric material on the metal film red-shifts the resonance peak to the longer wavelengths [1-6]. Also, the SPR sensitivity of sub-wavelength hole array depends on the bandwidth of the resonance and it is characterized by the resonance shift per refractive index unit (nm/RIU). An analytical expression was developed for describing the SPR sensitivity of a sub-wavelength hole array in terms of the resonance shift with respect to a RIU for illumination that is normal to the sub-wavelength hole array surface [1-45]:

$$S = \frac{\Delta\lambda}{\Delta n} = \lambda \frac{\varepsilon_m}{n(n^2 + \varepsilon_m)} = \frac{p}{\sqrt{i^2 + j^2}} \sqrt{\left(\frac{\varepsilon_m}{n^2 + \varepsilon_m}\right)^3} \quad 1-10$$

,where λ is wavelength, p is periodicity between holes, i and j define the scattering order of the holes (i.e. resonance modes), ε_m and n are the permittivity of the metal and refractive index of the dielectric, respectively. The SPR sensitivity depends significantly on the periodicity of holes and the resonance modes. For example, a low resonance mode of a sub-wavelength hole array (e.g. (0, 1) resonance mode) with a large periodicity can significantly increase the SPR sensitivity of a sub-wavelength hole array. In addition to the dependence of SPR sensitivity on the geometry of the sub-wavelength hole array, it has been demonstrated that a sub-wavelength hole array with a sharp-apex double hole had enhanced SPR sensitivity compared to a device with separate holes [1-46]. Also, an enhanced SPR sensitivity and a reduced bandwidth were observed for a sub-wavelength hole array fabricated with a lift-off free fabrication method [1-32]. In another study, sub-wavelength hole arrays fabricated on fluoropolymer substrate (FEP) enhanced the sensing performance for biological solutions by 20% due to the similar refractive indexes between the substrate and the solution [1-47].

For a sub-wavelength hole array with a low hole count (e.g. < 100 holes), it is well known that the optical transmission at EOT peak is lower and the bandwidth is wider than a sub-wavelength hole array with a large hole count (e.g. > 400 holes) [1-19]. SPR sensitivity values reported in the literature are 285 nm/RIU for sub-wavelength hole arrays with a low hole count versus 313 - 400 nm/RIU for sub-wavelength hole arrays with a high hole count [1-36]. An increase in the optical transmission of low hole count sub-wavelength hole arrays is possible by incorporation of a Bragg-reflector around the sub-wavelength hole array; however, the resonance bandwidth remains relatively unchanged [1-43]. Other sub-wavelength hole structures in 3D shape demonstrated different SPR sensitivity compared to the plane sub-wavelength hole arrays [1-48]-[1-50]. For example, a quasi 3D structure consisting of a sub-wavelength hole array having each hole aligned with a sub-wavelength disk demonstrated a higher SPR sensitivity of 700 to 800 nm/RIU [1-48]. Furthermore, the same structure with further distance between holes and disk showed a Fabry-Perot (FP) resonance peak, which had SPR sensitivity of 305 nm/RIU [1-49]. Another 3D structure with pyramid hole shape had a localized SPR due to the 3D structure of hole shape and its sensitive area for SPR sensing was localized within 60 nm from the metallic structure [1-50].

A sub-wavelength hole array in gold can be employed to monitor the binding of organic and biological molecules via changes in its resonance properties [1-51]-[1-53]. For example, it was demonstrated that a monolayer binding to 11-mercaptoundecanoic acid (MUA) on the sub-wavelength hole array changes the resonance position. In addition, attachment of bovine serum albumin (BSA) on top of MUA, changes further the resonance position of the sub-wavelength hole array [1-51]. The binding of an analyte to a metal surface is relatively long process and this results in gradual changes of the resonance transmission properties of a sub-wavelength hole array over time. However, the time response of this type of sensor can be improved by a sub-wavelength hole array with flow-through structure, which demonstrates multi-fold faster binding of an analyte [1-54] [1-55].

1.7.2. Surface Enhanced Raman Scattering (SERS)

Raman scattering signals acquired from molecules are weak using a normal Raman scattering spectroscopy method. However, if molecules are adsorbed in proximity of Plasmonic sub-wavelength structures, SERS signals from the molecules can be obtained [1-56] [1-57]. The enhancement factor (EF) of Raman signals can be multiple orders of magnitude when plasmonic structures are used. The EF of the SERS signal depends greatly on the sub-wavelength structure, its resonances, and the electric field enhancement on the surface of the structure. Various plasmonic sub-wavelength structures have been employed in SERS such as colloidal nano-particles, nano-particles on a substrate, and sub-wavelength hole arrays in a metal film. For example, a sub-wavelength hole array in a gold film significantly enhanced the Raman signal when the laser excitation matched the resonance transmission position of the structure. Specifically, the maximum measured SERS EF for an oxazine 720 molecule adsorbed on the sub-wavelength hole array structure was 10^5 relative to its normal Raman signal [1-57].

The SERS signal for sub-wavelength hole arrays can be enhanced even more by changing the shape of the sub-wavelength hole. A sub-wavelength hole array with a double hole structure provides for a strong electric field when the edges of two holes overlap to form sharp apexes. As a result, the SERS EF for a structure with sharp apexes was found to be an order of magnitude higher compared to a structure with standard holes [1-3].

A quasi-3D sub-wavelength hole array structure consisting of sub-wavelength hole array with an sub-wavelength disk aligned to each hole has been employed as a versatile SERS substrate [1-58]-[1-60]. This is due to the fact that it can be fabricated on various substrate materials, such as glass and polymer using a variety of fabrication methods. Also, its EF of SERS signal is about 10^7 and it is higher than that of 2D planar sub-wavelength hole array due to the SP interactions of a hole and the disk [1-60]. Moreover, the multiple resonance peaks of the structure related to FP, SP propagation and localized SP effects allow this quasi 3D structure to have high electric field in the wide spectrum. As a result, many studies have been performed to investigate the effect

of various substrates and materials as well as the effect of distance between hole and disk on SERS EF of this quasi-3D structure [1-58]-[1-60].

1.7.3. *Optical Trapping*

Optical trapping has been employed in a wide range of biological and non-biological particles such as cells, viruses, DNA, and colloidal spheres [1-61]-[1-63]. Recently, it has been demonstrated that a nano-polystyrene sphere (50-nm in diameter) can be trapped optically via the resonance transmission of a nano-hole in a metal film [1-61]. It has been demonstrated that a double-hole with sharp apex can provide more efficient optical trapping of a nano-sphere with small size (12-nm and 20-nm in diameter) compared to a single nano-hole [1-62]. This effect was due to a higher electric field intensity at the sharp apex of the double-hole than a single hole structure. Also, in the recent published article, a single protein BSA molecule with hydrodynamic radius of 3.4 nm was optically trapped using a nano-double-hole structure with sharp apexes [1-63].

Optical trapping of molecules and particles could potentially be one of the most important applications for sub-wavelength hole arrays due to the enhanced electric near-field in proximity of the structure. Also, the resonance transmission position of the sub-wavelength hole array can be easily tuned by hole periodicity in order to match the excitation wavelength of the laser. A sub-wavelength hole array having an optimized structure with the highest electric field could be designed specifically for the purpose of trapping a specific particle or molecules [1-4].

1.7.4. *Near-field scanning optical microscopy (NSOM)*

Near-field scanning optical microscopy (NSOM) has been explored as the first practical application of a sub-wavelength hole or holes. Early work demonstrated that NSOM used sub-wavelength holes in metal-coated optical probes. Unlike conventional microscopy, these hole based systems demonstrated that spatial resolution was dependent on the hole size rather than the wavelength of light. However, the optical transmission of a sub-wavelength hole was dependent on the hole size and it was inversely proportional to the square of hole area [1-8]. Other sub-wavelength hole

shapes were explored to improve the transmitted power at the resonance wavelength of the structure [1-64]-[1-67]. For example, a sub-wavelength hole with a C-shaped design increased the transmitted power with high near-field intensity compared to a circular hole shape [1-64] [1-65]. Other plasmonic structures employed a combination of a C-shaped hole with a nano-tip antenna for the NSOM tip in order to improve resolution and intensity and to reduce background illumination [1-66].

1.7.5. Optical filters

Sub-wavelength hole arrays in a metal film can be employed as a spectral filter and polarizer [1-68]. A resonance peak of a sub-wavelength hole array performs as a spectral filter in the optical and the near infrared regime. Due to various SP excitation modes of a sub-wavelength hole array by light, different resonance transmission peaks occur in the transmission spectra and can perform as multiple band pass spectral filters. Dickson et. al. demonstrated that a sub-wavelength hole array structure encapsulated by a liquid crystal such as E7 can be used as a tunable spectral filter by changing the refractive index of liquid crystals electrically [1-69]. It resulted in changing the resonance position of a sub-wavelength hole array. However, the resonance bandwidth depended on many parameters such as hole size, periodicity, hole shape, material characteristics, and fabrication method. As a result, the resonance bandwidth of a sub-wavelength hole array cannot be simply tuned to a desired value [1-23] [1-30].

The resonance transmission of a sub-wavelength hole array could depend on light polarization based on its hole shape and lattice arrangement [1-26] [1-29]. The structure with elliptical or rectangular hole shape can be employed as a sub-wavelength polarizer, which changes resonance transmission efficiency of the structure in terms of polarization orientation in incident light [1-26]. The similar influence of polarization control can be performed by the lattice arrangement of the structure but due to its dependence on the scattering direction of SP waves [1-29].

1.7.6. *Non-linear Optics*

Phase-matching and intense local fields can enhance nonlinear optical conversion by materials. Appropriately designed plasmonic sub-wavelength structures can provide highly localized electric fields as well as produce a phase-matching condition [1-70]-[1-74]. For example, a metallic single sub-wavelength hole surrounded by a periodic corrugation can provide a resonant enhancement of second-harmonic generation (SHG) by a factor of 10^4 [1-70]. This is due to enhanced transmission of the optical field below the diffraction limit of the light and produces an intensified electric field in the vicinity of the hole structure. Also, it has been demonstrated that a sub-wavelength hole array with a random distribution of holes generates a higher SHG signal compared to a structure with square lattice arrangement [1-71]. This effect resulted from the symmetry breaking property of the structure. However, a greater SHG signal was produced by a structure with a quasi-periodic lattice [1-72]. In another study, it was demonstrated that a sub-wavelength hole array with a double-hole structure produced the greatest SHG signal when the double-holes were just overlapping to make two sharp apexes [1-73] [1-74]. This could be expected due to high electric field at the two sharp apexes.

1.7.7. *Absorption spectroscopy*

Sub-wavelength hole arrays in a metal film could enhance absorption detection in infrared spectroscopy. For example, a 300-fold enhancement was achieved in infrared absorption of alkanethiol self-assembled monolayers on a sub-wavelength hole array in a Ni film and coated with Cu compared to reflection infrared absorption spectroscopy [1-75]. The enhancement was due to a strong coupling between molecules and an intensified electric near field on the metal surface in both the visible and the infrared regime [1-76].

In enhanced infrared absorption spectroscopy, the sub-wavelength hole sizes and hole spacing between adjacent holes are above micron sizes since infrared is the

regime of interest. Therefore, fabrication of a sub-wavelength hole array can be done simply by optical lithography instead of EBL and/or FIB.

1.8. Interpretation and analysis of the literature:

The effects of hole size, hole shape, and periodicity on optical transmission properties of a sub-wavelength hole array have been studied by means of simulation and experiments previously [1-13][1-15] [1-22]. However, various fabrication methods were used in different studies and resulted in inconsistent measurements of the optical transmission properties of sub-wavelength hole arrays. Moreover, major analysis in previous literature was done on the (1,0) optical resonance peak of the sub-wavelength hole array and other resonance peaks such as (1,1) were not thoroughly studied [1-13] [1-15]. Also, previous studies investigated an influence of the geometrical parameters by means of simulation and experiments separately. Therefore, a major systematic study on the geometrical parameters by experiments and matched simulation models were warranted in order to determine the effects of the geometrical parameters on the resonance properties of the sub-wavelength hole array.

The sub-wavelength hole array perforated in a gold film requires a thin adhesion layer between the gold film and the substrate. It has been demonstrated that the optical resonance transmissions of a sub-wavelength hole array related to the substrate-gold side were significantly reduced due to the presence of an adhesion layer [1-23]. However, no systematic study using the combined approach of simulation and experiment has been performed to investigate the effect of the composition and thickness of adhesion layer on the optical resonance properties of sub-wavelength hole arrays.

Throughout the previous studies, sub-wavelength hole arrays have been fabricated on a solid substrate such as a glass or polymer due to the delicacy of the thin metal film. It is also well-known that the SP energy matching results in 10-fold enhancement in optical resonance transmission compared to the case lacking the SP matching condition [1-6] [1-16]. Also, the electric near field intensity at the hole edges is

enhanced when the SP matching condition between the two surfaces of the sub-wavelength hole array is met. However, the SP energy matching condition between the top and bottom of a sub-wavelength hole array has been restricted to materials that can be deposited on to the film that have similar dielectric constant to the substrate [1-6]. Specifically in SPR sensing applications, it has been demonstrated that there is not always a good dielectric matching between the refractive indices of various biological solutions and the substrate of the sub-wavelength aperture array [1-47]. Based on this fact, the interference of the resonance peaks with the same mode from the substrate and biological solution could result in poor SPR sensitivity [1-47]. Furthermore, the SP energy matching between the top and bottom surfaces of the sub-wavelength hole array is not possible for materials such as gases and air. Based on all aforementioned studies, a sub-wavelength hole array structure with dynamic SP energy matching could have a significant impact in many related sub-wavelength hole array applications and specifically in SPR sensing applications.

Such a sub-wavelength hole array structure, with dynamic SP energy matching, could be evaluated in bulk-SPR sensing applications with respect to its performance capabilities in comparison to a conventional sub-wavelength hole array. In bulk-SPR sensing, homogeneous liquid materials with known refractive index are deposited on the structure and sensed by monitoring optical metrics such as transmission or reflection. The structure capable of dynamic SP energy matching provides SP energy matching between the top and bottom surfaces due to a presence of the same refractive index material on top and bottom surfaces of the metal film. The optical resonance performance of the SP matching structure can then be evaluated by transmission efficiency measures, bulk-SPR sensitivity measures, as well as the degree of overlap of a single mode resonance related to both sides of the structure. The higher sensitivity of the SP matched structure in bulk-SPR sensing applications could be inferred as better performance of the structure in SPR bio-sensing applications when compared to a conventional sub-wavelength hole array structure.

1.9. Thesis objective and scope:

The objective of the work presented in this thesis was to enhance the resonance transmission properties of sub-wavelength hole arrays for bulk-SPR sensing application. The material presented in the thesis falls into two main categories:

1- Systematic analysis: systematic studies on the effect of various geometrical parameters such as hole size, hole shape, spacing between adjacent holes as well as the effect of the adhesion layer material between the gold film and the substrate on the resonance transmission properties of a sub-wavelength hole array.

2- Novel sub-wavelength structures: introducing two sub-wavelength hole array structures and one sub-wavelength hole array structure with co-registered sub-wavelength disks at each hole. The presented structures demonstrated enhanced resonance transmission properties.

1.9.1. Research approach

The thesis contains the results of my research which have been published in 5 peer-reviewed journal articles (chapter 2 to chapter 6) and presents systematic studies and advancement in resonance transmission properties of sub-wavelength structures for SPR sensing applications. The order of the journal articles are based on the coherency of the thesis stream as well as the chronology of publication date, which is described in more detail below:

Chapter 2 corresponds to the article "M. Najiminaini, F. Vasefi, B. Kaminska, and J. J. L. Carson, "Experimental and numerical analysis on the optical resonance transmission properties of nano-hole arrays," Opt. Express 18, 22255-22270 (2010).", which describes a comprehensive experimental and numerical (FDTD) study on Extraordinary Optical Transmission (EOT) through various nano-hole arrays in a thick gold film within the visible and near infrared spectral regions. Also, the article presents an EBL fabrication methodology and Finite Difference Time Domain (FDTD) simulation of a nano-hole array in a gold film as well as optical characterization setup for measuring optical transmission spectra of the fabricated structures. The paper also presents

analysis on simulation and the optical characterization results of EOT of nano-hole arrays with respect to optical resonance peak position, optical resonance transmission efficiency, and optical resonance bandwidth. These results provide a broad knowledge about the effect of various geometrical parameters on EOT properties of the nano-hole array structures in order to design and employ them in various applications. Both simulation and experimental results described in the paper led me to hypothesize that various thicknesses and compositions of the adhesion layer between gold and the substrate could change the EOT properties of a nano-hole array. Therefore, I used the following approach in the chapter 3.

Chapter 3 presents the article “M. Najiminaini, F. Vasefi, B. Kaminska, and J. J. L. Carson, "Optical resonance transmission properties of nano-hole arrays in a gold film: effect of adhesion layer," *Opt. Express* 19, 26186-26197 (2011)”. which describes a systematic numerical and experimental analysis on the optical resonance transmission properties of nano-hole arrays in an optically thick gold film with various adhesion layers (5 nm titanium, 5 nm chromium, 10 nm titanium, and etched) between the Pyrex substrate and the gold film. The results also showed that both simulation and experimental results had good agreement for (1,0) optical resonance bandwidth and the optical resonance position for most nano-hole arrays. Also, it was discovered that the composition and thickness of the adhesion layer had a large effect on the optical resonance transmission properties of the nano-hole arrays. The results presented in the article demonstrate that the optical resonance properties of a nano-hole array can be improved by using a thin Ti adhesion later or by etching the adhesion layer. The results of a nano-hole array with an etched adhesion layer led me to hypothesize that a nano-hole array with a cavity beneath each hole or a nano-hole array with a large cavity beneath the entire nano-hole array structure could be fabricated by a means of wet etching process. This potentially could result in a sub-wavelength hole array structure with dynamic SP energy matching between top and bottom surfaces of the structure. Therefore, I used the following approach in chapter 4 and 5.

Chapter 4 presents the article “M. Najiminaini, F. Vasefi, B. Kaminska, and J. J. L. Carson, "Nano-hole array structure with improved surface plasmon energy matching

characteristics," *Appl. Phys. Lett.* 100, 043105 (2012)". The article introduced a novel nano-hole array structure in an opaque gold film. The nano-hole array structure contained a cavity beneath each nano-hole, thereby contributing to the surface plasmon energy matching between the top and bottom surfaces of the gold and within the nano-hole structures. It was determined that the SP energy matching between the top and bottom surfaces of the nano-hole array improved the optical properties of nano-hole array such as the EOT and the electric near-field intensity. This article showed numerical and experimental tests of SPR sensing, where a clear advantage over the conventional nano-hole array structure was observed. Also, this paper demonstrated that for SPR sensing, the dynamically SP-matched structure had nearly 3-fold higher differential transmission, 2-fold higher sensitivity, and up to 7-fold higher ratio of EOT to the nearby minimum (Wood's anomaly) when compared to a conventional nano-hole array.

Chapter 5 presents the article "M. Najiminaini, F. Vasefi, B. Kaminska, and J. J. L. Carson, "Effect of surface plasmon energy matching on the sensing capability of metallic nano-hole arrays," *Appl. Phys. Lett.* 100, 063110-4 (2012)". This article introduced a nano-hole array structure in an opaque gold film that provided perfect surface plasmon energy matching. The structure contained a large cavity beneath the nano-hole array, thereby contributing to the surface plasmon energy matching between the top and bottom surfaces of the gold. Specifically, the paper described fabrication details of the new devices and measurements proving that surface plasmon energy matching between top and bottom surfaces of the nano-hole array not only occurs, but it also greatly improves device performance. This article showed that for bulk surface plasmon resonance sensing, a structure containing a 350-nm cavity depth had a nearly 1.6-fold higher sensitivity and a nearly 3-fold higher figure of merit when compared to a similar device with a 5-nm cavity depth. In order to enhance SPR sensitivity of a nano-hole array structure with a large cavity, I hypothesized that a nano-hole array with a large cavity and a gold disk co-registered to each hole at the bottom of the cavity could potentially enhance the bulk SPR sensitivity due to strong SP coupling between hole and disk. Therefore, to test my hypothesis, I performed the following study in the chapter 6.

Chapter 6 presents the article “M. Najiminaini, F. Vasefi, B. Kaminska, and J. J. L. Carson, "A three-dimensional plasmonic nanostructure with extraordinary optical transmission," submitted to Journal of Plasmonics. This article introduced a novel 3D nano-structure, which produced an EOT due to an intensified LSP coupling between nano-holes and nano-disks. The 3D nano-structure contained a free-standing gold nano-hole array film above a cavity and an array of nano-disks at the bottom of the cavity that was co-registered with the nano-hole array. The structure provided surface plasmon energy matching, which resulted in enhanced EOT at the LSP resonance. Specifically, the article described the following in more detail:

1. A new fabrication method to precisely control the distance between the nano-holes and the nano-disks.
2. The observation of a new EOT transmission peak that depended highly on the nano-hole and nano-disk diameter as well as the proximity of the nano-holes and nano-disks.
3. Tests on the 3D nano-structure that highlighted its superior performance as a SPR sensor.
4. Simulations that indicated the presence of high electric fields between the nano-holes and nano-disks at the new EOT resonance that were up to 10-fold higher compared to SPP resonances.

Finally in Chapter 7, the summary of accomplishments and conclusions from previous chapters is presented, the relations between accomplishments in chapter 2 through chapter 6 are presented, and instructions for future work are proposed. The summary and conclusion sections are arranged by subject and chronology of publication dates to present a consistent discussion for each specific topic. The conclusion is organized to reflect the initial objectives of the thesis.

1.10. References

- 1-1. Genet, C., & Ebbesen, T. W. (2007). Light in tiny holes. *Nature*, 445(7123), 39-46. doi:10.1038/nature05350
- 1-2. Barnes, W. L., Dereux, A., & Ebbesen, T. W. (2003). Surface plasmon subwavelength optics. *Nature*, 424(6950), 824-830. Retrieved from <http://dx.doi.org/10.1038/nature01937>
- 1-3. Lesuffleur, A., Kumar, L. K. S., Brolo, A. G., Kavanagh, K. L., & Gordon, R. (2007). Apex-enhanced raman spectroscopy using double-hole arrays in a gold film. *The Journal of Physical Chemistry C*, 111(6), 2347-2350. doi:10.1021/jp067677e
- 1-4. Sinton, D., Gordon, R., & Brolo, A. G. (2008). *Nanohole arrays in metal films as optofluidic elements: Progress and potential* - Springer Berlin / Heidelberg. doi:-10.1007/s10404-007-0221-0
- 1-5. Ebbesen, T. W., Lezec, H. J., Ghaemi, H. F., Thio, T., & Wolff, P. A. (1998). Extraordinary optical transmission through sub-wavelength hole arrays. *Nature*, 391(6668), 667-669. Retrieved from <http://dx.doi.org/10.1038/35570>
- 1-6. Krishnan, A., Thio, T., Kim, T. J., Lezec, H. J., Ebbesen, T. W., Wolff, P. A., Garcia-Vidal, F. J. (2001). Evanescently coupled resonance in surface plasmon enhanced transmission. *Optics Communications*, 200(1-6), 1-7. Retrieved from <http://www.sciencedirect.com/science/article/pii/S0030401801015589>
- 1-7. Srituravanich, W., Fang, N., Sun, C., Luo, Q., & Zhang, X. (2004). Plasmonic nanolithography. *Nano Letters*, 4(6), 1085-1088. doi:10.1021/nl049573q
- 1-8. Bethe, H. A. (1944). Theory of diffraction by small holes. *Phys.Rev.*, 66, 163-182.
- 1-9. Raether, H. (1988). *Surface plasmons*. Berlin: Springer-Verlag.
- 1-10. Degiron, A., Lezec, H. J., Yamamoto, N., & Ebbesen, T. W. (2004). Optical transmission properties of a single subwavelength aperture in a real metal. *Optics Communications*, 239(1), 61-66. Retrieved from <http://www.sciencedirect.com/science/article/pii/S0030401804005395>
- 1-11. Tetz, K. (2006). *Plasmonics in the near-infrared: Spatial, spectral, and temporal studies of Surface plasmon polaritons*. (Unpublished)
- 1-12. Leathem, B. (2004). *Optical transmission through nanohole arrays*. (Unpublished)
- 1-13. Przybilla, F., Degiron, A., Laluet, J., Genet, C., & Ebbesen, T. W. (2006). Optical transmission in perforated noble and transition metal films. *Journal of Optics A: Pure and Applied Optics*, 8(5) 458. Retrieved from <http://stacks.iop.org/1464-4258/8/i=5/a=015>

- 1-14. Palik, E. D. (1985). *Handbook of optical constants of solids*. New York: Academic Press.
- 1-15. Rodrigo, S. G., García-Vidal, F. J., & Martín-Moreno, L. (2008). Influence of material properties on extraordinary optical transmission through hole arrays. *Physical Review B*, *77*(7), 075401. Retrieved from <http://dx.doi.org.proxy.lib.sfu.ca/10.1103/PhysRevB.77.075401>
- 1-16. de Dood, Michiel J. A., Driessen, E. F. C., Stolwijk, D., & van Exter, M. P. (2008). Observation of coupling between surface plasmons in index-matched hole arrays. *Physical Review B*, *77*(11), 115437. Retrieved from <http://link.aps.org/doi/10.1103/PhysRevB.77.115437>
- 1-17. Najiminaini, M., Vasefi, F., Kaminska, B., & Carson, J. J. L. (2012). Nano-hole array structure with improved surface plasmon energy matching characteristics *Appl.Phys.Lett.*, *100*(4), 043105 (2012). Retrieved from <http://dx.doi.org/10.1063/1.3679173>
- 1-18. Najiminaini, M., Vasefi, F., Kaminska, B., & Carson, J. J. L. (2012). Effect of surface plasmon energy matching on the sensing capability of metallic nano-hole arrays. *Applied Physics Letters*, *100*(6), 063110-4. Retrieved from <http://dx.doi.org/10.1063/1.3683536>
- 1-19. Przybilla, F., Degiron, A., Genet, C., Ebbesen, T., de Léon-Pérez, F., Bravo-Abad, J., Martín-Moreno, L. (2008). Efficiency and finite size effects in enhanced transmission through subwavelength apertures. *Optics Express*, *16*(13), 9571-9579. Retrieved from <http://www.opticsexpress.org/abstract.cfm?URI=oe-16-13-9571>
- 1-20. Lindquist, N. C., Lesuffleur, A., & Oh, S. (2007). Periodic modulation of extraordinary optical transmission through subwavelength hole arrays using surrounding bragg mirrors. *Physical Review B*, *76*(15), 155109. Retrieved from <http://link.aps.org/doi/10.1103/PhysRevB.76.155109>
- 1-21. Gordon, R., & Marthandam, P. (2007). Plasmonic bragg reflectors for enhanced extraordinary optical transmission through nano-hole arrays in a gold film. *Optics Express*, *15*(20), 12995-13002. Retrieved from <http://www.opticsexpress.org/abstract.cfm?URI=oe-15-20-12995>
- 1-22. van, d. M., Segerink, F. B., van Hulst, N. F., & Kuipers, L. (2004). Influence of hole size on the extraordinary transmission through subwavelength hole arrays. *Applied Physics Letters*, *85*(19), 4316-4318. Retrieved from <http://link.aip.org/link/?APL/85/4316/1>
- 1-23. Najiminaini, M., Vasefi, F., Kaminska, B., & Carson, J. J. L. (2010). Experimental and numerical analysis on the optical resonance transmission properties of nano-hole arrays. *Optics Express*, *18*(21), 22255-22270. Retrieved from <http://www.opticsexpress.org/abstract.cfm?URI=oe-18-21-22255>

- 1-24. Degiron, A., Lezec, H. J., Barnes, W. L., & Ebbesen, T. W. (2002). Effects of hole depth on enhanced light transmission through subwavelength hole arrays. *Applied Physics Letters*, 81(23), 4327-4329. Retrieved from <http://dx.doi.org/10.1063/1.1526162>
- 1-25. Kumar, L. K. S., Lesuffleur, A., Hughes, M. C., & Gordon, R. (2006). Double nanohole apex-enhanced transmission in metal films. *Applied Physics B: Lasers and Optics*, 84(1), 25-28. Retrieved from <http://dx.doi.org/10.1007/s00340-006-2291-1>
- 1-26. Gordon, R., Brolo, A. G., McKinnon, A., Rajora, A., Leathem, B., & Kavanagh, K. L. (2004). Strong polarization in the optical transmission through elliptical nanohole arrays. *Physical Review Letters*, 92(3), 037401. Retrieved from <http://link.aps.org/doi/10.1103/PhysRevLett.92.037401>
- 1-27. Thio, T., Ghaemi, H. F., Lezec, H. J., Wolff, P. A., & Ebbesen, T. W. (1999). Surface-plasmon-enhanced transmission through hole arrays in cr films. *Journal of the Optical Society of America B*, 16(10), 1743-1748. Retrieved from <http://josab.osa.org/abstract.cfm?URI=josab-16-10-1743>
- 1-28. Eftekhari, F., Gordon, R., Ferreira, J., Brolo, A. G., & Sinton, D. (2008). Polarization-dependent sensing of a self-assembled monolayer using biaxial nanohole arrays. *Applied Physics Letters*, 92(25), 253103-3. Retrieved from <http://dx.doi.org/10.1063/1.2949682>
- 1-29. Gordon, R., Hughes, M., Leathem, B., Kavanagh, K. L., & Brolo, A. G. (2005). Basis and lattice polarization mechanisms for light transmission through nanohole arrays in a metal film. *Nano Letters*, 5(7), 1243-1246. doi:10.1021/nl0509069
- 1-30. Najiminaini, M., Vasefi, F., Landrock, C. K., Kaminska, B., & Jeffrey J.L. Carson. (2010). Optical transmission analysis of nano-hole array as a function of incident light propagation angles. Paper presented at the BTuD105. Retrieved from <http://www.opticsinfobase.org/abstract.cfm?URI=BIOMED-2010-BTuD105>
- 1-31. Ghaemi, H. F., Thio, T., Grupp, D. E., Ebbesen, T. W., & Lezec, H. J. (1998). Surface plasmons enhance optical transmission through subwavelength holes. *Physical Review B*, 58(11), 6779-6782. Retrieved from <http://link.aps.org/doi/10.1103/PhysRevB.58.6779>
- 1-32. Yanik, A. A., Cetin, A. E., Huang, M., Artar, A., Mousavi, S. H., Khanikaev, A., Altug, H. (2011). Seeing protein monolayers with naked eye through plasmonic fano resonances. *Proceedings of the National Academy of Sciences*, Retrieved from <http://www.pnas.org/content/early/2011/06/28/1101910108.abstract>
- 1-33. Tseng, A. (2005). Recent developments in nanofabrication using focused ion beams. *Small*, 1(10), 924-939. doi:10.1002/sml.200500113

- 1-34. Chen, J., Shi, J., Decanini, D., Cambriil, E., Chen, Y., & Haghiri-Gosnet, A. (2009). Gold nanohole arrays for biochemical sensing fabricated by soft UV nanoimprint lithography. *Microelectronic Engineering*, 86(4), 632-635. Retrieved from <http://www.sciencedirect.com/science/article/pii/S0167931709000161>
- 1-35. Fan, W., Zhang, S., Malloy, K. J., & Brueck, S. R. J. (2005). Enhanced mid-infrared transmission through nanoscale metallic coaxial-aperture arrays. *Optics Express*, 13(12), 4406-4413. Retrieved from <http://www.opticsexpress.org/abstract.cfm?URI=oe-13-12-4406>
- 1-36. Henzie, J., Lee, M. H., & Odom, T. W. (2007). Multiscale patterning of plasmonic metamaterials. *Nat Nano*, 2(9), 549-554. Retrieved from <http://dx.doi.org/10.1038/nnano.2007.252>
- 1-37. Ctistis, G., Patoka, P., Wang, X., Kempa, K., & Giersig, M. (2007). Optical transmission through hexagonal arrays of subwavelength holes in thin metal films. *Nano Letters*, 7(9), 2926-2930. doi:10.1021/nl0712973
- 1-38. Najiminaini, M., Vasefi, F., Kaminska, B., & Carson, J. J. L. (2011). Optical resonance transmission properties of nano-hole arrays in a gold film: Effect of adhesion layer. *Optics Express*, 19(27), 26186-26197. Retrieved from <http://dx.doi.org/10.1364/OE.19.026186>
- 1-39. Aouani, H., Wenger, J., Gerard, D., Rigneault, H., Devaux, E., Ebbesen, T. W., S. (2009). Crucial role of the adhesion layer on the plasmonic fluorescence enhancement. *ACS Nano*, 3(7), 2043-2048. doi:10.1021/nn900460t
- 1-40. Zayats, A. V., Smolyaninov, I. I., & Maradudin, A. A. (2005). Nano-optics of surface plasmon polaritons. *Phys.Reports*, 408(3-4), 131-314.
- 1-41. Brolo, A. G., Irish, D. E., Szymanski, G., & Lipkowski, J. (1998). Relationship between SERS intensity and both surface coverage and morphology for pyrazine adsorbed on a polycrystalline gold electrode. *Langmuir*, 14(2), 517-527. doi:10.1021/la970051i
- 1-42. De Leebeeck, A., Kumar, L. K. S., de Lange, V., Sinton, D., Gordon, R., & Brolo, A. G. (2007). On-chip surface-based detection with nanohole arrays. *Analytical Chemistry*, 79(11), 4094-4100. doi:10.1021/ac070001a
- 1-43. Lindquist, N. C., Lesuffleur, A., Im, H., & Oh, S. (2009). Sub-micron resolution surface plasmon resonance imaging enabled by nanohole arrays with surrounding bragg mirrors for enhanced sensitivity and isolation. *Lab Chip*, 9(3), 382-387. Retrieved from <http://dx.doi.org/10.1039/B816735D>
- 1-44. Lesuffleur, A., Im, H., Lindquist, N. C., Lim, K. S., & Oh, S. (2008). Laser-illuminated nanohole arrays for multiplex plasmonic microarray sensing. *Optics Express*, 16(1), 219-224. Retrieved from <http://www.opticsexpress.org/abstract.cfm?URI=oe-16-1-219>

- 1-45. Pang, L., Hwang, G. M., Slutsky, B., & Fainman, Y. (2007). Spectral sensitivity of two-dimensional nanohole array surface plasmon polariton resonance sensor. *Applied Physics Letters*, *91*(12), 123112-3. Retrieved from <http://link.aip.org/link/?APL/91/123112/1>
- 1-46. Lesuffleur, A., Im, H., Lindquist, N. C., & Oh, S. (2007). Periodic nanohole arrays with shape-enhanced plasmon resonance as real-time biosensors. *Applied Physics Letters*, *90*(24), 243110-3. Retrieved from <http://link.aip.org/link/?APL/90/243110/1>
- 1-47. Yang, J., Ji, J., Hogle, J. M., & Larson, D. N. (2008). Metallic nanohole arrays on fluoropolymer substrates as small label-free real-time bioprobes. *Nano Letters*, *8*(9), 2718-2724. doi:10.1021/nl801043t
- 1-48. Stewart, M. E., Mack, N. H., Malyarchuk, V., Soares, J. A. N. T., Lee, T., Gray, S. K., Rogers, J. A. (2006). Quantitative multispectral biosensing and 1D imaging using quasi-3D plasmonic crystals. *Proceedings of the National Academy of Sciences*, *103*(46), 17143-17148. Retrieved from <http://www.pnas.org/content/103/46/17143.abstract>
- 1-49. Artar, A., Yanik, A. A., & Altug, H. (2009). Fabry-perot nanocavities in multilayered plasmonic crystals for enhanced biosensing. *Applied Physics Letters*, *95*(5), 051105-3. Retrieved from <http://link.aip.org/link/?APL/95/051105/1>
- 1-50. Yang, J., Gao, H., Suh, J. Y., Zhou, W., Lee, M. H., & Odom, T. W. (2010). Enhanced optical transmission mediated by localized plasmons in anisotropic, three-dimensional nanohole arrays. *Nano Letters*, *10*(8), 3173-3178. doi:10.1021/nl102078j
- 1-51. Brolo, A. G., Gordon, R., Leathem, B., & Kavanagh, K. L. (2004). Surface plasmon sensor based on the enhanced light transmission through arrays of nanoholes in gold films. *Langmuir*, *20*(12), 4813-4815. doi:10.1021/la0493621
- 1-52. Im, H., Lesuffleur, A., Lindquist, N. C., & Oh, S. (2009). Plasmonic nanoholes in a multichannel microarray format for parallel kinetic assays and differential sensing. *Analytical Chemistry*, *81*(8), 2854-2859. doi:10.1021/ac802276x
- 1-53. Ji, J., O'Connell, J. G., Carter, D. J. D., & Larson, D. N. (2008). High-throughput nanohole array based system to monitor multiple binding events in real time. *Analytical Chemistry*, *80*(7), 2491-2498. doi:10.1021/ac7023206
- 1-54. Yanik, A. A., Huang, M., Artar, A., Chang, T., & Altug, H. (2010). Integrated nanoplasmonic-nanofluidic biosensors with targeted delivery of analytes. *Applied Physics Letters*, *96*(2), 021101-3. Retrieved from <http://link.aip.org/link/?APL/96/021101/1>
- 1-55. Eftekhari, F., Escobedo, C., Ferreira, J., Duan, X., Giroto, E. M., Brolo, A. G., Sinton, D. (2009). Nanoholes as nanochannels: Flow-through plasmonic sensing. *Analytical Chemistry*, *81*(11), 4308-4311. doi:10.1021/ac900221y

- 1-56. Brolo, A. G., Arctander, E., Gordon, R., Leathem, B., & Kavanagh, K. L. (2004). Nanohole-enhanced raman scattering. *Nano Letters*, 4(10), 2015-2018. doi:10.1021/nl048818w
- 1-57. Djaker, N., Hostein, R., Devaux, E., Ebbesen, T. W., Rigneault, H., & Wenger, J. (2010). Surface enhanced raman scattering on a single nanometric aperture. *The Journal of Physical Chemistry C*, 114(39), 16250-16256. doi:10.1021/jp104971p
- 1-58. Li, J., Chen, S., Chou, Y., Wu, M., Hsueh, C., & Su, W. (2011). Effects of gold film morphology on surface plasmon resonance using periodic P3HT:PMMA/Au nanostructures on silicon substrate for surface-enhanced raman scattering. *The Journal of Physical Chemistry C*, doi:10.1021/jp203307f
- 1-59. Baca, A. J., Montgomery, J. M., Cambrea, L. R., Moran, M., Johnson, L., Yacoub, J., & Truong, T. T. (2011). Optimization of nanopost plasmonic crystals for surface enhanced raman scattering. *The Journal of Physical Chemistry C*, 115(15), 7171-7178. doi:10.1021/jp109066c
- 1-60. Xu, J., Guan, P., KvasnicíEka, P., Gong, H., Homola, J., & Yu, Q. (2011). Light transmission and surface-enhanced raman scattering of quasi-3D plasmonic nanostructure arrays with deep and shallow fabry-Perot nanocavities. *The Journal of Physical Chemistry C*, 115(22), 10996-11002. doi:10.1021/jp202110s
- 1-61. Juan, M. L., Gordon, R., Pang, Y., Eftekhari, F., & Quidant, R. (2009). Self-induced back-action optical trapping of dielectric nanoparticles. *Nat Phys*, 5(12), 915-919. Retrieved from <http://dx.doi.org/10.1038/nphys1422>
- 1-62. Pang, Y., & Gordon, R. (2011). Optical trapping of 12 nm dielectric spheres using double-nanoholes in a gold film. *Nano Letters*, 11(9), 3763-3767. doi:10.1021/nl201807z
- 1-63. Pang, Y., & Gordon, R. (2012). Optical trapping of a single protein. *Nano Letters*, 12(1), 402-406. doi:10.1021/nl203719v
- 1-64. Shi, X., & Hesselink, L. (2004). Design of a C aperture to achieve $\lambda/10$ resolution and resonant transmission. *Journal of the Optical Society of America B*, 21(7), 1305-1317. Retrieved from <http://josab.osa.org/abstract.cfm?URI=josab-21-7-1305>
- 1-65. Sun, L., & Hesselink, L. (2006). Low-loss subwavelength metal C-aperture waveguide. *Optics Letters*, 31(24), 3606-3608. Retrieved from <http://ol.osa.org/abstract.cfm?URI=ol-31-24-3606>
- 1-66. Schuller, J. A., Barnard, E. S., Cai, W., Jun, Y. C., White, J. S., & Brongersma, M. L. (2010). Plasmonics for extreme light concentration and manipulation. *Nat Mater*, 9(3), 193-204. Retrieved from <http://dx.doi.org/10.1038/nmat2630>

- 1-67. Cheng, Y., Takashima, Y., Yuen, Y., Hansen, P. C., Leen, J. B., & Hesselink, L. (2011). Ultra-high resolution resonant C-shaped aperture nano-tip. *Optics Express*, 19(6), 5077-5085. Retrieved from <http://www.opticsexpress.org/abstract.cfm?URI=oe-19-6-5077>
- 1-68. Gordon, R., Brolo, A. G., Sinton, D., & Kavanagh, K. L. *Resonant optical transmission through hole-arrays in metal films: Physics and applications* - WILEY-VCH Verlag. doi:- 10.1002/lpor.200810079
- 1-69. Dickson, W., Wurtz, G. A., Evans, P. R., Pollard, R. J., & Zayats, A. V. (2008). Electronically controlled surface plasmon dispersion and optical transmission through metallic hole arrays using liquid crystal. *Nano Letters*, 8(1), 281-286. doi:10.1021/nl072613g
- 1-70. Nahata, A., Linke, R. A., Ishi, T., & Ohashi, K. (2003). Enhanced nonlinear optical conversion from a periodically nanostructured metal film. *Optics Letters*, 28(6), 423-425. Retrieved from <http://ol.osa.org/abstract.cfm?URI=ol-28-6-423>
- 1-71. Airola, M., Liu, y., & Blair, S. (2005). Second-harmonic generation from an array of sub-wavelength metal apertures. *Journal of Optics A: Pure and Applied Optics*, 7(2), S118. Retrieved from <http://stacks.iop.org/1464-4258/7/i=2/a=016>
- 1-72. Xu, T., Jiao, X., Zhang, G., & Blair, S. (2007). Second-harmonic emission from sub-wavelength apertures: Effects of aperture symmetry and lattice arrangement. *Optics Express*, 15(21), 13894-13906. Retrieved from <http://www.opticsexpress.org/abstract.cfm?URI=oe-15-21-13894>
- 1-73. Lesuffleur, A., Kumar, L. K., & Gordon, R. (2006). Enhanced second harmonic generation from nanoscale double-hole arrays in a gold film. *Applied Physics Letters*, 88(26), 261104-3. Retrieved from <http://dx.doi.org/10.1063/1.2218057>
- 1-74. Lesuffleur, A., Kumar, L. K. S., & Gordon, R. (2007). Apex-enhanced second-harmonic generation by using double-hole arrays in a gold film. *Physical Review B*, 75(4), 045423. Retrieved from <http://link.aps.org/doi/10.1103/PhysRevB.75.045423>
- 1-75. Coe, J. V., Heer, J. M., Teeters-Kennedy, S., Tian, H., & Rodriguez, K. R. (2008). Extraordinary transmission of metal films with arrays of subwavelength holes. *Annual Review of Physical Chemistry*, 59(1), 179-202. doi:10.1146/annurev.physchem.59.032607.093703
- 1-76. Coe, J. V., Rodriguez, K. R., Teeters-Kennedy, S., Cilwa, K., Heer, J., Tian, H., & Williams, S. M. (2007). Metal films with arrays of tiny holes: spectroscopy with infrared plasmonic scaffolding. *The Journal of Physical Chemistry C*, 111(47), 17459-17472. doi:10.1021/jp072909a

2. Experimental and numerical analysis on the optical resonance transmission properties of nano-hole arrays¹

2.1. Abstract

In this paper, we present experimental and numerical analysis on Extraordinary Optical Transmission (EOT) or optical resonance transmission through various nano-hole arrays constructed from an optically thick metal film within the visible and near infrared spectrum. Nano-hole arrays with different geometrical parameters (hole size, hole shape, and hole periodicity) having their EOT properties in the visible and near-infrared regime were simulated based on Finite Difference Time Domain (FDTD). Large nano-hole arrays with geometric properties similar to the simulated arrays were fabricated using Electron Beam Lithography (EBL). The optical resonance transmission properties (resonance position, transmission efficiency, and spectral bandwidth of resonance peak) of the fabricated nano-hole arrays were characterized. Finally, the experimental and numerical results were analyzed to determine the dependencies and discrepancies between optical resonance transmission properties for various nano-hole arrays.

¹ The following chapter is published in Optics Express, Vol. 18, No. 21, 22255 (2010) under the co-authorship of Fartash Vasefi, Bozena Kaminska, and Jeffery J.L. Carson. Retrieved from <http://dx.doi.org/10.1364/OE.18.022255>.

This paper was published in [Optics Express] and is made available as an electronic reprint with the permission of OSA. The paper can be found at the following URL on the OSA website: [<http://www.opticsinfobase.org/oe/abstract.cfm?uri=oe-18-21-22255>]. Systematic or multiple reproduction or distribution to multiple locations via electronic or other means is prohibited and is subject to penalties under law.

2.2. Introduction

The interaction of light with perforated sub-wavelength holes in metallic films generates extraordinary effects that can be employed to miniaturize photonic devices to sub-wavelength scales. The optical characteristics of these sub-wavelength holes in a metallic film are created by the coupling of light with Surface Plasmon (SP) modes [2-1] [2-2]. Surface Plasmon (SP) is the oscillation of free electrons at the interface of a metal and a dielectric and has been recognized to transmit light through sub-wavelength holes causing Extraordinary Optical Transmission (EOT) within the specific spectral range. Hence, a flat metal film, with a thickness that blocks light transmission (optically thick), can be perforated with an array of sub-wavelength holes to transmit light efficiently. EOT has been exploited in many applications such as Surface Enhanced Raman Spectroscopy (SERS), Surface Enhanced Fluorescence Spectroscopy (SEFS), focusing of light below the sub-wavelength regime, non-linear optics, and biosensors [2-2]-[2-6].

Recently, studies have investigated the dependence of EOT on a variety of parameters to improve optical transmission properties of nano-hole arrays [2-7]-[2-17]. Regarding geometrical parameters, the excitation of SP modes depends highly on the spacing between adjacent holes (periodicity) and dielectric constants of the metal and dielectric. Ebbesen [2-1] [2-10] was first to derive an equation describing the dependence of the wavelength (λ_{max}) of the SP resonance modes (EOTs) on the arrangement of nano-holes for a square lattice when the incident light is normal to the plane of the nano-hole array:

$$\lambda_{max} = \frac{a_0}{\sqrt{m^2 + n^2}} \sqrt{\frac{\epsilon_m \epsilon_d}{\epsilon_m + \epsilon_d}} \quad 2-1$$

,where a_0 is the periodicity of holes, ϵ_d and ϵ_m are the dielectric constants of the incident medium (at the top or bottom surface of the nano-hole) and the metal film, and m and n are integers expressing the scattering mode indices. A transmission minimum is often observed before each EOT peak due to Wood's anomaly [2-2]. It has been

discovered that the nano-hole shape can robustly control both the polarization properties and the intensity of the EOT [2-7]. With regard to material properties, Ag, Au, and Cu have larger optical resonant transmission peaks than nano-hole arrays in a perfect metal conductor with the same geometrical parameters [2-8] [2-9]. However for Ni and Cr, the transmittance is much smaller due to the absorption properties of these metals [2-8]. In addition, it is recognized that some metals particularly Au and Ag are more likely to display EOT properties compared to others such as Ni and Co [2-9]. Also, variations in the nano-hole radii, groove period, groove depth, locations of the grooves and slab thickness can significantly influence the transmission spectrum [2-11]. The optical transmission efficiency of the nano-hole array reaches an asymptotic upper value with a specific finite number of holes in the array [2-12] [2-13]. The optical resonant transmission of a nano-hole array is enhanced by exploiting the same dielectric constant on the back and front surface of a nano-hole array as a result of the same Surface Plasmon energy on both sides [2-14]. Fabrication of a Bragg reflector on the boundary of a nano-hole array has been shown to enhance the optical resonance transmission of the array by preventing losses at the edges of the array such as those seen in classic optical diffraction filters [2-16].

Not only can nano-hole arrays in a metal film be used for enhancing the transmission of light by a means of the Surface Plasmon properties [2-17], their bandpass properties provide the opportunity to construct miniaturized spectral filters. Some groups have investigated the use of nano-hole arrays as color coding devices [2-18] [2-19]. Another potential application for miniaturized spectral filters is spectroscopic optical imaging such as multispectral fluorescence microscopy. Although many studies have investigated the dependence of EOT properties on various geometrical properties of the nano-hole array, a comprehensive and systematic analysis of the dependence of EOT on nano-hole array geometry and the impact of the geometric properties on usage of nano-hole arrays as miniaturized spectral filters has yet to be done. Hence, in this study, a more complete characterization of the optical properties related to EOT was performed. Properties of the nano-hole array in a thick metal film included the wavelength of the peak transmission (optical resonance position), the intensity of the

transmitted light at the peak (optical resonance transmission efficiency), and the spectral bandwidth (optical resonance bandwidth).

Our approach was to compare numerical and experimental analyses from a series of nano-hole arrays with various geometrical designs (hole size, hole shape and periodicity) having optical resonance properties in the visible and near infra-red spectral regions. Numerical analysis was performed with FDTD simulation. Large nano-hole arrays were fabricated with electron beam lithography and characterized with optical transmission spectroscopy.

2.3. Methods

2.3.1. *FDTD simulation of nano-hole arrays*

The three-dimensional (3D) FDTD method was employed to simulate the interaction between light and a nano-hole array in a thick metal film with the goal of predicting the optical transmission properties. FDTD is a numerical method to solve the two and three dimensional Maxwell's equations in linear and non-linear dispersive media. We used the FDTD package from Lumerical Inc. (Vancouver, Canada). Computations were performed with a computing grid (West grid (www.westgrid.ca)). With Lumerical, the user can specify arbitrary geometric structures and various input excitation sources. The software represents the electric $[E(x,y,z,t)]$, magnetic $[H(x,y,z,t)]$ and current density fields $[J(x,y,z,t)]$ on a spatial grid and employs time spacing algorithms to perform the FDTD [2-20] [2-21]. The dielectric constants for each material were defined by the relative dielectric constant $[\epsilon_r(x,y,z,\omega)]$. Since absorption and permittivity for a metallic material depend highly on frequency, the dispersion properties of the metal were considered. We used the dielectric constant for metallic and dielectric materials provided by Palik [2-22].

As shown in Figure 2-1 (a), in the simulation model, a single periodicity of nano-holes was surrounded by a simulation area and the x-, y-, and z-axis boundary conditions were set to Periodic, Periodic, and PML, respectively. The Periodic boundary conditions of the x- and y-axes were chosen due to the symmetric properties of the

physical structure and the electromagnetic field. Therefore, due to these properties, the periodic structure of a single period nano-hole was replicated into infinity. A non-uniform mesh was used with a highest accuracy of 5 nm. A plain wave source was used to illuminate the nano-hole array at normal incidence to the nano-hole array plane. Using this methodology, we simulated nano-hole arrays with various hole shapes (circular and square), hole sizes (150 nm, 200 nm, and 250 nm) and periodicities (375 nm, 400 nm, 425 nm, 450 nm, and 475 nm) in square lattice arrangements.

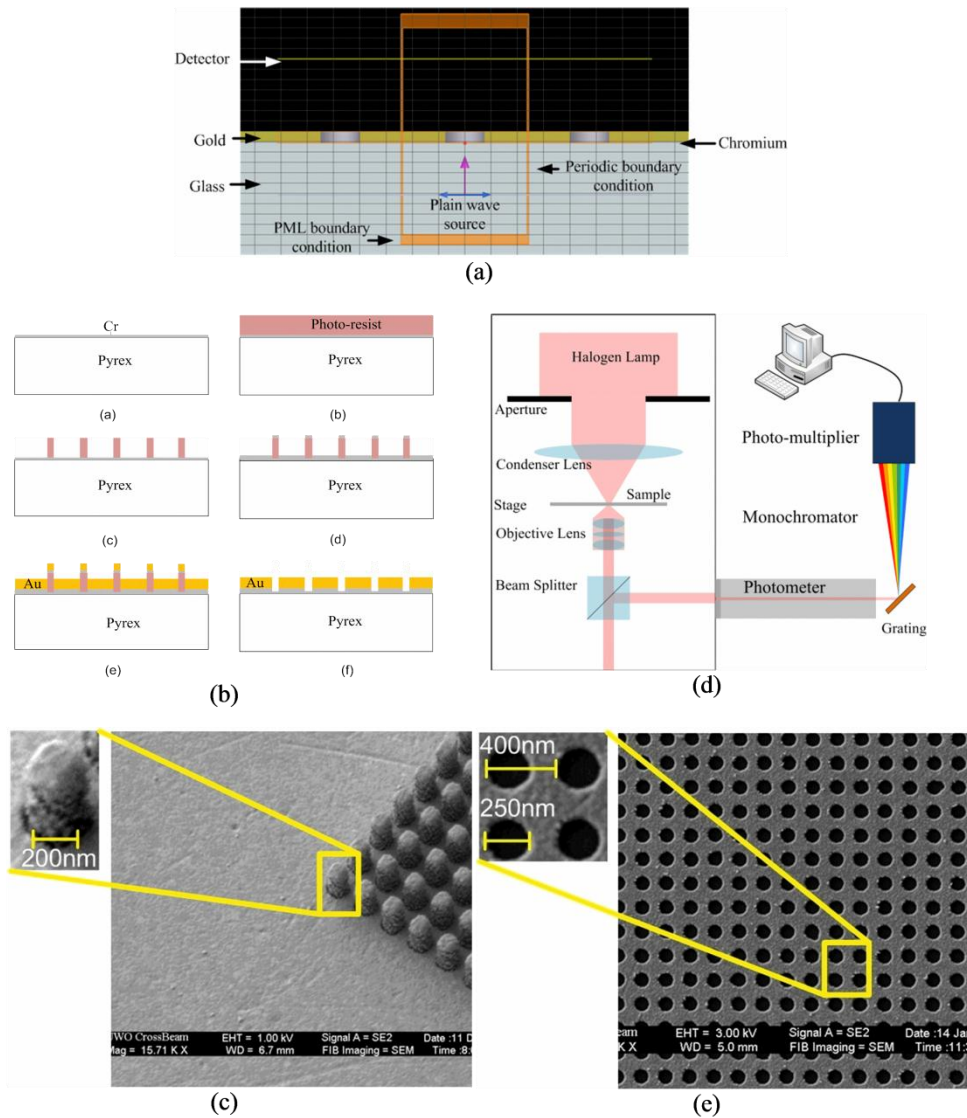


Figure 2-1. (a) Set up and boundary conditions for FDTD simulation of nano-hole array, (b) Electron beam lithography (EBL) for fabrication of nano-hole arrays, (c) SEM of an array of photo-resist nano-pillars, (d) Set up for optical characterization of nano-hole arrays, and (e) SEM of a nano-hole array with the circular nano-holes.

2.3.2. Electron Beam Lithography (EBL) fabrication methodology

We used electron beam lithography (EBL) fabrication methodology for fabricating nano-hole arrays in a 100-nm optically thick gold film. The fabrication process used is shown in Figure 2-1 (b). Chromium (5 nm) was deposited on a Pyrex substrate in order to make the substrate surface conductive for the EBL process. Afterward, 500 nm photo-resist (Negative Tone photo-resist ma-N 2403) was spin-coated and soft-baked on the chromium layer. The nano-hole array pattern was written using an EBL machine (LEO, 1530 e-beam lithography), the sample was developed leaving behind photo-resist pillars. Chromium (10 nm) was then deposited as an adhesion layer followed by 100 nm deposition of gold on to the sample. A SEM image of the photo-resist pillars covered with gold is shown in Figure 2-1 (c). Finally, in a lift-off process, the sample was exposed to Acetone and Nano-stripper to remove the pillars. A SEM image of a fabricated nano-hole array is shown in Figure 2-1 (e). We fabricated nano-hole arrays with various hole shapes (circular and square), hole sizes (150 nm, 200 nm, and 250 nm) and hole periodicities (375 nm, 400 nm, 425 nm, 450 nm, and 475 nm) in a square lattice arrangement. These geometrical parameters were selected to enable optical resonance transmission of each array in the visible and near-infrared regime. The number of holes in each nano-hole array was 150×150 .

2.3.3. Optical characterization setup

We used a standard inverted microscope (Nikon, TE300) attached to a photometer (PTI, D104), monochromator (PTI, 101), and photo-multiplier (PTI, 710) for the optical characterization of each nano-hole array as shown in Figure 2-1 (d). Unpolarized white light from a 100 W halogen lamp was focused on the sample using the bright-field and condenser lens (NA = 0.3) of the microscope. The scattered light was collected with a 20 \times objective (NA = 0.45; Nikon, 93150) and guided with a beam splitter to the photometer. Using the aperture adjustment on the photometer, light from a desired region of a given sample was selected, then guided to the monochromator for spectral characterization, and detection by the photo-multiplier tube. The optical transmission spectra were obtained by first subtracting the background signals obtained from a hole-free region of the gold film from the spectra transmitted through a given nano-hole array,

and then divided by the measured white light spectrum. The ratio cancels the wavelength variant signal caused by the light source, monochromator and the wavelength responsivity of the detector.

2.3.4. Analysis of the optical transmission spectra

In order to employ EOTs (optical resonance peaks) of a nano-hole array as a spectral filter, the optical characteristics of EOT related to spectral performance were analyzed. These optical properties consist of the center wavelength, the transmission efficiency of a center wavelength and the spectral bandwidth. In some instances, although the position of the peaks was measurable, the peak location was corrupted due to the large bandwidth of the spectral features and was not interpretable. In these cases, the peak positions were not reported. The spectral bandwidth of each EOT computed in such a way that the spectral bandwidth is the full width of the EOT where the optical transmission was $1/\sqrt{2}$ of the optical transmission peak.

2.4. Results

2.4.1. Experimental observations in Nano-hole array fabrication

Prior to writing nano-hole patterns with EBL, initial tests were performed to optimize the EBL area dose used for fabrication of nano-hole arrays with specific feature parameters (hole size, hole shape, and periodicity of hole). The area dose required to fabricate each design was dependent on hole shape, hole size, periodicity, and the type and age of the photo-resist. The area dose varied from $70 \mu\text{C}/\text{cm}^2$ to $125 \mu\text{C}/\text{cm}^2$.

All nano-hole array devices were imaged with SEM. The SEM measurements verified that the hole size and periodicity were within 5-10% of the intended size and periodicity. The average corner radius for nano-holes with square hole shape was measured and was about 50 nm. As a result, square nano-holes less than 100 nm on a side were effectively circular in shape. Also, for the 500 nm photo-resist pillars, the ratio of the top to the bottom diameter was 1.18.

2.4.2. *Simulation results*

The simulation results for optical transmission spectra of the nano-hole arrays with square lattice arrangement, various hole shapes (circular and square), hole sizes (150 nm, 200 nm, and 250 nm), and periodicities (375 nm, 400 nm, 425 nm, 450 nm, and 475 nm) are shown in Figure 2-2. The optical transmission spectrum of each nano-hole array was normalized to the combined area of the holes relative to the area corresponding to the lattice (i.e. square in shape and determined by the periodicity and number of holes). The optical resonance peaks related to (1,0) and (1,1) SP excitation modes from the Pyrex-gold side and (1,0) SP excitation mode from the air-gold side were generally observed (see Table 2-1) in the optical transmission spectrum of each nano-hole array and are indicated by two separate brown dashed lines (Pyrex-gold side resonance peaks) and blue dashed lines (air-gold side resonance peaks) in Figure 2-2. The optical resonance peaks were observed in the visible and near infra-red regime. A transmission minimum was observed between the (1,0) and (1,1) optical resonance peaks related to the Pyrex-gold side and is indicated in Figure 2-2 by the orange dashed line.

The position, transmission efficiency, and bandwidth of (1,0) optical resonance peaks related to the Pyrex-gold side was extracted from each optical transmission spectrum and shown in Figure 2-3. The optical resonance position related to the (1,0) SP excitation red-shifted as the periodicity increased (Figure 2-3 (a)). For a given periodicity, the resonance position generally slightly red-shifted as the hole size increased, except for arrays with square holes and larger hole sizes (200 nm and 250 nm), which showed a minor blue-shift as the hole size increased. In Figure 2-3 (b), the optical resonance transmission efficiency related to the (1,0) SP excitation decreased as periodicity increased. For a given periodicity, the transmission efficiency increased as the hole size increased. In Figure 2-3 (c), the (1,0) optical resonance bandwidth (see Table 2-1) was generally unaffected (e.g., D200) or decreased as the periodicity increased. In two specific instances, the bandwidth was smaller for the arrays with square hole shape when the periodicity was 375 nm compared to 400 nm. For all arrays at a given periodicity, the bandwidth increased with hole size.

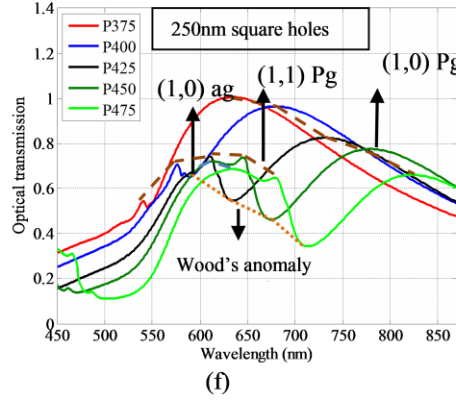
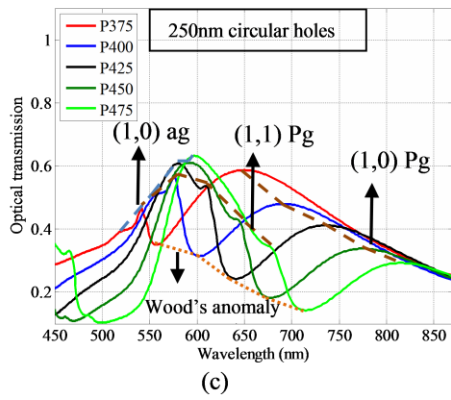
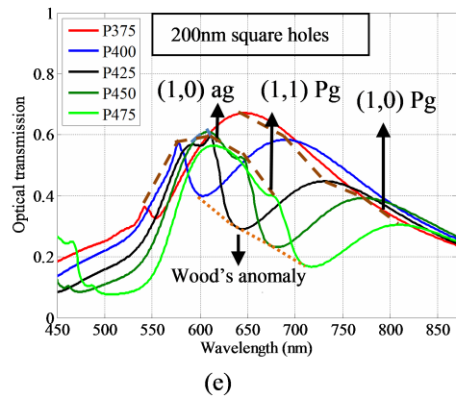
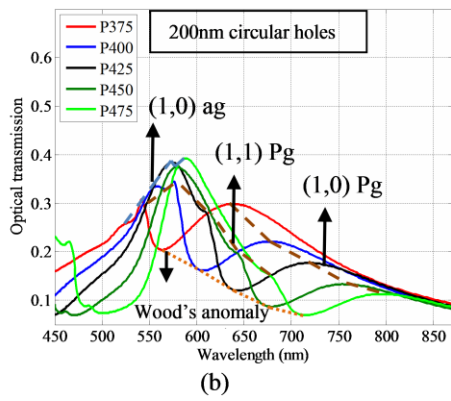
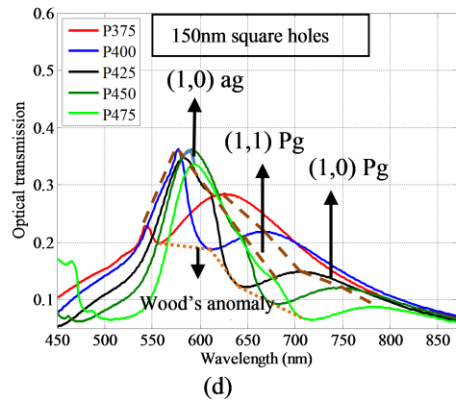
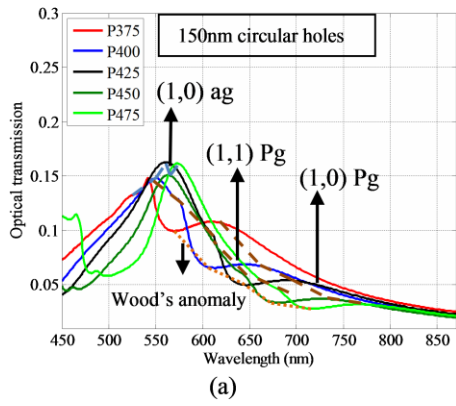


Figure 2-2. Optical transmission spectra for nano-hole arrays with various hole shape (square and circular), diameters (150 nm, 200 nm, and 250 nm), and periodicities or P (375 nm, 400 nm, 425 nm, 450 nm, and 475 nm) based on FDTD simulation: (a) circular holes with 150 nm diameter, (b) circular holes with 200 nm diameter, (c) circular holes with 250 nm diameter, (d) square holes with 150 nm length, (e) square holes with 200 nm length, and (f) square holes with 250 nm length. (ag) represents the optical resonance peak from air-gold side. (Pg) represents the optical resonance peak from Pyrex-gold side.

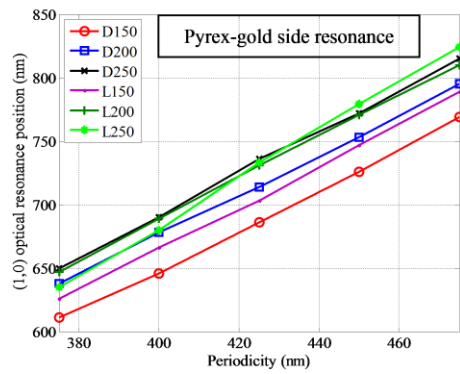
Table 2-1. Summary of simulation results related to optical resonance peaks

	circular hole			Square hole		
	(1,0) P	(1,1) P	(1,1) A	(1,0) P	(1,1) P	(1,1) A
S150-P375	NM	NM	NM	NM	NM	-
S150-P400	NM	NM	82	NM	40	-
S150-P425	NM	NM	76	NM	NM	59
S150-P450	NM	NM	68	NM	NM	64
S150-P475	NM	NM	56	NM	NM	62
S200-P375	151	55	NM	160	NM	-
S200-P400	149	59	NM	178	NM	-
S200-P425	154	NM	71	165	68	62
S200-P450	150	NM	66	159	NM	82
S200-P475	148	NM	63	151	NM	99
S250-P375	179	NM	NM	194	NM	-
S250-P400	178	54	NM	218	NM	-
S250-P425	172	NM	72	207	NM	NM
S250-P450	165	NM	85	195	93	96
S250-P475	158	NM	79	180	NM	117

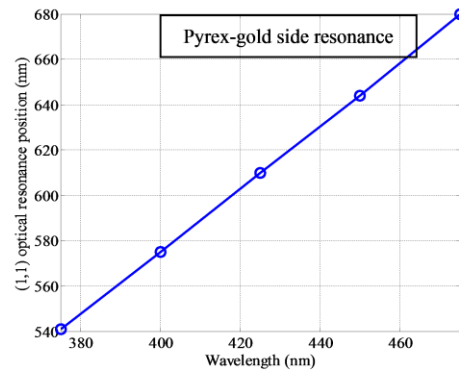
Not Measurable (NM), - (not observed)

The optical resonance position versus periodicity for the (1,1) optical resonance peaks from the Pyrex-gold side and the (1,1) optical resonance transmission efficiency from the Pyrex-gold side are shown in Figure 2-3 (d) and (e), respectively. The (1,1) resonance peaks red-shifted as the hole periodicity increased. However, at a given

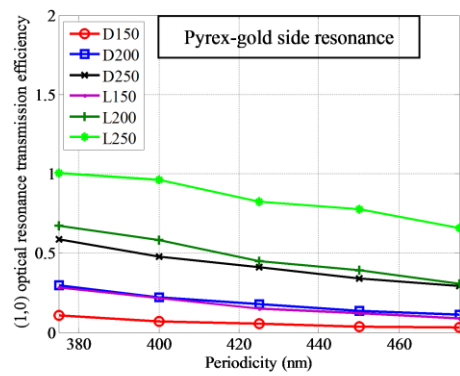
periodicity, all arrays of various hole shape and hole size had identical (1,1) optical resonance positions (therefore, only one line is plotted). In Figure 2-3 (e), the optical resonance transmission efficiency related to (1,1) SP excitation increased as the hole size increased. Also, as the hole size increased a transition from a decrease in transmission efficiency with periodicity to an increase in transmission efficiency with periodicity was observed in the simulation results. For example, the array with square hole size of 250 nm increased in transmission efficiency as a function of periodicity from 375 nm to 450 nm. The (1,0) optical resonance peak related to the air-gold side was observed for all arrays with circular hole shape, but only observed at higher periodicities for arrays with square hole shape (Table 2-1; Figure 2-3 (f)). In Figure 2-3 (f), the (1,0) optical resonance peak related to the air-gold side red-shifted as the periodicity of the holes increased. Also, as the hole size increased for arrays with square and circular holes, the (1,0) optical resonance position increased and this effect was more apparent for arrays with larger periodicities. For arrays with circular holes and smaller periodicities, no dependence on hole size was observed.



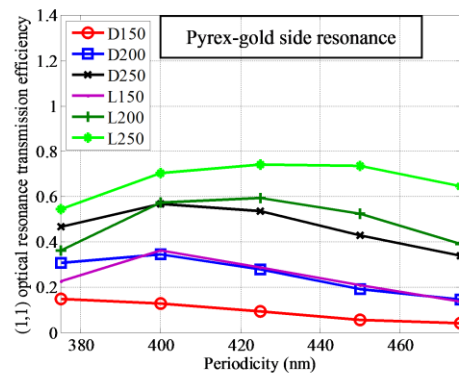
(a)



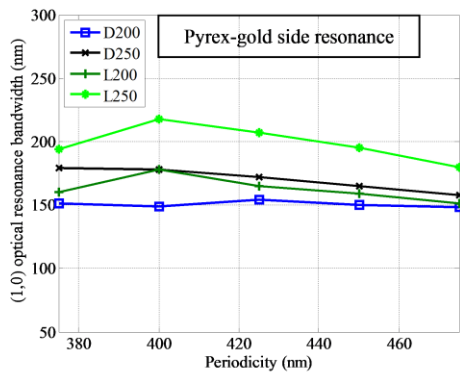
(d)



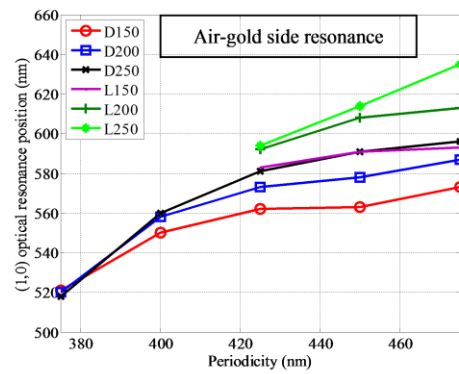
(b)



(e)



(c)



(f)

Figure 2-3. *(1,0) and (1,1) optical resonance analyses of the nano-hole arrays for simulation results (in the graphs legend, D circular hole diameter and L square hole length): (a) (1,0) Pyrex-gold side optical resonance position versus periodicity, (b) (1,0) Pyrex-gold side optical resonance transmission efficiency versus periodicity, (c) (1,0) Pyrex-gold side optical resonance bandwidth versus periodicity, (d) (1,1) Pyrex-gold side optical resonance position versus periodicity, (e) (1,1) Pyrex-gold side optical resonance transmission efficiency versus periodicity, and f) (1,0) air-gold side optical resonance transmission versus periodicity.*

2.4.3. Experimental results

The experimental results and analysis for optical transmission spectra of the nano-hole arrays with various hole shapes (circular and square), hole sizes (150nm, 200nm, and 250nm) and periodicities (375nm, 400nm, 425nm, 450nm, and 475nm) in the square lattice arrangement are shown in Figures 2-4 and 2-5. The experimental results (see Figure 2-4) are presented in a format that is similar to the presentation of the simulation results (see Figure 2-2). In general, the experimental optical transmission spectra were qualitatively similar to the simulated spectra. For example, the (1,0) and (1,1) optical resonance peaks related to the SP excitation from the Pyrex-gold side and Wood's anomaly were observed. However, there were differences in the number of observable peaks and measurable bandwidths (compare Table 2-2 to Table 2-1). For instance, the (1,0) resonance peak from the air-gold side was not clearly observed in the experimentally measured spectra for the most of the arrays except the arrays with 150 nm circular hole and periodicities of 450 nm and 475 nm. Furthermore, the (1,1) optical resonance peaks from Pyrex-gold side had measurable bandwidths for the most of the arrays in the experimental results, which were not generally measurable in simulation studies (compare Table 2-2 to Table 2-1).

The dependence of the (1,0) optical resonance position, (1,0) optical resonance transmission efficiency, and (1,0) optical resonance bandwidth on periodicity, hole size and hole shape were generally similar to the corresponding metrics derived from simulations (see Figure 2-3 and 2-5). Both simulation and experimental results agreed with respect to the red-shift of the (1,0) optical resonance position as the periodicity of the holes increased (see Figure 2-3 (a) and Figure 2-5 (a)). Also, the (1,0) optical

resonance position derived from the simulation results was in good agreement with the experimental results. However, the experimental results showed less dependence of the (1,0) optical resonance position on hole size compared to the simulation results for the arrays with the same periodicity. The red-shift was generally observed for the (1,0) resonance position as hole size increased in the simulation results, while there was no systematic dependence of resonance position on hole size for the experimental results (both blue-shifts and red-shifts were observed). With respect to the (1,0) optical resonance transmission efficiency, both the simulation and experimental results were generally in agreement for the smallest hole size (see Figure 2-3 (b) and Figure 2-5 (b)). However, as the hole size increased a transition from a decrease in transmission efficiency with periodicity to an increase in transmission efficiency with periodicity was observed in the experimental results. For example, the transmission efficiency of the array with 250 nm square hole size increased as a function of periodicity. This was largely true for the circular hole shaped arrays with 250 nm holes, except for devices with periodicities of 425 nm and higher where the transmission efficiency was observed to be relatively constant. Although the optical resonance bandwidth was not highly dependent on periodicity in the simulations, the bandwidth decreased with periodicity in the experimental results and bandwidths were significantly smaller (compare Tables 2-1 and 2-2) and (see Figure 2-3 (c) and Figure 2-5 (c)). Furthermore, the dependence of bandwidth on hole size was greater for the experimental results compared to the simulations. For example, for simulations, arrays with circular holes of 200 nm and 250 nm, the bandwidths were measured to be 149 and 178 nm, respectively, while the corresponding experimental observations resulted in bandwidths of 86 and 143 nm, respectively.

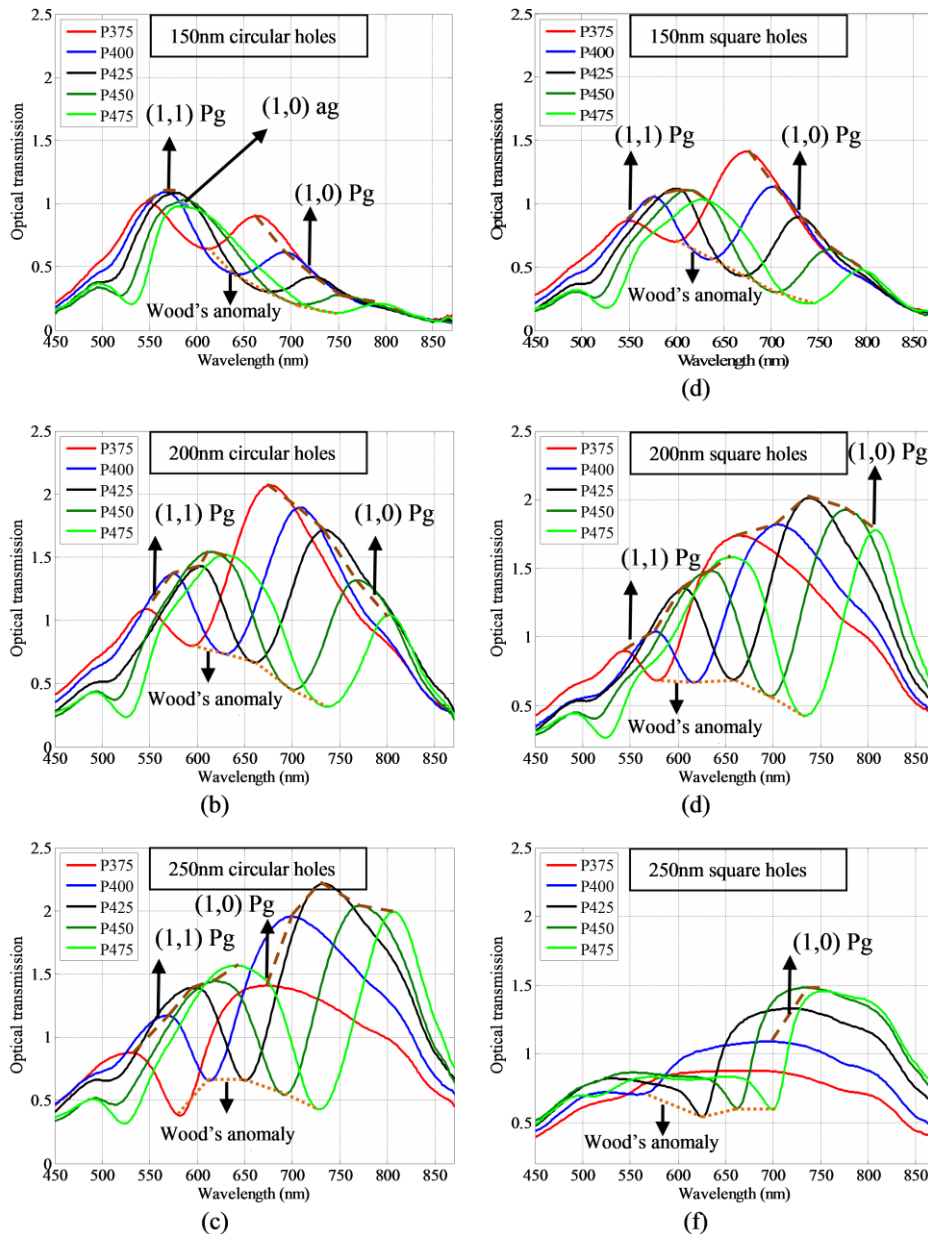


Figure 2-4 Optical transmission spectra for nano-hole arrays with various hole shape (square and circular), diameters (150nm, 200nm, and 250nm), and periodicities or P(375nm, 400nm, 425nm, 450nm, and 475nm) in experimental results: (a) circular holes with 150nm diameter, (b) circular holes with 200nm diameter, (c) circular holes with 250nm diameter, (d) square holes with 150nm length, (e) square holes with 200nm length, and (f) square holes with 250nm length. (ag) represents the optical resonance peak from air-gold side. (Pg) represents the optical resonance peak from Pyrex-gold side.

Table 2-2. Summary of experimental results related to optical resonance peaks

	circular hole			Square hole		
	(1,0)P	(1,1)P	(1,0)A	(1,0)P	(1,1)P	(1,0)A
S150-P375	NM	76	-	88	NM	-
S150-P400	NM	69	-	74	71	-
S150-P425	NM	79	-	67	77	-
S150-P450	NM	-	85	72	93	-
S150-P475	NM	-	86	54	108	-
S200-P375	94	NM	-	148	NM	-
S200-P400	86	70	-	125	74	-
S200-P425	80	76	-	104	74	-
S200-P450	74	96	-	86	84	-
S200-P475	53	110	-	58	94	-
S250-P375	186	87	-	-	-	-
S250-P400	143	74	-	NM	-	-
S250-P425	120	88	-	189	-	-
S250-P450	95	100	-	153	-	-
S250-P475	95	117	-	124	-	-

Not Measurable (NM), - (not observed)

Both simulation and experimental results agreed with respect to the red-shift of the (1,1) optical resonance position as the periodicity of the holes increased (see Figure 2-3 (d) and Figure 2-5 (d)). However, for a given periodicity, the (1,1) optical resonance position was slightly (blue-shifted or red-shifted) as the hole size increases in the experimental results which no change was observed in the simulation results. With respect to the (1,1) optical resonance transmission efficiency, similar behavior between simulation and experimental results was observed (see Figure 2-3 (e) and Figure 2-5 (e)); however, the increase in transmission efficiency with increasing hole size was not as apparent for the arrays with the largest hole size (e.g. 200 to 250 nm) and some instances decreases in efficiency were observed as the hole size increased (e.g. 200 to 250 nm at periodicity of 400 nm). As shown in Figure 2-5 (f), the (1,1) resonance

bandwidth increased with periodicity, except for smaller periodicities (375 nm and 400 nm). For a given periodicity, the (1,1) resonance bandwidths were similar for various hole sizes and shapes.

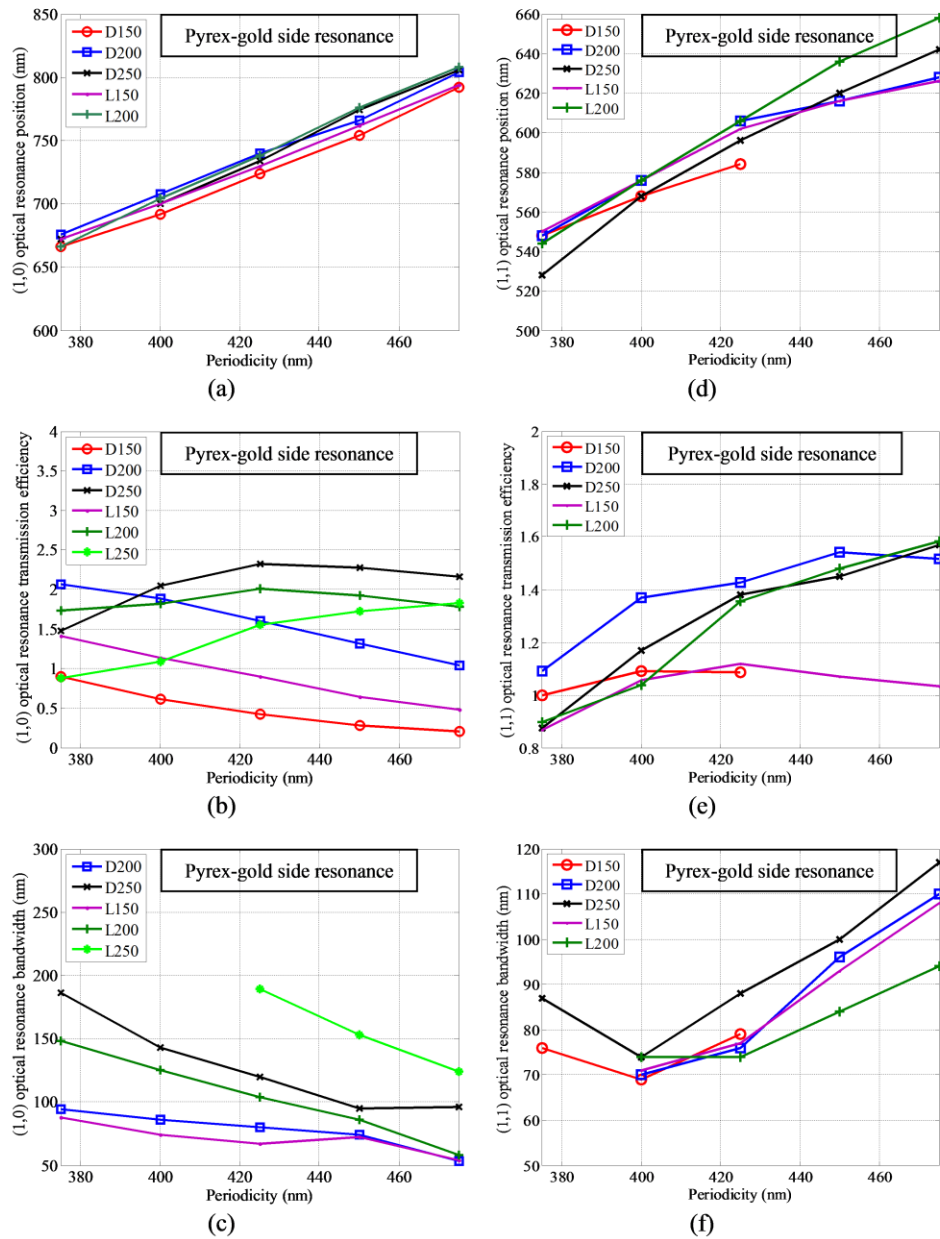


Figure 2-5. *(1,0) and (1,1) Pyrex-gold side optical resonance analyses of the nano-hole arrays for experimental results (in the graphs legend, D circular hole diameter and L square hole length): (a) (1,0) optical resonance position versus periodicity, (b) (1,0) optical resonance transmission efficiency versus periodicity, (c) (1,0) optical resonance bandwidth versus periodicity, (d) (1,1) optical resonance position versus periodicity, (e) (1,1) optical resonance transmission efficiency versus periodicity, and (f) (1,1) optical resonance bandwidth versus periodicity.*

2.5. Discussion

The (1,0) and (1,1) optical resonance positions related to the Pyrex-gold side of nano-hole arrays for various periodicities were calculated using equation (1-1). The (1,0) optical resonance positions for the periodicities of 375 nm, 400 nm, 425 nm, 450 nm, and 475 nm were 659 nm, 682 nm, 710 nm, 742 nm, and 776 nm, respectively. Also, the (1,1) optical resonance positions were computed to be 536 nm, 547 nm, 561 nm, 584 nm, and 616 nm for the corresponding periodicities. The resonance peak positions observed in experiment and simulation were in good qualitative agreement with the theoretical estimates.

Although there was general agreement between the optical properties of nano-hole arrays studied by experiment and simulation, there were several notable differences. First, the transmission efficiency for (1,0) and (1,1) resonance peaks related to the Pyrex-gold side obtained through simulation was significantly lower compared to the experimental results. This was likely due to the high sensitivity of the simulated transmission spectra on presence of the chromium layer. For example, sharp resonance peaks were observed when the chromium layer was excluded (data not shown) in a manner similar to other work [2-8]. It is possible that the selection of the mesh accuracy, although small enough to adequately sample the chromium layer, resulted in an underestimation of the transmission efficiency. The slight discrepancy between simulation and experimental results due to the selection of the mesh accuracy enabled manageable computation times. Second, although the optical resonance peaks related to the (1,0) air-gold side were observed in the simulation studies, they were not observed consistently in the experimental studies. This was most likely on account of the closeness of the (1,1) resonance peak position to (1,0) resonance and the poorer transmission efficiency of the (1,0) resonance from air-gold side. As a result, the (1,0) resonance peaks on the air-gold side were not observed for all of the arrays, except for the arrays with 150 nm circular hole size and higher periodicities (450 nm and 475 nm). Since the arrays with 150 nm holes and higher periodicities (450 nm and 475 nm) had a smaller total hole area compared to the other tested arrays, the resonance peaks of longer wavelength had lower transmission efficiency compared to other arrays with

larger hole sizes. As a result, the (1,1) resonance peak from the Pyrex-gold side and the (1,0) resonance peak from air-gold side appeared at longer and shorter wavelengths, respectively. This effect resulted in more pronounced (1,0) resonance peaks from the air-gold side for these arrays (150 nm circular hole with 450 nm and 475 nm periodicities) and suppression of the (1,1) resonance peak from the Pyrex-gold side. Third, in the simulations, the transmission efficiency of the (1,0) Pyrex-gold side resonance peak improved with hole size. Based on geometric considerations, the transmission behaviour was consistent with the total effective aperture of the nano-hole array, i.e. larger holes and closer hole spacing resulted in larger total opening size compared to nano-hole arrays with smaller holes and wider hole spacing. This geometric dependence of the optical transmission efficiency on hole area has been known for over a decade [2-10]. Although this general optical transmission behaviour was observed in experiments performed with nano-hole arrays with circular holes, the transmission efficiency determined through experiment did not increase in a manner consistent with the effective aperture hypothesis. The discrepancy was most apparent for nano-hole arrays with square holes. For example, nano-hole arrays with square holes 200 nm in size had greater transmission efficiency than arrays of identical periodicity with square holes either 150 nm or 250 nm in size. Although the reason for this behaviour is not fully understood, it may be related to more efficient coupling of the light to the SP with this specific hole size in the visible and near infra-red regime, which could potentially result in a higher transmission efficiency.

It has been reported in early literature that the optical resonance position is not dependent on hole size [2-1]. However, we found experimentally that the (1,0) optical resonance position varied slightly (blue-shifted or red-shifted) with hole size. In agreement with our results, it has been reported for nano-hole arrays with square hole shape that a similar shift in resonance position behavior occurs, which was attributed to a cutoff behavior related to the hole size [2-23]. Also, in agreement with literature (see ref. [2-10]), we also observed that the (1,0) optical resonance bandwidth became larger for larger holes and narrower for larger periodicities.

Using the EBL fabrication methodology, the pattern on the photoresist for a nano-hole array 1 mm by 1 mm can be written in a couple of hours with reasonable cost. However, compared to other methods such as Focused Ion Beam (FIB) milling technology, EBL fabrication methodology requires a thicker adhesion layer (such as 8 nm to 20 nm Chromium or Titanium) to allow for an aggressive lift-off process without damaging an array. Since the adhesion layer is deposited between the gold and Pyrex substrate, the optical performance of the nano-hole array is affected. For example, we observed that the bandwidth of the (1,0) and (1,1) resonance peak was broadened and the transmission efficiency was lower. However, deposition of metal materials such as aluminum or silver on the Pyrex substrate does not require an adhesion layer, but these materials are sensitive to oxidization that leads to loss of the SP properties. Also, unlike other methods for nano-hole-array fabrication, patterns such as grooves, corrugations, and dimples cannot be fabricated about the holes easily with EBL. Other fabrication methodologies such as Nano-Imprint Lithography (NIL) and FIB are proven methods for fabrication of nano-hole arrays [2-24]-[2-26]. FIB fabrication methodology can be used to fabricate arbitrary nano-hole array designs with fine resolution, but at the cost of speed. Alternatively, very large nano-hole arrays can be fabricated with NIL methodology very quickly, but with poorer resolution and higher cost. Therefore, EBL provides a rapid and competitive fabrication solution for nano-hole arrays of intermediate size where fidelity of nanostructures is important.

Although the motivation for this study was the potential development of nano-hole arrays as spectral filters. The analysis of the EOT properties of various nano-hole array designs revealed that the band-pass characteristics of the devices simulated and tested was far from optimal when compared to conventional commercially available interference filters. Typically, it was observed that the nano-hole arrays had at least two pass bands with poor blocking between and on either side. Poor out of band blocking would result in bleed through of out of band wavelengths and corruption of spectroscopic data, for example. To improve band-pass performance several options remain including manipulation of the dielectrics on either side of the gold and incorporation of nano-scale features to enhance wavelength selectivity and transmission efficiency. For example, a nano-hole array surrounded with the material of the same dielectric constant on both

sides is known to increase the transmission efficiency of the resonance peak due to SP energy coincidence on both sides of a nano-hole array [2-14]. Also, structures such as grooves, corrugations, and dimples about the holes of a nano-hole array or surrounding an entire nano-hole array can enhance transmission efficiency of the resonance peak [2-11] [2-16]. For example, it has been shown that a nano-hole array surrounded by dimples with the same size and shape as the holes and at half periodicity of the holes can improve transmission efficiently by a factor of two [2-16]. In addition to the hole size effect on the bandwidth of the resonance peaks, the bandwidth can be reduced if the nano-hole array is fabricated in a thicker metal film. However, the transmission efficiency of the resonance peak decays as thickness of metal film increases [2-1]. Also, a 10 to 20 nm adhesion layer of Chromium can cause broadening of the bandwidth of the resonance peaks related to the Pyrex-gold side of the nano-hole array. As a result, by exploiting other materials such as Ag or Al [2-8], the need for a Chromium layer can be eliminated and narrower bandwidths can be achieved.

Regardless of the poor blocking characteristics of the nano-hole arrays studied here, an interesting aspect of nano-hole arrays is their scalable size. The nano-hole array dimension can be varied from several microns to several centimeters in size. This provides interesting opportunities to utilize the same base technology for applications that work at microscopic scales to applications that work at macroscopic scales. For example, the optical resonance of nano-hole arrays for various geometrical parameters can be exploited in applications such as SEFS and bio-sensing applications, where the optical resonance transmission properties of the nano-hole arrays can enhance the detectability of fluorescence emission and bio-molecules [2-2]-[2-5].

In the future, additional studies will need to be directed at improving the optical resonance transmission efficiency of nano-hole arrays and reducing bandwidth if nano-hole arrays are to be used as spectral band-pass filters for biomedical applications. Probably the most success will come from examining new substrates and dielectric matching of the top and bottom layers. As a result, in future work, we are planning to do a comprehensive experimental and numerical analyses on optical transmission of nano-

hole arrays when they are surrounded by transparent materials such as Polymethyl methacrylate (PMMA), transparent SU-8, and silicon dioxide.

2.6. Conclusion

We presented a comprehensive experimental and numerical (FDTD) study on Extraordinary Optical Transmission (EOT) through various nano-hole arrays in a thick metal film within the visible and near infra-red spectral regions. Large nano-hole arrays were fabricated using EBL methodology and they were optically characterized. We analyzed the simulation and the optical characterization results of optical resonance of nano-hole arrays with respect to optical resonance peak position, optical resonance transmission efficiency, and optical resonance bandwidth. As a result, regarding these parameters, the simulation results showed relatively good agreement with the experimental analyses although there were some notable differences. The hole size was recognized as a main factor in the appearance of the optical resonance peaks in the transmission spectra. There were no significant differences between optical transmission spectra of nano-hole arrays with circular or square hole shapes. However, the opening area of the hole had a major effect on the optical resonance transmission properties. The effect of the chromium adhesion layer between the gold film and the Pyrex substrate reduced the transmission efficiency for the optical resonance peaks related to SP excitation from Pyrex-gold side. Finally, the analyses showed that for macroscopic applications such as optical band-pass filters, improved out of band blocking are needed. One possibility for achieving this optical characteristic is the matching of the SP energy on both sides of the array by index-matching.

2.7. References

- 2-1. Thio, T., Ghaemi, H. F., Lezec, H. J., Wolff, P. A., & Ebbesen, T. W. (1999). Surface-plasmon-enhanced transmission through hole arrays in cr films. *Journal of the Optical Society of America B*, 16(10), 1743-1748. Retrieved from <http://josab.osa.org/abstract.cfm?URI=josab-16-10-1743>

- 2-2. Gordon, R., Brolo, A. G., Sinton, D., & Kavanagh, K. L. (2010). *Resonant optical transmission through hole-arrays in metal films: Physics and applications* - WILEY-VCH Verlag. doi:- 10.1002/lpor.200810079
- 2-3. Brolo, A. G., Kwok, S. C., Moffitt, M. G., Gordon, R., Riordon, J., & Kavanagh, K. L. (2005). Enhanced fluorescence from arrays of nanoholes in a gold film. *Journal of the American Chemical Society*, 127(42), 14936-14941. doi:10.1021/ja0548687
- 2-4. Lakowicz, J. R., Chowdury, M. H., Ray, K., Zhang, J., Fu, Y., Badugu, R. Geddes, C. D. (2006). Plasmon-controlled fluorescence: A new detection technology. Paper presented at the , 6099(1) 609909-15. Retrieved from <http://dx.doi.org/10.1117/12.673106>
- 2-5. Lesuffleur, A., Im, H., Lindquist, N. C., Lim, K. S., & Oh, S. (2008). Laser-illuminated nanohole arrays for multiplex plasmonic microarray sensing. *Optics Express*, 16(1), 219-224. Retrieved from <http://www.opticsexpress.org/abstract.cfm?URI=oe-16-1-219>
- 2-6. Huang, F. M., Zheludev, N., Chen, Y., & de Abajo, F. Javier Garcia. (2007). Focusing of light by a nanohole array. *Applied Physics Letters*, 90(9), 091119-3. Retrieved from <http://link.aip.org/link/?APL/90/091119/1>
- 2-7. Gordon, R., Brolo, A. G., McKinnon, A., Rajora, A., Leathem, B., & Kavanagh, K. L. (2004). Strong polarization in the optical transmission through elliptical nanohole arrays. *Physical Review Letters*, 92(3), 037401. Retrieved from <http://link.aps.org/doi/10.1103/PhysRevLett.92.037401>
- 2-8. Rodrigo, S. G., García-Vidal, F. J., & Martín-Moreno, L. (2008). Influence of material properties on extraordinary optical transmission through hole arrays. *Physical Review B*, 77(7), 075401. Retrieved from <http://dx.doi.org.proxy.lib.sfu.ca/10.1103/PhysRevB.77.075401>
- 2-9. Przybilla, F., Degiron A., Laluet J-Y., Genet C. & Ebbesen, T. W. (2006). Optical transmission in perforated noble and transition metal films. *Journal of Optics A: Pure and Applied Optics*, 8(5) 458. Retrieved from <http://stacks.iop.org.proxy.lib.sfu.ca/1464-4258/8/i=5/a=015>
- 2-10. Ebbesen, T. W., Lezec, H. J., Ghaemi, H. F., Thio, T., & Wolff, P. A. (1998). Extraordinary optical transmission through sub-wavelength hole arrays. *Nature*, 391(6668), 667-669. Retrieved from <http://dx.doi.org/10.1038/35570>
- 2-11. Shuford, K. L., Ratner, M. A., Gray, S. K., & Schatz, G. C. (2006). Finite-difference time-domain studies of light transmission through nanohole structures. *Applied Physics B: Lasers and Optics*, 84(1), 11-18. Retrieved from <http://dx.doi.org/10.1007/s00340-006-2218-x>
- 2-12. Bravo-Abad, J., Martín-Moreno, L., & Garcia-Vidal, F. J. (2006). Resonant transmission of light through subwavelength holes in thick metal films. *IEEE J. of Selected Topics in Quantum Electronics*, 12, 1221.

- 2-13. Przybilla, F., Degiron, A., Genet, C., Ebbesen, T., de León-Pérez, F., Bravo-Abad, J., Martín-Moreno, L. (2008). Efficiency and finite size effects in enhanced transmission through subwavelength apertures. *Optics Express*, 16(13), 9571-9579. Retrieved from <http://www.opticsexpress.org/abstract.cfm?URI=oe-16-13-9571>
- 2-14. Krishnan, A., Thio, T., Kim, T. J., Lezec, H. J., Ebbesen, T. W., Wolff, P. A., Garcia-Vidal, F. J. (2001). Evanescently coupled resonance in surface plasmon enhanced transmission. *Optics Communications*, 200(1-6), 1-7. Retrieved from <http://www.sciencedirect.com/science/article/pii/S0030401801015589>
- 2-15. Garcia, d. A. (2002). Light transmission through a single cylindrical hole in a metallic film. *Optics Express*, 10(25), 1475-1484. Retrieved from <http://www.opticsexpress.org/abstract.cfm?URI=oe-10-25-1475>
- 2-16. Gordon, R., & Marthandam, P. (2007). Plasmonic bragg reflectors for enhanced extraordinary optical transmission through nano-hole arrays in a gold film. *Optics Express*, 15(20), 12995-13002. Retrieved from <http://www.opticsexpress.org/abstract.cfm?URI=oe-15-20-12995>
- 2-17. Genet, C., & Ebbesen, T. W. (2007). Light in tiny holes. *Nature*, 445(7123), 39-46. doi:10.1038/nature05350
- 2-18. van Hulst, N. F. (2008). Plasmonics: Sorting colours. *Nat Photon*, 2(3), 139-140. Retrieved from <http://dx.doi.org/10.1038/nphoton.2008.10>
- 2-19. Barnes, W. L., Dereux, A., & Ebbesen, T. W. (2003). Surface plasmon subwavelength optics. *Nature*, 424(6950), 824-830. Retrieved from <http://dx.doi.org/10.1038/nature01937>
- 2-20. Yee, K. S. (1966). Numerical solution of initial boundary value problems involving Maxwell's equations in isotropic media. *IEEE Trans.Ant.Prop.*, 14, 302.
- 2-21. Taflove, A., & Hagness, S. C. (Eds.). (2000). *Computational electrodynamics: The finite-difference time-domain method* (Second ed.). Boston: Artech House.
- 2-22. Palik, E. D. (1985). *Handbook of optical constants of solids*. New York: Academic Press.
- 2-23. van, d. M., Segerink, F. B., van Hulst, N. F., & Kuipers, L. (2004). Influence of hole size on the extraordinary transmission through subwavelength hole arrays. *Applied Physics Letters*, 85(19), 4316-4318. Retrieved from <http://link.aip.org/link/?APL/85/4316/1>
- 2-24. Yu, Z., Gao, H., Wu, W., Ge, H., & Chou, S. Y. (2003). Fabrication of large area subwavelength antireflection structures on si using trilayer resist nanoimprint lithography and liftoff. *J. Vac. Sci. Technol. B*, 216, 2874.

- 2-25. Malyarchuk, V., Hua, F., Mack, N., Velasquez, V., White, J., Nuzzo, R., & Rogers, J. (2005). High performance plasmonic crystal sensor formed by soft nanoimprint lithography. *Optics Express*, 13(15), 5669-5675. Retrieved from <http://www.opticsexpress.org/abstract.cfm?URI=oe-13-15-5669>
- 2-26. Tseng, A. (2005). Recent developments in nanofabrication using focused ion beams. *Small*, 1(10), 924-939. doi:10.1002/sml.200500113
- 2-27. Chen, J., Shi, J., Decanini, D., Cambril, E., Chen, Y., & Haghiri-Gosnet, A. (2009). Gold nanohole arrays for biochemical sensing fabricated by soft UV nanoimprint lithography. *Microelectronic Engineering*, 86(4), 632-635. Retrieved from <http://www.sciencedirect.com/science/article/pii/S0167931709000161>

3. Optical resonance transmission properties of nano-hole arrays in a gold film: effect of adhesion layer²

3.1. Abstract

In this paper, we present a systematic study on the influence of composition of the adhesion layer between gold and a Pyrex substrate on the optical resonance transmission properties of nano-hole arrays in an optically thick gold film. Large nano-hole arrays with different hole periodicities in a square lattice arrangement were fabricated using Electron Beam Lithography using different adhesion layers (chromium, titanium, or etched adhesion layer). The fabricated nano-hole arrays were optically characterized using transmission spectroscopy. The optical performance of each nano-hole array was numerically simulated using a Finite Difference Time Domain (FDTD) method. The experiments and simulations revealed that the optical resonance transmission properties (i.e. the resonance wavelength, the spectral transmission modulation ratio, and the resonance bandwidth) of the nano-hole arrays depended highly on the composition and the thickness of the adhesion layer. The optical

² The following chapter is published in Optics Express, Vol. 19, No. 27, 26186 (2011) under the co-authorship of Fartash Vasefi, Bozena Kaminska, and Jeffery J.L. Carson. Retrieved from <http://dx.doi.org/10.1364/OE.19.026186>

This paper was published in [Optics Express] and is made available as an electronic reprint with the permission of OSA. The paper can be found at the following URL on the OSA website: [<http://www.opticsinfobase.org/oe/abstract.cfm?URI=oe-19-27-26186>]. Systematic or multiple reproduction or distribution to multiple locations via electronic or other means is prohibited and is subject to penalties under law.

resonance bandwidths were larger for the nano-hole arrays with chromium or titanium adhesion layers. Also, a red-shift of the optical resonance peak was observed for nano-hole arrays with a metal adhesion layer compared to the corresponding nano-hole arrays with an etched adhesion layer, but the red-shift was greatest for the nano-hole array with the titanium adhesion layer. For adhesion layers of greater thickness, the optical resonance peaks were reduced in magnitude. Finally, nano-hole arrays with an etched adhesion layer had a significant blue-shift in the optical resonance peak and a narrower optical resonance bandwidth compared to nano-hole arrays with a titanium or a chromium adhesion layer. Consequently, a narrow optical resonance bandwidth characteristic of a nano-hole array with an etched adhesion layer can potentially enhance the spectral selectivity and offer improved optical performance.

3.2. Introduction

A nano-hole array, that is an array of periodic sub-wavelength apertures fabricated in an optically thick metal film, can exhibit extraordinary optical transmission (EOT). This unique property has enabled researchers to design and miniaturize optical elements in a way that surpasses the diffraction limit from standard aperture theory [3-1]. The EOT or optical resonance transmission property of nano-hole arrays is caused by the interaction of light with the Surface Plasmon (SP) that exists between the metal and dielectric surfaces and results in the resonant transmission of light through nano-holes by exploiting the tunneling effect [3-2]. That is, light incident on one side of the metallic film of the nano-hole array is coupled to SPs that enter the nano-holes and decouple on the other side of the film. The EOT properties of nano-hole arrays have many potential applications in sub-wavelength photolithography, near-field scanning optical microscopy, wavelength-tunable filters, surface enhanced fluorescence spectroscopy, and molecular sensing [3-3]-[3-7].

It is well-known that the optical resonance transmission properties of nano-hole arrays depend greatly on the lattice arrangement of holes, the distance between adjacent holes (periodicity), and the dielectric constants of the metal and surrounding

dielectrics. For normal incidence of light, the spectral position of the optical transmission maximum of a nano-hole array is well-described by

$$\lambda_{max} = \frac{a_0}{\sqrt{i^2 + j^2}} \sqrt{\frac{\epsilon_m \epsilon_d}{\epsilon_m + \epsilon_d}} \quad 3-1$$

and its corresponding optical transmission minimum by

$$\lambda_{min} = \frac{a_0}{\sqrt{i^2 + j^2}} \sqrt{\epsilon_d} \quad 3-2$$

These relations hold for holes in a square lattice arrangement, where a_0 is the periodicity of holes, ϵ_d and ϵ_m are the dielectric constants of the incident medium (at the top or bottom surface of the nano-hole) and the metal film, and i and j are integers expressing the scattering mode indices [3-1] [3-2]. Many studies have investigated the effect of various metals and dielectrics on the optical transmission properties of nano-hole arrays [3-8]-[3-12]. For instance, nano-hole arrays fabricated in metallic films such as Ag, Au, and Cu have larger optical resonance transmission peaks than nano-hole arrays with the same geometrical parameters in a perfect metal conductor [3-8]. However, Cr and Ni have high absorption properties in the optical region, which greatly influences the optical transmission properties of nano-hole arrays incorporating these materials [3-9]. Matching the dielectric constant surrounding the back and front of nano-hole array in a metal film enhances the optical resonance transmission efficiency due to the coincidence of SP energy on both sides [3-10]. In addition to the material effects on the optical resonance transmission properties, various geometrical effects such as hole shape, hole size, and hole periodicity have been explored [3-11]- [3-13]. For instance, the optical resonance transmission peaks of nano-hole arrays with elliptical hole shape depend highly on the angle of polarization of the incident light although no polarization dependency was observed for circular and square hole shapes [3-11]. Also, the hole size has a significant effect on the optical resonance transmission efficiency and the resonance bandwidth of nano-hole arrays [3-12] [3-13].

3.3. Motivation and objective

A nano-hole array fabricated in a noble metal such as gold has a higher optical resonance transmission compared to nano-hole arrays in other metals [3-8]. Unlike other noble metals such as Ag and Cu, gold does not suffer from oxidation and is chemically unreactive. As a result, gold has been the material of choice for fabrication of nano-hole arrays for applications such as bio-sensing and chemical sensing based on the Surface Plasmon Resonance (SPR) [3-14]. Nevertheless, there is a need for a thin adhesion layer between the glass substrate and the gold film during fabrication. Several studies have explored the effect of the adhesion layer on the optical properties of various plasmonic structures and its impact on performance in various applications [3-15]-[3-20]. For example, a thin titanium adhesion layer between gold and a semiconductor substrate caused a 20 nm red-shift on the resonance position of slit-ring resonators (SRR) [3-15]. Also, the effect of the adhesion layer on the Short Range Surface Plasmon Polariton (SR-SPP) of gold bowtie antennae was numerically calculated and it was observed that the SR-SPP quenched when the adhesion layer was titanium or chromium. The suppression of the SR-SPP was stronger for chromium due to its higher extinction coefficient [3-17]. Motivated by the reported effects of the adhesion layer on the optical properties of slit-ring resonators and bowtie antennae, we performed a systematic study on the effect of the adhesion layer on the EOT properties of nano-hole arrays in a gold film, which could potentially impact spectral filtering and bio-sensing applications.

Our approach was to perform numerical and experimental analyses on the optical resonance transmission properties of a series of nano-hole arrays in a gold film, where various adhesion layers were used (thin Ti, thin Cr, thicker Ti or etched thicker Ti adhesion layer). Nine different nano-hole arrays with various geometrical parameters (hole size and periodicity) were fabricated in a square lattice arrangement in 100 nm gold film for each adhesion layer case. The geometrical design of each nano-hole array was selected so that the optical resonance transmission properties were within the visible and near infra-red regime. Nano-hole arrays were fabricated using Electron Beam Lithography (EBL). Each nano-hole array was characterized with optical transmission

spectroscopy and the experimental results were compared with numerical calculations by Finite Difference Time Domain (FDTD) with respect to the (1,0) optical resonance transmission properties related to (1,0) SP excitation from Pyrex-gold side.

3.4. Methods

3.4.1. *Electron Beam Lithography (EBL)*

We used electron beam lithography (EBL) to fabricate nano-hole arrays in a 100 nm optically thick gold film. The fabrication process is shown in Figure 3-1. In order to fabricate gold nano-hole arrays on a Pyrex substrate using EBL, we first deposited a conductive layer to enable the electron beam to be focused on the Pyrex substrate when writing patterns. We deposited a 3 nm thin conductive layer of chromium or titanium on the Pyrex substrate using electron beam physical vapor deposition (EB_PVD) (see Figure 3-1 (a)). Then, a 500 nm photo-resist (Negative Tone photo-resist ma-N 2403) was spin-coated and soft-baked on the conductive layer (see Figure 3-1 (b)). The pattern of nano-hole arrays was written with the EBL machine (LEO, 1530 e-beam lithography) and followed by development of the sample to leave behind photo-resist pillars (see Figure 3-1 (c)). The adhesion layer (similar metal to the conductive layer with thickness of 5 nm for a thin chromium adhesion layer, 5 nm for a thin titanium adhesion layer and 10 nm for a thicker titanium adhesion layer) was deposited (see Table 3-1 for a summary of the fabricated nano-hole arrays with various conductive and adhesion layers) (see Figure 3-1 (d)) and followed by deposition of a 100 nm gold layer (see Figure 3-1 (e)). Finally, the sacrificial mask layer (photo-resist pillars) was lifted off to leave behind the nano-hole array patterns in the gold film (see Figure 3-1 (f)). The SEM images of a fabricated nano-hole array are shown in Figure 3-2. Previous AFM work by another group employing the same EB_PVD system determined that the surface roughness of the gold layer was 1.9 nm [3-21].

For one device with a 10 nm titanium adhesion layer, we used a titanium etchant (TFT, Transene company, Inc.) to isotropically etch away the titanium adhesion layer. The etching rate of TFT for titanium was 2.5 nm/s at 20°C. Also, since the etchant

contained 30% Hydrofluoric (HF) acid, it also etched the Pyrex substrate at approximate 4.3 nm/s. As a result, after the titanium conductive and adhesion layers within the holes were removed, the etchant had the opportunity to etch the Pyrex substrate and the titanium adhesion layer between the holes and beneath the gold film. For example, a nano-hole array with a 3 nm titanium conductive layer and a 10 nm titanium adhesion layer placed in the titanium etchant for 20 s resulted in removal of the 3 nm conductive layer, the 10 nm adhesion layer, and approximately 64 nm of Pyrex.

Table 3-1. Summary of the conductive and adhesion layer composition and thickness

Sample name (abbreviated name)	Conductive layer	Adhesion layer
Thin chromium adhesion layer (Cr5)	3 nm	5 nm
Thin titanium adhesion layer (Ti5)	3 nm	5 nm
Thicker titanium adhesion layer (Ti10)	3 nm	10 nm
Etched thicker titanium adhesion layer (Ti10-etched)	Not measured	Not measured
No adhesion layer	0	0
No adhesion layer sample only presented in the simulation results.		

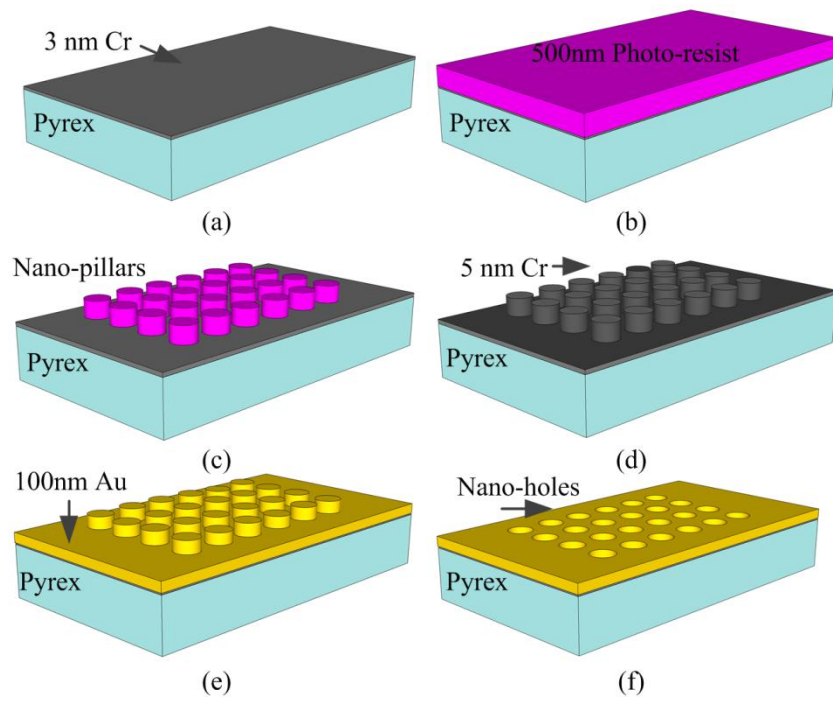


Figure 3-1. Electron beam lithography (EBL) for fabrication of nano-hole arrays.

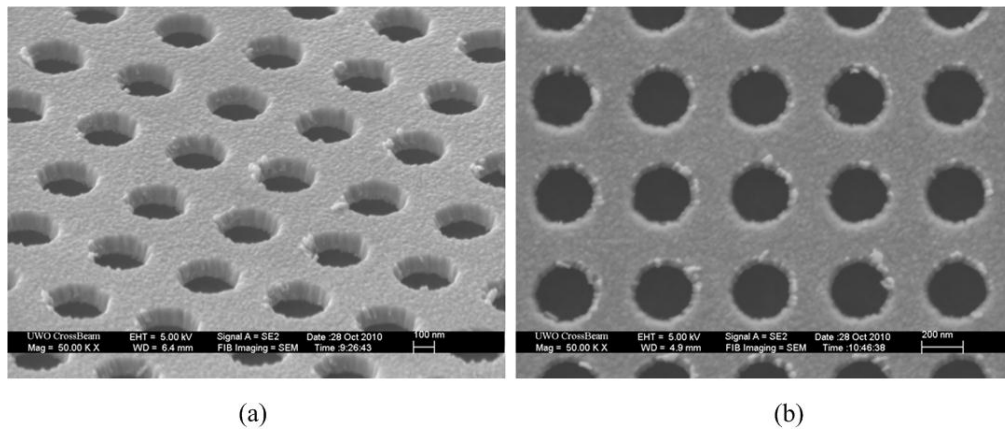


Figure 3-2. SEM images of a nano-hole array in a 100 nm gold film: (a) angle view, and (b) top view.

We fabricated nine different nano-hole arrays with various hole sizes and periodicities for each adhesion layer case (see Table 3-1). The ratio of the hole area (area of circle) to the background area (square area of periodicity) was 0.21 and the same for all arrays. A summary of the geometrical parameters (hole size and periodicity) of the fabricated nano-hole arrays is provided in Table 3-2. The hole periodicities were chosen to observe optical resonance transmission of each array in the visible and near-infrared regime. The dimension of each array was 50 μm by 50 μm .

Table 3-2. Summary of the geometrical parameters of the simulated and fabricated nano-hole arrays

Nano-hole arrays (geometrical parameters)	
D200-P381	D229-P436
D206-P392	D235-P447
D212-P403	D241-P458
D217-P414	D246-P469
D223-P425	
Diameter-size nm (D), Periodicity-size nm (P)	

3.4.2. Optical characterization setup

To optically characterize each nano-hole array, we employed an inverted microscope (Nikon, TE300) attached to a photometer (PTI, D104), monochromator (PTI, 101), and photo-multiplier tube detector (PTI, 710). Unpolarized white light from a 100 W halogen lamp was focused on to the sample from the air-gold side using the bright-field condenser lens (NA = 0.3) of the microscope. The transmitted light was collected by a 20X objective (NA = 0.45; Nikon, 93150). Utilizing the aperture adjustment on the photometer, light from a desired region was captured for spectroscopic analysis by the monochromator and detector. For each device, optical transmission spectra were collected from the region containing the nano-hole array (sample) and a hole-free region (background). The background and lamp properties were accounted for by subtracting the background spectrum from the sample spectrum and then dividing the result by the

measured white light spectrum (collected with the Pyrex substrate in front of the objective).

3.4.3. FDTD simulation of nano-hole arrays

We used the three-dimensional (3D) FDTD method to simulate the interaction between light and a nano-hole array in an optically thick metal film with the purpose of calculating the optical transmission properties [3-22] [3-23]. We used the FDTD package from Lumerical Inc. (Vancouver, Canada) with dielectric constants for metallic and dielectric materials provided by Palik [3-24]. The minimum grid size was 2 nm in the FDTD simulation analysis. The details of the numerical simulation model are described in more detail elsewhere [3-12].

3.4.4. Analysis of the optical transmission spectra

In order to analyze the effect of various adhesion layers on the EOT properties of nano-hole arrays, the optical resonance peaks related to SP excitation from the Pyrex-gold side were examined. For each optical transmission spectra, we computed the optical resonance position (resonance wavelength), spectral transmission modulation ratio (STMR), and optical resonance bandwidth. The STMR of the optical resonance peak was defined as

$$STMR = \frac{T_{max} - T_{min}}{T_{max} + T_{min}} \quad 3-3$$

, where T_{max} was the transmission of the (1,0) resonance peak and T_{min} was the transmission of the (1,0) minimum. The optical resonance bandwidth was computed as the full width of the EOT, where the optical transmission was $1/\sqrt{2}$ of the maximum.

3.5. Results

All fabricated nano-hole arrays were optically characterized experimentally and with simulation. The optical transmission spectra for nano-hole arrays employing the same composition and thickness adhesion layer obtained by simulation and experiment were in good agreement. The optical transmission spectra for nano-hole arrays simulated and fabricated with various conductive and adhesion layers (5 nm chromium (Cr5), 5 nm titanium (Ti5), 10 nm titanium (Ti10), etched 10 nm titanium (Ti10-etched), and no adhesion layer) between gold and Pyrex substrate are shown in Figure 3-3. The (1,0) optical resonance peaks related to SP excitation from Pyrex-gold side were clearly observed in both simulation and experiment for all nano-hole arrays (brown dashed line in the Figure 3-3), except the Ti10 case. The (1,0) transmission minimum before each (1,0) optical resonance peak was clearly observed for each nano-hole array (yellow dotted line in Figure 3-3), except for the Ti10 case. As shown in Figure 3-3 for both simulation and experimental results, the position, transmission and bandwidth of the (1,0) optical resonance peak was dependant on the type of adhesion layer.

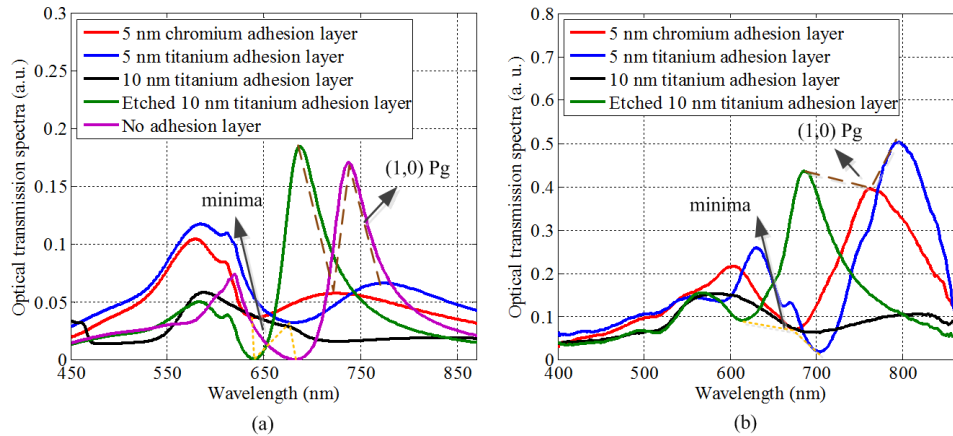


Figure 3-3. Optical transmission spectra of nano-hole arrays with circular holes, 223 nm in diameter, and 425 nm periodicity in a 100 nm thick gold film for various adhesion layers between gold and Pyrex substrate [5 nm chromium (red curve), 5 nm titanium (blue curve), 10 nm titanium (black curve), etched 10 nm titanium (green curve) and no adhesion layer (purple curve in simulation results)]: (a) simulation results and (b) experimental results. (Pg: Pyrex-gold side).

The position of the (1,0) optical resonance peak related to SP excitation from the Pyrex-gold side was extracted from the optical transmission spectrum of each nano-hole array for each adhesion layer case. The (1,0) resonance position versus hole periodicity of nano-hole arrays for various adhesion layers are shown in Figure 3-4 as well as the theoretical results calculated by the Ebbesen equation. In both simulation and experimental results, the (1,0) resonance position red-shifted as the periodicity of the nano-holes increased. In addition, for a given periodicity, the presence of the Ti and Cr adhesion layers resulted in a red-shift in the resonance peaks compared to the resonance peak of the Ti10-etched. However, the red-shift was greater for Ti5 compared to Cr5 for each periodicity. In the experimental measurements, the average red-shifts of the (1,0) resonance peaks for Cr5 and Ti5 with respect to the resonance position of Ti10-etched were 79 nm and 106 nm for a given periodicity, respectively. The (1,0) resonance position for Ti5 was red-shifted on average 27 nm compared to Cr5. However, the difference in the resonance peak position between Cr5 and Ti5 became smaller as the hole periodicity increased. Both experimental and simulation results for

the effect of various adhesion layers with respect to the (1,0) resonance position were similar. Also, the (1,0) resonance positions found by experiment were very close to simulation results except for the nano-hole arrays with lower periodicities fabricated with a Cr adhesion layer, where the simulation results showed a slight shift to shorter wavelengths compared to the experimental data.

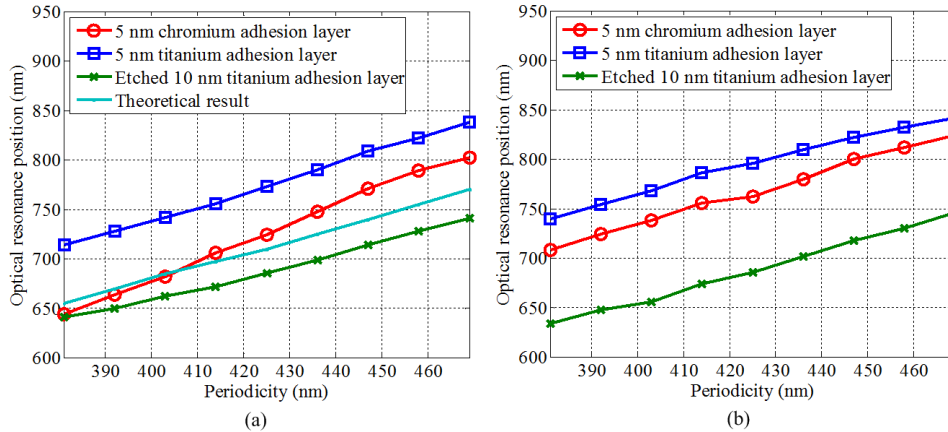


Figure 3-4. *The (1,0) optical resonance position versus hole periodicity for nano-hole arrays in a 100 nm gold film with various adhesion layers between the gold and Pyrex substrate [5 nm chromium (red curve), 5 nm titanium (blue curve), etched 10 nm titanium (green curve), and theoretical results (light blue curve in simulation results)]: (a) simulation results and (b) experimental results.*

Figure 3-5 shows the STMR versus nano-hole periodicity for nano-hole arrays with various adhesion layers obtained from simulation and experimental results. In simulation, for a given periodicity, the STMR for the Ti10-etched layer was higher compared to the STMR for Cr5 or Ti5. The STMR for Ti5 was higher than the STMR for Cr5 although the difference was not large. As the periodicity of the nano-holes increased, the STMR increased slightly for all nano-hole arrays regardless of the adhesion layer type. From experiment, the STMR for Ti5 had the highest value compared to Cr5 or Ti10-etched for a given periodicity. The STMR for Ti10-etched had a lower STMR compared to Cr5. The STMR remained approximately constant as the periodicity increased for nano-hole arrays with the various adhesion layers. Both

simulation and experiments revealed a higher STMR for Ti5 compared to the STMR for Cr5. In contrast to the experimental results, the STMR for Ti10-etched obtained from simulation was higher than the STMR for Cr5 or Ti5.

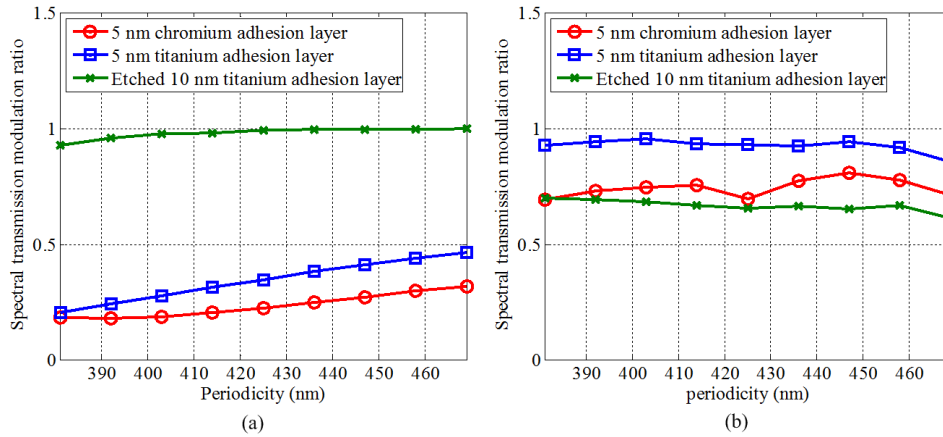


Figure 3-5. *The spectral transmission modulation ratio for (1,0) resonance peak and its respective minimum versus hole periodicity for nano-hole arrays in a 100 nm gold film with various adhesion layers between gold and Pyrex substrate [5 nm chromium (red curve), 5 nm titanium (blue curve), and etched 10 nm titanium (green curve)]: (a) simulation results and (b) experimental results.*

The (1,0) optical resonance bandwidth versus periodicity for nano-hole arrays with various adhesion layer materials is shown in Figure 3-6. In both simulation and experimental results, the (1,0) resonance bandwidth was lower for the Ti10-etched layer than Ti5 or Cr5 for a given periodicity. However, the (1,0) resonance bandwidth for Cr5 was higher compared to Ti5. In both the simulation and experimental results, the bandwidth remained nearly constant as periodicity increased for each case.

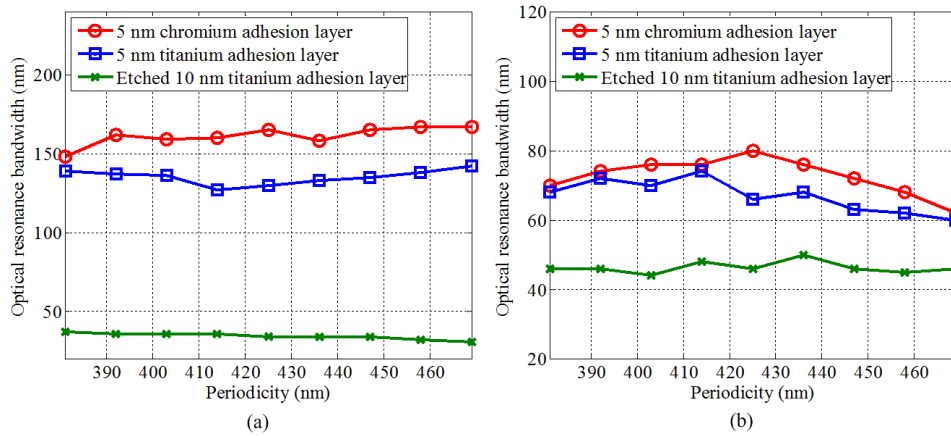


Figure 3-6. *The (1,0) optical resonance bandwidth versus hole periodicity for nano-hole arrays in a 100 nm gold film with various conductive and adhesion layers between the gold and Pyrex substrate [5 nm chromium (red curve), 5 nm titanium (blue curve), and etched 10 nm titanium (green curve)]: (a) simulation results and (b) experimental results.*

The spatial distributions of the electric field intensity (log scale) are shown in Figure 3-7 for nano-hole arrays with 223 nm hole diameter and 425 nm periodicity for various adhesion layer cases at their corresponding (1,0) resonance wavelength. The spatial distributions were computed for a xy surface near the hole (6 nm away from the hole in air-gold side) and the xz cross section through the hole. For all the adhesion layer cases, the highest electric field intensity was observed at the edges of the holes (hot-spots). The hole with the Ti10-etched layer had a much higher electric field intensity at the edges compared to holes with the Cr5 or Ti5 layers. The enhancement of the electric field intensity in the hot-spot of the Ti10-etched case was 34 and 98 times larger compared to the Ti5 and the Cr5 cases, respectively. The magnitude of electric field intensity was higher for the Ti5 case compared to the hole with the Cr adhesion layer.

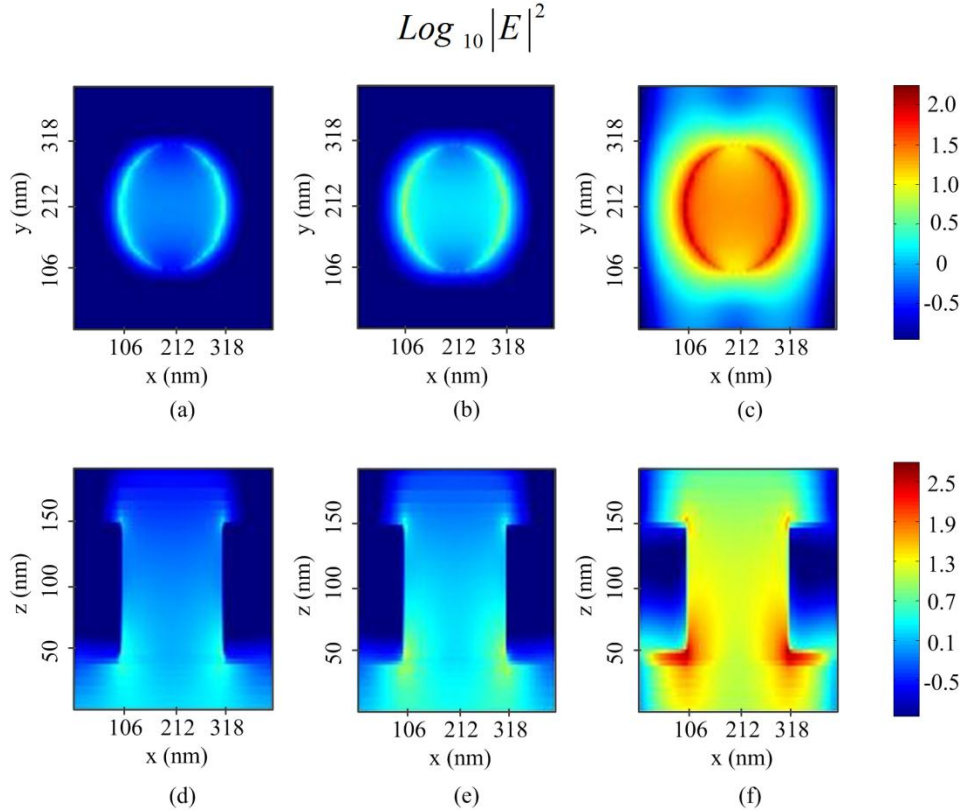


Figure 3-7. *The spatial distribution of electric field intensity for a xy surface 6 nm above the hole from air-gold side: (a) 5 nm Cr adhesion layer, (b) 5 nm Ti adhesion layer, and (c) etched 10 nm Ti adhesion layer. Spatial distribution of the electric field intensity in the central xz plane of the structure (d) 5 nm Cr adhesion layer, (e) 5 nm Ti adhesion layer, and (f) etched 10 nm Ti adhesion layer.*

3.6. Discussion

3.6.1. Overall findings

The (1,0) optical resonance transmission properties of nano-hole arrays from the Pyrex-gold side depended on composition of the adhesion layer. Both the 5 nm Ti and the 5 nm Cr adhesion layers caused a red-shift in the (1,0) resonance position of nano-hole arrays compared to the etched adhesion layer case. From the experimental results,

the (1,0) STMRs for Cr5 or Ti5 were higher than the etched adhesion layer case. Also, the Ti and Cr adhesion layers had a major effect on increasing the optical resonance bandwidth of the nano-hole arrays.

In the simulation results (see Figure 3-3 (a)), the position of the (1,0) resonance peak was lower for the Ti10-etched case compared to the one without an adhesion layer (no adhesion layer). This difference was caused by the etched region in the Ti10-etched. The etched region decreased the effective refractive index on the Pyrex-gold side and blue-shifted the (1,0) resonance peak compared to the nano-hole array without an adhesion layer. Also, a larger etched region is expected to result in a lower effective refractive index on the Pyrex-gold side of the holes and, in turn, result in a greater blue-shift in the resonance peak.

3.6.2. Fabrication of nano-hole arrays

In addition to EBL used in this study, Focused Ion Beam (FIB) milling and Nano-Imprint Lithography (NIL) are common methods for fabrication of nano-hole arrays [3-25]-[3-27]. Each method requires a thin adhesion layer to be deposited between the substrate and the gold film; however, the thickness of the adhesion layer can be considerably different for each fabrication methodology. For example, FIB milling requires an adhesion layer with a thickness of 2-3 nm, while due to the aggressive fabrication nature of EBL, a thicker adhesion layer is required. Based on our fabrication experiments, an adhesion layer with a thickness of 4 to 8 nm was sufficient to adhere the gold film to the Pyrex substrate and avoid peel off during the lift-off process.

We employed an EB-PVD system for deposition of the Ti and Cr adhesion layers to achieve uniform deposition of each metal. The deposition rates for both Ti and Cr materials were calibrated in order to achieve the desired thickness. However, due to material property differences between Cr and Ti, the deposition process was expected to result in thickness difference of a few angstroms between the two adhesion layer types for a 5 nm target thickness. This may have contributed to the slight differences in the optical resonance bandwidth and the STMR for nano-hole arrays fabricated with adhesion layers of each material. After the optical characterization of nano-hole arrays

with the thicker Ti adhesion layer, we etched the adhesion layer of the samples and very different optical properties were observed in both experiment and simulation (see Figure 3-3). According to the measured optical resonance properties of the (1,0) resonance peak from the Pyrex-gold side, it is probable that the Ti within and to the sides of each hole, and the Pyrex beneath and to the sides of each hole were partially etched away. SEM analysis of the etched nano-hole arrays confirmed that the gold film remained intact and did not peel off in the area of nano-hole array. This may be a result of resilient bonding between the gold nano-structure and the gold film beyond the nano-hole array, where the Ti etchant had no effect.

3.6.3. *Analyses of the experimental and simulation results*

The notable differences between the optical resonance properties of nano-hole arrays employing various adhesion layers were clearly observed in both simulation and experimental data. The composition and thickness of the adhesion layer had a significant effect on the optical resonance properties of the nano-hole arrays. Due to the high optical absorption properties of Ti and Cr, a greater thickness of these materials between Pyrex substrate and the gold caused a significant change in optical resonance properties related to the SP excitation from the Pyrex-gold side of the nano-hole array. For example, compared to the 5 nm Ti adhesion layer case, the (1,0) optical resonance peak for the 10 nm Ti adhesion layer was suppressed due to the high thickness of Ti and its strong absorption properties. Other major effects of the adhesion layer thickness were the widening of the optical resonance bandwidth and a change in the STMR. The optical resonance peak position was not significantly affected by the thickness of the adhesion layer.

Although there was good agreement between the (1,0) optical resonance position and bandwidth of nano-hole arrays studied in experiment and simulation, there were notable differences in the STMR observed by simulation and experiment. In experimental data, the STMR of nano-hole arrays with a Cr or Ti adhesion layer was higher than the STMR measured from simulation data. This discrepancy could have been due to limitations of the FDTD method when modeling the thin adhesion layer and the material dispersion properties used in the simulations. This is supported by the good

agreement between the simulation and experimental optical transmission spectra for the thicker Ti adhesion layer (Ti10).

In both simulation and experimental results, the different absorption properties of Ti and Cr likely resulted in the observed differences in the (1,0) optical resonance positions between nano-hole arrays with Ti and Cr adhesion layers. Based on the dielectric constants of these materials, Cr has a stronger optical absorption compared to Ti although the difference in absorption between Cr and Ti becomes less apparent at higher wavelengths. As a result, the optical resonance positions of Ti5 approached those of Cr5 at higher periodicities.

The STMR measured by experiment for the Ti10-etched cases were lower than the STMR for the Cr5 or the Ti5 cases. This was due to the optical absorption properties of Ti or Cr, which caused the (1,0) transmission minimum to be lower in the Cr and Ti cases resulting in a higher STMR. Also, the large difference between the STMR for Ti5 compared to the STMR for Cr5 may have been due to the higher absorption properties of Cr compared to Ti. Based on the experimental results, a thin adhesion layer of Ti resulted in an increased STMR at the expense of a larger optical resonance bandwidth.

3.6.4. *Implications of the adhesion layer composition to surface Plasmon sensing*

Optical resonance peaks of nano-hole arrays can be employed in applications such as spectral filters and Surface Plasmon Resonance (SPR) sensing. In SPR sensing applications such as bio-sensing, a narrow bandwidth and a steep slope in the optical resonance transmission spectrum are desired since they result in enhanced sensitivity of the nano-hole array for detection of bio-molecules. Based on the experimental results, the optical resonance peak for Ti10-etched and Ti5 had narrower bandwidth and sharper slopes compared to the nano-hole arrays with a Cr adhesion layer suggesting nano-hole arrays with a Ti adhesion layer or an etched adhesion layer are more suitable for SPR sensing applications. This is supported by recent SPR sensing work where a Ti adhesion layer was preferred over a Cr adhesion layer in Kretschmann SPR sensing configuration due to the lower absorption properties of Ti compared to Cr [3-14].

3.7. Conclusions

In this study, we presented a systematic numerical and experimental analysis on the optical resonance transmission properties of nano-hole arrays in an optically thick gold film with various adhesion layers (5 nm titanium, 5 nm chromium, 10 nm titanium, and etched) between the Pyrex substrate and the gold film. The fabricated nano-hole arrays were optically characterized and compared with corresponding simulation results. Good agreement was observed between the simulation and experimental results for the (1,0) optical resonance bandwidth and the optical resonance position for most nano-hole arrays. However, some differences between the STMR values obtained from simulations and experimental measurements were observed. The composition and thickness of the adhesion layer had a large effect on the optical resonance transmission properties of the tested nano-hole arrays. The Cr and Ti adhesion layers caused an increase in (1,0) optical resonance position and bandwidth compared to the etched case. The measured STMR value was greatest for nano-hole arrays fabricated with a 5 nm adhesion layer of Ti. The results confirmed that the composition of the adhesion layer is an important parameter for optimization of nano-hole arrays for sensing applications.

3.8. Acknowledgments

The authors thank Dr. Todd Simpson and Dr. Rick Glew for his technical support at the Nanofab Laboratory at University of Western Ontario (UWO). This project was funded by grants from the Natural Sciences and Engineering Research Council of Canada (NSERC) to Dr. Bozena Kaminska and Dr. Jeffrey J.L. Carson. Dr. Fartash Vasefi was supported by a London Regional Cancer Program Translational Breast Cancer Research Trainee Fellowship.

3.9. References

- 3-1. Ebbesen, T. W., Lezec, H. J., Ghaemi, H. F., Thio, T., & Wolff, P. A. (1998). Extraordinary optical transmission through sub-wavelength hole arrays. *Nature*, 391(6668), 667-669. Retrieved from <http://dx.doi.org/10.1038/35570>
- 3-2. Thio, T., Ghaemi, H. F., Lezec, H. J., Wolff, P. A., & Ebbesen, T. W. (1999). Surface-plasmon-enhanced transmission through hole arrays in cr films. *Journal of the Optical Society of America B*, 16(10), 1743-1748. Retrieved from <http://josab.osa.org/abstract.cfm?URI=josab-16-10-1743>
- 3-3. Gordon, R., Brolo, A. G., Sinton, D., & Kavanagh, K. L. (2010). *Resonant optical transmission through hole-arrays in metal films: Physics and applications* - WILEY-VCH Verlag. doi:- 10.1002/lpor.200810079
- 3-4. Brolo, A. G., Kwok, S. C., Moffitt, M. G., Gordon, R., Riordon, J., & Kavanagh, K. L. (2005). Enhanced fluorescence from arrays of nanoholes in a gold film. *Journal of the American Chemical Society*, 127(42), 14936-14941. doi:10.1021/ja0548687
- 3-5. Lakowicz, J. R., Chowdury, M. H., Ray, K., Zhang, J., Fu, Y., Badugu, R., Geddes, C. D. (2006). Plasmon-controlled fluorescence: A new detection technology. Paper presented at the , 6099(1) 609909-15. Retrieved from <http://dx.doi.org/10.1117/12.673106>
- 3-6. Lesuffleur, A., Im, H., Lindquist, N. C., Lim, K. S., & Oh, S. (2008). Laser-illuminated nanohole arrays for multiplex plasmonic microarray sensing. *Optics Express*, 16(1), 219-224. Retrieved from <http://www.opticsexpress.org/abstract.cfm?URI=oe-16-1-219>
- 3-7. Huang, F. M., Zheludev, N., Chen, Y., & de Abajo, F. Javier Garcia. (2007). Focusing of light by a nanohole array. *Applied Physics Letters*, 90(9), 091119-3. Retrieved from <http://link.aip.org/link/?APL/90/091119/1>
- 3-8. Rodrigo, S. G., García-Vidal, F. J., & Martín-Moreno, L. (2008). Influence of material properties on extraordinary optical transmission through hole arrays. *Physical Review B*, 77(7), 075401. Retrieved from <http://dx.doi.org.proxy.lib.sfu.ca/10.1103/PhysRevB.77.075401>
- 3-9. Przybilla, F., Degiron A., Laluet J-Y., Genet C. & Ebbesen, T.W. (2006). Optical transmission in perforated noble and transition metal films. *Journal of Optics A: Pure and Applied Optics*, 8(5) 458. Retrieved from <http://stacks.iop.org.proxy.lib.sfu.ca/1464-4258/8/i=5/a=015>
- 3-10. Krishnan, A., Thio, T., Kim, T. J., Lezec, H. J., Ebbesen, T. W., Wolff, P. A., Garcia-Vidal, F. J. (2001). Evanescently coupled resonance in surface plasmon enhanced transmission. *Optics Communications*, 200(1-6), 1-7. Retrieved from <http://www.sciencedirect.com/science/article/pii/S0030401801015589>

- 3-11. Gordon, R., Brolo, A. G., McKinnon, A., Rajora, A., Leathem, B., & Kavanagh, K. L. (2004). Strong polarization in the optical transmission through elliptical nanohole arrays. *Physical Review Letters*, *92*(3), 037401. Retrieved from <http://link.aps.org/doi/10.1103/PhysRevLett.92.037401>
- 3-12. Najiminaini, M., Vasefi, F., Kaminska, B., & Carson, J. J. L. (2010). Experimental and numerical analysis on the optical resonance transmission properties of nanohole arrays. *Optics Express*, *18*(21), 22255-22270. Retrieved from <http://www.opticsexpress.org/abstract.cfm?URI=oe-18-21-22255>
- 3-13. van, d. M., Segerink, F. B., van Hulst, N. F., & Kuipers, L. (2004). Influence of hole size on the extraordinary transmission through subwavelength hole arrays. *Applied Physics Letters*, *85*(19), 4316-4318. Retrieved from <http://link.aip.org/link/?APL/85/4316/1>
- 3-14. Chen, X., Pan, M., & Jiang, K. (2010). Sensitivity enhancement of SPR biosensor by improving surface quality of glass slides. *Microelectronic Engineering*, *87*(5), 790-792. Retrieved from <http://www.sciencedirect.com/science/article/pii/S0167931709007564>
- 3-15. Lahiri, B., Dylewicz, R., Rue, D. L., & Johnson, N. P. (2010). Impact of titanium adhesion layers on the response of arrays of metallic split-ring resonators (SRRs). *Optics Express*, *18*(11), 11202-11208. Retrieved from <http://www.opticsexpress.org/abstract.cfm?URI=oe-18-11-11202>
- 3-16. Aouani, H., Wenger, J., Gérard, D., Rigneault, H., Devaux, E., Ebbesen, T. W., Blair, S. (2009). Crucial role of the adhesion layer on the plasmonic fluorescence enhancement. *ACS Nano*, *3*(7), 2043-2048. doi:10.1021/nn900460t
- 3-17. Jiao, X., Goeckeritz, J., Blair, S., & Oldham, M. (2009). Localization of near-field resonances in bowtie antennae: Influence of adhesion layers. *Plasmonics*, *4*(1), 37-50. Retrieved from <http://dx.doi.org/10.1007/s11468-008-9075-x>
- 3-18. Djaker, N., Hostein, R., Devaux, E., Ebbesen, T. W., Rigneault, H., & Wenger, J. (2010). Surface enhanced raman scattering on a single nanometric aperture. *The Journal of Physical Chemistry C*, *114*(39), 16250-16256. doi:10.1021/jp104971p
- 3-19. Sexton, B. A., Feltis, B. N., & Davis, T. J. (2008). Characterisation of gold surface plasmon resonance sensor substrates. *Sensors and Actuators A: Physical*, *141*(2), 471-475. Retrieved from <http://www.sciencedirect.com/science/article/pii/S0924424707007273>
- 3-20. Pan, J., Pafchek, R. M., Judd, F. F., & Baxter, J. B. (2006). Effect of Chromium–Gold and Titanium–Titanium Nitride–Platinum–Gold metallization on Wire/Ribbon bondability. *IEEE Transactions on Advanced Packaging*, *29*, 707.
- 3-21. Galarreta, B. C., Norton, P. R., & Lagugneñe-Labarthe, F. (2011). SERS detection of Streptavidin/Biotin monolayer assemblies. *Langmuir*, *27*(4), 1494-1498. doi:10.1021/la1047497

- 3-22. Yee, K. S. (1966). Numerical solution of initial boundary value problems involving Maxwell's equations in isotropic media. *IEEE Trans.Ant.Prop.*, 14, 302.
- 3-23. Taflove, A., & Hagness, S. C. (Eds.). (2000). *Computational electrodynamics: The finite-difference time-domain method* (Second ed.). Boston: Artech House.
- 3-24. Palik, E. D. (1985). *Handbook of optical constants of solids*. New York: Academic Press.
- 3-25. Tseng, A. (2005). Recent developments in nanofabrication using focused ion beams. *Small*, 1(10), 924-939. doi:10.1002/sml.200500113
- 3-26. Kim, J., Sim, Y., Cho, Y., Seo, J., Kwon, S., Park, J., Lee, S. (2009). Large area pattern replication by nanoimprint lithography for LCDâ€TFT application. *Microelectronic Engineering*, 86(12), 2427-2431. Retrieved from <http://www.sciencedirect.com/science/article/pii/S0167931709003967>
- 3-27. Chen, J., Shi, J., Decanini, D., Cambriil, E., Chen, Y., & Haghiri-Gosnet, A. (2009). Gold nanohole arrays for biochemical sensing fabricated by soft UV nanoimprint lithography. *Microelectronic Engineering*, 86(4), 632-635. Retrieved from <http://www.sciencedirect.com/science/article/pii/S0167931709000161>

4. Nano-hole array structure with improved surface plasmon energy matching characteristics³

4.1. Abstract

We present a nano-hole array (NHA) structure in an opaque gold film that contains a cavity beneath each nano-hole. The cavity contributes to surface plasmon energy matching between the top and bottom surfaces of the gold and within the nano-hole structures. In bulk Surface Plasmon Resonance (SPR) sensing experiments, the SP-matched structure had 2.8-fold higher differential transmission, 2-fold higher sensitivity, and a 7-fold higher ratio of extraordinary optical transmission at resonance to the nearby minimum compared to a conventional NHA. The results suggest the structure with cavities has potential to improve performance of bulk SPR sensing applications.

³ The following chapter is published in Applied Physics Letter, Vol. 100, No. 4, 043105 (2012) under the co-authorship of Fartash Vasefi, Bozena Kaminska, and Jeffery J.L. Carson. Retrieved from <http://dx.doi.org/10.1063/1.3679173>

Reprinted with permission from [M. NAJIMINAINI, F. VASEFI, B. KAMINSKA, AND J. J.L. CARSON, "NANO-HOLE ARRAY STRUCTURE WITH IMPROVED SURFACE PLASMON ENERGY MATCHING CHARACTERISTICS," VOL. 100 NO. 4, 043105 (2012)]. Copyright [2012], American Institute of Physics.

4.2. Introduction

A sub-wavelength aperture or an array of sub-wavelength apertures in an opaque metal film is a common optical element in many photonic structures [4-1]. For example, the nano-hole array (NHA) has been recognized as a sub-diffraction optical element that provides benefits of extraordinary optical transmission (EOT) and high localized electric near-field intensities [4-2] [4-3]. These unique benefits are due to the coupling of incident light to Surface Plasmons (SP)s, the evanescent transfer through the nano-holes to the other side of the metal film, the decoupling of light from SPs, and radiation to free-space on the opposite side of the metal film [4-4]. Since SPs are the collective oscillation of free electrons at the interface between metal and dielectric, the SP characteristics (e.g. SP energy) depend highly on the properties of these materials. The SP excitation modes of NHAs are dependent on the scattering orders of the holes and dielectric properties of the materials on the top and bottom of a metal film as well as the composition of the metal [4-5]. Optimization of EOT and the electric near-field intensity of NHAs has been performed most commonly by changing hole shape, lattice arrangement, and material composition [4-6]-[4-15]. For instance, it has been shown that NHAs in a noble metal have a higher EOT compared to other metals [4-9]. Also, a nano-hole with a sharp apex double-hole structure proved to have a higher localized electric near-field intensity compared to a structure where the holes were completely separated [4-10] [4-11]. Also, NHAs fabricated on fluoropolymer substrate (FEP) improved the sensing performance for biological solutions by 20% due to the similar refractive indexes between the substrate and the solution [4-15].

Dielectric materials with the same dielectric constant on the top and bottom surfaces of the NHA result in the coincidence of the SP energy on both surfaces of the metal film. Surface plasmon energy matching results in coupling of the same SP excitation modes from both the top and bottom surfaces of the NHA and enhances the transmission intensity by several orders of magnitude [4-4]. However, current fabrication approaches have restricted the implementation of SP matching to top-side materials that

have dielectric properties that are similar to the substrate. Hence, the dielectric properties of the bottom layer are usually fixed [4-4] and matched over a very narrow range of refractive index [4-15]. Here, we report on a NHA structure that is capable of precise SP energy matching that can be utilized with materials that cover a wide range of refractive index. The basic improvement relates to a cavity beneath one or more nano-holes within the array that provides the means to SP energy match. Since the cavity is straight-forward to fabricate, it could be applied to existing nanostructure designs to enhance the sensitivity of biological and chemical sensing, Surface Enhanced Raman Spectroscopy (SERS), Near-field Scanning Optical microscopy (NSOM), non-linear optics, super-lensing, and nano-lithography.

4.3. Methods

A schematic of a NHA structure in an optically thick gold film on a Pyrex substrate (Pyrex 7740 from semi wafer Inc.) is displayed in Figure 4-1 (a), where beneath every nano-hole there is a cavity in the Pyrex substrate. The cavity allows SP energy matching between the top and bottom surfaces and within the nano-holes. The structure is amenable to deposition of any material, including the flow of liquids or gasses and it operates similar to the NHA structure with depletion zone [4-16]. The structure enables the coincidence of SP energy matching on both surfaces of the NHA, which depends on the dielectric properties of the chosen material and not the substrate, thereby enabling precise SP energy matching. To show the benefit of the cavity in NHA based applications, we performed numerical and experimental studies to evaluate the contribution of the SP energy matching due to the presence of the cavity on the performance of SPR sensing. We fabricated different NHAs with various hole sizes and periodicities in a 100 nm gold film using Electron Beam Lithography (EBL). The ratio of the hole area (area of circle) to the background area (square area of periodicity) was 0.11 and the same for all arrays. The periodicity of holes (360 nm, 370 nm, 380 nm, 390 nm) was selected in such a way that the (1,0) and (1,1) resonance peaks ($\lambda_{(1,0)}$ and $\lambda_{(1,1)}$) of NHAs appeared within the visible and near-infrared regime. A 3 nm titanium conductive layer followed by a 4 nm titanium adhesion layer were deposited during the

fabrication process. Additional details on the NHA EBL fabrication process can be found elsewhere [4-17]. In order to create a cavity underneath each nano-hole, we employed an isotropic wet-etching process using a titanium etchant (TFT, Transene company, Inc.) to remove the titanium layers as well as isotropically etch the Pyrex substrate underneath each hole in each NHA. TFT etches the Pyrex due to the presence of 30% HydroFluoric acid. The etching rates of TFT for titanium and Pyrex were 2.5 nm/s and 4.3 nm/s at 20°C, respectively. We exposed each NHA to the etchant for 30 s, resulting in a cavity beneath each nano-hole. A SEM image of the tilted sample (54°) with cross sectional visualization obtained after FIB cutting through NHA structure is shown in Figure 4-1 (b). The image reveals a 100 nm deep cavity as well as an undercutting beneath the gold. The undercut region between two adjacent holes (i.e. one period) was on average 253 nm. Also, the non-etched area between two adjacent cavities functioned as a support column that prevented peel off and breakage of the gold layer. We used optical transmission spectroscopy to perform optical characterization for each NHA sample. More details about the setup can be found in [4-17]. However, each NHA sample was illuminated by unpolarized collimated white light with less than 3° collimation deviation and the transmitted light through each sample was collected by 20 X objective (numerical aperture = 0.45).

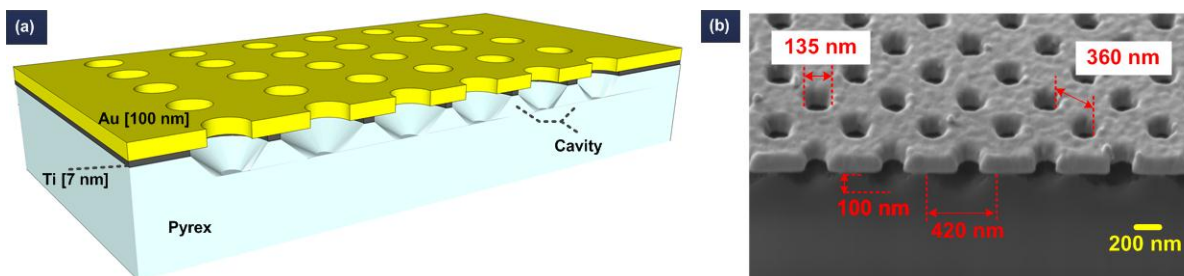


Figure 4-1. (a) A three dimensional schematic view of a NHA with cavities beneath each nano-hole.(b) SEM image of a NHA revealing the cavities (FIB cutting performed in order to observe a cavity beneath each nano-hole).

It is well known that the SP field drops exponentially in a direction normal to the surface of a metal or dielectric. The decay length for metal is related to the skin depth

and for a dielectric the decay length is approximately half the wavelength of light [4-18]. Based on calculations, the skin depth for gold is about 28 nm and the decay length of the SP in air and Pyrex is about 280 nm and 150 nm at a wavelength of 600 nm, respectively [4-19]. These decay length estimates led us to conclude that the cavity with the aforementioned dimensions greatly reduced the effect of the substrate and the metal film on the drop in the SP field. However, the influence of the Pyrex-metal interface on the SP field was observed as the cavity became smaller in dimension. Smaller cavities had an effective refractive index related to both air and Pyrex, which led to a blue shift in the resonance peak when compared to a conventional NHA.

4.4. Results and discussion

We performed numerical simulations to compute the electric near-field intensity around the structures for a conventional NHA (without cavities) and a NHA with cavities. A dielectric with a 1.43 refractive index was used to cover the surface and fill the cavity and each nano-hole as shown in Figure 4-2 (a). The dielectric was selected to match the refractive index of the substrate ($n = 1.474$) to ensure near optimal performance of the conventional NHA. The spatial distributions of the electric field intensity are shown in Figure 4-2 (b) and were computed for the xz cross section through a nano-hole with 135 nm diameter and 360 nm periodicity within a conventional NHA (at $\lambda_{(1,0)}=670$ nm resonance peak) and a NHA with cavities (at $\lambda_{(1,0)}=680$ nm resonance peak). For both NHAs, the highest electric field intensity was observed at the edges of the holes (hot-spots). The magnitude of the electric field intensity at the openings at the top and bottom of the nano-hole was 8 times higher for the case with the cavity compared to the case without. Also, the average electric field intensity was higher through the nano-hole for NHAs with the cavity. The enhancement of the electric field intensity occurred not only due to the near perfect index matching between top and bottom of the perforated metal film, but also because of the removal of the absorptive titanium conductive and adhesion layers as discussed in our previous work [4-17].

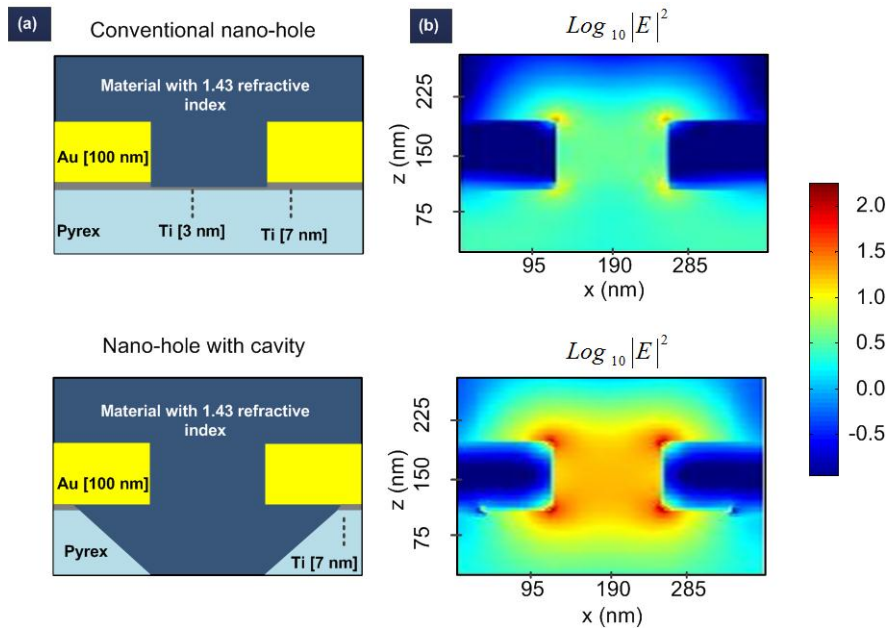


Figure 4-2. (a) Schematic of a conventional nano-hole (top) and a nano-hole with cavity (bottom). (b) Spatial distribution of the electric field intensity (log scale) within the nano-hole (xz side view) for a conventional nano-hole (top) and a nano-hole with a cavity (bottom).

We also performed a series of experimental analyses to evaluate the improvement in EOT for the NHA with cavities as well as its bulk SPR sensing performance. We measured the optical transmission spectra of NHAs using optical transmission spectroscopy with liquids of well-known refractive index (Cargille Inc., Cedar Grove, USA) deposited on to the top surface of each NHA. We used a refractive index liquid close to the substrate refractive index ($n = 1.474$) in order to demonstrate the improved sensitivity over a conventional NHA as described in [4-15]. The experiments were done on the same NHA before and after creation of the cavities. The optical transmission spectra for the conventional NHA and the NHA with cavities are presented for liquids of various refractive indexes in Figure 4-3 (a) and (b), respectively. The two optical resonance peaks related to (1,0) and (1,1) SP excitation modes ($\lambda_{(1,0)}$ and $\lambda_{(1,1)}$) were clearly observed for both NHAs. For the NHA structure with the cavities, the refractive index liquids deposited on the top surface penetrated into the cavities providing coincidence of the resonance position for the same scattering mode for the

bottom and top of the gold film [4-4]. As a result, resonance peaks related to the Pyrex-gold side were not observed, while the conventional NHA had a small $\lambda_{(1,0)}$ related to the Pyrex-gold side, which resulted in overlapping optical transmission spectra between 660 nm and 720 nm for the various refractive indices (see orange shaded region in Figure 4-3 (a)). Both $\lambda_{(1,0)}$ and $\lambda_{(1,1)}$ were red-shifted for liquids with higher refractive indices. However, the change in the optical transmission spectra of the NHA with cavities showed a red shift that was consistent over a greater range of wavelengths compared to the conventional NHA as liquids of greater refractive index were applied. For all transmission spectra, a resonance peak at 500 nm was observed and was related to the bulk plasmon resonance for gold.

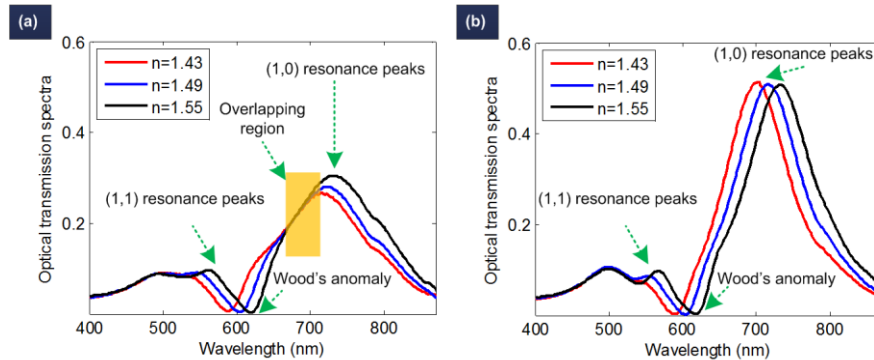


Figure 4-3. *Optical transmission spectra for (a) a conventional NHA and (b) a NHA with cavities when liquids of 1.43, 1.49, and 1.55 refractive index were applied to the top surface. Each NHA had 135 nm circular hole size and 360 nm periodicity.*

We analyzed the optical transmission spectra and present the summary results in Figure 4-4. The ratio (η) between the $\lambda_{(1,0)}$ resonance transmission and its corresponding transmission minimum (Wood's Anomaly) was computed for various refractive indices for both NHAs with and without cavities and shown in Figure 4-4 (a). For different refractive indices, η was 1.5 to 7 times higher for the NHA with cavities compared to the conventional NHA. As the refractive index increased, the ratio decreased for the NHA with cavities. This was due to the red-shift of the resonance peak when liquids of higher refractive index were applied resulting in a shift of the resonance peak further away from

the cut-off frequency of the nano-hole. However, the trend was different for the conventional NHA. The ratio η increased for liquids of 1.43 to 1.55 refractive index and then decreased as the refractive index of the liquid was increased further. For the conventional NHA, the maximum transmission was expected to be intermediate to the transmission results for liquids with refractive index of 1.46 and 1.49 due to the surface plasmon matching between the top liquid and the Pyrex substrate [4-4]. However, this hypothesized result was not observed due to the presence of the titanium conductive and adhesion layers, which increased the optical absorption and the effective refractive index at the underside of the gold film ($n \sim 1.55$) [4-17]. Others have demonstrated that a higher value of η results in an improvement in the sensitivity of SPR sensing applications for detection of biomolecules [4-20] [4-21]. Figure 4-4 (b) illustrates the sensitivity of the $\lambda_{(1,0)}$ resonance peak for NHAs with and without the cavities, where the periodicity of each NHA was different. Sensitivity was computed as the shift in the $\lambda_{(1,0)}$ resonance wavelength. Almost 2-fold higher sensitivity was obtained for the NHAs with cavities compared to the conventional NHAs. The sensitivity related to the $\lambda_{(1,0)}$ resonance peak for NHAs with cavities increased with respect to the periodicity of the nano-holes. The result was somewhat expected as it had been described for conventional NHAs by other groups [4-22]. However, in these experiments the conventional NHAs showed little change in sensitivity, except for a slight increase in the case of the NHA with 390 nm periodicity. The lower sensitivity was likely a result of the existence of the (1,0) resonance peak related to the Pyrex-gold side, which interfered with the (1,0) resonance peak from the other side of the film (see orange shaded region in Figure 4-3 (a)). Poorer sensitivity of the conventional NHA was also related to the broader bandwidth of the $\lambda_{(1,0)}$ resonance peak compared to the narrower peak (typically 60% of the conventional NHA at the FWHM) observed for the NHA with cavities. These results confirmed the well-known principle that sharpness of the resonance peak improves SPR sensing sensitivity [4-6] and emphasized that the cavities robustly contribute to enhanced sensitivity through multiple mechanisms. Real time SPR sensing with NHAs can be accomplished via differential transmission intensity measurements using a narrow band detector or illumination source. The differential transmission intensity for the conventional NHA at 632 nm wavelength [maximum difference] and NHA with cavity at 686 nm wavelength are shown for liquids of various refractive indices in Figure 4-4 (c). A near linear

relationship was observed for the differential transmission intensity with respect to refractive index for both types of NHA. However, the NHA with cavities showed an almost 3-fold steeper slope compared to the conventional NHA. When taken together the results (Figure 4-4) demonstrate the superior bulk SPR sensing performance of a NHA with cavities over a conventional NHA. Furthermore, even for technically simple implementations such as transmission-based bulk SPR sensing, multi-fold improvement in sensing performance have been achieved.

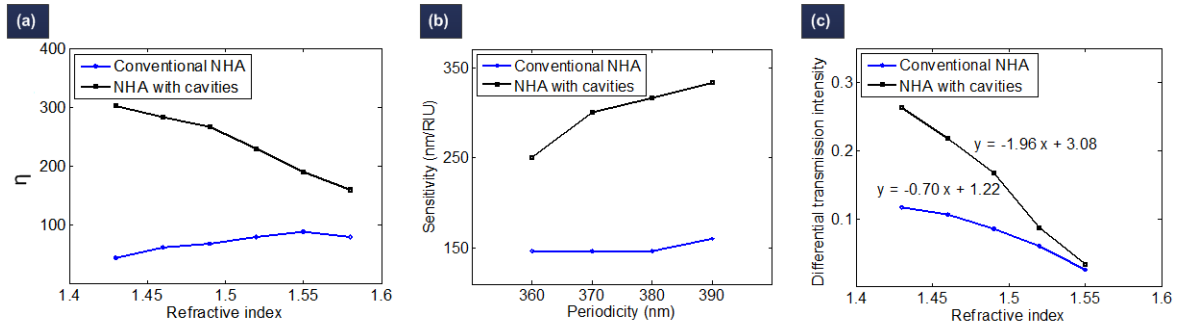


Figure 4-4. (a) The ratio (η) of the (1,0) resonance peak to (1,0) Wood's Anomaly versus refractive index. (b) Sensitivity [nm/refractive index unit (RIU)] of the (1,0) resonance peak for NHAs of different periodicities. (c) Differential transmission intensity obtained for different refractive index liquids compared to a liquid with a refractive index of 1.58. Measurements were made at 632 nm for the conventional NHA and at 686 nm for the NHA with cavities.

4.5. Conclusions

In conclusion, a metallic NHA structure with cavities beneath each nano-hole has been fabricated and tested by numerical simulation and optical experimentals. The NHA structure had the capacity for true SP energy matching at the top and bottom surfaces of the metal film. The SP energy coincidence provided a higher enhancement of the intensity of the electric near-field as observed in numerical simulations as well as enhanced EOT compared to NHAs without cavities. The structure showed a 2-fold improvement at bulk SPR sensing when metrics related to the $\lambda_{(1,0)}$ resonance peak were

compared and a nearly 3-fold improvement when differential transmission measurements were compared. This approach to guaranteeing SP energy matching in NHA structures should result in more flexible selection of materials for SP energy matching purposes and provide a method for improving the sensitivity to liquid and gaseous analytes in SPR sensing applications.

4.6. References

- 4-1. Genet, C., & Ebbesen, T. W. (2007). Light in tiny holes. *Nature*, *445*(7123), 39-46. doi:10.1038/nature05350
- 4-2. Ebbesen, T. W., Lezec, H. J., Ghaemi, H. F., Thio, T., & Wolff, P. A. (1998). Extraordinary optical transmission through sub-wavelength hole arrays. *Nature*, *391*(6668), 667-669. Retrieved from <http://dx.doi.org/10.1038/35570>
- 4-3. Yin, L., Vlasko-Vlasov, V., Pearson, J., Hiller, J. M., Hua, J., Welp, U., Kimball, C. W. (2005). Subwavelength focusing and guiding of surface plasmons. *Nano Letters*, *5*(7), 1399-1402. doi:10.1021/nl050723m
- 4-4. Krishnan, A., Thio, T., Kim, T. J., Lezec, H. J., Ebbesen, T. W., Wolff, P. A., Garcia-Vidal, F. J. (2001). Evanescently coupled resonance in surface plasmon enhanced transmission. *Optics Communications*, *200*(1-6), 1-7. Retrieved from <http://www.sciencedirect.com/science/article/pii/S0030401801015589>
- 4-5. Thio, T., Ghaemi, H. F., Lezec, H. J., Wolff, P. A., & Ebbesen, T. W. (1999). Surface-plasmon-enhanced transmission through hole arrays in cr films. *Journal of the Optical Society of America B*, *16*(10), 1743-1748. Retrieved from <http://josab.osa.org/abstract.cfm?URI=josab-16-10-1743>
- 4-6. Sinton, D., Gordon, R., & Brolo, A. G. (2008). *Nanohole arrays in metal films as optofluidic elements: Progress and potential* - Springer Berlin / Heidelberg. doi:- 10.1007/s10404-007-0221-0
- 4-7. Gordon, R., Brolo, A. G., Sinton, D., & Kavanagh, K. L. (2010). *Resonant optical transmission through hole-arrays in metal films: Physics and applications* - WILEY-VCH Verlag. doi:- 10.1002/lpor.200810079
- 4-8. Garcia-Vidal, F. J., Martin-Moreno, L., Ebbesen, T. W., & Kuipers, L. (2010). Light passing through subwavelength apertures. *Reviews of Modern Physics*, *82*(1), 729-787. Retrieved from <http://link.aps.org/doi/10.1103/RevModPhys.82.729>

- 4-9. Przybilla, F., Degiron, A., Laluet, J., Genet, C., & Ebbesen, T. W. (2006). Optical transmission in perforated noble and transition metal films. *Journal of Optics A: Pure and Applied Optics*, 8(5) 458. Retrieved from <http://stacks.iop.org/1464-4258/8/i=5/a=015>
- 4-10. Lesuffleur, A., Im, H., Lindquist, N. C., & Oh, S. (2007). Periodic nanohole arrays with shape-enhanced plasmon resonance as real-time biosensors. *Applied Physics Letters*, 90(24), 243110-3. Retrieved from <http://link.aip.org/link/?APL/90/243110/1>
- 4-11. Lesuffleur, A., Kumar, L. K. S., Brolo, A. G., Kavanagh, K. L., & Gordon, R. (2007). Apex-enhanced raman spectroscopy using double-hole arrays in a gold film. *The Journal of Physical Chemistry C*, 111(6), 2347-2350. doi:10.1021/jp067677e
- 4-12. Gordon, R., & Marthandam, P. (2007). Plasmonic bragg reflectors for enhanced extraordinary optical transmission through nano-hole arrays in a gold film. *Optics Express*, 15(20), 12995-13002.
- 4-13. Ctistis, G., Patoka, P., Wang, X., Kempa, K., & Giersig, M. (2007). Optical transmission through hexagonal arrays of subwavelength holes in thin metal films. *Nano Letters*, 7(9), 2926-2930. doi:10.1021/nl0712973
<http://www.opticsexpress.org/abstract.cfm?URI=oe-15-20-12995>
- 4-14. Lindquist, N. C., Lesuffleur, A., Im, H., & Oh, S. (2009). Sub-micron resolution surface plasmon resonance imaging enabled by nanohole arrays with surrounding bragg mirrors for enhanced sensitivity and isolation. *Lab Chip*, 9(3), 382-387. Retrieved from <http://dx.doi.org/10.1039/B816735D>
- 4-15. Yang, J., Ji, J., Hogle, J. M., & Larson, D. N. (2008). Metallic nanohole arrays on fluoropolymer substrates as small label-free real-time bioprobes. *Nano Letters*, 8(9), 2718-2724. doi:10.1021/nl801043t
- 4-16. Yanik, A. A., Huang, M., Artar, A., Chang, T., & Altug, H. (2010). Integrated nanoplasmonic-nanofluidic biosensors with targeted delivery of analytes. *Applied Physics Letters*, 96(2), 021101-3. Retrieved from <http://link.aip.org/link/?APL/96/021101/1>
- 4-17. Najiminaini, M., Vasefi, F., Kaminska, B., & Carson, J. J. L. (2011). Optical resonance transmission properties of nano-hole arrays in a gold film: Effect of adhesion layer. *Optics Express*, 19(27), 26186-26197. Retrieved from <http://dx.doi.org/10.1364/OE.19.026186>
- 4-18. Barnes, W. L., Dereux, A., & Ebbesen, T. W. (2003). Surface plasmon subwavelength optics. *Nature*, 424(6950), 824-830. Retrieved from <http://dx.doi.org/10.1038/nature01937>
- 4-19. Raether, H. (1988). *Surface plasmons*. Berlin: Springer-Verlag.

- 4-20. Im, H., Lesuffleur, A., Lindquist, N. C., & Oh, S. (2009). Plasmonic nanoholes in a multichannel microarray format for parallel kinetic assays and differential sensing. *Analytical Chemistry*, 81(8), 2854-2859. doi:10.1021/ac802276x
- 4-21. Yanik, A. A., Cetin, A. E., Huang, M., Artar, A., Mousavi, S. H., Khanikaev, A., Altug, H. (2011). Seeing protein monolayers with naked eye through plasmonic fano resonances. *Proceedings of the National Academy of Sciences*, Retrieved from <http://www.pnas.org/content/early/2011/06/28/1101910108.abstract>
- 4-22. Pang, L., Hwang, G. M., Slutsky, B., & Fainman, Y. (2007). Spectral sensitivity of two-dimensional nanohole array surface plasmon polariton resonance sensor. *Applied Physics Letters*, 91(12), 123112-3. Retrieved from <http://link.aip.org/link/?APL/91/123112/1>

5. Effect of Surface Plasmon energy matching on the sensing capability of metallic nano-hole arrays⁴

5.1. Abstract

We report on a nano-hole array (NHA) structure with a single cavity beneath the perforated gold film. Structures were fabricated with a variety of cavity depths. The optical resonance of each structure as well as the Surface Plasmon energy matching between the top and bottom of the gold film were investigated. We also experimentally evaluated the sensitivity of the structures as Surface Plasmon Resonance (SPR) sensors. We observed a 1.6-fold enhancement in bulk SPR sensitivity and a 3-fold improvement in figure of merit for a structure with a 350-nm cavity depth compared to a structure with a 5-nm cavity depth.

⁴ The following chapter is published in Applied Physics Letter, Vol. 100, No. 6, 063110 (2012) under the co-authorship of Fartash Vasefi, Bozena Kaminska, and Jeffery J.L. Carson. Retrieved from <http://dx.doi.org/10.1063/1.3683536>

Reprinted with permission from [M. NAJIMINAINI, F. VASEFI, B. KAMINSKA, AND J. J.L. CARSON, "Effect of Surface Plasmon energy matching on the sensing capability of metallic nano-hole arrays," VOL. 100 NO. 6, 063110 (2012)]. Copyright [2012], American Institute of Physics.

5.2. Introduction

Arrays of nano-holes in metal films have become a key component of many plasmonic structures and have many useful applications in optics [5-1]. An array of a periodic nano-holes or a nano-hole surrounded with periodic structures (e.g. grooves and dimples) allows incident light to couple to the Surface Plasmons (SP)s on one side of the film, with evanescent transfer of light through the nano-holes, and subsequent decoupling on the other side of the film [5-2]. This phenomenon results in multiple optical resonance peaks, which display higher transmission than the incident light when normalized to the aperture size [i.e. so-called Extraordinary Optical Transmission (EOT)] and contradicts standard aperture theory [5-1]. Nano-hole arrays (NHAs) also display highly intensified electric fields in the vicinity of the nano-holes within the structure at the resonance wavelengths [5-3]. The optical resonance transmission properties (e.g. resonance position and transmission) of NHAs greatly depend on the dielectric properties of the metal film, the dielectrics above and below the film, and the geometry and lattice arrangement of the nano-holes [5-4] [5-5].

NHAs have been employed in sensing applications such as Surface Plasmon Resonance (SPR) sensing and Surface Enhanced Raman Spectroscopy (SERS) [5-6]-[5-8]. In SPR sensing, changes in the refractive index of the material at the top or bottom of the film results in a measurable change in the optical resonance position [5-6] [5-9]-[5-12]. The bulk SPR sensitivity of NHAs is dependent on the bandwidth of the optical resonance and characterized by the resonance shift per refractive index unit (nm/RIU). For a NHA with a low hole count (e.g. < 100 holes), it is well known that the optical transmission at resonance is lower and the bandwidth is wider compared to a NHA with a large hole count (e.g. > 400 holes). Lower transmission and wider bandwidth result in lower bulk SPR sensitivity for smaller NHA structures [5-13]. Bulk SPR sensitivity values reported in the literature are 285 nm/RIU for NHAs with a low hole count to 313 - 400

nm/RIU for NHAs with a high hole count [5-6] [5-14]. Increases in the optical transmission of low hole count NHAs is possible by incorporation of a Bragg-reflector around the NHA; however, the resonance bandwidth remains relatively unchanged [5-15] [5-16]. Based on the desire to build compact SPR sensors, alternative methods for increasing the bulk SPR sensitivity of low hole count NHAs are needed. We investigated the concept of SP energy matching and how it could be utilized to increase the bulk SPR sensitivity of a low hole count NHA.

The optical resonances of NHAs are related to SP energy matching properties on the top and bottom of NHAs. The SP energy difference between top and bottom of the NHA results in the occurrence of the resonance peaks at different wavelengths for the same scattering mode [5-2]. It was reported that the SP matching energy between two sides of a NHA enhance the EOT of the NHA by up to 10-fold, which was a result of refractive index matching between both side of the NHA [5-3]. However, NHA fabrication is most commonly performed on a solid substrate, which limits the SP energy matching to a very small range of refractive indices on the free-side of the NHA resulting in lower transmission efficiency and degradation of sensing performance. Therefore, we designed a NHA structure, which provides SP energy matching between the top and bottom surfaces of the metal film. SP energy matching was facilitated by a cavity between the gold film and the substrate. The structure resulted in a freestanding NHA in a suspended gold film that enabled liquids to flow through the nano-holes thereby resulting in index matching and hence SP energy matching between the top and bottom of the gold film. A series of structures were fabricated, where each had a different cavity depth and was tested as a bulk SPR sensor.

5.3. Methods

Electron beam lithography (EBL) followed by a lift-off process was used to fabricate NHAs in a gold film. To facilitate accurate depth of the cavity beneath the gold film, a sacrificial Ti layer was deposited on the Pyrex substrate prior to spin-coating of photo-resist for EBL process [5-4]. After NHA fabrication, a titanium etchant (TFTN, Transene company, Inc.) was used to remove the sacrificial layer in the vicinity of the

nano-holes, which resulted in a large cavity between the gold film and the substrate. We fabricated a series of NHAs with 120 nm circular hole size and 360 nm, 400 nm, and 440 nm periodicities in a 70-nm thick gold film on Pyrex substrate. The NHAs were fabricated on Titanium sacrificial layers with different thicknesses (5 nm, 50 nm, 100 nm, 200 nm, and 350 nm), which resulted in well-controlled cavity depths after the wet-etching process. The fabricated NHAs had a low hole count with only 64 holes in a 8×8 square lattice. Figure 5-1 (a) displays a schematic of a NHA before and after the Ti wet-etching process. Figure 5-1 (b) displays an SEM image of a fabricated NHA device with a 200-nm cavity depth. Focussed Ion Beam (FIB) milling was used to cut through the metal layers and into the substrate to reveal the features below the metal film. Based on Figure 5-1 (b) it is evident that the gold film was free standing and the etchant undercut the gold film from 900 nm to 1900 nm beyond the array of nano-holes. We then used optical transmission spectroscopy (described in [5-4]) to characterize NHAs with different geometries and cavity depths.

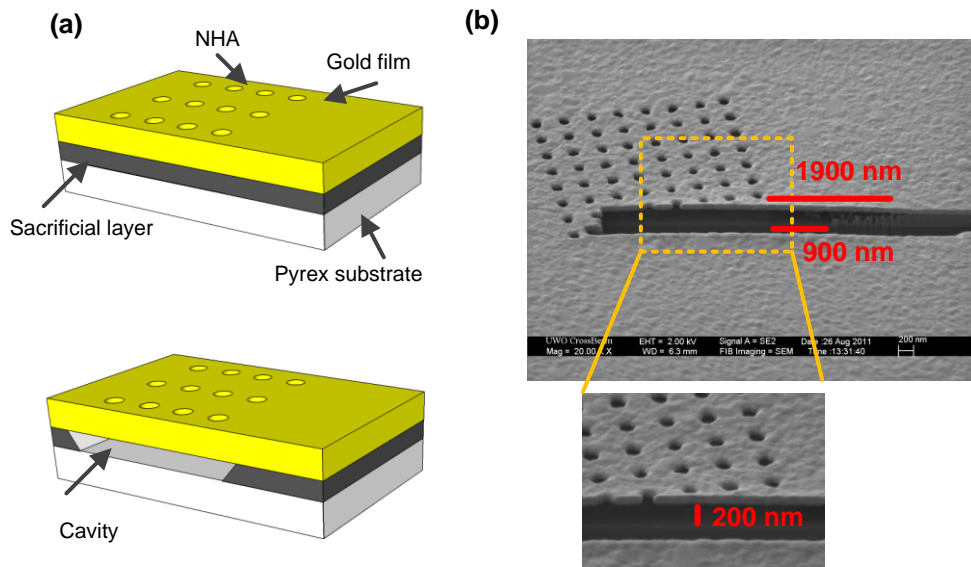


Figure 5-1. (a) A schematic of a NHA in a gold film fabricated on top of sacrificial and substrate layers (top). Also shown is a schematic of a NHA in a gold film where the sacrificial layer has been selectively removed to produce a cavity between the gold film and the substrate (bottom). (b) SEM image (shown at an angle of 54°) of a NHA in a gold film that was FIB milled to reveal the titanium sacrificial layer, the Pyrex substrate, and the presence of a cavity that had a depth of 200 nm (see lower panel).

5.4. Results and discussion

We investigated the effect of various cavity depths on the optical transmission spectra of NHAs. The optical transmission spectra of NHAs with 120-nm diameter holes and 400-nm periodicity for 5-nm and 350-nm cavity depths are shown in Figure 5-2 (a). The NHA with a 5-nm cavity depth had two optical resonance peaks ($\lambda_{(1,0)}^{\text{sub}}$ and $\lambda_{(1,1)}^{\text{sub}}$), which were related to the (1,0) and (1,1) SP modes of the substrate-gold side. However, the NHA with a 350-nm cavity depth had only one resonance peak ($\lambda_{(1,0)}$) due to coincidence of the SP modes on both sides of the gold film. No resonance peaks related to the free-gold side ($\lambda_{(\text{modes})}^{\text{free}}$) for either NHA were observed. Based on computation of the SP propagation length into the dielectric (e.g. air or Pyrex) perpendicular to the metal film (see Refs [5-17] [5-18]), the NHA with the 350-nm cavity

depth had perfect SP energy matching between the top and bottom of the metal film. Coincidence of the SP modes for the NHA with the 350-nm cavity depth resulted in enhanced transmission at resonance and a significant blue-shift of the resonance position with respect to the NHA with the 5-nm cavity depth. The blue-shift in $\lambda_{(1,0)}$ was simply due to the lower refractive index of air ($n = 1$) relative to the Pyrex substrate ($n = 1.474$). Also, the $\lambda_{(1,1)}$ for the NHA with 350-nm cavity depth was not observed due to its occurrence above the bulk plasmon frequency of gold (at $\lambda = 500$ nm), where no coupling can occur. In Figure 5-2 (b), the (1,0) resonance positions are shown for NHAs as a function of hole periodicity and cavity depth. As the cavity depth increased, $\lambda_{(1,0)}$ of NHAs with various periodicities were blue-shifted. A large blue-shift in $\lambda_{(1,0)}$ occurred for NHAs with a cavity depth of 5 nm and 100 nm, while a small blue-shift of $\lambda_{(1,0)}$ was observed for NHAs with cavity depth of 100 nm to 350 nm. The results demonstrated that the effect of the Pyrex substrate on the $\lambda_{(1,0)}$ of NHAs with cavity depths ≥ 100 nm was significantly reduced.

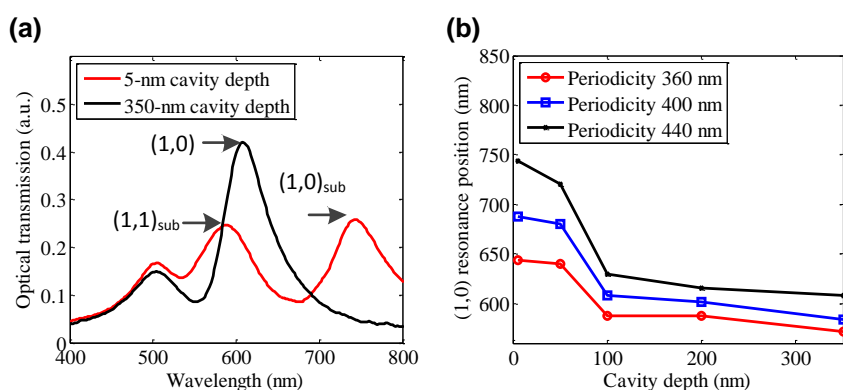


Figure 5-2 (a) Optical transmission spectra of NHAs with 120-nm circular hole size and 400-nm periodicity for 5-nm and 350-nm cavity depths. (b) (1,0) optical resonance position of NHAs versus different cavity depths for NHAs with 120-nm circular hole size and periodicities of 360 nm, 400 nm, and 440 nm.

We performed bulk SPR sensing experiments with NHAs containing 5-nm and 350-nm cavity depths. Bulk refractive index liquids ($n = 1.30 - 1.39$, Cargille Inc., Cedar

Grove, USA) were applied and a transmission spectrum of each NHA was measured. The optical transmission spectra of NHAs with 120-nm diameter holes at a periodicity of 400 nm are shown in Figure 5-3 (a) and Figure 5-3 (b) for NHAs with 5-nm and 350-nm cavity depths, respectively. In each case, liquids of refractive index of 1.3 and 1.33 were applied to the free surface. For the NHA with a 5-nm cavity depth, the optical resonances related to the gold-free side ($\lambda_{(1,0)}^{\text{free}}$ and $\lambda_{(1,1)}^{\text{free}}$) and the substrate-gold side ($\lambda_{(1,0)}^{\text{sub}}$ and $\lambda_{(1,1)}^{\text{sub}}$) were observed. However, for the NHA with the 350-nm cavity depth, only two resonances ($\lambda_{(1,0)}$ and $\lambda_{(1,1)}$) were observed due to SP energy matching between the top and the bottom surface of metal film. The higher refractive index fluid resulted in a red-shift in the resonances regardless of the cavity depth; however, the NHA with the 350-nm cavity depth had lower bandwidth and marginally higher peak height at $\lambda_{(1,0)}$ compared to the NHA with the 5-nm cavity depth.

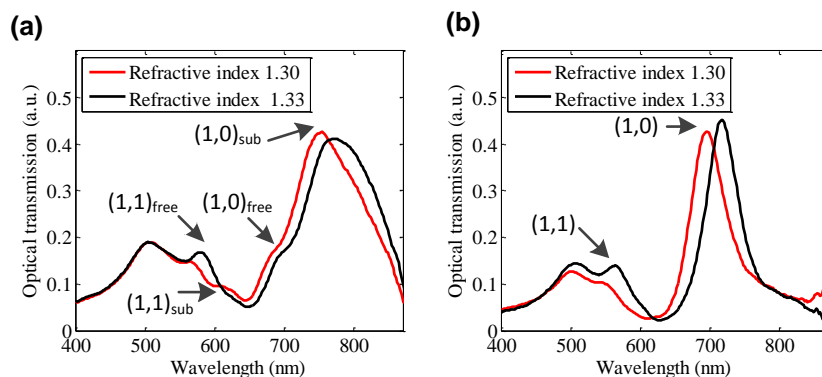


Figure 5-3. *Optical transmission spectra of NHAs with 120-nm circular hole size and 400-nm periodicity collected after a fluid with a refractive index of 1.30 or 1.33 was applied to the free surface. (a) NHA with a 5-nm cavity depth. (b) NHA with a 350-nm cavity depth.*

Bulk SPR sensitivity (nm/RIU) based on $\lambda_{(1,0)}$ was measured for a series of NHAs. Sensitivity was computed as the slope of the line of best fit of the measured resonance position versus index of refraction at the free surface for a series of NHAs. Liquids with refractive indices of 1.30 to 1.39 were tested in 0.03 increments. The bulk SPR sensitivities of NHAs with various periodicities (360 nm, 400 nm, and 440 nm) and 5-nm

and 350-nm cavity depths are shown in Figure 5-4 (a). For each cavity depth, the bulk SPR sensitivity tended to increase with respect to hole periodicity, except for the NHA with the 5-nm cavity depth and 440-nm periodicity, where the bulk SPR sensitivity was similar to the 400-nm periodicity case. This result was consistent with earlier work, where an increase in the SPR sensitivity of NHAs correlated with longer periodicities due to the grating based properties [5-19]. NHAs with a 350-nm cavity depth had overall higher bulk SPR sensitivity than NHAs with a 5-nm cavity depth. The highest bulk SPR sensitivity was obtained for the NHA with 440-nm periodicity and a 350-nm cavity depth, which was about 1.6-fold higher than a similar NHA with a 5-nm cavity depth. The figure of merit (FOM) was computed based on bulk SPR sensitivity over the resonance bandwidth [5-14]. The FOM for NHAs with 120-nm circular hole size and various periodicities and cavities of 5-nm and 350-nm depth are shown in Figure 5-4 (b). The FOM increased almost linearly with respect to periodicity for NHA structures with different cavity depths. The highest FOM was achieved for NHAs with a 350-nm cavity depth, which resulted from the higher bulk SPR sensitivity and the lower resonance bandwidth. The NHA with the 350-nm cavity depth had an almost 3-fold higher FOM compared to the similar NHA with the 5-nm cavity. Therefore, NHAs with a 350-nm cavity depth that enables SP energy matching between the top and bottom surfaces of the metal film provide significantly better bulk SPR sensitivity compared to NHAs with a 5-nm cavity depth, where SP energy matching is poor.

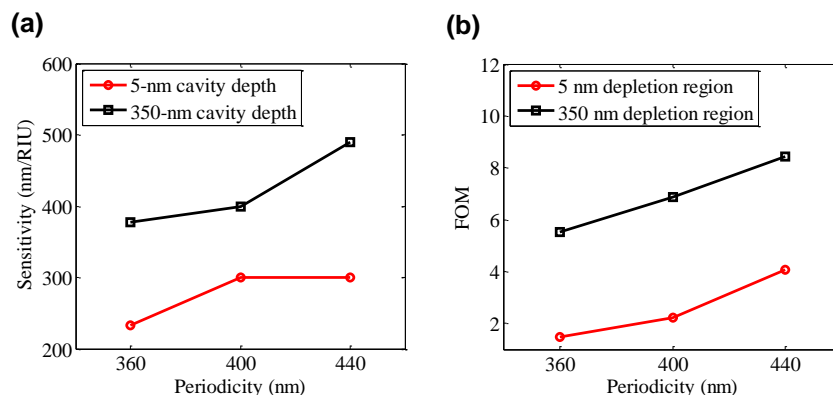


Figure 5-4. (a) Bulk SPR sensitivity (nm/RIU) (b) Figure of Merit (FOM) for NHAs with 120-nm circular hole size and various periodicities of 360 nm, 400 nm, and 440 nm for 5-nm and 350-nm cavity depths.

Inspection of Figure 5-1 (b) qualitatively revealed the appearance of a rough gold surface for the selected NHA, which could result in reduced SPR sensitivity. One possible solution would be to use an annealing process to reduce the roughness of the gold surface as has been described by others [5-20].

The NHA with cavity represents a free-standing membrane with accessibility to the surfaces on the top and bottom. Therefore, in addition to the enhanced bulk SPR sensitivity due to SP-matching, the device could be implemented in a flow through paradigm that could potentially offer shorter response time to changes in the bulk refractive index in a manner analogous to the work of others, who have studied SPR sensing with flow through devices [5-11].

Aside from SPR sensing, other applications of NHAs can potentially benefit from the SP energy matching characteristics imparted by the presence of a cavity. For example, other groups have shown that SP energy matching results in higher electric fields nearby the nano-holes, thereby enhancing sensitivity in SERS applications [5-3] [5-7]. The presence of a cavity could facilitate this beneficial effect for a wider variety of substances at the free surface. Also, a more complex nano-structure consisting partly of a single nano-hole or a series of nano-holes for NSOM applications could potentially

have improved detection performance with the presence of cavities beneath one or more nano-holes [5-21] [5-22].

5.5. Conclusions

In summary, NHAs in gold films were fabricated with an underlying cavity. For all of the NHA devices tested, the presence of the cavity resulted in a blue-shift in the transmission resonance. When the depth of the cavity was 350-nm, near perfect SP energy matching was obtained, which was evident by coincidence of the SP modes related to the top and bottom surfaces. Bulk SPR sensing tests revealed that the sensitivity and FOM for a NHA with a 350-nm cavity depth were enhanced 1.6-fold and 3-fold, respectively in comparison to a NHA with a 5-nm cavity depth. The findings demonstrated a practical example of how SP energy matching between the top and bottom of the gold film can be used to enhance sensing performance.

5.6. References

- 5-1. Genet, C., & Ebbesen, T. W. (2007). Light in tiny holes. *Nature*, *445*(7123), 39-46. doi:10.1038/nature05350
- 5-2. Ebbesen, T. W., Lezec, H. J., Ghaemi, H. F., Thio, T., & Wolff, P. A. (1998). Extraordinary optical transmission through sub-wavelength hole arrays. *Nature*, *391*(6668), 667-669. Retrieved from <http://dx.doi.org/10.1038/35570>
- 5-3. Krishnan, A., Thio, T., Kim, T. J., Lezec, H. J., Ebbesen, T. W., Wolff, P. A., Garcia-Vidal, F. J. (2001). Evanescently coupled resonance in surface plasmon enhanced transmission. *Optics Communications*, *200*(1-6), 1-7. Retrieved from <http://www.sciencedirect.com/science/article/pii/S0030401801015589>
- 5-4. Najiminaini, M., Vasefi, F., Kaminska, B., & Carson, J. J. L. (2010). Experimental and numerical analysis on the optical resonance transmission properties of nano-hole arrays. *Optics Express*, *18*(21), 22255-22270. Retrieved from <http://www.opticsexpress.org/abstract.cfm?URI=oe-18-21-22255>
- 5-5. Przybilla, F., Degiron, A., Genet, C., Ebbesen, T., de Léon-Pérez, F., Bravo-Abad, J., Martín-Moreno, L. (2008). Efficiency and finite size effects in enhanced transmission through subwavelength apertures. *Optics Express*, *16*(13), 9571-9579. Retrieved from <http://www.opticsexpress.org/abstract.cfm?URI=oe-16-13-9571>

- 5-6. Sinton, D., Gordon, R., & Brolo, A. G. (2008). *Nanohole arrays in metal films as optofluidic elements: Progress and potential* - Springer Berlin / Heidelberg. doi:-10.1007/s10404-007-0221-0
- 5-7. Brolo, A. G., Arctander, E., Gordon, R., Leathem, B., & Kavanagh, K. L. (2004). Nanohole-enhanced raman scattering. *Nano Letters*, 4(10), 2015-2018. doi:10.1021/nl048818w
- 5-8. Garcia-Vidal, F. J., Martin-Moreno, L., Ebbesen, T. W., & Kuipers, L. (2010). Light passing through subwavelength apertures. *Reviews of Modern Physics*, 82(1), 729-787. Retrieved from <http://link.aps.org/doi/10.1103/RevModPhys.82.729>
- 5-9. Yanik, A. A., Huang, M., Artar, A., Chang, T., & Altug, H. (2010). Integrated nanoplasmonic-nanofluidic biosensors with targeted delivery of analytes. *Applied Physics Letters*, 96(2), 021101-3. Retrieved from <http://link.aip.org/link/?APL/96/021101/1>
- 5-10. Brolo, A. G., Gordon, R., Leathem, B., & Kavanagh, K. L. (2004). Surface plasmon sensor based on the enhanced light transmission through arrays of nanoholes in gold films. *Langmuir*, 20(12), 4813-4815. doi:10.1021/la0493621
- 5-11. Eftekhari, F., Escobedo, C., Ferreira, J., Duan, X., Girotto, E. M., Brolo, A. G., Sinton, D. (2009). Nanoholes as nanochannels: Flow-through plasmonic sensing. *Analytical Chemistry*, 81(11), 4308-4311. doi:10.1021/ac900221y
- 5-12. Yanik, A. A., Cetin, A. E., Huang, M., Artar, A., Mousavi, S. H., Khanikaev, A., Altug, H. (2011). Seeing protein monolayers with naked eye through plasmonic fano resonances. *Proceedings of the National Academy of Sciences*, Retrieved from <http://www.pnas.org/content/early/2011/06/28/1101910108.abstract>
- 5-13. Przybilla, F., Degiron, A., Laluet, J., Genet, C., & Ebbesen, T. W. (2006). Optical transmission in perforated noble and transition metal films. *Journal of Optics A: Pure and Applied Optics*, 8(5) 458. Retrieved from <http://stacks.iop.org/1464-4258/8/i=5/a=015>
- 5-14. Henzie, J., Lee, M. H., & Odom, T. W. (2007). Multiscale patterning of plasmonic metamaterials. *Nat Nano*, 2(9), 549-554. Retrieved from <http://dx.doi.org/10.1038/nnano.2007.252>
- 5-15. Gordon, R., & Marthandam, P. (2007). Plasmonic bragg reflectors for enhanced extraordinary optical transmission through nano-hole arrays in a gold film. *Optics Express*, 15(20), 12995-13002. Retrieved from <http://www.opticsexpress.org/abstract.cfm?URI=oe-15-20-12995>
- 5-16. Lindquist, N. C., Lesuffleur, A., Im, H., & Oh, S. (2009). Sub-micron resolution surface plasmon resonance imaging enabled by nanohole arrays with surrounding bragg mirrors for enhanced sensitivity and isolation. *Lab Chip*, 9(3), 382-387. Retrieved from <http://dx.doi.org/10.1039/B816735D>

- 5-17. Barnes, W. L., Dereux, A., & Ebbesen, T. W. (2003). Surface plasmon subwavelength optics. *Nature*, *424*(6950), 824-830. Retrieved from <http://dx.doi.org/10.1038/nature01937>
- 5-18. Raether, H. (1988). *Surface plasmons*. Berlin: Springer-Verlag.
- 5-19. Pang, L., Hwang, G. M., Slutsky, B., & Fainman, Y. (2007). Spectral sensitivity of two-dimensional nanohole array surface plasmon polariton resonance sensor. *Applied Physics Letters*, *91*(12), 123112-3. Retrieved from <http://link.aip.org/link/?APL/91/123112/1>
- 5-20. Snopok, B., Strizhak, P., Kostyukevich, E., Serebriy, V., Lysenko, S., Shepeliavii, P., Venger, E. (1999). Interfacial architecture on the fractal support: Polycrystalline gold films as support for self-assembling monolayers. *Semiconductor Physics, Quantum Electronics & Optoelectronics*, *2*(3), 86.
- 5-21. Schuller, J. A., Barnard, E. S., Cai, W., Jun, Y. C., White, J. S., & Brongersma, M. L. (2010). Plasmonics for extreme light concentration and manipulation. *Nat Mater*, *9*(3), 193-204. Retrieved from <http://dx.doi.org/10.1038/nmat2630>
- 5-22. Neumann, L., Pang, Y., Houyou, A., Juan, M. L., Gordon, R., & van Hulst, N. F. (2011). Extraordinary optical transmission brightens near-field fiber probe. *Nano Letters*, *11*(2), 355-360. doi:10.1021/nl102657m

6. A three-dimensional plasmonic nanostructure with extraordinary optical transmission⁵

6.1. Abstract

We report a 3D plasmonic nanostructure having an extraordinary optical transmission due to localized surface plasmon (LSP) coupling between nanoholes and nanodisks. The nanostructure contains a free-standing gold nanohole array (NHA) film above a cavity and an array of nanodisks at the bottom of the cavity that is aligned with the NHA. For the device, the LSP-mediated resonance position was dependent on the hole and nanodisk diameter as well as the separation distance. Also, the effect of LSP coupling between each hole and corresponding nanodisk became negligible for cavities deeper than 200 nm as observed as a disappearance of the LSP resonance. The greatest LSP resonance transmission and the highest electric field intensity were observed for the structure with the shallowest cavity. In addition, the structure had high surface plasmon resonance sensitivity and may have potential for surface enhanced Raman spectroscopy and optical trapping applications.

⁵ The following chapter is published in *Plasmonics*, 1-8, (2012) under the co-authorship of Fartash Vasefi, Bozena Kaminska, and Jeffery J.L. Carson. Retrieved from <http://dx.doi.org/10.1007/s11468-012-9378-9> (The original source of this publication is www.springerlink.com)

6.2. Introduction

The extraordinary optical transmission (EOT) of light through an array of periodic holes in metal films has been of great interest to researchers working in the areas of nanooptics and plasmonic applications [6-1] [6-2]. In contrast to standard aperture theory, at the resonances of a nanohole array (NHA) the light transmission efficiency can exceed 100% when compared to the light incident on the nanoholes. There also exist high electric fields in the vicinity of the nanoholes at the resonance wavelength [6-3]. The transmission resonances result when light incident on the NHA excites surface plasmon polaritons (SPPs) or standing electromagnetic waves that are present at the interface between the metal and the dielectric [6-1]. The transmission resonances of a NHA depend greatly on the dielectric functions of the metal film and the dielectric material, as well as the spacing between the nanoholes, the hole lattice arrangement, and the propagation direction of the excited SPP modes [6-4]–[6-8]. Also, the angle of incidence of illumination has a significant influence on the excited SPP modes, resulting in various transmission resonances [6-4].

Recent research on quasi-3D and 3D nanostructures has revealed that these devices have unique and advantageous optical properties [6-9]–[6-17]. For example, it was recently demonstrated that an NHA with a 3D nanohole structure displayed an optical resonance that could not be observed with planar NHAs [6-9]. This new resonance was associated with localized surface plasmon (LSP) excitation of the 3D nanohole structure and the resonance position was dependent on the hole size rather than the hole periodicity or the angle of incidence of the illumination. Also, at the LSP resonance, the transmission efficiency and the local electric field intensity were higher compared to the SPP-mediated resonance [6-9]. Moreover, quasi-3D nanostructures demonstrated that an interaction of SPs between nanodisks and nanoholes resulted in new transmission resonances [6-10]–[6-17]. In contrast to resonances observed with planar NHAs, the new resonances were associated with LSPs, the interaction between LSPs and SPPs, and the Fabry-Perot (FP) effect due to the presence of a nanocavity between the nanohole and the nanodisk [6-10], [6-12], [6-13]. Consequently, enhancements in surface plasmon resonance (SPR) sensing and surface-enhanced

Raman spectroscopy (SERS) for the detection of analytes were achieved by exploitation of quasi-3D nanostructures [6-10], [6-13]–[6-17].

Inspired by the previous studies on quasi-3D and 3D nanostructures, we developed a novel 3D nanostructure and fabrication process, which offers greater control on the nanocavity depth with complete separation between the nanohole and the nanodisk. The fabrication process eliminated the need for additional layers such as adhesive or conductive layers to further enhance the optical resonance properties. The 3D nanostructure displayed strong resonance transmission mediated by the LSP effect due to small nanocavity depths and SP coupling between the nanoholes and nanodisks. We performed a series of simulations and experiments on the 3D nanostructure in order to investigate the effect of cavity depth, nanohole diameter, and nanodisk diameter on the optical transmission properties.

6.3. Methods

6.3.1. *Finite difference time domain simulation*

We employed a 3D finite difference time domain (FDTD) method (see ref. [6-18], [6-19]) to simulate the interaction between light and a combined metallic nanohole and nanodisk structure with the purpose of computing its optical transmission properties. We used the FDTD package from Lumerical Inc. (Vancouver, Canada) with dielectric functions for metallic and dielectric materials provided by Palik [6-20]. A single cell containing a metallic nanohole and nanodisk was simulated for two different boundary conditions to calculate the interaction between light and an infinite periodic structure or a single cell structure. The x- and y-axes, and z-axis were set to periodic and perfect match layer (PML) boundary conditions for an infinite structure, respectively. For a single cell structure, all boundary conditions were set to PML. A non-uniform mesh was used with a highest accuracy of 3 nm. A plain wave source was used to illuminate the structure at various illumination angles. More detail on FDTD simulation procedures can be found in [6-7].

6.3.2. 3D nanostructure fabrication

Figure 6-1 (a) displays a schematic of the fabrication process of a 3D nanostructure that includes a free-standing perforated gold film, a cavity of uniform depth, and an array of gold nanodisks at the bottom of the cavity. Each nanohole array (8 x 8; square lattice) was fabricated in a 70-nm gold film on a thick Ti sacrificial layer on to Pyrex substrate using electron beam lithography (EBL; see Figure 6-1 (a) top) [6-7]. A Ti etchant (TFTN, Transene company, Inc.) was used to remove the Ti sacrificial layer beneath the NHA, which resulted in a free-standing NHA in a gold film and a cavity underneath the NHA (see Figure 6-1 (a) middle). Thirty (30) nm of gold was deposited on to the sample using electron beam deposition, which resulted in a 30-nm thick nanodisk beneath each hole at the bottom of the cavity and increased the film thickness to 100 nm (see Figure 6-1 (a) bottom).

We fabricated a series of NHA devices in a free-standing 70-nm-thick gold film, where the hole diameter was 100, 120, 140, or 160 nm (circular); the periodicity was 360 nm; and the cavity depth was 100 or 200 nm. We then deposited 30-nm gold, which resulted in a 100-nm-thick free-standing perforated film with 30-nm-thick nanodisks at the bottom of the cavity located directly beneath each hole. The diameter of each nanodisk was similar to the hole diameter. Figure 6-1 (b) displays an SEM image of a device with a 100-nm cavity depth and 30-nm-thick nanodisks at the bottom of the cavity.

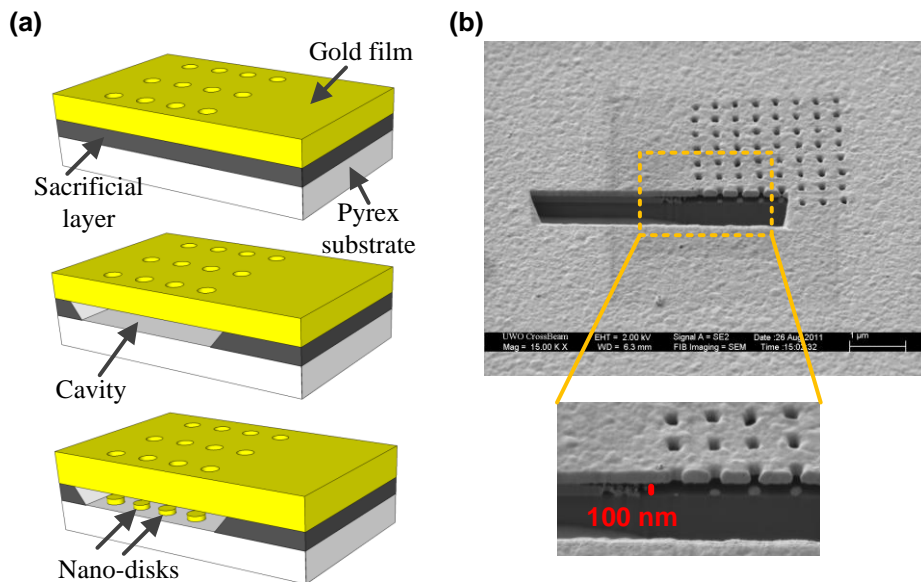


Figure 6-1. (a) A schematic of a NHA in a gold film fabricated on top of sacrificial and substrate layers (top), a schematic of a NHA in a gold film where the sacrificial layer has been etched to form a cavity with uniform depth beneath the NHA (middle), and a schematic of a NHA with nanodisks at the bottom of the cavity (bottom). (b) SEM image (shown at an angle of 54°) of a NHA in a 100-nm gold film that was FIB milled to reveal the titanium sacrificial layer, the Pyrex substrate, and the presence of a 100-nm deep cavity that contained the nanodisks.

6.3.3. Optical characterization setup

We used an optical transmission microscope (Nikon, TE300, Tokyo, Japan) attached to a photometer (PTI, D104, New Jersey, USA), monochromator (PTI, 101, New Jersey, USA), photo-multiplier tube (PMT) housing (PTI, 710, New Jersey, USA), and PMT (Hamamatsu, R928, Tokyo, Japan) to measure the optical transmission spectrum of each device from 400 to 850 nm. Unpolarized collimated white light from the halogen lamp of the microscope was focused by a bright field condenser (NA=0.3) to the sample located on the microscope stage. The bright field diaphragm on top of the condenser was adjusted to 6 mm in order to illuminate the sample with angular deviation of less than 3° from the normal to the plane of the microscope stage. The light

transmitted through the sample was collected by a $\times 100$ objective (NA=0.9, Plan Fluor, Nikon, Japan). Light reaching the photometer was restricted by a rectangular aperture to select the desired sample region for spectral measurement by the monochromator and PMT. The measured transmission intensity from each device was subtracted from the light transmitted through the gold film and normalized by spectral dependence of the halogen lamp transmitted through the glass substrate.

6.4. Results

Figure 6-2 (a) displays simulated optical transmission spectra for free-standing NHAs in a 100-nm-thick gold film with 50, 100, 150, and 200 nm cavity depths, where holes had a diameter of 140 nm, and the periodicity was 360 nm. A resonance related to (1,0) SPP excitation mode was seen for all NHAs. The resonances occurred almost at the same wavelength position for all structures, with small changes in the resonance transmission. The small differences in transmission may have been due to different SP fields for various cavity depths, which resulted in changes in the (1,0) resonance transmission. Figure 6-2 (b) displays a simulated optical transmission spectrum of a nanodisk with 140-nm circular diameter and 30-nm-thickness on a Pyrex substrate. Absorption of the nanodisk related to the LSP property was observed at 686 nm. Figure 6-2 (c) displays simulated optical transmission spectra for a free-standing NHA in a 100-nm-thick gold film, where the holes had a diameter of 140 nm, the periodicity was 360 nm, the nanodisks had a thickness of 30 nm, and the cavity depth was varied (50, 100, 150, and 200 nm). Resonant transmission associated with the LSP interaction between nanoholes and nanodisks was observed when the cavity depth was 50 and 100 nm. We concluded that the transmission resonance was related to excitation of LSP since simulation of a structure with a single hole and nanodisk had the same transmission resonance (data not shown) as the periodic structure. Another resonance peak was observed at a shorter wavelength for structures with 100-, 150-, and 200-nm cavity depths (Figure 6-2 (c)). We concluded that the transmission resonance was due to (1,0) SPP excitation at the top and bottom interfaces of the NHA as illustrated in Figure 6-2 (a) for the simulated NHAs. However, in the nanostructure with 50-nm cavity depth, the

(1,0) SPP resonance was not clearly observed due to suppression by the extensive minimum related to the LSP absorption (Figure 6-2 (c)). As the cavity depth increased, the effect of LSP coupling between hole and nanodisk decreased and this resulted in a reduced LSP resonance transmission efficiency and a higher SPP resonance transmission efficiency for the structure. Also, when the distance between the nanohole and nanodisk was large (i.e., in 200-nm cavity depth), the optical transmission properties of the NHA and nanodisks were similar to their individual behavior and LSP coupling between nanohole and nanodisk was not observed (see Figure 6-2 (a) and (b)). Therefore, the optical transmission of light through the structure demonstrated optical transmission related to the product of the transmission of a NHA and an array of nanodisks. For example, the (1,0) SPP resonance of the NHA at 570 nm and the absorption due to the nanodisks at 686 nm were clearly present (Figure 6-2 (c), 200-nm cavity depth).

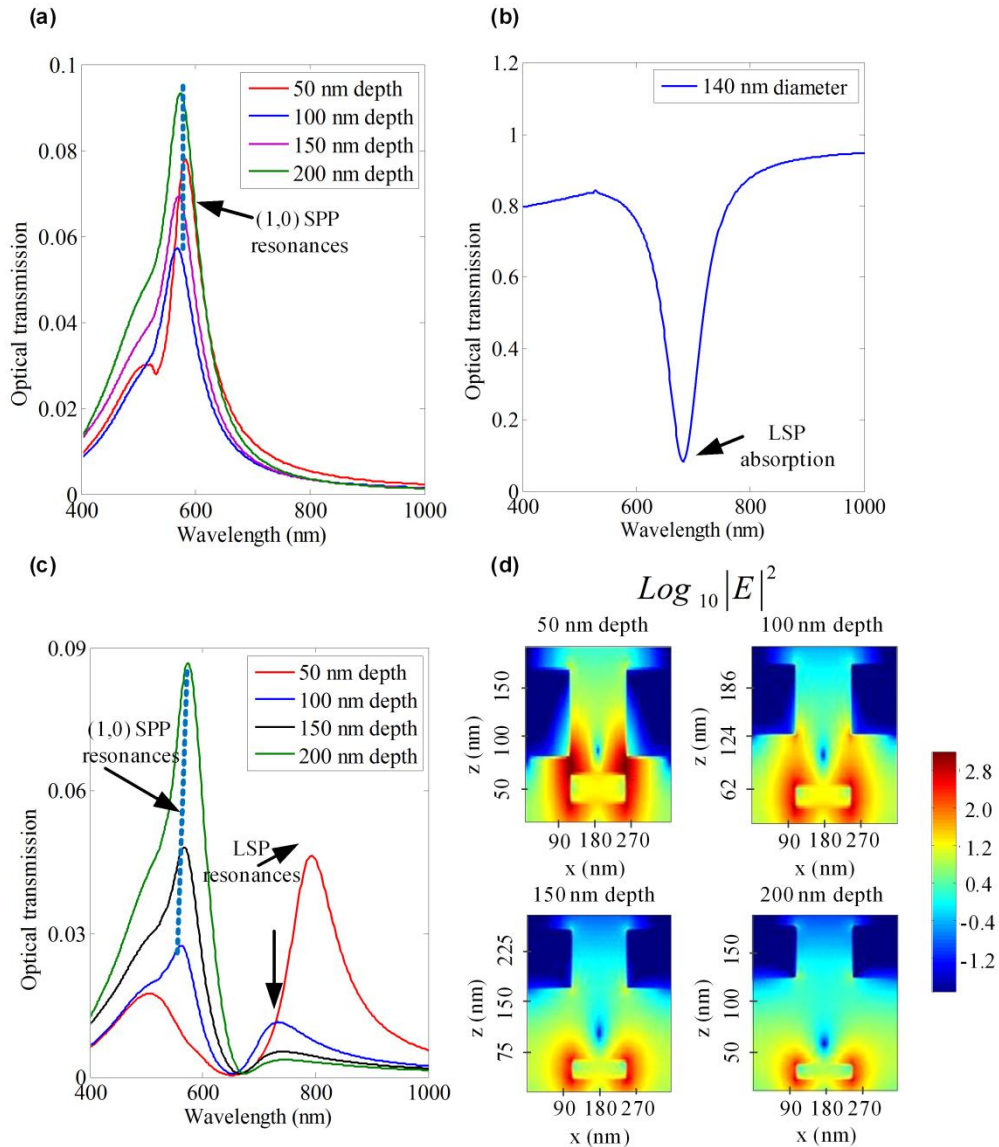


Figure 6-2 *Simulated optical transmission spectra of (a) NHAs with various cavity depths (50 nm, 100 nm, 150 nm, and 200 nm), 140 nm hole diameter and 360 nm periodicity, (b) a nanodisk with 140 nm diameter and 30 nm thickness, and (c) 3D nanostructure containing a NHA in a 100-nm thick gold film (140 nm hole diameter; 360 nm periodicity; cavity depths: 50 nm, 100 nm, 150 nm, or 200 nm; 30-nm thick nano-disks at bottom of the cavity). (d) Visualization of the electric field intensity (xz cross section; LSP coupling resonance wavelength) of a nanohole and a nanodisk for four cavity depths (as indicated at top of each panel; log scale).*

Figure 6-2 (d) illustrates the computed electric-field intensity at the LSP resonance wavelength for a nanohole and nanodisk cell at a variety of cavity depths. All simulation cells displayed LSP coupling between the hole and nanodisk at the LSP resonance wavelength except for the cell with a 200-nm cavity depth. The cell with a 50-nm cavity depth had the highest electric field intensity between the nanohole and nanodisk at the LSP resonance wavelength compared to the electric field intensity for cells with 100- and 150-nm cavity depths. For the 200-nm cavity case, the high intensity electric field was localized to the nanodisk. The electric field intensity at hot spots for the cell with a 50-nm cavity was 2.5-, 4.1-, and 5.3-fold higher than the electric field intensity at the hot spots calculated for the cells with 100-, 150-, and 200-nm cavities, respectively. The results clearly demonstrate that a shorter distance between the nanohole and nanodisk resulted in higher intensity electric fields in between.

The experimental optical transmission spectra of NHAs with 140-nm circular hole diameter, 360-nm hole periodicity, and 100- and 200-nm cavity depths without and with 30-nm-thick nanodisks at the bottom of the cavity are shown in Figure 6-3 (a) and (b), respectively. In Figure 6-3 (a), NHAs with 100- and 200-nm cavity depths had a resonance transmission related to (1,0) SPP excitation from top and bottom of the perforated gold film. The same (1,0) SPP excitation occurred at both interfaces of the NHA gold film due to the same SP energy on top and bottom of the NHA, which resulted from the presence of material of identical refractive index on both the top and the bottom of the NHA ($n_{\text{air}}=1$) [6-3]. As illustrated in Figure 6-3 (b), the existence of nanodisks at the bottom of the cavity transformed the optical transmission spectra of NHAs. In the structure with a 100-nm cavity and nanodisks, a new resonance peak related to LSP coupling between holes and nanodisks was observed at 720 nm. Also, a minimum was observed at 640 nm for the 100-nm cavity structure and resulted from absorption due to LSP interaction between nanoholes and nanodisks. However, no resonance transmission associated with LSP coupling between nanoholes and nanodisks was observed for the 200-nm cavity structure. This was due to the smaller SP decay length away from the metallic surface and into the dielectric materials for both the NHA and the nanodisks compared to the 200-nm cavity depth [6-21]. Also, for the 200-nm cavity structure, a minimum at 650 nm was observed due to nanodisk absorption. Therefore,

similar to the simulation results for the 200-nm cavity structure, the optical transmission spectrum was consistent with the product of the NHA and the nanodisk spectra.

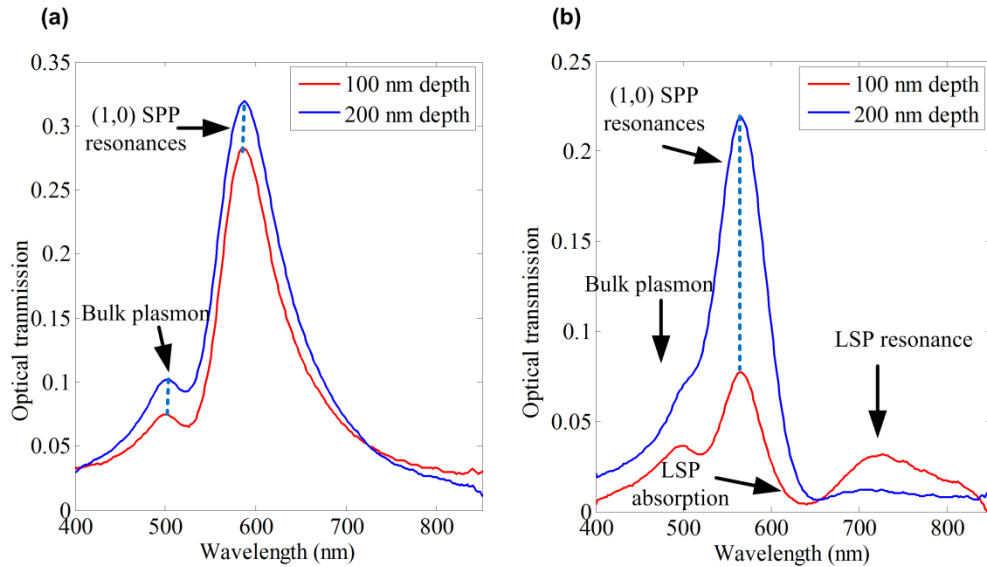


Figure 6-3. (a) *Experimental optical transmission spectra of a 3D nanostructure with a NHA in a 100-nm thick gold film with 140 nm hole diameter and 360 nm periodicity for 100 nm and 200 nm cavity depths without nano-disks and (b) with 30-nm thick nano-disks at the bottom of the cavity.*

The resonance position related to LSP coupling between nanohole and nanodisk for 100-nm-thick gold NHAs with 360-nm hole periodicity; 50-, 75- and 100-nm cavity depths; and 30-nm-thick nanodisks at the bottom of the cavity, but with various hole and nanodisk diameters is shown in Figure 6-4 (a) for both experiments and simulations. As the nanohole and the nanodisk diameter increased, the LSP resonance position red-shifted for the 50-, 75-, and 100- nm cavity structures. For the 100-nm cavity structure, there was agreement between the optical resonance position calculated from simulated optical spectra and the optical resonance position measured from optical spectra collected by experiment. An estimated difference between resonance positions obtained from simulation and experiment for a given structure was between 1 and 14 nm. A similar red-shift occurred for simulated structures with 50- and 75-nm cavity depths as

the nanohole and nanodisk diameter increased. Also, for the structures with 50- and 75-nm cavity depths, the LSP resonance position shifted to a longer wavelength compared to the 100-nm cavity structure, for a given hole and nanodisk diameter. However, it was seen that the resonance peak had the largest resonance shift for the 50-nm cavity structure with respect to hole and nanodisk diameters compared to the 75- and 100-nm cavity depth structures. As a result, both the nanohole and nanodisk diameter and the distance between the nanohole and nanodisk influenced the LSPs resonance position of this structure, which was expected due to the localized SP property of the LSP resonance transmission peak [6-22].

The simulated optical transmission spectra of the 100-nm-thick gold NHA with 100-nm hole diameter, 360-nm periodicity, 50-nm cavity, and 30-nm-thick nanodisk at the bottom of the cavity as a function of incident angle of illumination are shown in Figure 6-4 (b). Among the 3D structures, the 3D structure with the 50-nm cavity depth was selected for simulation using various incident angles of illumination due to the strong LSP resonance transmission peak at various illumination angles. A broad resonance peak related to LSP coupling between the nanohole and nanodisk was observed at all angles and did not depend greatly on illumination angle. However, the LSP resonance transmission intensity decayed slightly at larger angles of illumination and this likely resulted from a shadowing effect [6-23]. A broadband minimum between the LSP-mediated resonance and (1,0) SPP-mediated resonance occurred at all incident angles of illumination and was attributed to LSP nanohole and nanodisk absorption. The (1, 0) resonance peak related to the SPP of the NHA from both sides of the film appeared at incident angles greater than 6° and appeared to red-shift slightly at higher angles. The low transmission of the (1,0) SPP-mediated resonance was due to a suppression of the resonance by the broad nanohole and nanodisk absorption.

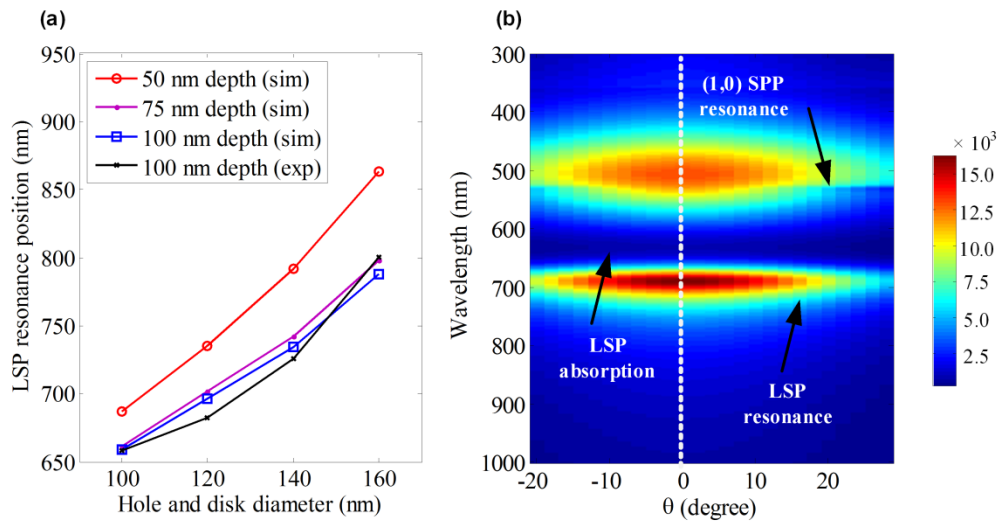


Figure 6-4. (a) Resonance position (LSP coupling between hole and nano-disk) of a perforated 100-nm thick gold film with 360-nm hole periodicity, 50-nm, 75 nm, and 100-nm cavity depth, and 30-nm thick nano-disks at the bottom of the cavity as a function of circular hole and nano-disk diameter taken from simulation (sim) and experimental (exp) results. (b) Optical transmission spectra as a function of incident angle of illumination for NHAs with 100-nm hole diameter, 360-nm periodicity, 50-nm cavity depth, and 30-nm thick nano-disks at the bottom of the cavity.

We measured SPR sensitivity of the simulated and fabricated NHAs with cavity and nanodisks at the bottom of the cavity for refractive indices between 1.33 and 1.40. The SPR sensitivity of the LSP resonance peak was ~ 215 and 220 nm/refractive index units (RIU) for a NHA with 30-nm thick nanodisks at the bottom of a 100-nm cavity obtained from simulations and experiments, respectively. The simulated SPR sensitivity for the structure with 30-nm nanodisks at the bottom of a 50-nm cavity was ~ 550 nm/RIU. The higher sensitivity of the LSP resonance peak for the device with the 50-nm cavity was expected due to the higher electric field intensity between holes and nanodisks. Previously, the SPR sensitivity for planar NHAs was reported to be about 400 nm/RIU for the (1,0) SPP-mediated resonance peak [6-10]. Also, the sensitivity related to the FP resonance of a 3D nanostructure was measured to be ~ 305 nm/RIU [6-13].

6.5. Discussion

The LSP interference between nanoholes and nanodisks in the 3D nanostructure resulted in resonant light transmission through the structure. The LSP-mediated transmission resonance was due to an antenna-like behavior between the nanohole and nanodisk, which enabled evanescent transmission of the light. The LSP-mediated transmission resonance was dependent on nanohole and nanodisk size as well as the distance between the nanohole and the nanodisk. Stronger LSP coupling between nanohole and nanodisk was seen for shallower cavity depths. The close spacing resulted in higher transmission at the LSP resonance peak as well as a red-shift in the peak position compared to devices with deeper cavities. Also, due to the dependence of the resonance position on LSP coupling, the resonance position was dependent on the size of the nanohole and nanodisk.

The fabricated NHA devices had small surface roughness features, which resulted in changes in SPP propagation along the surface. The gold surface roughness caused the SPP resonance bandwidth of each NHA to widen resulting in lower SPR sensitivity. However, the LSP-mediated resonance properties would not change significantly based on the gold surface roughness and would more likely be dependent on the geometry of the hole and disk features. Also, the LSP-mediated resonance position of the NHA and nanodisk structure did not depend on illumination angle while the SPP mediated resonance position is expected to change with illumination angle.

The fabrication process offered many benefits compared to other quasi-3D nanostructure fabrication processes. (1) The Ti layer had precise and uniform thickness and provided for a cavity of precise depth and depth uniformity compared to the photoresist spin-coating process used by others [6-15]. (2) The glass substrate acted as an etchant stop layer to preserve cavity depth over a large area. (3) A free-standing gold membrane could be achieved without the use of adhesive or conductive layers, which are known to influence and degrade the optical properties of plasmonic structures [6-24]. (4) The structure provided for SP energy matching between the top and bottom surface of the perforated gold film, which is recognized to enhance the optical properties [6-3], [6-25]. (5) The structure is amenable to deposition of liquids and gases and benefits from

the same refractive index above and below the gold film, which is not possible with other quasi-3D nanostructure designs (e.g., see [6-10]–[6-17]). (6) The free-standing perforated gold film (e.g., membrane) provides for complete separation between the nanohole and the nanodisk, which is not easily achieved with other fabrication methods for small cavity depths.

Nevertheless, there are some limitations to the fabrication of a large NHA with a cavity and nanodisks at the bottom of the cavity. For example, we observed that a gold NHA film with a size of 30 by 30 μm tended to sag and come in contact with the bottom of the cavity after the cavity fabrication process. We hypothesized that this effect resulted from surface tension effects due to the liquids used during etching and rinsing of the 3D nanostructure. Given the Young's Modulus of gold 79 GPa, it is likely that a thin gold film cannot resist surface tension effects at the nano and micro scale. A metal or doped semi-conductor with a higher Young's Modulus could provide for a larger freestanding NHA with a cavity below. For the 8 x 8 NHAs with shallower cavity depths (i.e., less than 100 nm), the film tended to sag to a greater degree compared to NHAs with cavity depths larger than 100 nm. This effect was likely due to surface tension effects and capillary forces during the rinsing and drying steps of the fabrication process. However, a smaller NHA area size could potentially allow a successful fabrication of a NHA with a smaller cavity depth.

The high electric field intensity between the nanoholes and nanodisks at LSP resonance for the 3D structure could improve performance of plasmonic applications. For example, the broadband LSP resonance of the 3D nanostructure could be tailored to enhance efficiency of surface-enhanced Raman spectroscopy (SERS) [6-26]. The high electric field of the 3D nanostructure between the nanoholes and nanodisks at the LSP resonance could provide an increase in the SERS signal of nearby bio-molecules. Alternatively, the directive and enhanced electric field intensity between the nanoholes and nanodisks at the LSP resonance could potentially be employed in optical trapping applications, such as trapping of nanoparticles. We expect that the 3D nanostructure with Plasmonics nanoholes and nanodisks will provide higher efficiency particle trapping

compared to nanohole or double-hole structures (e.g., see ref [6-27]) due to its uniquely high electric field intensity between the nanoholes and nanodisks at the LSP resonance.

6.6. Conclusions

In conclusion, a 3D nanostructure designed to have a resonance transmission related to LSP coupling between a freestanding perforated gold film and gold nanodisks at the bottom of a cavity was tested through simulations and experiments. Simulations revealed enhanced electric field intensity between nanoholes and nanodisks at the LSP resonance wavelength. The greatest electric field intensity was observed for the structure with a 50-nm cavity depth, suggesting that similar devices with smaller cavity depths could have even larger electric fields localized to the nanohole/nanodisk region. A broadband LSP resonance was observed and was dependent on both the nanohole and nanodisk diameter and the proximity to one another. However, the LSP resonance position did not depend significantly on the illumination angle ($<30^\circ$). It was observed that the LSP resonance was not pronounced for the structure with a cavity depth of 200 nm. The broadband LSP-mediated resonance provides several advantages over devices with SPP-mediated resonances such as independence from angle of illumination, enhanced optical transmission, and higher bulk SPR sensitivity. The 3D nanostructure can potentially be employed in SPR sensing and SERS of bio-molecules and optical trapping of nanoparticles.

6.7. Acknowledgments

The authors thank Dr. Todd Simpson for his technical support at the Nanofab Laboratory at University of Western Ontario (UWO). This project was funded by grants from the Natural Sciences and Engineering Research Council of Canada (NSERC) to Dr. Bozena Kaminska and Dr. Jeffrey J.L. Carson. Dr. Fartash Vasefi was supported by a London Regional Cancer Program Translational Breast Cancer Research Trainee Fellowship.

6.8. References

- 6-1. Ebbesen, T. W., Lezec, H. J., Ghaemi, H. F., Thio, T., & Wolff, P. A. (1998). Extraordinary optical transmission through sub-wavelength hole arrays. *Nature*, 391(6668), 667-669. Retrieved from <http://dx.doi.org/10.1038/35570>
- 6-2. Lesuffleur, A., Im, H., Lindquist, N. C., Lim, K. S., & Oh, S. (2008). Laser-illuminated nanohole arrays for multiplex plasmonic microarray sensing. *Optics Express*, 16(1), 219-224. Retrieved from <http://www.opticsexpress.org/abstract.cfm?URI=oe-16-1-219>
- 6-3. Krishnan, A., Thio, T., Kim, T. J., Lezec, H. J., Ebbesen, T. W., Wolff, P. A., Garcia-Vidal, F. J. (2001). Evanescently coupled resonance in surface plasmon enhanced transmission. *Optics Communications*, 200(1-6), 1-7. Retrieved from <http://www.sciencedirect.com/science/article/pii/S0030401801015589>
- 6-4. Thio, T., Ghaemi, H. F., Lezec, H. J., Wolff, P. A., & Ebbesen, T. W. (1999). Surface-plasmon-enhanced transmission through hole arrays in cr films. *Journal of the Optical Society of America B*, 16(10), 1743-1748. Retrieved from <http://josab.osa.org/abstract.cfm?URI=josab-16-10-1743>
- 6-5. Przybilla, F., Degiron, A., Laluet, J., Genet, C., & Ebbesen, T. W. (2006). Optical transmission in perforated noble and transition metal films. *Journal of Optics A: Pure and Applied Optics*, 8(5) 458. Retrieved from <http://stacks.iop.org/1464-4258/8/i=5/a=015>
- 6-6. Gordon, R., Brolo, A. G., McKinnon, A., Rajora, A., Leathem, B., & Kavanagh, K. L. (2004). Strong polarization in the optical transmission through elliptical nanohole arrays. *Physical Review Letters*, 92(3), 037401. Retrieved from <http://link.aps.org/doi/10.1103/PhysRevLett.92.037401>
- 6-7. Najiminaini, M., Vasefi, F., Kaminska, B., & Carson, J. J. L. (2011). Optical resonance transmission properties of nano-hole arrays in a gold film: Effect of adhesion layer. *Optics Express*, 19(27), 26186-26197. Retrieved from <http://dx.doi.org/10.1364/OE.19.026186>
- 6-8. van, d. M., Segerink, F. B., van Hulst, N. F., & Kuipers, L. (2004). Influence of hole size on the extraordinary transmission through subwavelength hole arrays. *Applied Physics Letters*, 85(19), 4316-4318. Retrieved from <http://link.aip.org/link/?APL/85/4316/1>
- 6-9. Yang, J., Gao, H., Suh, J. Y., Zhou, W., Lee, M. H., & Odom, T. W. (2010). Enhanced optical transmission mediated by localized plasmons in anisotropic, three-dimensional nanohole arrays. *Nano Letters*, 10(8), 3173-3178. doi:10.1021/nl102078j

- 6-10. Stewart, M. E., Mack, N. H., Malyarchuk, V., Soares, J. A. N. T., Lee, T., Gray, S. K., Rogers, J. A. (2006). Quantitative multispectral biosensing and 1D imaging using quasi-3D plasmonic crystals. *Proceedings of the National Academy of Sciences*, 103(46), 17143-17148. Retrieved from <http://www.pnas.org/content/103/46/17143.abstract>
- 6-11. Li, J., Chen, S., Chou, Y., Wu, M., Hsueh, C., & Su, W. (2011). Effects of gold film morphology on surface plasmon resonance using periodic P3HT:PMMA/Au nanostructures on silicon substrate for surface-enhanced raman scattering. *The Journal of Physical Chemistry C*, 115(49), 24045-24053. doi:10.1021/jp203307f
- 6-12. Li, W., Hu, J., & Chou, S. Y. (2011). Extraordinary light transmission through opaque thin metal film with subwavelength holes blocked by metal disks. *Optics Express*, 19(21), 21098-21108. Retrieved from <http://www.opticsexpress.org/abstract.cfm?URI=oe-19-21-21098>
- 6-13. Artar, A., Yanik, A. A., & Altug, H. (2009). Fabry-perot nanocavities in multilayered plasmonic crystals for enhanced biosensing. *Applied Physics Letters*, 95(5), 051105-3. Retrieved from <http://link.aip.org/link/?APL/95/051105/1>
- 6-14. Xu, J., Kvasnicka, P., Idso, M., Jordan, R. W., Gong, H., Homola, J., & Yu, Q. (2011). Understanding the effects of dielectric medium, substrate, and depth on electric fields and SERS of quasi-3D plasmonic nanostructures. *Optics Express*, 19(21), 20493-20505. Retrieved from <http://www.opticsexpress.org/abstract.cfm?URI=oe-19-21-20493>
- 6-15. Xu, J., Guan, P., Kvasnicka, P., Gong, H., Homola, J., & Yu, Q. (2011). Light transmission and surface-enhanced raman scattering of quasi-3D plasmonic nanostructure arrays with deep and shallow fabry-Perot nanocavities. *The Journal of Physical Chemistry C*, 115(22), 10996-11002. doi:10.1021/jp202110s
- 6-16. Bezares, F., Caldwell, J., Glembocki, O., Rendell, R., Feygelson, M., Ukaegbu, M., . . . Hosten, C. (2012). The role of propagating and localized surface plasmons for SERS enhancement in periodic nanostructures. *Plasmonics*, 7(1), 143-150. Retrieved from <http://dx.doi.org/10.1007/s11468-011-9287-3>
- 6-17. Baca, A. J., Montgomery, J. M., Cambrea, L. R., Moran, M., Johnson, L., Yacoub, J., & Truong, T. T. (2011). Optimization of nanopost plasmonic crystals for surface enhanced raman scattering. *The Journal of Physical Chemistry C*, 115(15), 7171-7178. doi:10.1021/jp109066c
- 6-18. Yee, K. S. (1966). Numerical solution of initial boundary value problems involving Maxwell's equations in isotropic media. *IEEE Trans.Ant.Prop.*, 14, 302.
- 6-19. Taflove, A., & Hagness, S. C. (Eds.). (2000). *Computational electrodynamics: The finite-difference time-domain method* (Second ed.). Boston: Artech House.

- 6-20. Palik, E. D. (1985). *Handbook of optical constants of solids*. New York: Academic Press.
- 6-21. Barnes, W. L., Dereux, A., & Ebbesen, T. W. (2003). Surface plasmon subwavelength optics. *Nature*, 424(6950), 824-830. Retrieved from <http://dx.doi.org/10.1038/nature01937>
- 6-22. Chu, Y., & Crozier, K. B. (2009). Experimental study of the interaction between localized and propagating surface plasmons. *Optics Letters*, 34(3), 244-246. Retrieved from <http://ol.osa.org/abstract.cfm?URI=ol-34-3-244>
- 6-23. Kim, H., & Lee, B. (2009). Unidirectional surface plasmon polariton excitation on single slit with oblique backside illumination. *Plasmonics*, 4(2), 153-159. doi:10.1007/s11468-009-9086-2
- 6-24. Najiminaini, M., Vasefi, F., Kaminska, B., & Carson, J. J. L. (2011). Optical resonance transmission properties of nano-hole arrays in a gold film: Effect of adhesion layer. *Opt.Express*, 19(27), 26186-26197. doi:10.1364/OE.19.026186
- 6-25. Najiminaini, M., Vasefi, F., Kaminska, B., & Carson, J. J. L. (2012). Nano-hole array structure with improved surface plasmon energy matching characteristics. *Applied Physics Letters*, 100(4), 043105. doi:10.1063/1.3679173
- 6-26. Djaker, N., Hostein, R., Devaux, E., Ebbesen, T. W., Rigneault, H., & Wenger, J. (2010). Surface enhanced raman scattering on a single nanometric aperture. *The Journal of Physical Chemistry C*, 114(39), 16250-16256. doi:10.1021/jp104971p
- 6-27. Pang, Y., & Gordon, R. (2011). Optical trapping of 12 nm dielectric spheres using double-nanoholes in a gold film. *Nano Letters*, 11(9), 3763-3767. doi:10.1021/nl201807z

7. Summary and future work

7.1. Overview

This chapter summarizes the dissertation based on results from the studies that have been described in chapters 2 through 6. Also, a perspective and outlook to future research are discussed. The summary is categorized into two sections: 1) systematic studies and 2) novel plasmonic nano-structures. Finally, the chapter ends with a conclusion section, where main results from each chapter are reviewed and linked to the objectives and goals in the introduction chapter.

7.2. Systematic studies

In order to employ a plasmonic sub-wavelength hole array for any of its related applications, optical parameters must be extracted from the resonance transmission spectrum. Parameters include the resonance position, the transmission efficiency at the resonance wavelength, and the spectral bandwidth of the resonance. Also, the localized electric field in the vicinity of each hole is another important parameter. Nevertheless, aforementioned parameters of sub-wavelength hole array can be changed by possible geometrical variations such as hole size, hole shape, array shape, dielectric and metal thickness, dielectric and metal materials, hole periodicity, groove period, and groove depth. Therefore, all these factors may improve or degrade the optical properties of a sub-wavelength hole array.

One of the most common ways to fabricate a sub-wavelength hole array in a metal film is to employ EBL technique with lift-off process. Using this technique, various hole shapes, hole sizes, and hole periodicities in different metal films can be fabricated while structures such as groove, or dimples around a sub-wavelength hole array in a

metal film cannot be simply fabricated. The fabrication method could change optical properties of a sub-wavelength hole array due to some defects in fabricated structures or some additional layers (i.e. adhesion and conductive layers) [7-1] [7-2].

In chapter 2, large nano-hole arrays with various geometrical parameters in a square lattice arrangement were fabricated using the EBL/lift-off technique. The geometrical parameters are various hole shapes (circular and square), hole sizes, and hole periodicities. Each nano-hole array in a gold film was optically characterized using optical transmission spectroscopy. Two optical resonance related to (1, 0) and (1, 1) SP excitation from substrate-gold side were observed in transmission spectra between 400 nm and 870 nm of all arrays. This was due to the fact that the periodicities for the nano-hole arrays were selected in such a way that the (1, 0) and (1, 1) optical resonance peaks of arrays would occur in 400 nm to 870 nm wavelength range. The hole periodicities were between range of 375 nm and 475 nm. Another resonance peak related to (1, 0) SP excitation from air-gold side was observed for a few nano-hole arrays with larger periodicity (i.e. 475 nm) at lower wavelengths. The optical resonance parameters (i.e. resonance position, transmission efficiency, and bandwidth) related to each SP mode were extracted and compared by simulation results from FDTD model. The simulation model was constructed based on the fabricated nano-hole array structures and layers. In the fabricated nano-hole array structures, a 5 nm Cr conductive layer was used for performing EBL writing process and 10 nm Cr was later employed in order to adhere gold on the Pyrex substrate. The simulation results proved that the 5-nm conductive layer and 10-nm adhesion layer had a significant effect on optical transmission properties of a nano-hole array.

Both simulation and experimental results indicated that as the hole periodicity increased, the optical resonance position related to (1, 0) and (1, 1) SP excitation shifted to longer wavelengths. Also, the results showed that the (1, 0) and (1, 1) resonance properties were not dependent on square and circular hole shapes. For a given periodicity, both (1, 0) and (1, 1) resonance position slightly shifted for hole size change from 150 nm to 250 nm in diameter in both simulated and measured results. However, there were some discrepancies between simulation and experimental results. For

example, it was shown that (1, 0) resonance bandwidth decayed as periodicity increased in experimental measurements, while the (1, 0) resonance bandwidth did not change significantly for various periodicities in simulations. This could be due to the fact that the simulated structure was constructed based on the assumption of a smooth metal surface as well as the absence of ridges on the simulated hole structure compared to the fabricated hole structures. For a given periodicity, the (1,0) resonance bandwidth decayed as the hole size increased for both simulation and empiric results although the dependence of bandwidth on hole size was greater for the experimental measurements than for the simulation results. The reason behind the (1, 0) resonance bandwidth decay for smaller hole size could be due to the fact that the resonance shifted further from the hole cut-off wavelength for smaller hole sizes.

In the simulated results, the (1, 0) resonance peak related to SP excitation from air-gold side was more pronounced in most of the arrays while the (1, 1) resonance peak related to Pyrex-gold side was more apparent in the tested structures. This could be due to the fact that the (1, 1) resonance peak from Pyrex-gold side was more suppressed in the simulated structures due to the presence of chromium conductive and adhesion layers. Also, a wide resonance bandwidth of the fabricated structures was due to the chromium layers beneath the gold layer. Therefore, the results from the studies conducted in chapter 2 led me to investigate the effect of the adhesion layers on the resonance transmission properties of a nano-hole array in a gold film.

In chapter 3, large nano-hole arrays with various hole periodicities in a gold film on a Pyrex substrate were fabricated using EBL/lift-off fabrication process. In order to adhere gold to the Pyrex substrate, various compositions and thicknesses of adhesion layers were employed in the EBL/lift-off fabrication process. In particular, 5 nm chromium, 5 nm titanium, 10 nm titanium, and etched 10 nm titanium were used to analyze the effect of adhesion layers on the resonance transmission properties of nano-hole arrays. The periodicities of the nano-hole arrays were selected in such a way that the (1, 0) resonance peak related to SP excitation from Pyrex-gold was present between 400 nm and 870 nm. For each adhesion layer composition, nano-hole arrays with nine different periodicities were fabricated and characterized optically using optical

transmission spectroscopy. The experimental results were analyzed with respect to (1, 0) resonance transmission properties and validated with the FDTD simulation analysis.

In both simulation and experimental results, no resonance peak was seen for the nano-hole arrays with 10 nm Ti adhesion layers. This expected result was due to high absorption of coupled light to SP by the 10-nm Ti adhesion layer from Pyrex-gold side. However, the (1, 0) resonance peaks related to SP excitation from Pyrex-gold side were observed for 5-nm Ti and 5-nm Cr adhesion layers. Other nano-hole arrays with a 10-nm Ti adhesion layer were exposed to a Ti etchant to remove the Ti adhesion layer to some extent. The etching of these nano-hole arrays resulted in the appearance of the (1,0) resonance peak related to SP excitation from Pyrex-gold. Since some of the adhesion layer and the Pyrex substrate were etched, an undercut region was created between adjacent holes. The presence of the undercut region resulted a blue-shift of the (1, 0) resonance peak compared to nano-hole arrays that were in contact with the Pyrex substrate.

In both simulation and experimental results, it was observed that the (1, 0) resonance position red-shifted as the periodicity of hole increased for all adhesion layer compositions as well as for the etched 10-nm Ti adhesion layer. Furthermore, for a given periodicity, the (1, 0) resonance peak for the 5-nm Ti adhesion layer red-shifted when compared to the peak for the 5-nm Cr adhesion layer. The (1, 0) resonance peak for the etched 10-nm Ti adhesion layer blue-shifted in comparison with both 5-nm Cr and 5-nm Ti adhesion layer compositions. In the experiments, the average red-shift of the (1,0) resonance peaks for the 5-nm Cr and 5-nm Ti adhesion layers with respect to the resonance position of the etched 10-nm adhesion layer case were 79 nm and 106 nm for a given periodicity, respectively. The (1, 0) resonance position for 5-nm Ti adhesion layer case was red-shifted on average 27 nm compared to 5-nm Cr adhesion layer case. It was seen that the (1, 0) STMR was higher for a nano-hole array with 5-nm adhesion layer case than for a nano-hole array with 5-nm Cr adhesion layer. The lowest (1, 0) resonance bandwidth was observed for a nano-hole array with etched 10-nm Ti adhesion layer. The bandwidth was lower for a nano-hole array with a 5-nm Ti adhesion

layer versus a 5-nm Cr adhesion layer. Also, the (1, 0) resonance bandwidths were almost constant as periodicity of hole increased.

In the simulated structures, a localized high electric field was observed on the edge of the hole for all adhesion layers studied at the (1, 0) resonance wavelength. Also, it was seen that the localized electric field formed a dipole on the edges of the hole. The electric field intensity for each nano-hole array was measured based on the highest electric field intensity (hot-spot) at the edges of the holes. The highest electric field intensity was obtained for the nano-hole array with the etched 10-nm Ti adhesion layer. Also, the electric field was higher for the 5-nm Ti adhesion layer case compared to the 5-nm Cr adhesion layer case. The enhancement of the electric field intensity in the hot-spot of the etched 10-nm Ti adhesion layer was 34 and 98 times larger compared to the 5-nm Ti and the 5-nm Cr adhesion layer cases, respectively.

A nano-hole array with an etched adhesion layer was shown to have the lowest resonance bandwidth and the steepest resonance slope compared to the non-etched adhesion layer cases. As a result, the device could be used to simply improve the SPR sensitivity for detecting various bio-molecules and chemicals. Also, the enhanced electric field around and through a nano-hole, as observed for the etched adhesion layer at resonance wavelength, could potentially improve Raman signal in the SERS application. Based on all advantages of a nano-hole array with etched adhesion layer, I was inspired to investigate more about the undercutting and etched regions beneath the nano-hole arrays. As a result, my studies led me to a series of novel nano-structures with SP energy matching between the top and bottom of the nano-hole array structure as described in chapters 4 through 6.

7.3. Novel plasmonic sub-wavelength structures

The SP energy matching of a sub-wavelength hole array in a metal film between its top and bottom surfaces occurs when materials with the same dielectric constant are used at top and bottom of the metal film. The SP energy matching between two surfaces of a sub-wavelength hole array results in 10-fold resonance transmission enhancement

and higher localized electric field intensity on a hole and through the hole at the resonance wavelength [7-3].

Generally, nano-hole arrays have been fabricated on solid substrates such as glass, quartz, Pyrex, polymer, SU8, or so forth due to the delicacy of the thin metal. Therefore, matching the dielectric properties of the top and bottom surfaces of the nano-hole array in the metal film has been limited to materials with dielectric properties similar to the substrate that can be deposited on to the film. Also, each of the index matching approaches to fabrication may have one or more limitations. Furthermore, with current fabrication methodologies it is not possible to dynamically change the material below the metal film due to the presence of the substrate material. For example, the resonance peaks from top side of sub-wavelength hole arrays can be tuned by selecting a top side material with an appropriate refractive index. However, the resonances from the substrate side cannot be changed. Therefore, in order to match the resonances with the same mode from both the top and bottom side of a sub-wavelength hole array, one would have to select a material with the same refractive index as the substrate for deposition on top of the sub-wavelength hole array in order to gain high transmission at the resonance peaks. Some materials like gases, such as air, have a refractive index close to one and there is no suitable substrate material available with a similar refractive index. Therefore, refractive index matching may not be readily accomplished for a wide range of materials using current sub-wavelength hole array fabrication methodologies. In chapter 4 through chapter 6, novel nano-structures were presented, which provided dynamically index-matching condition between top and bottom of the nano-hole array surfaces to allow flowing of any type of liquids and gases as well as isotropic deposition of solid materials [7-4]-[**Error! Reference source not found.**].

In chapter 4, a novel nano-hole array structure in an optically thick gold film was presented. The structure contained a cavity beneath each nano-hole, thereby contributing to the SP energy matching between top and bottom surfaces of the gold film. The nano-hole arrays in a gold film with various periodicities (360-nm, 370-nm, 380-nm, and 390-nm) were fabricated by EBL/lift-off fabrication method, using Ti conductive and adhesion layers in the fabrication process. In order to create a cavity underneath

each hole within the substrate layer that also penetrated through both the adhesion layer and the conduction layer, isotropic wet-etching was employed.

The (1,0) resonance of nano-hole arrays without and with cavities were evaluated in bulk SPR sensing application in order to demonstrate the superior performance of nano-hole arrays with cavities. For bulk SPR sensing, the optical transmission of a nano-hole array was measured when liquids of various refractive indexes were deposited on the top surface of the nano-hole array. In the transmission spectra of both nano-hole arrays without and with cavities, two optical resonance peaks related to (1,0) and (1,1) SP excitation modes were observed. For the nano-hole array with cavities, the liquid dielectric materials penetrated into the holes and the cavities, resulting in the same index of refraction above, within, and below each hole. The index matching capability of the nano-hole array with cavities resulted in greater transmission at and nearby (1,0) resonance compared to the one without cavities. Furthermore, resonance peaks related to the Pyrex-gold side were not observed, while for the device lacking the cavities a small (1,0) resonance related to Pyrex-gold side resulted in significant overlap in transmission spectra for the various refractive index liquids. This overlap decreased SPR sensing performance dramatically as the different liquid dielectric materials were not distinguishable.

The ratio between the (1, 0) resonance transmission and its corresponding transmission minimum (Wood's Anomaly) were computed for various refractive indices for both nano-hole arrays with and without cavities. The nano-hole array with cavities performed with higher dynamic range. The ratio of the peak to the minimum was quantitatively much higher for the nano-hole array with cavities compared to the nano-hole array without cavities. As the refractive index of the dielectric material was decreased, the performance improvement increased from 1.5-times at an index of 1.58 to 7-times at an index of 1.43. The sensitivity of the (1,0) resonance peak for the novel nano-hole array structure with various periodicities and the sensitivity was measured using dielectric materials of refractive index within the range of 1.43 to 1.58. Almost 2-fold higher sensitivity was obtained for the nano-hole arrays with cavities compared to the device lacking cavities. The lower sensitivity of the device without cavities could be

due to the existence of the (1, 0) resonance peak related to Pyrex-gold side, which interfered with the (1,0) resonance peak from the other side of the film. The sensitivity of the (1, 0) resonance peak for nano-hole arrays with cavities increased with the periodicity of the holes. However, the device lacking the cavity showed almost no change in sensitivity for different periodicities. Also, a wide bandwidth of the (1,0) resonance peaks reduced the sensitivity of nano-hole arrays without cavities. The differential transmission intensity for nano-hole arrays lacking the cavities at 632 nm wavelength (maximum difference) and nano-hole arrays with cavities at 686 nm wavelength (maximum difference) for various refractive indexes were extracted. A linear relationship was observed for the differential transmission intensity with respect to the refractive index for nano-hole arrays. However, the nano-hole array with the cavities showed a higher difference with respect to the reference point (1.58 refractive index). For example, 2.3 times higher differential intensity was obtained for the nano-hole array with cavities, at 1.43 refractive index, when compared to the nano-hole array lacking cavities. Also, a large variation of differential intensity was observed for the nano-hole arrays with cavities of about 2.8 times higher compared to the nano-hole arrays lacking the cavities.

The novel nano-hole array with cavities presented in Chapter 4 can be fabricated at a large scale and can maintain its structural integrity without breakage or bending. However, the structure does not provide perfect SP energy matching between the top and bottom of the film due to existence of the substrate close to the gold film in regions between holes. As a result, a nano-hole array structure with no connection to the substrate could potentially provide a perfect SP energy match between the top and bottom surfaces of the metal film. That is, a free standing nano-hole array film (membrane) with a cavity depth larger than the SP decay length could provide for the perfect SP matching condition.

Therefore, in chapter 5, I considered a novel nano-hole array structure consisting of a large cavity beneath the nano-hole array structure and above the Pyrex substrate. The large cavity of the novel structure provided the SP energy matching between top and bottom of the nano-hole array surfaces. It also provided for a much larger cavity

which could facilitate faster flow of bio-molecules to the bottom side of the array from the top side. However, a nano-scale cavity depth between the nano-hole array structure and the Pyrex substrate changes the SP energy matching properties. Therefore, the effect of cavity depth on optical resonance position was investigated experimentally. Also, devices fabricated with the smallest and largest cavity depths were tested in the bulk SPR sensing application.

To enable accurate depth of the cavity beneath the gold film, a sacrificial Ti layer was deposited on the Pyrex substrate prior to fabrication of the nano-hole array by EBL. Then, after nano-hole array fabrication, a titanium etchant (TFTN, Transene company, Inc.) was employed to etch the sacrificial layer in the vicinity of the nano-holes, which resulted in a large cavity between the gold film and the substrate. The nano-hole arrays were fabricated on Ti sacrificial layers with different thicknesses (5 nm, 50 nm, 100 nm, 200 nm, and 350 nm) resulting in well-controlled cavity depths after the wet-etching process.

The measured transmission spectra of nano-hole arrays revealed that the nano-hole array with 5-nm cavity depth had two optical resonance peaks, which were related to the (1,0) and (1,1) SP excitation modes of the substrate-gold side. However, the nano-hole array with a 350-nm cavity depth had only one resonance peak (i.e. (1, 0) resonance) due to coincidence of the SP modes on both sides of the gold film. Coincidence of the SP modes for the nano-hole array with the 350-nm cavity depth resulted in a significant blue-shift of the resonance position with respect to the one with the 5-nm cavity depth. The blue-shift in (1, 0) resonance was simply due to the lower refractive index of air ($n = 1$) relative to the Pyrex substrate ($n = 1.474$). Also, the (1, 0) resonance positions as a function of cavity depth demonstrated that the effect of the Pyrex substrate on the (1, 0) resonance of structures with cavity depths greater than 100 nm was considerably reduced.

The bulk SPR sensing experiments for nano-hole arrays with 5-nm and 350-nm cavity depths were performed using bulk refractive index liquids ($n = 1.30, 1.33, 1.36,$ and 1.39) applied to the free surface. The optical resonances related to the (1,0) and (1,1) gold-free side and the substrate-gold side were observed for the nano-hole array

with a 5-nm cavity depth. However, only two resonances ((1,0) and (1,1)) were observed for the nano-hole array with the 350-nm cavity depth due to SP energy matching between the top and the bottom surface of metal film. The nano-hole array with the 350-nm cavity depth had lower bandwidth and marginally higher resonance transmission at the (1,0) resonance compared to the array with the 5-nm cavity depth. For each cavity depth, the bulk SPR sensitivity generally increased with periodicity. A nano-hole array with a 350-nm cavity depth had higher bulk SPR sensitivity than the one with a 5-nm cavity depth. The highest bulk SPR sensitivity was obtained for the nano-hole array with the largest periodicity and a 350-nm cavity depth and it was 1.6-fold higher than a similar one with a 5-nm cavity depth. The FOM was computed with respect to bulk SPR sensitivity over the resonance bandwidth. The FOM increased with periodicity. The highest FOM was obtained for structures with a 350-nm cavity depth. This resulted from the higher bulk SPR sensitivity and the lower resonance bandwidth. The array with the 350-nm cavity depth had an almost 3-fold higher FOM compared to a similar structure with a 5-nm cavity depth.

The SP energy matching of the novel nano-hole array structure demonstrated higher electric field intensity within and near the edges of the holes at the resonance wavelength of the structure. This effect could potentially enhance performance of the nano-hole array structures in various sensing applications. However, it was discovered that the localized electric field of the nano-hole array could be further enhanced by interaction of the hole with plasmonic particles. In chapter 6, the 3D plasmonic nano-structure was introduced. The structure had a nano-hole array with a cavity and benefitted from the localized SP interaction between holes and coregistered nano-disks located at the bottom of the cavity. For this structure, a new resonance peak appeared from the SP interaction of the holes and disks and provided a higher intensity electric field between the hole and disk compared to a separate hole structure. In order to study the effect of the geometrical parameters related to the 3D nanostructure on the new resonance peak properties, various plasmonic nano-structures were fabricated with different cavity depths, hole sizes and hole periodicities. Also, the 3D structures were simulated by FDTD for various cavity depths and hole sizes to compare results with the

experimental measurements as well as to investigate variations of electric field intensity at the new resonance peak between the holes and disks.

The EBL/liftoff fabrication process was employed to fabricate the nano-hole arrays on various Ti sacrificial layers. The wet-etching process was employed to remove the Ti sacrificial layer beneath the nano-hole array structure and form the nano-hole array with a large cavity beneath. Then, a 30-nm gold layer was deposited on the structure and resulted in 30-nm thick disks at the bottom of the cavity.

In the FDTD simulations, a new resonance peak associated with the LSP interaction between each hole and the associated nano-disk was observed when the cavity depth was 50 nm and 100 nm deep. The resonance was associated with the LSP interaction between the holes and disks since the resonance did not change with respect to periodicity of the 3D structure. As the cavity depth increased, the effect of the LSP coupling between holes and nano-disks decreased resulting in a reduced LSP resonance transmission efficiency. Also, the FDTD simulation results for the electric field in the structures at LSP resonance peak demonstrated that the LSP coupling between the holes and nano-disks were observed for the cavity depth less than a 200-nm. The structure with a 50-nm cavity depth had the highest electric field intensity between the nano-hole and nano-disk at the LSP resonance wavelength compared to the electric field intensity for structures with 100-nm and 150-nm cavity depths.

The relationship between the LSP resonance position was determined to be dependent on the hole and disk size based on the excellent agreement of simulation and experimental results. As the hole and disk diameters increased, the LSP resonance position red-shifted. This would be expected due to the localized SP property of the LSP resonance transmission peak. The simulation results demonstrated the LSP resonance was blue shifted as the distance between hole and disk increased. In the simulation results, a resonance peak related to LSP coupling between the nano-hole and nano-disk was observed as a function of incident angle of light and its resonance position did not depend on the incident angle of the light.

The SPR sensitivity of the LSP resonance of the 3D structure with the 100 nm cavity depth was ~215 nm/RIU and 220 nm/RIU for simulation and experimental results, respectively. However, the simulated SPR sensitivity for the 3D structure with a 50-nm cavity was ~550 nm/RIU. The higher sensitivity of the LSP resonance peak for the device with the 50 nm cavity could be due to the higher electric field intensity between holes and nano-disks.

7.4. Some simulation and fabrication constrains

Throughout this thesis, I have employed a numerical method based on Finite Domain Time Difference (FDTD) methodology in order to validate optical transmission spectra of metallic nano-structures measured from experiments. However, in a simulation model, many fabrication features and defects could not be easily simulated because it is limited to computing requirements for a whole structure. For example, one of the fabrication features could be surface roughness of a metal film that is dependent greatly on deposition methods. Also, a NHA structure fabricated by EBL fabrication process can produce non-uniform ridges on each hole, which is considered a fabrication defect. As a result, fabrication features and defects have changed the experimental results in the measured transmission spectra of a nano-structure compared to those of the simulation results. The changes are apparent as small discrepancies in the resonance transmission properties of a nanostructure between experimental and simulation results. For instance, one of the most prominent examples is that in a simulation model of a nano-hole array without any surface roughness and ridges around a hole, transmission resonances of a NHA have a narrow bandwidth compared to the measured experimental results. Therefore, due to this limitation, the aim of the FDTD simulation model in this thesis is to:

- 1) Validate presences of resonance transmissions of a nano-structure due to various SPP modes or LSP effects in experimental results, which both simulation and experimental results had an excellent agreement in this case throughout this thesis.
- 2) Observe effects of various geometrical parameters and material compositions on resonance transmission properties of a nano-structure (i.e. examining of increase or

decrease trends in resonance properties between simulation and experimental results).

- 3) Find resonance transmission properties for various incident angles of light.

The optical transmission spectra of nano-hole arrays fabricated with the same geometrical parameters and material compositions could be slightly different due to fabrication features and defects. For example, based on the study in this thesis, the optical resonance position of nano-hole arrays with the same structure and material composition for 16 cases were measured and their resonance position had ± 3 nm difference.

7.5. Future work

The plasmonic nano-hole arrays and 3D nano-structures presented in chapter 4 through chapter 6 were fabricated and developed to improve the sensitivity of bulk SPR sensing. However, they could potentially be used in various other applications such as SERS, non-linear optics, NSOM, and optical trapping. The use of a single nano-hole with a cavity, or with cavity and disk at the bottom of the cavity, could enhance the performance of many related single plasmonic hole applications. In addition, larger sub-wavelength structures (i.e. hole and periodicity at micron scale) could be fabricated for potential use in absorption spectroscopy in infrared regime.

A single nano-hole with a cavity either with or without a nano-disk at the bottom of the cavity could provide a higher enhancement in the electric field at the edges of the hole and through the hole compared to a single nano-hole without cavity. The presence of the cavity could potentially provide an enhancement for detecting a single fluorescent molecule as well as improving SERS signal for bio-molecules compared to a nano-hole lacking a cavity. Enhanced signal is expected due to the beneficial optical effects related to SP energy matching between the top and bottom of the single hole with a cavity.

A single C-shape nano-hole with a cavity in connection with a nano-tip could be employed as a tip for NSOM application. My hypothesis is that a C-shape hole with a cavity could provide a higher transmission at the LSP resonance compared to the one without cavity and it could potentially conduct the enhanced electric field from the hole to the top of the nano-tip. This could provide a higher electric field at the top of the nano-tip, which may result in higher resolution of detection.

A single nano-hole with a cavity and a nano-disk at the bottom of the cavity could have an application in optical trapping of nano-particles or bio-molecules. The localized intensified electric field of this structure between hole and disk is almost 100-fold higher compared to the structure without cavity and disk. As a result, my assumption is that a single hole with a cavity and a disk at the bottom of the cavity could provide a faster and stronger optical trapping of nano-particles and bio-molecules compared to the previous structures [7-6].

Nano-hole arrays with cavities either with or without disks are a good candidate to enhance the non-linear response such as SHG. For example, a nano-hole array with a cavity and disk at the bottom of the cavity could potentially generate a higher SHG signals compared to the structure lacking both cavity and disk. This is due to the fact that this structure has the highest localized electric field at its LSP resonance wavelength and benefits from its phase-matching condition between two sides of the hole and disk structure. As a result, an investigation on non-linear optical resonance of this structure would potentially lead to development of a novel non-linear structure, which might have many applications in the field of photonics.

A nano-hole array with cavities may be used as an electrically controlled optical filter by electrically biasing an electrically sensitive dielectric layer, such as a liquid crystal. Electrical biasing results in a change in the effective refractive index and thereby modifies the optical transmission and reflection properties of the device. The nano-hole array with cavities could provide better optical filtering and switching than the one without cavities because of a higher ratio between resonance transmission and Wood's anomaly.

7.6. Conclusions

Through the duration of this dissertation, multiple systematic studies on resonance transmission properties of a nano-hole array were described as well as several novel plasmonic nano-structures with higher transmission resonance properties were introduced. The major outcome of the dissertation was to introduce novel plasmonic nano-structures, which could provide a dynamic SP energy matching between top and bottom of the structure and their advancement was shown through bulk-SPR sensing applications.

In chapter 2, the dependency of resonance transmission properties of a nano-hole array on various geometrical parameters (i.e. hole size, hole shape and periodicity) were experimentally and numerically investigated. The resonance properties were not greatly dependent on the symmetrical hole shapes while both the hole size and periodicity changed the optical resonance properties significantly. Also, some differences observed between experimental and simulation results of resonance properties of the nano-hole arrays would be due to the existence of a thin adhesion layer used in this study.

Therefore, in chapter 3, the effects of an adhesion between gold and substrate on resonance properties of a nano-hole array were systematically studied by means of FDTD simulation and experiments. Both simulation and experimental results demonstrated that both thickness and composition of adhesion layer materials change the resonance properties of a nano-hole array. Moreover, a nano-hole array with an etched adhesion layer had a higher localized electric field at its resonance wavelength at the edges of a hole compared to nano-hole arrays with adhesion layers. Also, the lowest resonance bandwidth was observed for a nano-hole array with an etched adhesion layer.

In chapter 4, a novel nano-hole array structure was presented, which had a cavity beneath each nano-hole, thereby contributing to SP energy matching between the top and bottom of the nano-hole array structure. The novel device generated the same resonances from top and bottom of a nano-hole array for the same scattering mode. This

resulted in a higher resonance transmission of the structure and higher electric field intensity at the edges of the hole at the resonance wavelength. The novel devices were evaluated in bulk-SPR sensing applications and compared to the corresponding devices lacking cavities. The structure demonstrated a 2-fold enhancement at bulk SPR sensing and an approximately 3-fold improvement for the cases of resonance shift and differential transmission intensity, respectively.

In chapter 5, a finite nano-hole array structure with a large cavity on the substrate underneath the entire structure was introduced. The structure provided a near SP energy matching between top and bottom of the nano-hole array structure as well as a higher resonance transmission compared to the conventional nano-hole array. The effect of various cavity depths on resonance transmission properties of a nano-hole array with a cavity were investigated experimentally. The structures with the largest and smallest cavity depths were evaluated in bulk SPR sensing. The results demonstrated that the fabricated nano-hole array with the largest cavity depth had 3-fold improvement in FOM and 1.6-fold increase in SPR sensitivity over the nano-hole array with the smallest cavity depth.

In chapter 6, a novel 3D plasmonic nanostructure was presented, which demonstrated a new transmission resonance due to the strong localized SP property of the structure. The structure consisted of a nano-hole array with a large cavity and each nano-hole was co-registered to a nano-disk at the bottom of the cavity. The LSP resonance peak was due to the LSP coupling between each nano-hole and nano-disk. Therefore, the LSP resonance properties were investigated with respect to the hole size and distance between hole and disk by simulation and experimental procedures. The LSP resonance position and its transmission efficiency were dependent on the distance between hole and disk as well as its position was greatly dependent on the hole and disk size. The SPR sensitivity measurement of the LSP resonance of the 3D nano-structure with the smallest simulated distance between hole and disk revealed a higher SPR sensitivity compared to the resonance transmission of nano-hole arrays.

7.7. References

- 7-1. Najiminaini, M., Vasefi, F., Kaminska, B., & Carson, J. J. L. (2010). Experimental and numerical analysis on the optical resonance transmission properties of nano-hole arrays. *Optics Express*, 18(21), 22255-22270. Retrieved from <http://www.opticsexpress.org/abstract.cfm?URI=oe-18-21-22255>
- 7-2. Najiminaini, M., Vasefi, F., Kaminska, B., & Carson, J. J. L. (2011). Optical resonance transmission properties of nano-hole arrays in a gold film: Effect of adhesion layer. *Optics Express*, 19(27), 26186-26197. Retrieved from <http://www.opticsexpress.org/abstract.cfm?URI=oe-19-27-26186>
- 7-3. Krishnan, A., Thio, T., Kim, T. J., Lezec, H. J., Ebbesen, T. W., Wolff, P. A., Garcia-Vidal, F. J. (2001). Evanescently coupled resonance in surface plasmon enhanced transmission. *Optics Communications*, 200(1-6), 1-7. Retrieved from <http://www.sciencedirect.com/science/article/pii/S0030401801015589>
- 7-4. Najiminaini, M., Vasefi, F., Kaminska, B., & Carson, J. J. L. (2012). Nano-hole array structure with improved surface plasmon energy matching characteristics *Appl.Phys.Lett.*, 100(4). Retrieved from <http://dx.doi.org/10.1063/1.3679173>
- 7-5. Najiminaini, M., Vasefi, F., Kaminska, B., & Carson, J. J. L. (2012). Effect of surface plasmon energy matching on the sensing capability of metallic nano-hole arrays. *Applied Physics Letters*, 100(6), 063110-4. Retrieved from <http://dx.doi.org/10.1063/1.3683536>
- 7-6. Najiminaini, M., Vasefi, F., Kaminska, B., & Carson, J. J. L. (2012). A three-dimensional plasmonic nanostructure with extraordinary optical transmission. *Plasmonics*, 1-8. Retrieved from <http://dx.doi.org/10.1007/s11468-012-9378-9>
- 7-7. Juan, M. L., Gordon, R., Pang, Y., Eftekhari, F., & Quidant, R. (2009). Self-induced back-action optical trapping of dielectric nanoparticles. *Nat Phys*, 5(12), 915-919. Retrieved from <http://dx.doi.org/10.1038/nphys1422>

Appendices

Appendix A.

Experimental analysis of optical resonance transmission properties of sub-wavelength hole arrays in optically thick metal films⁶

Abstract

In this paper, we present detailed experimental analysis on the optical resonance transmission properties of nano-hole arrays in metallic films. Arrays of sub-wavelength holes with different periodicity (spacing between adjacent holes) in a square lattice arrangement were fabricated in optically thick metal films (Au, Ag, and Al) on a Pyrex substrate using Electron Beam Lithography. The optical transmission spectra of the nano-hole arrays were characterized in the visible and near infrared regime. The optical resonance transmission properties were observed to depend on the type of metal film and the periodicity in the lattice arrangement.

Introduction

Surface plasmons (SP)s result from the oscillation of free electrons, which occurs at the interface of a metal and a dielectric. Surface plasmons have been harnessed to build novel nano-optical devices [A1]. For periodic sub-wavelength holes in an optically thick metal film, light can be transmitted and the phenomenon of extraordinary optical transmission (EOT) can occur in defined spectral ranges [A2] [A3]. EOT occurs above the cut-off wavelength of the holes, which it is not predicted by Bethe aperture theory [A3]. This is due to the coupling of the light to SP on one side of the metal film, which passes through the sub-wavelength holes to reach to the other side. Finally, the light decouples from the SP on the other side of metal and is radiated to free space. The EOT of sub-wavelength holes fabricated in metal films has been used in many applications such as near field scanning optical microscopy (NSOM), and surface enhanced fluorescent spectroscopy [A4]-[A6].

The EOT of nano-hole arrays in a metal film was first described by Ebbesen in 1998 [A3]. Ebbesen discovered that the EOT properties depend highly on the material properties of the

⁶ The following chapter is published in Proc. Of SPIE, 7911, 791117 (2011) under the co-authorship of Fartash Vasefi, Bozena Kaminska, and Jeffery J.L. Carson. Retrieved from <http://dx.doi.org/10.1117/12.876027>

Copyright 2012 Society of Photo Optical Instrumentation Engineers. One print or electronic copy may be made for personal use only. Systematic electronic or print reproduction and distribution, duplication of any material in this paper for a fee or for commercial purposes, or modification of the content of the paper are prohibited.

metal and dielectric, and the hole arrangement. The fundamental equation was derived for EOT position of a square hole lattice arrangement:

$$\lambda_{max} \cong \frac{a_0}{\sqrt{i^2 + j^2}} \sqrt{\frac{\epsilon_m \epsilon_d}{\epsilon_m + \epsilon_d}} \quad \text{A-1}$$

,where a_0 is the periodicity of holes, ϵ_d and ϵ_m are the dielectric constants of the incident medium (at the top or bottom surface of the nano-hole) and the metal films, and i and j are integers expressing the scattering mode indices [A2].

Several studies have investigated the effect of various materials and geometrical parameters on the optical resonance peaks of nano-hole arrays [A7]-[A11]. It has been shown that nano-hole arrays fabricated in the noble metals such as Ag, Au, and Cu have better EOT than nano-hole arrays in a perfect conductor [A8]. In both numerical and experimental analysis, nanohole arrays in Cu and Au films with the same geometrical parameters showed approximately the same (1,0) optical resonance position for the glass-metal side. The corresponding resonance position for nano-hole arrays in an Ag film was lower with respect to nano-hole arrays in Cu and Au metal films. Nano-hole arrays in Al film had lower transmittance in the EOT compared to the noble metals [A8] [A9]. Taken together these experimental studies have provided basic insight into the effects of the selection of the metal film material on the EOT properties of nano-hole arrays. Here we report a systematic study on the effect of the metal film material on nano-hole array optical transmission. We further report the effect of the metal film material on the (1,1) optical resonance peak, Wood's anomaly, and resonances from both the Pyrex-gold and air-gold sides of the array. We fabricated large nano-hole arrays in a square lattice arrangement in various metal films (Au, Ag, and Al). An optical transmission spectrum of each nano-hole array was measured in the visible and near infrared region using transmission optical spectroscopy. The (1,0) and (1,1) optical resonance peaks related to SP excitation from the Pyrex-gold side were analyzed for each nano-hole array with respect to the optical resonance position, spectral transmission modulation ratio (STMR) and the optical resonance bandwidth.

Methods

Fabrication process of nano-hole arrays

Electron beam lithography (EBL) was used to fabricate nano-hole arrays in various optically thick metal films (Ag, Al, or Au). Briefly, a 3 nm chromium conductive layer was deposited on the Pyrex substrate in order to make the substrate surface conductive for the EBL writing process. A 500 nm negative tone photo-resist was spin-coated on to the sample and followed by a soft-bake process. The nano-hole array patterns were then written using the EBL machine. Afterward, the sample was developed in order to leave behind the pillars of the photo-resist. Before metal deposition, a thin 5 nm chromium adhesion layer was deposited, although no adhesion layer was used for Al and Ag. Metal deposition was then performed and resulted in 100 nm Au, 100 nm Ag, or 100 nm Al. Finally, the pillars of the photo-resist were lifted off to leave behind the nano-hole arrays in the metal films. Additional details of the fabrication methodology have been published elsewhere [A7].

Six (6) nano-hole arrays were fabricated with 150 nm square hole shape and various periodicities in a square lattice arrangement in each metal film (Ag, Al, and Au). The periodicities were 350 nm, 375 nm, 400 nm, 425 nm, 450 nm, and 475 nm. These periodicities were selected so that

the (1,0) and (1,1) optical resonance peaks of the nano-hole arrays from Pyrex-gold side were in the visible and near-infrared regime. The number of holes in each array was 150 by 150. A SEM image of a portion of one nano-hole array is shown in Figure A-1.

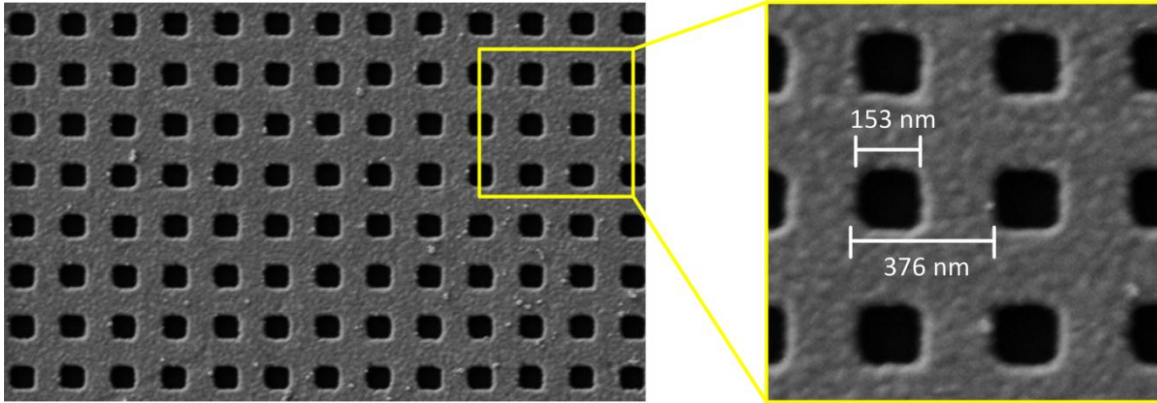


Figure A-1. SEM images of a nano-hole array in a 100 nm gold film

Optical characterization setup

We used optical transmission spectroscopy in order to characterize each nano-hole array. The optical characterization system was equipped with an inverted microscope attached to a photometer, monochromator, and photo-multiplier tube detector. More details about the characterization setup can be found elsewhere [A7]. In order to obtain spectral transmission of each nano-hole array, the optical transmission spectra were collected from the region comprising the nano-hole array (sample), a hole-free region (background) and metal-free region (Pyrex). The background spectrum was subtracted from the sample spectrum and divided by the Pyrex spectrum (white light spectrum).

Analysis of the optical resonance peaks

The optical resonance peaks related to the (1,0) and (1,1) SP excitation modes from the Pyrex-gold side were analyzed for each nano-hole array. Three properties were extracted from each optical resonance peak: the optical resonance position (resonance wavelength), STMR, and the optical resonance bandwidth. The STMRs of the (1,0) and (1,1) resonance peaks were calculated using the relations:

$$STMR_{(1,0)} = \frac{T_{(1,0)max} - T_{(1,0)min}}{T_{(1,0)max} + T_{(1,0)min}} \quad A-2$$

and

$$STMR_{(1,1)} = \frac{T_{(1,1)max} - T_{(1,0)min}}{T_{(1,1)max} + T_{(1,0)min}} \quad A-3$$

,where $T_{(1,0)max}$ represents the transmission of the (1,0) resonance peak, $T_{(1,0)min}$ represents the transmission of the (1,0) minimum, and $T_{(1,1)max}$ represents the transmission of the (1,1) resonance peak. The optical resonance bandwidth was computed as the full width of the optical resonance peak, where the optical transmission was $1/\sqrt{2}$ of the maximum.

Results and discussion

The optical transmission spectra for nano-hole arrays with 150 nm square hole shape and 425 nm periodicity in various 100 nm metal films (Ag, Al, and Au) are shown in Figure A-2. The two optical resonance peaks related to (1,0) and (1,1) SP excitation modes from Pyrex-gold side were observed for nano-hole arrays in Ag, Al, and Au thick films (indicated with the brown dashed lines in Figure A-2). In addition, the Wood's anomaly related to the (1,0) mode from Pyrex-gold side was observed between the (1,0) and (1,1) optical resonance peaks and shown with the green dashed line. For nano-hole arrays in Ag and Al films, another resonance peak was observed and indicated with orange dotted line. This optical resonance peak was related to the (1,0) SP excitation from air-metal side. The non-existence of the (1,0) resonance peak from the air-gold side was related to the occurrence of this resonance mode above the bulk plasma frequency of gold, which occurs at 588 THz (510 nm wavelength). As a result, most of the light above the plasma frequency was reflected and results in no excitation of the SP by the incident light in this regime. However, since the bulk plasma frequencies of Ag and Al are in the ultra-violet regime, all resonance peaks below the ultra-violet frequency were observed.

Although the appearance of the (1,0) and (1,1) optical resonance peaks for nano-hole arrays in various metal films were in the visible and near infra-red regime, measurable differences were observed. For example, the (1,0) optical resonance positions from Pyrex-metal side of nano-hole arrays were different at the 425 nm hole periodicity, which motivated us to study a wide range of hole periodicities for each metal film.

The (1,0) and (1,1) optical resonance positions related to SP excitation from the Pyrex-metal side were extracted from the optical transmission spectrum of each nano-hole array for each metal film case. The (1,0) and (1,1) resonance positions versus hole periodicity are shown in Figure A-3 (a) and (b), respectively. Both (1,0) and (1,1) resonance peaks were red-shifted as the periodicity of the holes increased, as predicted by equation (A-1). For a given periodicity, there were notable differences between the optical resonance positions of nano-hole arrays in the three metal films. At each periodicity, the (1,0) optical resonance peak positions were larger for nano-hole arrays in the 100 nm Ag film compared to the corresponding nano-hole arrays in the 100 nm Al or the Au film. The (1,0) optical resonance position for nano-hole arrays in the 100 nm Au film was larger than the corresponding position in the Al film at each periodicity. The (1,0) optical resonance position difference between nano-hole arrays in the Al and the Au films, and nano-hole arrays in the Ag film became smaller at higher periodicities. The reduced difference was more significant between Ag and Au, which could be due to the similar dielectric constant properties of Ag and Au film at higher wavelengths.

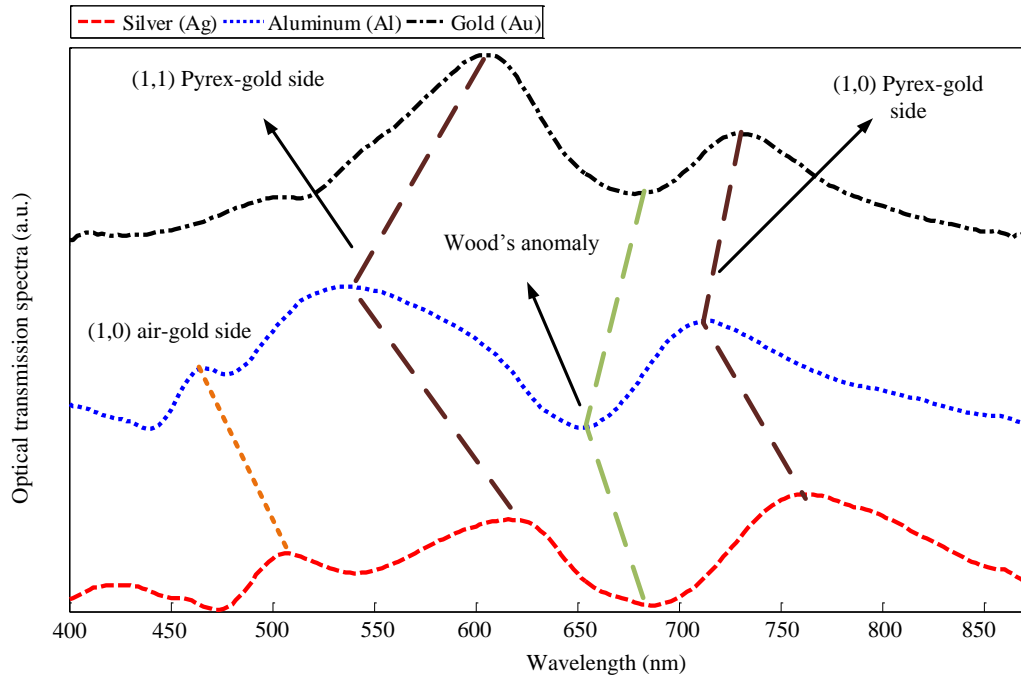


Figure A-2. *Optical transmission spectra of nano-hole arrays with 150 nm square hole shape and 425 nm periodicity in various 100 nm thick metal films. Red curve represents the nano-hole array in 100 nm silver (Ag), blue curve represents the nano-hole array in 100 nm aluminum (Al), and black curve represents the nano-hole array in 100 nm gold (Au). The transmission spectra for Al and Ag cases were shifted vertically for clarity.*

Previously, it has been reported that the (1,0) optical resonance position of nano-hole arrays in a gold film was slightly higher than the corresponding (1,0) resonance peak position of nano-hole arrays in a Ag film [A8]. This could be due to the difference in fabrication process between the previous work and our experiments. We used a 3 nm chromium conductive and a 5 nm Cr adhesion layer for the EBL fabrication of nano-hole arrays in a 100 nm gold film, while a 3 nm Cr conductive layer was used for the fabrication of nano-hole arrays in Ag and Al films. In the previous work [A8], the fabrication of each nano-hole array was performed with focused ion beam (FIB) milling, which required no conductive layer. Therefore, the existence of additional material layers between the substrate and metal film could potentially account for the differences between the two sets of results.

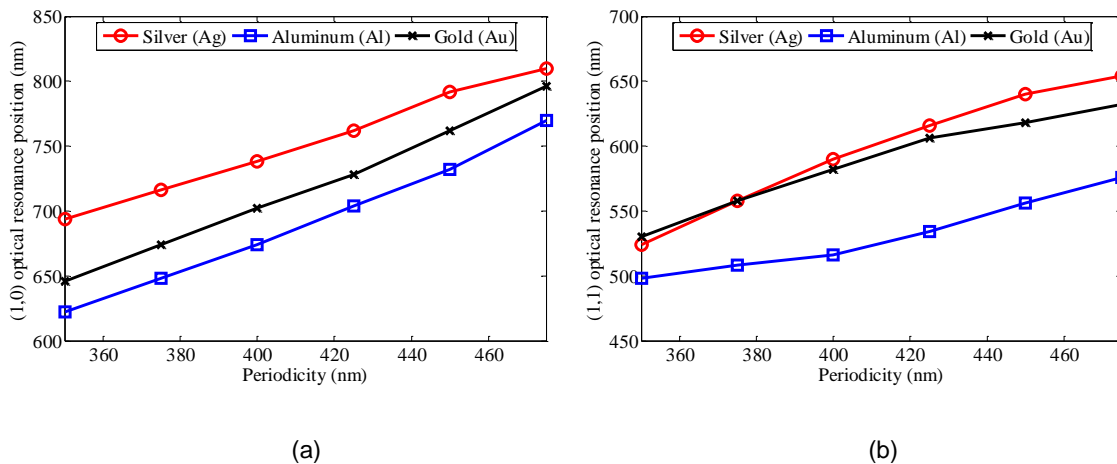


Figure A-3. (a) The (1,0) optical resonance position versus hole periodicity for nano-hole arrays in various metal films and (b) the (1,1) optical resonance position versus hole periodicity for nano-hole arrays in various metal films. The red, blue, black curves represent the Ag, Al, and Au, respectively.

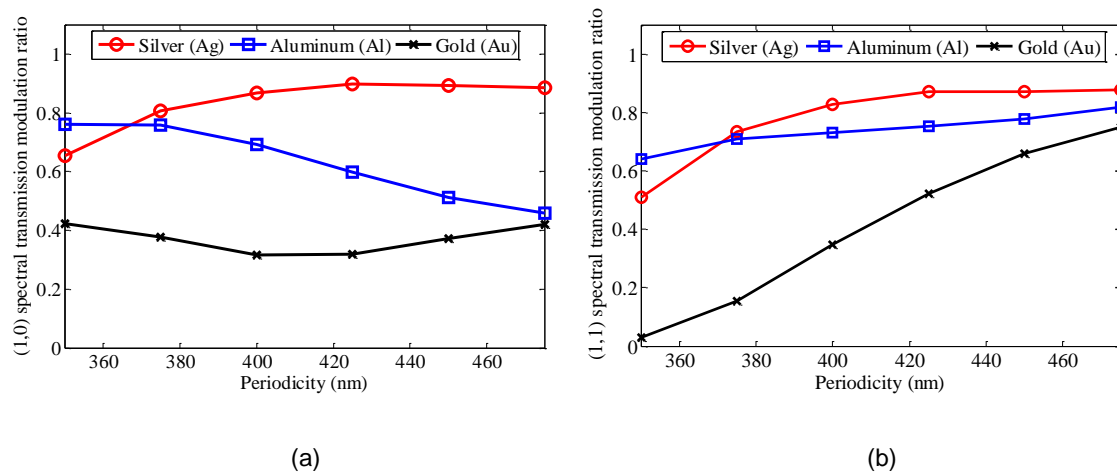


Figure A-4. (a) The (1,0) spectral transmission modulation ratio versus hole periodicity for nano-hole arrays in various metal films and (b) the (1,1) spectral transmission modulation ratio versus hole periodicity for nano-hole arrays in various metal films. The red, blue, black curves represent the Ag, Al, and Au, respectively.

The (1,1) optical resonance position of nano-hole arrays in Ag and Au films behaved in a similar manner to the (1,0) optical resonance position, although the differences between the resonance positions became more obvious at higher periodicities. For a given periodicity, the nano-hole arrays in a 100 Al film had the lowest (1,1) optical resonance position compared to the two other metals. Also, the (1,1) optical resonance position difference between Al, Au, and the Ag samples were larger at higher periodicities.

For each nano-hole array, the (1,0) and (1,1) STMR values were computed and are shown in Figure A-4 (a) and Figure A-4 (b), respectively. The (1,0) STMR increased for nano-hole arrays in the Ag film as periodicity increased then reached a plateau at higher periodicities, whereas the (1,0) STMR decreased monotonically for the nano-hole arrays in the Al film. The (1,0) STMR remained approximately constant for nano-hole arrays in the 100 nm gold film. For nano-hole arrays in the Ag film, the (1,0) STMR values were greater than the corresponding STMR values for the Al and Au cases, except at the 350 nm periodicity. However, the (1,0) STMR values for nano-hole arrays in the Au film were much lower than the corresponding STMR values for nano-hole arrays in Al and Ag films. This was likely due to the presence of the 5 nm chromium adhesion layer between the gold and the Pyrex substrate. The significant reduction in the STMR values for the resonance peaks from Pyrex-gold side were likely due to the high optical absorption properties of chromium. A greater (1,0) STMR value would be expected for nano-hole arrays in the gold film if the adhesion layer were absent. The reduction of the (1,0) STMR of nano-hole arrays in a 100 nm Al film for higher periodicities was likely due to the higher optical absorption properties of Al at longer wavelengths.

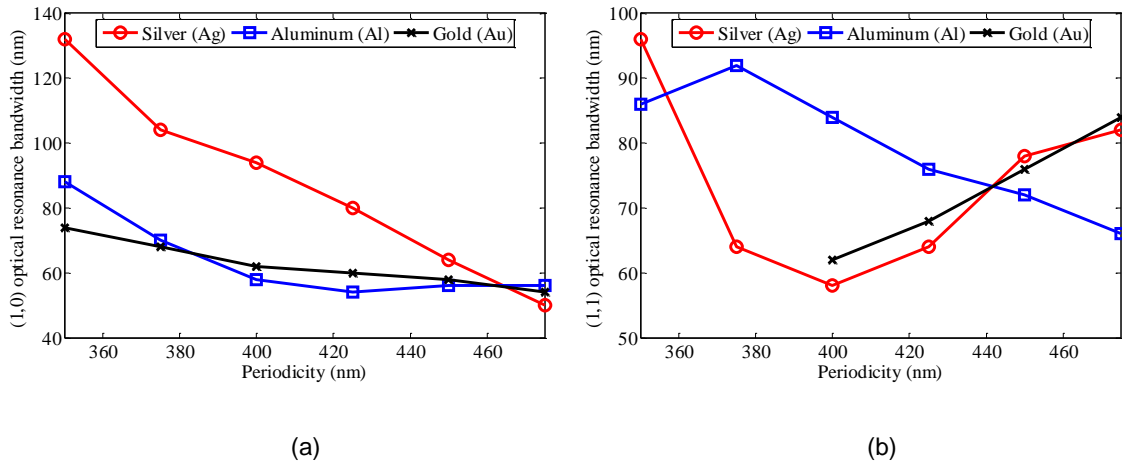


Figure A-5. (a) The (1,0) optical resonance bandwidth versus hole periodicity for nano-hole arrays in various metal films and (b) The (1,1) optical resonance bandwidth versus hole periodicity for nano-hole arrays in various metal films. The red, blue, black curves represent the Ag, Al, and Au metal films, respectively.

As periodicity of the holes increased, the (1,1) STMR value of nano-hole arrays in the various metal films increased. The (1,1) STMR of nano-hole arrays in the Ag film had the highest values compared to the corresponding STMR values from nano-hole arrays in the Al and the Au films for a given periodicity, except for 350 nm periodicity. However, due to the existence of the chromium

adhesion layer for nano-hole arrays in a 100 nm gold film, the lowest (1,1) STMR values were obtained. The (1,1) STMR for nano-hole arrays in the Al film had high values and this was likely due to the lower absorption properties of aluminum in this optical regime (500 nm to 580 nm).

The (1,0) and (1,1) optical resonance bandwidths versus hole periodicity are shown in Figure A-5 (a) and (b), respectively. The (1,0) optical resonance bandwidth decreased as periodicity of hole increased for nano-hole arrays in the Ag and the Au films. However, the (1,0) optical resonance bandwidth for nano-hole arrays in the Al film displayed a decreasing trend at lower periodicities that changed to an increasing trend at higher periodicities. Also, the effect of the ratio of the hole area to background area (periodicity) appeared to play a major role in the (1,0) optical resonance bandwidth. According to the ratio effect, the (1,0) optical resonance bandwidth was expected to decrease as periodicity of holes increased. For a given periodicity, the (1,0) optical resonance bandwidth of nano-hole arrays with 350 nm to 450 nm periodicities had the largest bandwidth compared to the corresponding nano-hole arrays in the Al and the Ag films. However, all nano-hole arrays in various metal films had almost the same bandwidth at the 475 nm periodicity.

In previous studies, a large difference in the (1,0) optical resonance bandwidth between nano-hole arrays in Au and Ag films was not observed [A8] [A9]. We must conclude that the large difference in bandwidth between nano-hole arrays fabricated from these two metals in our work must be due to the effect of the 3 nm Cr conductive layer on the (1,0) optical resonance bandwidth. However, the nano-hole arrays fabricated in the Au film had a 5 nm adhesion layer, which was expected to broaden the bandwidth, which was not observed.

The (1,1) optical resonance bandwidth of nano-hole arrays in the Au film for 350 nm and 375 nm periodicities could not be quantified due to the small ratio between maximum and minimum. At the higher periodicities, the (1,1) resonance bandwidth was measurable and increased as the hole periodicity increased. A decreasing trend with increasing hole periodicity was observed for nano-hole arrays in the Al film, except for the 350 nm to 375 nm periodicities. The nano-hole arrays in the Ag film had similar (1,1) resonance bandwidth as the nano-hole arrays in the Au film from 400 nm to 475 nm; however, a decreasing trend was observed for nano-hole arrays in the Ag film from 350 nm to 400 nm hole periodicity.

Conclusions

We studied the optical resonance transmission properties of nano-hole arrays fabricated in metal films of different composition. Large nano-hole arrays for a range of hole periodicities (spacing between adjacent holes) in a square lattice arrangement were fabricated in the various optically thick metal films (Ag, Al, and Au) on a Pyrex substrate using Electron Beam Lithography (EBL). The optical transmission spectrum of each array was measured in the visible and near infrared region using optical transmission spectroscopy. The optical resonance peaks related to (1,0) and (1,1) SP excitation modes from the Pyrex side were analyzed with respect to the optical resonance position, spectral transmission modulation ratio (STMR) and the optical resonance bandwidth.

Analysis of the optical resonance peaks revealed that the nano-hole arrays in Ag film had higher (1,0) optical resonance position and wider (1,0) optical resonance bandwidth compared to the corresponding nano-hole arrays in Au and Al films. Also, due to the existence of a 5 nm adhesion layer for nano-hole arrays in the gold film, the (1,0) and (1,1) STMR values were significantly reduced, which complicated comparison to the corresponding results from the Ag and Al films. Finally, we concluded that not only did the various metal films result in unique optical resonance peak properties for nano-hole arrays, but also that there was a significant influence of the conductive and adhesion layers on the optical transmission properties of the nano-hole arrays.

Acknowledgments

The authors thank Dr. Todd Simpson for his support and help in Nanofab Laboratory at University of Western Ontario (UWO). This project was funded by grants from the Natural Sciences and Engineering Research Council of Canada (NSERC) to Dr. Bozena Kaminska and Dr. Jeffery J.L. Carson. Fartash Vasefi was supported by a London Regional Cancer Program Translational Breast Cancer Research Trainee Fellowship.

References

- A1. Barnes, W. L., Dereux, A., & Ebbesen, T. W. (2003). Surface plasmon subwavelength optics. *Nature*, 424(6950), 824-830. Retrieved from <http://dx.doi.org/10.1038/nature01937>
- A2. Thio, T., Ghaemi, H. F., Lezec, H. J., Wolff, P. A., & Ebbesen, T. W. (1999). Surface-plasmon-enhanced transmission through hole arrays in cr films. *Journal of the Optical Society of America B*, 16(10), 1743-1748. Retrieved from <http://josab.osa.org/abstract.cfm?URI=josab-16-10-1743>
- A3. Ebbesen, T. W., Lezec, H. J., Ghaemi, H. F., Thio, T., & Wolff, P. A. (1998). Extraordinary optical transmission through sub-wavelength hole arrays. *Nature*, 391(6668), 667-669. Retrieved from <http://dx.doi.org/10.1038/35570>
- A4. Gordon, R., Brolo, A. G., Sinton, D., & Kavanagh, K. L. (2010). *Resonant optical transmission through hole-arrays in metal films: Physics and applications* - WILEY-VCH Verlag. doi:- 10.1002/lpor.200810079
- A5. Brolo, A. G., Kwok, S. C., Moffitt, M. G., Gordon, R., Riordon, J., & Kavanagh, K. L. (2005). Enhanced fluorescence from arrays of nanoholes in a gold film. *Journal of the American Chemical Society*, 127(42), 14936-14941. doi:10.1021/ja0548687
- A6. Lakowicz, J. R., Chowdury, M. H., Ray, K., Zhang, J., Fu, Y., Badugu, R., & Geddes, C. D. (2006). Plasmon-controlled fluorescence: A new detection technology. *Proc. of SPIE*, 6099(1) 609909-15. Retrieved from <http://dx.doi.org/10.1117/12.673106>
- A7. Najiminaini, M., Vasefi, F., Kaminska, B., & Carson, J. J. L. (2010). Experimental and numerical analysis on the optical resonance transmission properties of nano-hole arrays. *Optics Express*, 18(21), 22255-22270. Retrieved from <http://www.opticsexpress.org/abstract.cfm?URI=oe-18-21-22255>
- A8. Przybilla, F., Degiron A., Laluet J-Y., Genet C. & Ebbesen, T. W. (2006). Optical transmission in perforated noble and transition metal films. *Journal of Optics A: Pure and Applied Optics*, 8(5) 458. Retrieved from <http://stacks.iop.org.proxy.lib.sfu.ca/1464-4258/8/i=5/a=015>

- A9. Rodrigo, S. G., García-Vidal, F. J., & Martín-Moreno, L. (2008). Influence of material properties on extraordinary optical transmission through hole arrays. *Physical Review B*, 77(7), 075401. Retrieved from <http://dx.doi.org.proxy.lib.sfu.ca/10.1103/PhysRevB.77.075401>
- A10. Shuford, K. L., Ratner, M. A., Gray, S. K., & Schatz, G. C. (2006). Finite-difference time-domain studies of light transmission through nanohole structures. *Applied Physics B: Lasers and Optics*, 84(1), 11-18. Retrieved from <http://dx.doi.org/10.1007/s00340-006-2218-x>
- A11. Krishnan, A., Thio, T., Kim, T. J., Lezec, H. J., Ebbesen, T. W., Wolff, P. A., & Garcia-Vidal, F. J. (2001). Evanescently coupled resonance in surface plasmon enhanced transmission. *Optics Communications*, 200(1-6), 1-7. Retrieved from <http://www.sciencedirect.com/science/article/pii/S0030401801015589>

Appendix B.

Effect of adhesion layer on optical resonance transmission properties of nano-hole arrays in an optically thick gold film⁷

Abstract

In this paper, we present experimental analysis on the effect of composition of the adhesion layer (chromium or titanium) between gold and a Pyrex substrate on the optical resonance transmission properties of nano-hole arrays in an optically thick gold film. Nano-hole arrays of different hole periodicities in a square lattice arrangement were fabricated with three types of adhesion layer (5 nm Cr, 5 nm Ti or 10 nm Ti). The optical transmission of each nano-hole array was measured and the optical resonance transmission properties were analyzed and compared as a function of hole periodicity and type of adhesion layer.

Introduction

Periodic sub-wavelength holes fabricated in an optically thick metal film results in extraordinary optical transmission (EOT) phenomena [B1] [B2]. This unique property surpasses the diffraction limit of light and results from surface plasmon (SP) excitation between the surfaces of the metal and dielectric. The excitation of SP happens due to the momentum matching between the SP and the light on account of the periodic arrangement of the nano-holes [B2]. This results in the coupling of the light to the SP and resonant transmission through the nano-hole array. Finally, the light decouples from SP and radiates to free space. The EOT or optical resonance transmission of nano-hole arrays have been exploited in many applications such as enhanced surface raman scattering (SERS), bio-sensing, and chemical sensing [B3]-[B5].

The optical resonance transmission properties of nano-hole arrays depend greatly on geometrical parameters of hole, hole arrangements, and dielectric constants of the metal and surrounding dielectrics. For normal incidence of light, the spectral position of the optical transmission maximum and its corresponding minimum of a nano-hole array in a square lattice arrangement are:

⁷ The following chapter is published in Proc. Of SPIE, 7911, 791118 (2011) under the co-authorship of Fartash Vasefi, Bozena Kaminska, and Jeffery J.L. Carson. Retrieved from <http://dx.doi.org/10.1117/12.876056>

Copyright 2012 Society of Photo Optical Instrumentation Engineers. One print or electronic copy may be made for personal use only. Systematic electronic or print reproduction and distribution, duplication of any material in this paper for a fee or for commercial purposes, or modification of the content of the paper are prohibited.

$$\lambda_{\max} \cong \frac{a_0}{\sqrt{i^2 + j^2}} \sqrt{\frac{\epsilon_m \epsilon_d}{\epsilon_m + \epsilon_d}} \quad \text{B-1}$$

and

$$\lambda_{\min} \cong \frac{a_0}{\sqrt{i^2 + j^2}} \sqrt{\epsilon_d} \quad \text{B-2}$$

,where a_0 is the periodicity of holes, ϵ_d and ϵ_m are the dielectric constants of the incident medium (at the top or bottom surface of the nano-hole) and the metal film, and i and j are integers expressing the scattering mode indices [B1] [B2]. Many studies have investigated the effect of the geometrical parameters of nano-hole arrays in various metal films [B6]-[B9]. For instance, the optical resonant transmission peaks for nano-hole arrays in noble metal films such as Au, Ag, and Cu were higher than the other metal films with the same geometrical parameters [B7]. Also, a higher optical resonant transmission efficiency of a nano-hole array can be obtained by matching the dielectric constant surrounding the back and front of nano-hole array in a metal, which results in coincidence of the SP energy on both sides of the metal film [B8].

Gold has been a common material for fabrication of nano-hole arrays for applications such as bio-sensing and chemical sensing due to the unreactive property of this material to oxygen and many other chemicals. Gold necessitates the need for a thin adhesion layer between the glass substrate and the gold film. Several studies have performed investigations on the influence of the adhesion layer on the optical properties of different plasmonic structures and its effect on the performance in different applications [B10]-[B15]. For instance, the resonance position of slit-ring resonators (SRR) was 20 nm red-shifted when a Ti adhesion layer was used [B11]. Also, the influence of the adhesion layer on the Short Range Surface Plasmon Polariton (SR-SPP) of bowtie antennae fabricated in a gold film was numerically computed and the quenching of the SR-SPP was observed in the case of Ti and Cr adhesion layers [B13]. According to the previous reported studies on adhesion layer effects, we were motivated to perform a systematic study on the effect of the adhesion layer on the optical resonance transmission properties of nano-hole arrays in a gold film.

We performed an experimental study and analysis on the optical resonance transmission properties of a series of nano-hole arrays fabricated in a gold film with various composition and thickness of adhesion layer. Five nano-hole arrays with various periodicities were fabricated for each adhesion layer case (5 nm Cr, 5 nm Ti, and 10 nm Ti). The geometrical parameters of nano-hole arrays were selected in a way that the optical resonance peaks from Pyrex-gold side were in the visible and near infra-red regime. All nano-hole arrays were characterized using optical transmission spectroscopy. Finally, the optical resonance peaks related to (1,0) and (1,1) SP excitation from the Pyrex-gold side were analyzed with respect to resonance wavelength (position), spectral transmission modulation ratio (STMR) and optical resonance bandwidth for each adhesion layer case.

Methods

Fabrication process of nano-hole arrays

During the EBL fabrication process of nano-hole arrays in an optically thick gold film, two additional layers need to be deposited: 1) a conductive layer and 2) an adhesion layer. First, we deposited a 3 nm chromium or 3 nm titanium conductive layer on to the Pyrex substrate to enable focusing of the electron beam used to write the pattern. After deposition, a 500 nm negative tone photo-resist was spin-coated and soft-baked on the sample. The pattern of the nano-hole array was written with the EBL machine and followed by sample development to leave behind the pillars of photo-resist. Before deposition of the 100 nm gold film, a thin adhesion layer (the same material type used for the conductive layer) was deposited on the sample and followed by gold deposition. Finally, the pillars of photo-resist covered with gold were lifted off to leave behind the nano-hole array in the gold film.

We fabricated nano-hole arrays with various thickness and material types for the adhesion layer (5 nm chromium, 5 nm titanium, or 10 nm titanium). The geometrical designs of nano-hole arrays were selected in such a way that the optical resonance peaks related to the Pyrex-gold side of the nano-hole array were in the visible and near infrared regime. Nano-hole arrays with periodicity of 381 nm, 403 nm, 425 nm, 447 nm, and 469 nm were fabricated in a 100 nm gold film for each adhesion layer case. Also, the ratio between the hole area and the background area was constant between all nano-hole arrays. SEM images of a nano-hole array sample are shown in Figure B-1.

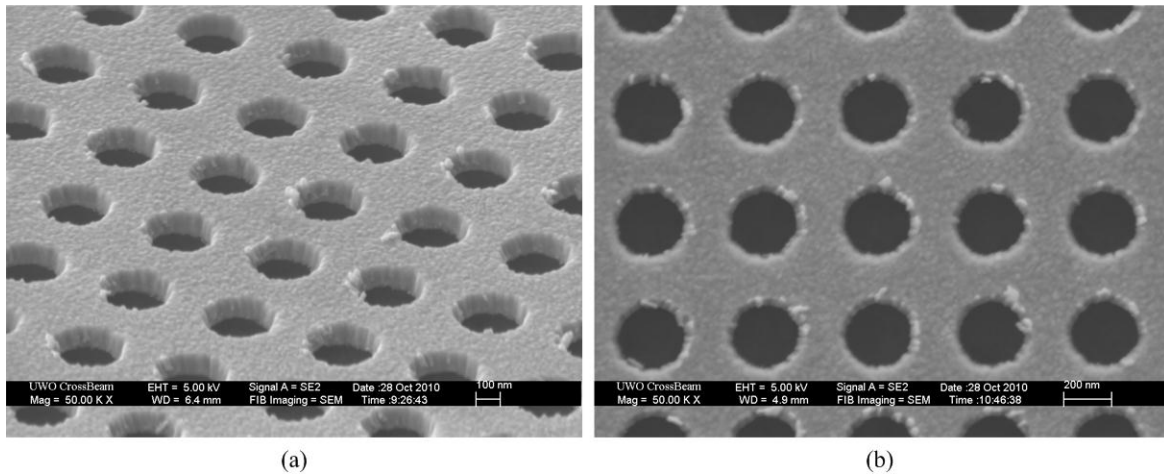


Figure B-1. SEM images of a nano-hole array in a 100 nm metal film (a) angle view and (b) top view

Optical characterization setup

We employed a standard inverted microscope (Nikon, TE300) connected to a photometer (PTI, D104), monochromator (PTI, 101), and photo-multiplier (PTI, 710) for the optical characterization of each nano-hole array. The bright-field condenser of the microscope was used to focus unpolarized white light on to the nano-hole array sample. The light transmitted through the nano-hole array was collected with an objective and directed to the photometer. Using the photometer,

a desired region of the nano-hole array sample was selected and guided to the monochromator for spectral characterization, and detection by the photo-multiplier tube. Spectral measurements of a nano-hole array region, a hole free region (gold with no holes), and the substrate (Pyrex only) were obtained for each device. Finally, the optical transmission spectra of each nano-hole array was computed by subtracting the light intensity of the hole free region from the light intensity from the nano-hole array region with the difference divided by the light intensity transmitted through the Pyrex substrate. More details about the optical characterization setup can be found in [B9].

Analysis of the optical resonance peaks

The optical resonance peaks related to (1,0) and (1,1) SP excitation mode from the Pyrex-gold side were examined for each nano-hole array. To analyze the optical resonance peak properties, three parameters were extracted from each (1,0) and (1,1) peak within each spectrum: the optical resonance position (resonance wavelength), STMR, and the optical resonance bandwidth. The STMRs of the (1,0) and (1,1) SP excitation mode were computed using the equations:

$$STMR_{(1,0)} = \frac{T_{(1,0)max} - T_{(1,0)min}}{T_{(1,0)max} + T_{(1,0)min}} \quad B-1$$

and

$$STMR_{(1,1)} = \frac{T_{(1,1)max} - T_{(1,1)min}}{T_{(1,1)max} + T_{(1,1)min}} \quad B-2$$

,where $T_{(1,0)max}$ was the transmission of the (1,0) resonance peak, $T_{(1,0)min}$ was the transmission of the (1,0) minimum and $T_{(1,1)max}$ was the transmission of the (1,1) resonance peak. The optical resonance bandwidth was the full width of the optical resonance peak, where the optical resonance transmission was $1/\sqrt{2}$ of the maximum.

Results and discussion

The optical transmission spectra of nano-hole arrays in a square lattice arrangement with circular hole shape, 223 nm hole diameter, 425 nm periodicity, and an adhesion layer of 5 nm chromium, 5 nm Titanium, or 10 nm Titanium are shown in Figure B-2. The (1,0) and (1,1) optical resonance transmission peaks related to the SP excitation modes from the Pyrex-gold side were clearly observed in the transmission spectra of nano-hole arrays with either 5 nm Cr or 5 nm Ti adhesion layers. Also, the (1,0) Wood's anomaly between the (1,0) and (1,1) optical resonance peaks from the Pyrex-gold side of nano-hole arrays with either the 5 nm Cr or the 5 nm Ti adhesion layers were present. Both the (1,0) and the (1,1) resonance peaks of nano-hole array with a 10 nm Ti adhesion layer were suppressed due to the higher absorption properties of the thicker layer of Ti. There were noticeable differences between the optical resonance peak properties of nano-hole arrays with 5 nm Cr and 5 nm Ti adhesion layers. For example, the (1,0) optical resonance position for the nano-hole array with 425 nm periodicity and a 5 nm Ti adhesion layer was red-shifted compared to the corresponding nano-hole array with the 5 nm Cr adhesion layer.

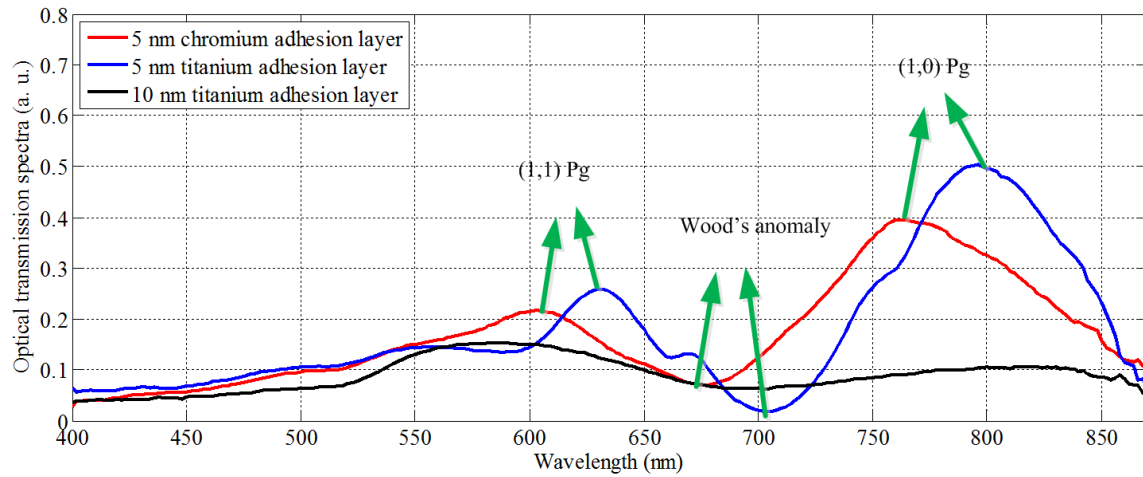


Figure B-2. *Optical transmission spectra of nano-hole arrays with circular hole shape, 223 nm diameter, and 425 nm periodicity in 100 nm thick gold film for a 5 nm Chromium (red curve), a 5 nm Titanium (blue curve), or a 10 nm Titanium (black curve) adhesion layer.*

The (1,0) and (1,1) optical resonance positions from the Pyrex-gold side of nano-hole arrays with a 5 nm Cr and a 5 nm Ti adhesion layer were extracted from the transmission spectra of each nano-hole array. The (1,0) and (1,1) optical resonance positions versus hole periodicity are shown in Figure B-3 (a) and (b), respectively. Both the (1,0) and the (1,1) optical resonance positions of nano-hole arrays with a 5 nm Cr or a 5 nm Titanium adhesion layer red-shifted with increasing periodicity. For a given periodicity, both the (1,0) and the (1,1) resonance positions for the nano-hole arrays with a 5 nm Ti adhesion layer showed higher optical resonance position compared to nano-hole arrays with a 5 nm Cr adhesion layer. For a specific periodicity, the (1,0) optical resonance position of nano-hole arrays with a 5 nm Ti adhesion layer was red-shifted 27 nm on average compared to the nano-hole arrays with a 5 nm Cr adhesion layer. Also, the (1,1) optical resonance peak for the 5 nm Ti adhesion layer group was 25 nm red-shifted on average compared to the 5 nm Cr adhesion layer group. However, the difference in the resonance peak position between nano-hole arrays with 5 nm Cr and 5 nm Ti adhesion layers became smaller as the hole periodicity increased.

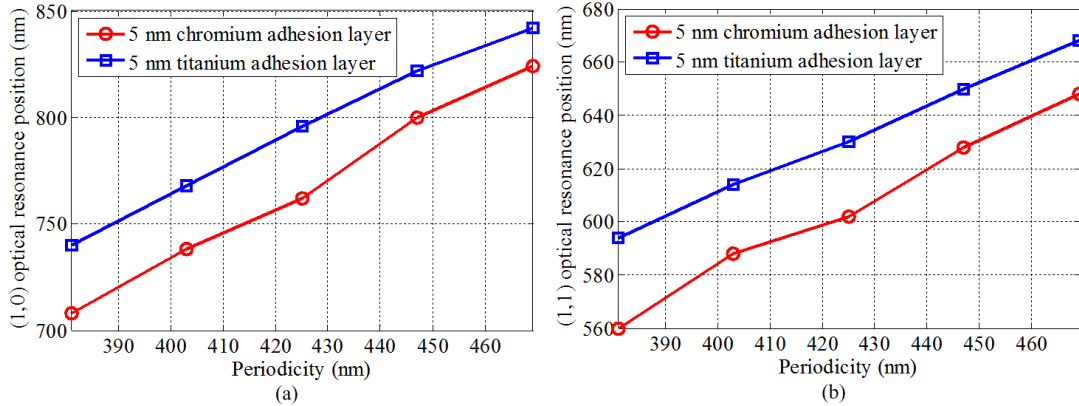


Figure B-3. The optical resonance positions versus hole periodicity for nano-hole arrays in 100 nm gold films with 5 nm chromium or 5 nm titanium adhesion layers: (a) (1,0) optical resonance position and (b) (1,1) optical resonance position.

The different absorption properties of Ti and Cr likely resulted in the observed differences in the (1,0) and (1,1) optical resonance positions between nano-hole arrays with Ti and Cr adhesion layers. Based on the dielectric constants of these materials, Cr has stronger optical absorption compared to Ti although the difference in absorption between Cr and Ti becomes lower at higher wavelengths. As a result, the optical resonance positions of nano-hole arrays with a 5 nm Ti adhesion layer became slightly closer to the corresponding resonance positions of nano-hole arrays with a 5 nm Cr adhesion layer at higher periodicities.

Figure B-4 displays the STMR versus nano-hole periodicity for nano-hole arrays with various adhesion layers for both the (1,0) and (1,1) resonance peaks from the Pyrex-gold side. For a given periodicity, the (1,0) STMR for nano-hole arrays with a 5 nm Ti adhesion layer was higher than the nano-hole arrays with a 5 nm Cr adhesion layer. The (1,0) STMR remained approximately constant as the periodicity increased for nano-hole arrays with either adhesion layer. However, the difference between the (1,0) STMR of nano-hole arrays with the 5 nm Ti versus 5 nm Cr adhesion layer was smaller at higher periodicities. This could have been due to the closer absorption properties of Ti and Cr at longer wavelengths. Similar results were obtained for the (1,1) STMR.; however, the values were smaller than those obtained for the (1,0) STMR.

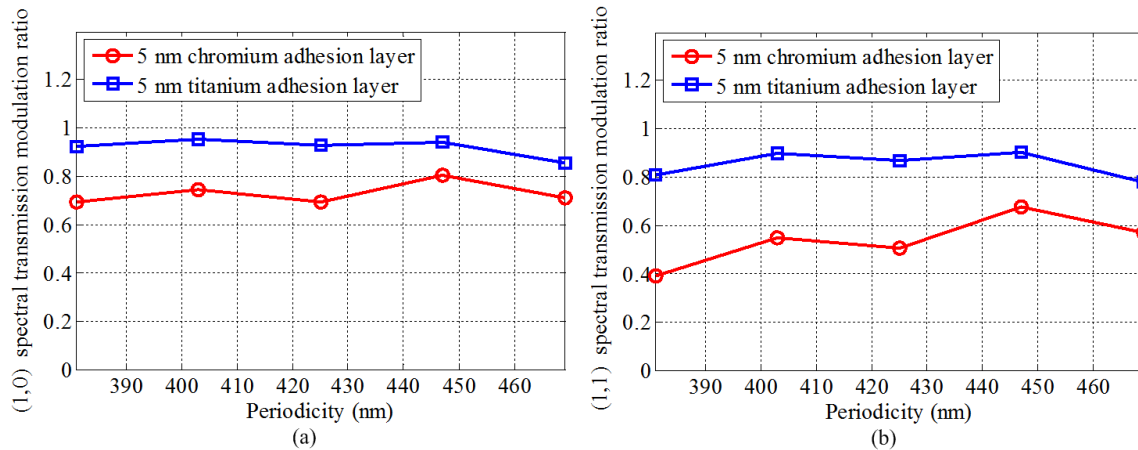


Figure B-4. *The spectral transmission modulation ratio (STMR) versus hole periodicity for nano-hole arrays in 100 nm gold films with a 5 nm chromium, or a 5 nm titanium adhesion layer: (a) (1,0) spectral transmission modulation ratio and (b) (1,1) spectral transmission modulation ratio.*

The (1,0) and (1,1) optical resonance bandwidth versus periodicity for nano-hole arrays with various adhesion layer materials are shown in Figure B-5 (a) and (b), respectively. For a given periodicity, the (1,0) optical resonance bandwidth was lower for nano-hole arrays with a 5 nm Ti adhesion layer than for nano-hole arrays with a 5 nm Cr adhesion layer. Due to the same ratio between hole area and background area of all nano-hole arrays, the (1,0) optical resonance bandwidths were expected to remain approximately constant for all nano-hole arrays. However, a slight decreasing trend of the (1,0) optical resonance bandwidth was observed as periodicity increased. At each periodicity tested, the (1,1) optical resonance bandwidth for nano-hole arrays with a Ti adhesion layer was generally lower than the corresponding measure for nano-hole arrays with a Cr adhesion layer. Also, the difference between the (1,1) optical resonance bandwidth of nano-hole arrays with a Ti versus a Cr adhesion layer was greatest at lower periodicities. The (1,1) optical resonance bandwidth was not measurable for the nano-hole array with a Ti adhesion layer and 381 nm periodicity due to the low ratio between the maximum and minimum. Generally, an uptrend in the (1,1) optical resonance bandwidth versus hole periodicity was observed for nano-hole arrays with a Ti adhesion, while a downward trend was observed for nano-hole arrays with a 5 nm Cr adhesion layer.

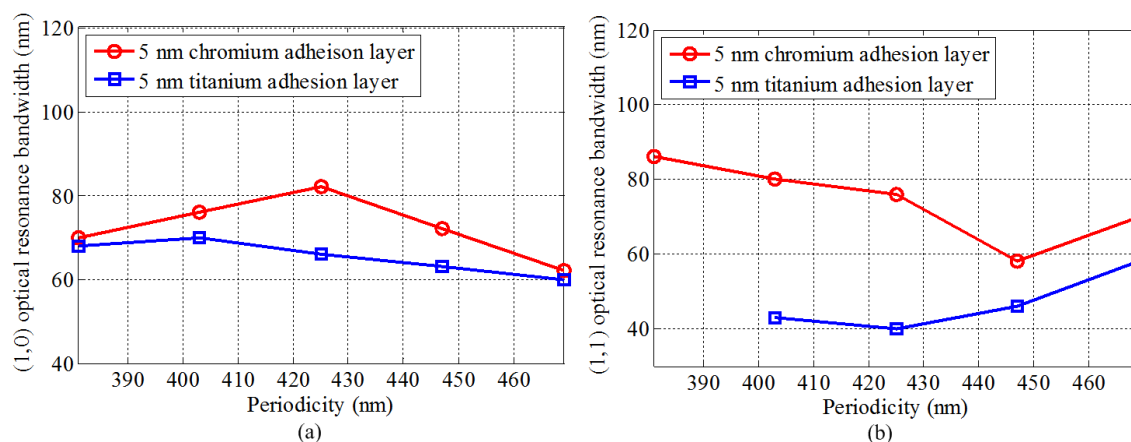


Figure B-5. *The optical resonance bandwidths versus hole periodicity for nano-hole arrays in 100 nm gold films with either a 5 nm chromium or a 5 nm titanium adhesion layer: (a) (1,0) optical resonance bandwidth and (b) (1,1) optical resonance bandwidth.*

Conclusions

In this study, we presented a systematic experimental study on the optical resonance transmission properties of nano-hole arrays in gold films when various compositions of adhesion layer materials between the Pyrex and the gold film were used. Large nano-hole arrays each with different hole periodicity were fabricated in gold films, but with different adhesion layers (5 nm chromium, 5 nm titanium, or 10 nm Titanium). The nano-hole arrays were characterized using optical transmission spectroscopy. The (1,0) and (1,1) optical resonance peaks from the Pyrex-gold side of each nano-hole array were analyzed with respect to resonance wavelength, spectral transmission modulation ratio, and optical resonance bandwidth. The experimental analyses revealed that the (1,0) and (1,1) optical resonance peaks of nano-hole arrays with a 5 nm Ti adhesion layer were red-shifted 27 nm and 25 nm on average, respectively, compared to the corresponding nano-hole arrays with a 5 nm Cr adhesion layer. Also, a larger STMR and smaller optical resonance bandwidth were observed for nano-hole arrays with the 5 nm Ti adhesion layer. The optical resonance transmission properties for nano-hole arrays with a Cr and a Ti adhesion layer were less different for devices with higher periodicities, which was likely due to the similar optical absorption properties of Ti and Cr at longer wavelengths.

Acknowledgements

The authors thank Dr. Todd Simpson for his support and help in Nanofab Laboratory at University of Western Ontario (UWO). This project was funded by grants from the Natural Sciences and Engineering Research Council of Canada (NSERC) to Dr. Bozena Kaminska and Dr. Jeffery J.L. Carson. Fartash Vasefi was supported by a London Regional Cancer Program Translational Breast Cancer Research Trainee Fellowship.

References

- B1. Ebbesen, T. W., Lezec, H. J., Ghaemi, H. F., Thio, T., & Wolff, P. A. (1998). Extraordinary optical transmission through sub-wavelength hole arrays. *Nature*, 391(6668), 667-669. Retrieved from <http://dx.doi.org/10.1038/35570>
- B2. Thio, T., Ghaemi, H. F., Lezec, H. J., Wolff, P. A., & Ebbesen, T. W. (1999). Surface-plasmon-enhanced transmission through hole arrays in cr films. *Journal of the Optical Society of America B*, 16(10), 1743-1748. Retrieved from <http://josab.osa.org/abstract.cfm?URI=josab-16-10-1743>
- B3. Gordon, R., Brolo, A. G., Sinton, D., & Kavanagh, K. L. (2010) *Resonant optical transmission through hole-arrays in metal films: Physics and applications* - WILEY-VCH Verlag. doi:- 10.1002/lpor.200810079
- B4. Brolo, A. G., Kwok, S. C., Moffitt, M. G., Gordon, R., Riordon, J., & Kavanagh, K. L. (2005). Enhanced fluorescence from arrays of nanoholes in a gold film. *Journal of the American Chemical Society*, 127(42), 14936-14941. doi:10.1021/ja0548687
- B5. Lesuffleur, A., Im, H., Lindquist, N. C., Lim, K. S., & Oh, S. (2008). Laser-illuminated nanohole arrays for multiplex plasmonic microarray sensing. *Optics Express*, 16(1), 219-224. Retrieved from <http://www.opticsexpress.org/abstract.cfm?URI=oe-16-1-219>
- B6. Rodrigo, S. G., García-Vidal, F. J., & Martín-Moreno, L. (2008). Influence of material properties on extraordinary optical transmission through hole arrays. *Physical Review B*, 77(7), 075401. Retrieved from <http://dx.doi.org.proxy.lib.sfu.ca/10.1103/PhysRevB.77.075401>
- B7. Przybilla F., Degiron A., Laluet J-Y., Genet C. & Ebbesen, T.W. (2006). Optical transmission in perforated noble and transition metal films. *Journal of Optics A: Pure and Applied Optics*, 8(5) 458. Retrieved from <http://stacks.iop.org.proxy.lib.sfu.ca/1464-4258/8/i=5/a=015>
- B8. Krishnan, A., Thio, T., Kim, T. J., Lezec, H. J., Ebbesen, T. W., Wolff, P. A., Garcia-Vidal, F. J. (2001). Evanescently coupled resonance in surface plasmon enhanced transmission. *Optics Communications*, 200(1-6), 1-7. Retrieved from <http://www.sciencedirect.com/science/article/pii/S0030401801015589>
- B9. Najiminaini, M., Vasefi, F., Kaminska, B., & Carson, J. J. L. (2010). Experimental and numerical analysis on the optical resonance transmission properties of nano-hole arrays. *Optics Express*, 18(21), 22255-22270. Retrieved from <http://www.opticsexpress.org/abstract.cfm?URI=oe-18-21-22255>

- B10. Chen, X., Pan, M., & Jiang, K. (2010). Sensitivity enhancement of SPR biosensor by improving surface quality of glass slides. *Microelectronic Engineering*, 87(5), 790-792. Retrieved from <http://www.sciencedirect.com/science/article/pii/S0167931709007564>
- B11. Lahiri, B., Dylewicz, R., Rue, D. L., & Johnson, N. P. (2010). Impact of titanium adhesion layers on the response of arrays of metallic split-ring resonators (SRRs). *Optics Express*, 18(11), 11202-11208. Retrieved from <http://www.opticsexpress.org/abstract.cfm?URI=oe-18-11-11202>
- B12. Aouani, H., Wenger, J., Gerard, D., Rigneault, H., Devaux, E., Ebbesen, T. W., Blair, S. (2009). Crucial role of the adhesion layer on the plasmonic fluorescence enhancement. *ACS Nano*, 3(7), 2043-2048. doi:10.1021/nn900460t
- B13. Jiao, X., Goeckeritz, J., Blair, S., & Oldham, M. (2009). Localization of near-field resonances in bowtie antennae: Influence of adhesion layers. *Plasmonics*, 4(1), 37-50. Retrieved from <http://dx.doi.org/10.1007/s11468-008-9075-x>
- B14. Sexton, B. A., Feltis, B. N., & Davis, T. J. (2008). Characterisation of gold surface plasmon resonance sensor substrates. *Sensors and Actuators A: Physical*, 141(2), 471-475. Retrieved from <http://www.sciencedirect.com/science/article/pii/S0924424707007273>
- B15. Pan, J., Pafchek, R. M., Judd, F. F., & Baxter, J. B. (2006). Effect of Chromium–Gold and Titanium–Titanium Nitride–Platinum–Gold metallization on Wire/Ribbon bondability. *IEEE Transactions on Advanced Packaging*, 29, 707.

Appendix C.

Surface plasmon resonance sensing using index-matched metallic nano-hole array structures⁸

Abstract

We present a novel three-dimensional nano-hole array structure in an optically thick gold film, which benefits from Surface Plasmon (SP) energy matching between the top and bottom of the gold film. We have experimentally evaluated both a conventional and an SP energy-matched nano-hole array structure for Surface Plasmon Resonance (SPR) sensing. Also, detection of various bulk refractive index liquids has been tested for both structures based on the transmission intensity differences in a narrow detection band. We observed a 2-fold higher sensitivity during SPR sensing with the new structure compared to a conventional nano-hole array.

Introduction

An array of sub-wavelength holes in an opaque metal film exhibits Extraordinary Optical Transmission (EOT) and this unexpected phenomenon results from a coupling of incident light to surface plasmons (SPs), where an oscillation of free electrons occur at the interfaces between metal and dielectrics [C1] [C2]. The SP-coupled light from one side of the metal film evanescently transfers through the holes, radiates to free space from other side of the metal film and cause EOTs or resonances in the visible and near infrared regions of the electromagnetic spectrum [C3]. The resonance properties of nano-hole arrays have given a rise to many photonic applications such as Surface Plasmon Resonance (SPR) sensing and Surface Enhanced Raman Spectroscopy (SERS) [C4]-[C5]. The EOT properties (e.g. resonance wavelength) of nano-hole arrays depend highly on the characteristics of dielectrics above and below the metal film [C6]. For example, a change in the composition of the dielectric material on top of the nano-hole array can be detected as a change in one or more optical parameters thereby providing a means to detect a variety of chemical and biological agents based on SPR sensing principles [C4].

⁸ The following chapter is published in Proc. Of SPIE, 8234, 82341N (2012) under the co-authorship of Fartash Vasefi, Bozena Kaminska, and Jeffery J.L. Carson. Retrieved from <http://dx.doi.org/10.1117/12.909723>

Copyright 2012 Society of Photo Optical Instrumentation Engineers. One print or electronic copy may be made for personal use only. Systematic electronic or print reproduction and distribution, duplication of any material in this paper for a fee or for commercial purposes, or modification of the content of the paper are prohibited.

For SPR sensing applications, the optical and physical characteristics of nano-hole arrays enable device miniaturization, integration into microfluidic structures, and multiplexed analysis in contrast to the conventional Kretschmann configuration and colloidal nano-particles [C7]. The optical transmission of nano-hole arrays can be easily controlled by hole shape, hole size, spacing between holes and lattice arrangement of the holes [C8] [C9]. Nano-hole arrays with various geometrical parameters can be fabricated on a single substrate, which can provide various optical responses from different nano-hole arrays for a specific analyte [C10]. Many numerical and experimental studies have been performed to investigate and improve SPR sensing characteristics of nano-hole arrays [C11]-[C17]. Also, an analytical expression was developed for describing the SPR sensitivity of a nano-hole array in terms of the resonance shift with respect to a refractive index unit (RIU) for illumination that is normal to the nano-hole array surface [C14]:

$$S = \frac{\Delta\lambda}{\Delta n} = \lambda \frac{\varepsilon_m}{n(n^2 + \varepsilon_m)} = \frac{p}{\sqrt{i^2 + j^2}} \sqrt{\left(\frac{\varepsilon_m}{n^2 + \varepsilon_m}\right)^3} \quad \text{C-1}$$

,where λ is wavelength, p is periodicity between holes, i and j define the scattering order of the holes (i.e. resonance modes), ε_m and n are the permittivity of the metal and refractive index of the dielectric. The SPR sensitivity depends significantly on the periodicity of holes and the resonance modes. For example, a low resonance mode of a nano-hole array (e.g. (1,0) resonance mode) with a large periodicity can significantly increase the SPR sensitivity of a nano-hole array. In addition to the dependence of SPR sensitivity on the geometry of the nano-hole array, it has been demonstrated that a nano-hole array with a sharp-apex double hole enhanced the SPR sensitivity over that of a device with separate holes [C11]. Also, an enhanced SPR sensitivity and a reduced bandwidth were observed for a nano-hole array fabricated with a lift-off free fabrication method [C13]. In another study, nano-hole arrays fabricated on fluoropolymer substrate (FEP) enhanced the sensing performance for biological solutions by 20% due to the similar refractive indexes between the substrate and the solution [C16].

A nano-hole array with materials of the same dielectric constant on the top and bottom of the metal film benefits from SP energy matching and results in 10-fold enhancement in its EOT [C6] [C16]. However, current fabrication methods have limited SP matching to top-side materials that have the same dielectric constant as the bottom-side material. Hence, the dielectric properties of the bottom layer are usually fixed and matched over a very narrow range of refractive index [C16]. Here, we report on a novel nano-hole array structure that provides SP energy matching on the top and bottom of the perforated gold film. The new structure has a cavity beneath each nano-hole, thereby contributing to SP energy matching. We performed experimental analysis on this novel nanostructure and compared its SPR sensitivity to a nano-hole array without cavities (conventional nano-hole array).

Methods

EBL fabrication method

We used electron beam lithography (EBL) to fabricate nano-hole arrays in gold films on Pyrex substrates (Pyrex 7740 DSP; see Figure C-1 (a)) in combination with a lift-off process. First, a 3-nm Ti layer was deposited on to the Pyrex substrate to make its surface conductive for EBL writing (see Figure C-1 (b)) and followed by spin-coating of 500-nm negative tone photo-resist

(see Figure C-1 (c)). After a soft-baking process, the nano-hole array patterns were written on the photo-resist using the EBL system (LEO, 1530 e-beam lithography). The sample was developed leaving behind an array of periodic nano-pillars (see Figure C-1 (d)). Then, a 4-nm Ti adhesion layer was deposited and followed by 100-nm deposition of a gold film using electron beam deposition (see Figure C-1 (e)). Finally, the nano-pillars were lifted off and resulted in a nano-hole array in a gold film (see Figure C-1 (f)).

In order to create a cavity beneath each nano-hole, we used Ti etchant (TFT from Transient Inc.) for isotropic etching the Ti and Pyrex beneath each nano-hole (see Figure C-1 (g)). The nano-hole array sample was left for 30 sec in the etchant and resulted in 100-nm deep cavities and 285-nm undercutting between adjacent nano-holes. We fabricated a nano-hole array with 135-nm circular hole diameter and 360 nm periodicity in a square lattice arrangement in a 100 nm gold film without and with 100-nm deep cavities. Figure C-2 displays a SEM image of a nano-hole array with 100-nm deep cavities.

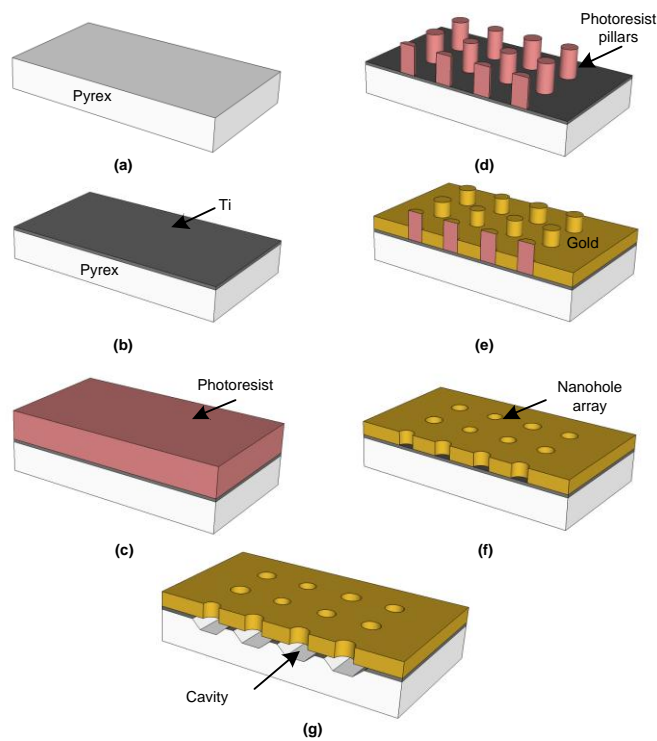


Figure C-1. EBL/lift-off fabrication process for a nano-hole array without and with cavities.

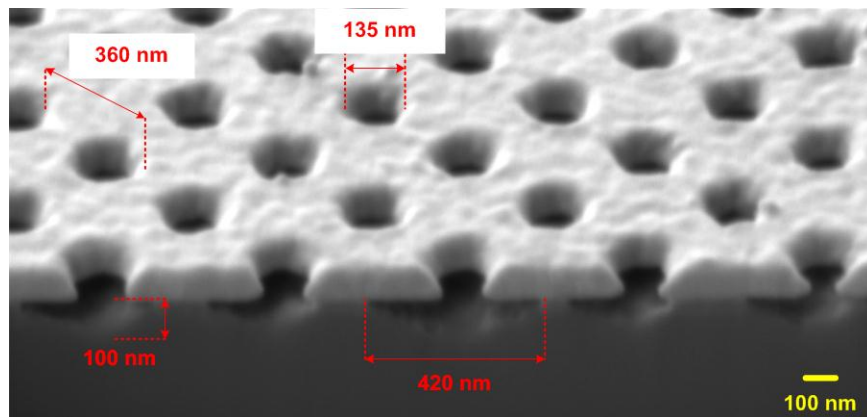


Figure C-2. *An SEM of a nano-hole array with 135-nm circular holes, 360-nm periodicity, and 100-nm deep cavities.*

Characterization setup

We used an optical transmission microscope (Nikon, TE300) with a photometer (PTI, D104) connected to a monochromator (PTI, 101) and a photo-multiplier detector (PTI, 710) for measuring the optical transmission spectrum of each nano-hole array. Unpolarized and collimated white light was employed to illuminate each nano-hole array using a bright field condenser. The light transmitted through the sample was collected with a 20X objective (NA = 0.45; Nikon, 93150) and guided through the photometer to select the desired region. Then, the selected region was spectrally resolved by the monochromator and detected by the PMT at each wavelength band (bandwidth of the monochromator was ± 2 nm). The optical transmission spectra of each nano-hole array was computed by subtracting the system noise from the transmitted light through the nano-hole array and then dividing the difference by the light transmission through a bare Pyrex wafer.

Experimental method for SPR sensing

We measured the optical transmission of a nano-hole array when liquids of well-known refractive index (Cargill Inc., Cedar Grove, USA) were deposited on to the top surface of the nano-hole array. The refractive index liquids (between 1.43 and 1.58) were selected close to the refractive index of the Pyrex-substrate ($n=1.474$) in order to provide the optimum SPR sensing performance for nano-hole arrays without cavities. Also, we employed an FCS2 Closed Chamber System (Bioptechs Inc., Butler, PA, U.S.A) to flow through refractive index liquids on top of the nano-hole array structure for real-time SPR sensing of the liquids based on light transmission intensity variations through the nano-hole array at a single wavelength band.

Results and discussion

Figure C-3 (a) and (b) display optical transmission spectra of a nano-hole array with 135 nm circular hole diameter and 360 nm periodicity for the case without and with 100-nm deep cavities, respectively. The panels also display the optical transmission spectra obtained when various refractive index liquids (1.43, 1.49, and 1.55) were deposited on top of the structures. In Figure C-3 (a), two optical resonance peaks related to (1, 0) and (1, 1) SP excitations were observed for

the nano-hole array without cavities. As well, Wood's Anomaly was present between the $\lambda_{(1,0)}$ and $\lambda_{(1,1)}$ resonance peaks. Since overall, the refractive index of the top and Pyrex side of the nano-hole array was similar at each condition, transmission enhancement was expected for the $\lambda_{(1,0)}$ and $\lambda_{(1,0)}$ resonance peaks across all wavelength bands. However, due to the constant refractive index of the Pyrex substrate, an overlap region between 660 nm and 720 nm in the transmission spectra (see Figure C-3 (a) the orange rectangle) was observed. In Figure C-3 (b), the $\lambda_{(1,0)}$ and $\lambda_{(1,1)}$ resonance peaks were observed for the nano-hole array with cavities. These resonances were associated with coincidence of the SP excitation modes from both sides of the nano-hole array, where SP matching between the top and bottom interfaces of the nano-hole array was present. The matching effect resulted from penetration of the refractive index liquid into cavities of the nano-hole array.

Higher resonance transmission intensity was achieved for the nano-hole array with cavities compared to the nano-hole array without cavities. This occurred due to the precise SP matching condition for the nano-hole array with cavities. The measured transmission intensity at the $\lambda_{(1,0)}$ resonance peak was 2-fold higher compared to the transmission intensity for the structure lacking cavities. Also, a lower transmission at the Wood's Anomaly was measured for the nano-hole array with cavities and resulted in a higher ratio of the $\lambda_{(1,0)}$ resonance transmission to the respective Wood's Anomaly. Hence, there was a steeper slope between the Wood's Anomaly and the $\lambda_{(1,0)}$ resonance peak, which facilitated better SPR sensitivity.

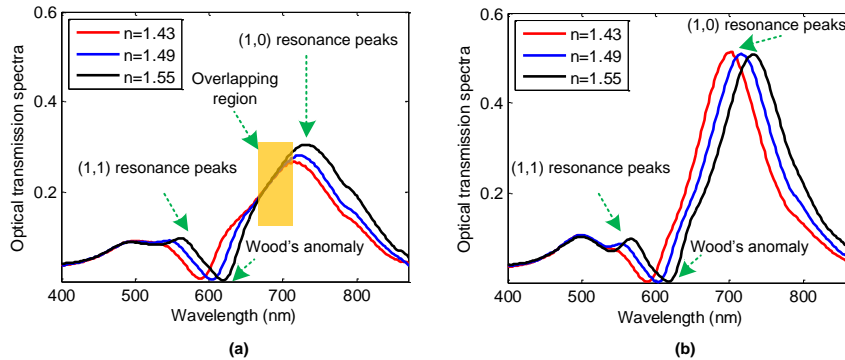


Figure C-3. Optical transmission spectra of the nano-hole array with 135 nm circular hole diameter, 360 nm periodicity in case of : (a) without cavities and (b) with cavities, when various refractive indexes (1.43, 1.49, and 1.55) were deposited.

Both the $\lambda_{(1,0)}$ and the $\lambda_{(1,1)}$ resonance peaks red-shifted as the refractive index increased for both structures without and with cavities. The measured SPR sensitivity for $\lambda_{(1,0)}$ resonance peak of the nano-hole array without and with cavities were 149 nm/RIU and 250 nm/RIU, respectively. The SPR sensitivity of $\lambda_{(1,0)}$ resonance peak was estimated at about 300 nm/RIU using equation C-1. The estimated result from equation C-1 was more accurate for the SPR sensitivity of the nano-hole array with cavities compared to the nano-hole array without cavities. The lower sensitivity of a nano-hole array without cavities was due to an interference of the $\lambda_{(1,0)}$ resonance peaks from top and bottom of a nano-hole arrays, which resulted in broadening of the bandwidth. The figure of merit (FOM) was computed based on the SPR sensitivity of $\lambda_{(1,0)}$ resonance peak

over the full width and half maximum (FWHM) of the bandwidth. The measured FOM for the $\lambda_{(1,0)}$ resonance peak of the nano-hole arrays without and with cavities was 1 and 2.5, respectively. The higher FOM of the nano-array with cavities was not only due to the higher SPR sensitivity but also due to the 40% smaller bandwidth compared to the structure without cavities.

SPR sensing with nano-hole arrays was accomplished via differential transmission intensity measurements using a narrow band illumination source. Figure C-4 (a) and (b) display the differential transmission spectra obtained with liquids of various refractive index for a nano-hole array without and with cavities, respectively. The differential transmission spectra were computed by subtracting the transmission spectrum obtained with a 1.58 refractive index liquid from the transmission spectrum obtained using a liquid of the indicated refractive index. As shown in Figure C-4 (a) and (b), the maximum differences were observed at 632 nm and 686 nm for the nano-hole array without and with cavities, respectively. A larger differential intensity was observed for the nano-hole array with cavities. Also, due to the existence of the $\lambda_{(1,0)}$ resonance peak from Pyrex-gold side for the nano-hole array without cavities, an overlapping region between differential transmission spectra obtained from liquids of various refractive index was observed (see Figure C-4 (a), orange rectangle). The differential transmission intensity for the nano-hole array without cavities at 632 nm (maximum difference (see Figure C-4 (a)) and the nano-hole array with cavities at 686 nm (maximum difference (see Figure C-4 (b)) was measured for a range of liquids of different refractive index. A near linear relationship was found for the differential transmission intensity with respect to refractive index for both the nano-hole array without and with cavities. However, the nano-hole array with cavities demonstrated an almost 3-fold greater variation compared to the nano-hole array without cavities.

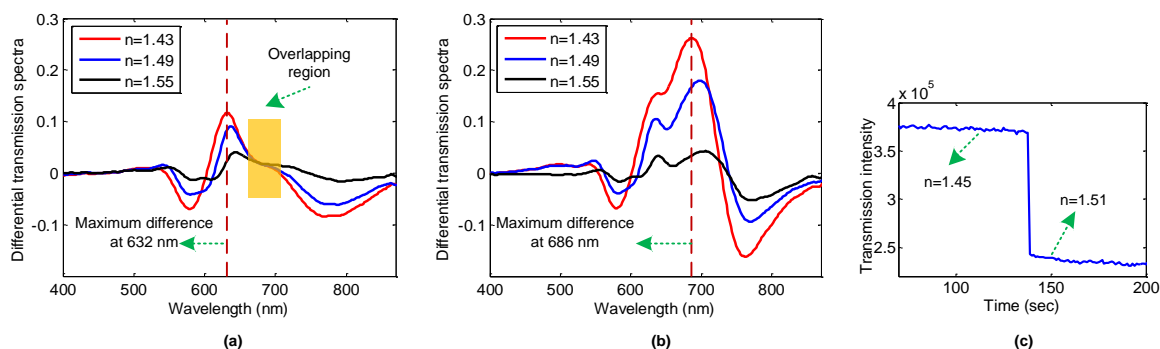


Figure C-4. *Differential transmission spectra of a nano-hole array with 135-nm circular hole diameter and 360-nm periodicity in case of (a) without cavities and (b) with cavities. Each differential spectrum illustrates the subtraction of the optical transmission spectrum (obtained with a liquid of refractive index of 1.58) from the optical transmission spectrum obtained for a liquid with the indicated refractive index, and (c) real-time transmission intensity from a nano-hole array with cavities when refractive index liquids of $n=1.45$ and $n=1.51$ were injected into the FCS2 closed chamber in sequence.*

We performed real-time SPR sensing for a nano-hole array with cavities using light transmission at 686 nm (at maximum difference (see Figure C-4 (b)) as the readout. Figure C-4 (c) illustrates transmission intensity variation for the nano-hole array with cavities at 686 nm wavelength versus

time when 1.45 and 1.51 refractive index liquids were injected in to the FCS2 closed chamber in sequence. The transmission intensity was reduced by 35% when $n=1.51$ refractive index liquid was injected into the chamber. Also, the transmission intensity changed rapidly during the injection then remained constant over an extended time. Taken together the results demonstrated that the liquid penetrated into the cavities.

Conclusions

In summary, we presented a three-dimensional nano-hole array structure, which contained a cavity beneath each nano-hole. This structure benefited from SP energy matching between its top and bottom interfaces and resulted in an enhanced transmission at the optical resonances. SPR sensing using the structure with cavities was evaluated against a similar structure without cavities. The results demonstrated that the nano-hole array with cavities had a 2-fold enhanced SPR sensitivity and 3-fold higher differential transmission intensity compared to the structure lacking cavities. Also, real-time SPR sensing with the nano-hole array with cavities was experimentally tested for with SP-matched condition and resulted in a sudden change in transmission intensity that coincided with the step change in refractive index of the liquid.

Acknowledgments

The authors would like to thank Dr. Todd Simpson for his support and help in Nanofab Laboratory of University of Western Ontario (UWO). This project was funded by grants from the Natural Sciences and Engineering Research Council of Canada (NSERC) to Dr. Bozena Kaminska and Dr. Jeffery J.L. Carson.

References

- C1. Ebbesen, T. W., Lezec, H. J., Ghaemi, H. F., Thio, T., & Wolff, P. A. (1998). Extraordinary optical transmission through sub-wavelength hole arrays. *Nature*, 391(6668), 667-669. Retrieved from <http://dx.doi.org/10.1038/35570>
- C2. Barnes, W. L., Dereux, A., & Ebbesen, T. W. (2003). Surface plasmon subwavelength optics. *Nature*, 424(6950), 824-830. Retrieved from <http://dx.doi.org/10.1038/nature01937>
- C3. Genet, C., & Ebbesen, T. W. (2007). Light in tiny holes. *Nature*, 445(7123), 39-46. doi:10.1038/nature05350
- C4. Im, H., Lesuffleur, A., Lindquist, N. C., & Oh, S. (2009). Plasmonic nanoholes in a multichannel microarray format for parallel kinetic assays and differential sensing. *Analytical Chemistry*, 81(8), 2854-2859. doi:10.1021/ac802276x
- C5. Lesuffleur, A., Kumar, L. K. S., Brolo, A. G., Kavanagh, K. L., & Gordon, R. (2007). Apex-enhanced raman spectroscopy using double-hole arrays in a gold film. *The Journal of Physical Chemistry C*, 111(6), 2347-2350. doi:10.1021/jp067677e

- C6. Krishnan, A., Thio, T., Kim, T. J., Lezec, H. J., Ebbesen, T. W., Wolff, P. A., Garcia-Vidal, F. J. (2001). Evanescently coupled resonance in surface plasmon enhanced transmission. *Optics Communications*, 200(1-6), 1-7. Retrieved from <http://www.sciencedirect.com/science/article/pii/S0030401801015589>
- C7. Sinton, D., Gordon, R., & Brolo, A. G. (2008). *Nanohole arrays in metal films as optofluidic elements: Progress and potential* - Springer Berlin / Heidelberg. doi:- 10.1007/s10404-007-0221-0
- C8. Cstis, G., Patoka, P., Wang, X., Kempa, K., & Giersig, M. (2007). Optical transmission through hexagonal arrays of subwavelength holes in thin metal films. *Nano Letters*, 7(9), 2926-2930. doi:10.1021/nl0712973
- C9. Przybilla, F., Degiron A., Laluet J-Y, Genet C., & Ebbesen T.W. (2006). Optical transmission in perforated noble and transition metal films. *Journal of Optics A: Pure and Applied Optics*, 8(5) 458. Retrieved from <http://stacks.iop.org.proxy.lib.sfu.ca/1464-4258/8/i=5/a=015>
- C10. Lindquist, N. C., Lesuffleur, A., Im, H., & Oh, S. (2009). Sub-micron resolution surface plasmon resonance imaging enabled by nanohole arrays with surrounding bragg mirrors for enhanced sensitivity and isolation. *Lab Chip*, 9(3), 382-387. Retrieved from <http://dx.doi.org/10.1039/B816735D>
- C11. Lesuffleur, A., Im, H., Lindquist, N. C., & Oh, S. (2007). Periodic nanohole arrays with shape-enhanced plasmon resonance as real-time biosensors. *Applied Physics Letters*, 90(24), 243110-3. Retrieved from <http://link.aip.org/link/?APL/90/243110/1>
- C12. Yanik, A. A., Huang, M., Artar, A., Chang, T., & Altug, H. (2010). Integrated nanoplasmonic-nanofluidic biosensors with targeted delivery of analytes. *Applied Physics Letters*, 96(2), 021101-3. Retrieved from <http://link.aip.org/link/?APL/96/021101/1>
- C13. Yanik, A. A., Cetin, A. E., Huang, M., Artar, A., Mousavi, S. H., Khanikaev, A., Altug, H. (2011). Seeing protein monolayers with naked eye through plasmonic fano resonances. *Proceedings of the National Academy of Sciences*, Retrieved from <http://www.pnas.org/content/early/2011/06/28/1101910108.abstract>
- C14. Pang, L., Hwang, G. M., Slutsky, B., & Fainman, Y. (2007). Spectral sensitivity of two-dimensional nanohole array surface plasmon polariton resonance sensor. *Applied Physics Letters*, 91(12), 123112-3. Retrieved from <http://link.aip.org/link/?APL/91/123112/1>
- C15. Gordon, R., Brolo, A. G., Sinton, D., & Kavanagh, K. L. *Resonant optical transmission through hole-arrays in metal films: Physics and applications* - WILEY-VCH Verlag. doi:- 10.1002/lpor.200810079

- C16. Yang, J., Ji, J., Hogle, J. M., & Larson, D. N. (2008). Metallic nanohole arrays on fluoropolymer substrates as small label-free real-time bioprobes. *Nano Letters*, 8(9), 2718-2724. doi:10.1021/nl801043t
- C17. Najiminaini, M., Vasefi, F., Kaminska, B., & Carson, J. J. L. (2011). Optical resonance transmission properties of nano-hole arrays in a gold film: Effect of adhesion layer. *Optics Express*, 19, 26186-26197.

Appendix D.

Effect of surface plasmon cross-talk on optical properties of closely packed nano-hole arrays⁹

Abstract

The integration and miniaturization of nanostructure-based optical devices based on interaction with surface plasmons requires the fabrication of patterns of multiple nanostructures with tight spacing. The effect of surface plasmon energy interchange (cross-talk) across large grids of nanostructures and its effect on the optical characteristics of individual nanostructures have not been investigated. In this paper, we experimentally fabricated a large grid of individual nano-hole arrays of various hole diameter, hole spacing, and inter-array spacing. The spectral optical transmission of each nano-hole array was measured and the effect of inter-array spacing on the transmission spectra and resonance wavelength was determined.

Introduction

The coupling of light to surface plasmons (SP)s in nano-hole arrays (NHA)s depends highly on the dielectric properties of the metal film and the supporting material in contact with the metal film [D1]. A change in the refractive index of the dielectric material at the surface of the metal film gives rise to a shift in the resonance wavelength and is the basis for SPR sensing [D2]. In multiplexed SPR sensing devices based on NHAs, a grid of NHAs is fabricated on to a single substrate, where each NHA has unique geometric properties and hence distinct optical properties. The miniaturization of multiplexed NHA devices inevitably requires that NHAs be fabricated with smaller size and closer inter-array spacing. However, as a grid of NHA elements is scaled down, cross-talk between elements can affect the spectral transmission of each element [D3] [D4]. Cross-talk between two nano-hole arrays arises due to the constructive or destructive effect between two scattered SP waves between closely-packed nano-hole arrays. In order to minimize the SP interactions between NHAs, several groups have taken advantage of the design freedoms to include various SP optical isolators such as Bragg mirrors to reduce neighbor to neighbor cross-talk and enhance light transmission [D5] [D6]. However, the crosstalk effect and

⁹ The following chapter is published in Optics Express, Vol. 19, No. 25, 25773 (2011) under the authorship of Fartash Vasefi, Mohamadreza, Najiminaini, Bozena Kaminska, and Jeffery J.L. Carson. Retrieved from: <http://dx.doi.org/10.1364/OE.19.025773>

This paper was published in [Optics Express] and is made available as an electronic reprint with the permission of OSA. The paper can be found at the following URL on the OSA website: [<http://www.opticsinfobase.org/vjbo/fulltext.cfm?uri=oe-19-25-25773&id=225605>]. Systematic or multiple reproduction or distribution to multiple locations via electronic or other means is prohibited and is subject to penalties under law.

its consequence on spectral transmission and resonance wavelength for large systems of closely packed NHAs has yet to be systematically analyzed.

Hence, the objective of this work was to experimentally investigate the effect of inter-array spacing on the EOT properties of a grid of NHAs that was representative of a multiplexed SPR sensor. The approach was to fabricate different sets of NHAs with various hole diameter (D), hole periodicity (P), and inter-array spacing (S). The NHAs were arranged on a grid of 4 × 4 blocks where each block contained 4 NHAs (distributed as a 2 × 2 grid) with four specific periodicities and hole diameters. The transmission spectrum of each nano-hole array on the grid was measured and the effect of inter-array spacing on the transmission spectra was analyzed.

Materials and methods

Surface plasmon propagation

We estimated the propagation length of the SP wave along the surface of the metal and dielectric material using the relation:

$$\delta_{sp} = \frac{c}{\omega} \left(\frac{\epsilon'_m + \epsilon_d}{\epsilon'_m \epsilon_d} \right)^{3/2} \frac{(\epsilon'_m)^2}{\epsilon''_m}, \quad \text{D-1}$$

where ϵ'_m and ϵ''_m are the real and imaginary parts of the dielectric function of the metal and ϵ_d is the dielectric constant of the dielectric material [D7] [D8]. We used dielectric functions for gold and chromium from Palik [D9]. Due to the high absorption of chromium, the SP propagation length for Pyrex-chromium is very low (Figure D-1 (a)), while the SP propagation length for Pyrex-gold can be as high as 35 μm at 1000 nm (Fig. 1a). The SP propagation length is greatest for air-gold and reaches 100 μm at a wavelength of 1000 nm (Figure D-1 (a)).

Nano-hole array fabrication

Samples were fabricated using an Electron Beam Lithography (EBL) lift off technique to produce a 100-nm-thick gold film perforated with circular nano-scale apertures. We started with a Pyrex wafer coated with a 3-nm Cr conductive layer that enabled electron beam writing. Afterward, 500 nm photo-resist (Negative tone photo-resist ma-N 2403) was spin-coated on to the sample. The nanostructure patterns were written using EBL (LEO, 1530 e-beam lithography) leaving behind nano-scale photo-resist pillars after development. In order to improve adhesion between the gold layer and the substrate, a 4-nm Cr adhesion layer was deposited on to the sample before 100-nm thick gold deposition. Finally, the sacrificial layer of nano-pillars was lifted off resulting in a nano-hole array in the gold layer. More detail on the fabrication methodology has been presented elsewhere [D10] [D11]. Each sample was patterned with 16 blocks on a 4 × 4 grid. Each block contained four NHAs in a 2 × 2 grid with each NHA 30 μm × 30 μm in size and with circular nano-holes on a square lattice. Each NHA in the block had a unique hole diameter and spacing, which gave rise to a distinct resonance wavelength. In each sample, all NHAs were spaced by 2 μm , 5 μm , 10 μm , or 20 μm respectively to study the effect of inter-array spacing on the transmission spectra. Figure D-1 (b) shows the scanning electron micrographs of a block of 4 NHAs with 2 μm spacing. The four nano-hole array designs named NHA1 to NHA4 had hole diameters of 215 nm, 247 nm, 273 nm, and 303 nm with periodicities of 382 nm, 433 nm, 483 nm, and 536 nm, respectively. Typical variation in the hole diameter and spacing was 4 – 6 nm (standard deviation).

Figure.D-1 (c) and Figure D-1 (d) show the transmission spectra of NHA1-NHA4 for samples with 100 μm and 20 μm inter-array spacing collected using a microscope setup [D10]. Although The NHA sample with 20 μm inter-array spacing showed a slightly greater variation in resonance peaks compared to the 100 μm sample, the NHA sample with 20 μm inter-array spacing had a small crosstalk effect compared to 2 μm , 5 μm , 10 μm cases and was used for comparison.

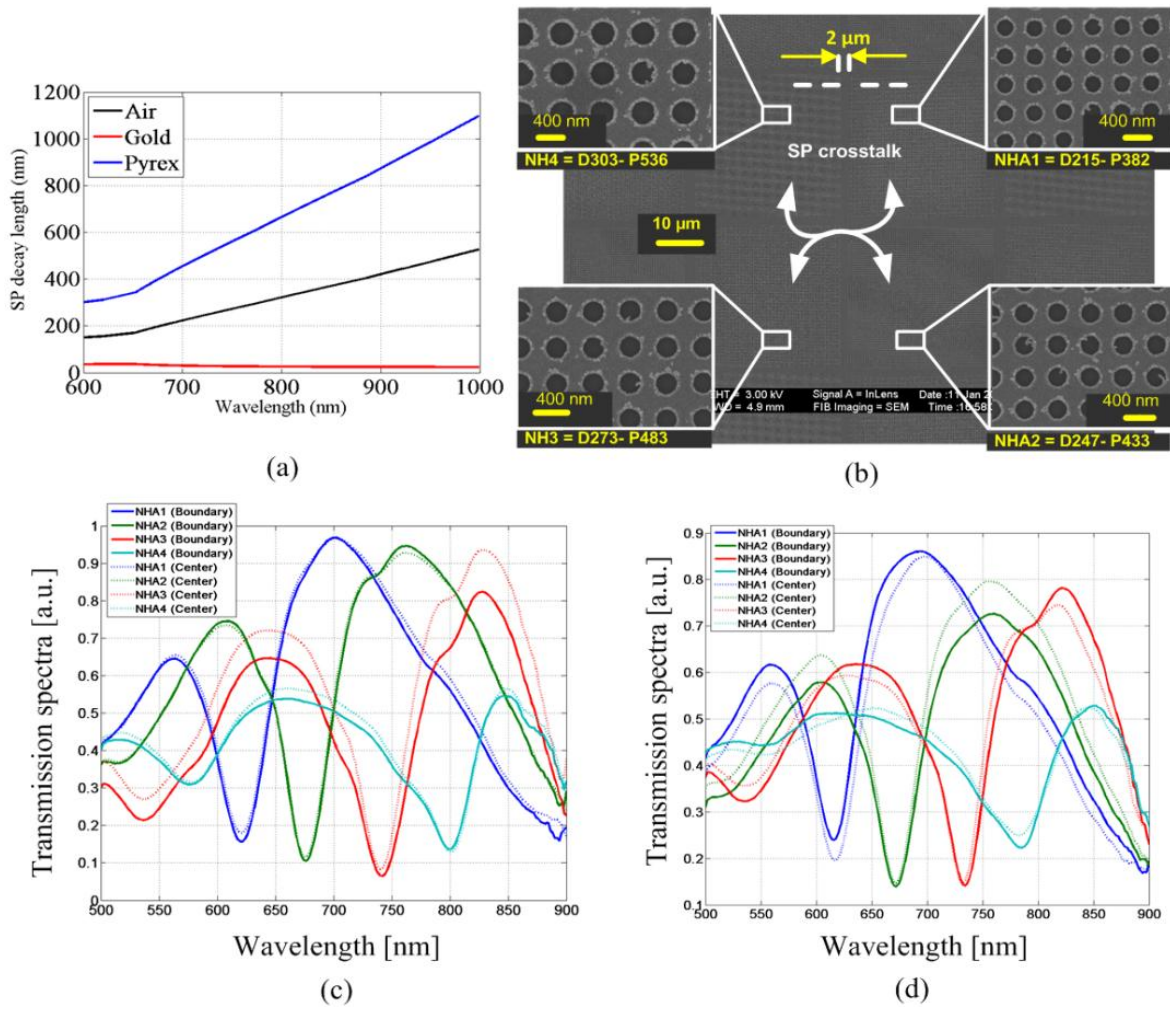


Figure D-1. (a) SP propagation length [Eq. D-1] along the surface for Pyrex-gold, air-gold, and Pyrex-chromium interfaces. (b) SEM image of a series nano-hole arrays in a gold film. In this design, all nano-hole arrays had an inter-array spacing of 2 μm. (c) Transmission spectra of (NHA1-NHA4) for boundary versus center blocks with 100 μm inter-array spacing. (d) Transmission spectra of (NHA1-NHA4) for boundary versus center blocks with 20 μm inter-array spacing. The solid lines are the NHAs at the boundary region while the dashed lines are for NHAs at the central region. The transmission spectra measured using microscope setup (described in 10)].

Device characterization

We employed a multispectral transillumination imaging system with a spectral scanning procedure using a broadband halogen lamp source and a random access monochromator (DeltaRAM V™, PTI, Birmingham, NJ), which enabled parallel characterization of all NHAs in each device. Unpolarized white light from a 100 W halogen lamp was focused on the input to the random access monochromator. The input and output slits were set to provide light with a bandwidth of 4 nm (FWHM) at each scanning step. The output from the random access monochromator was delivered to the NHA sample using a broadband liquid light guide (Series 2000 Lumatec, Germany) and a NIR achromatic pair 1:2.86 with 35 mm and 100 mm EFL achromats (NT47-297, Thorlabs, Newton, NJ, USA). The output light intensity from the NHA sample was collected and delivered to a CMOS camera with a NIR achromatic pair (1:1) with 75 mm and 75 mm EFL achromats (NT47-300, Thorlabs, Newton, NJ, USA). A NIR-enhanced monochromatic CMOS camera with 1312 × 1082 pixels was used to capture the images (MV1-D1312I, Photonfocus AG, Switzerland). The monochromator was scanned by computer control from 652 nm to 985 nm in 86 steps with a step size of ~4 nm. Twenty (20) images were captured at each monochromator step. Each image was 3 × 3 median filtered to remove salt and pepper noise due to the CMOS camera. Each set of 20 filtered images was then averaged on a pixel-by-pixel basis to produce a single image. Repetition of the process at each scan step resulted in an image stack (data cube), which was interrogated in the spectral direction on a pixel by pixel basis. Each spectrum was normalized to the transmission spectrum for the Pyrex substrate. The resonance wavelength was estimated for each NHA by first computing the first derivative of the transmission spectrum at each pixel in the image stack. Next, a search algorithm was used to locate the wavelength of the zero-crossing representative of the largest peak within each first-order spectrum, which was interpreted as the resonance wavelength of the EOT. Utilizing a region of interest analysis, the mean ± standard deviation of the resonance wavelength for each NHA was computed.

Results and discussion

Spectral response of NHAs within a block

Figure D-2 shows the optical transmission spectra experimentally acquired from a central block (third row and the third column of the 4 × 4 block grid) for four different devices fabricated with inter-array spacings of 2 μm, 5 μm, 10 μm, and 20 μm. The spectra show a number of distinct spectral features. The larger peaks at longer wavelengths corresponded to the (1,0) resonance mode for the Pyrex-gold side ($\lambda(1,0)$). Resonance peaks representative of the air-gold side were not observed. The minima in transmission spectra for NHA2, NHA3, and NHA4 corresponded to Wood's anomaly [D12]. The smaller peaks in the spectra for NHA3 and NHA4 corresponded to the Pyrex-gold (1,1) resonance mode ($\lambda(1,1)$). The Pyrex-gold $\lambda(1,1)$ for NHA2 and NHA1 as well as the Wood's anomaly for NHA1 were not observed as they were expected to lie outside the spectral range of the instrumentation. The experimental optical transmission spectra were qualitatively similar to the transmission spectra observed in previous work for isolated NHAs [D10] [D11] [D13] [D14].

Due to the effects of cross-talk, the position of the resonance peak was hypothesized to depend on the inter-array spacing. Analysis of Figure D-2 confirmed that the Pyrex-gold $\lambda(1,0)$ for all 4 NHAs within a block were blue shifted (dotted lines) when the spacing between the arrays was decreased. The average Pyrex-gold $\lambda(1,0)$ blue shift resulting from a decrease in the inter-array spacing from 20 μm to 2 μm was roughly equivalent for all four NHAs. For example, blue shifts (mean ± s.d.) of 32 ± 15 nm, 31 ± 18 nm, 35 ± 19 nm, and 36 ± 13 nm, were observed for NHA1 through NHA4, respectively. Similar blue shifts in the wavelength of each Wood's anomaly

were observed as the inter-array spacing decreased. One of the reasons for resonance blue shifting might be related to a SP reflection effect. Specifically, neighboring NHAs can reflect back the scattered SP waves from the NHA edge with a similar mechanism shown for Bragg mirrors described in [D5]. The blue shift effect has been shown in for NHAs with Bragg mirrors as well. Another experimental study with super-lattice NHAs with the same periodicities but with the different pitches shows the same effect of resonance blue shift [D15]. Although a strong dependence of transmission on inter-array spacing was not observed, NHAs spaced 2 μm apart had the highest transmission at the Pyrex-gold $\lambda(1,0)$ compared to the others.

Variation in spectral response of NHAs across each device

Since each sample contained 64 NHAs in an 8x8 grid pattern, some NHAs were situated in closer proximity to the edge of the device than others. We hypothesized that the NHAs on the perimeter of the device would be less affected by cross-talk effects compared to NHAs near the center of the device. For example, NHAs at each corner were adjacent to only three neighboring NHAs, while a NHA at least one position in from an edge had 8 NHAs immediately adjacent.

The resonance wavelength measurements supported the hypothesis since for NHAs near the boundary (see Figure D-3 (a)-(c)), the resonance wavelength tended to be blue shifted to a smaller degree than NHAs near the center of the device. The spatially dependent blue shift of the resonance wavelength was observed in all devices, but became progressively larger as the inter-array spacing decreased (see difference maps in Figure D-3 (d) and Figure D-3 (e)).

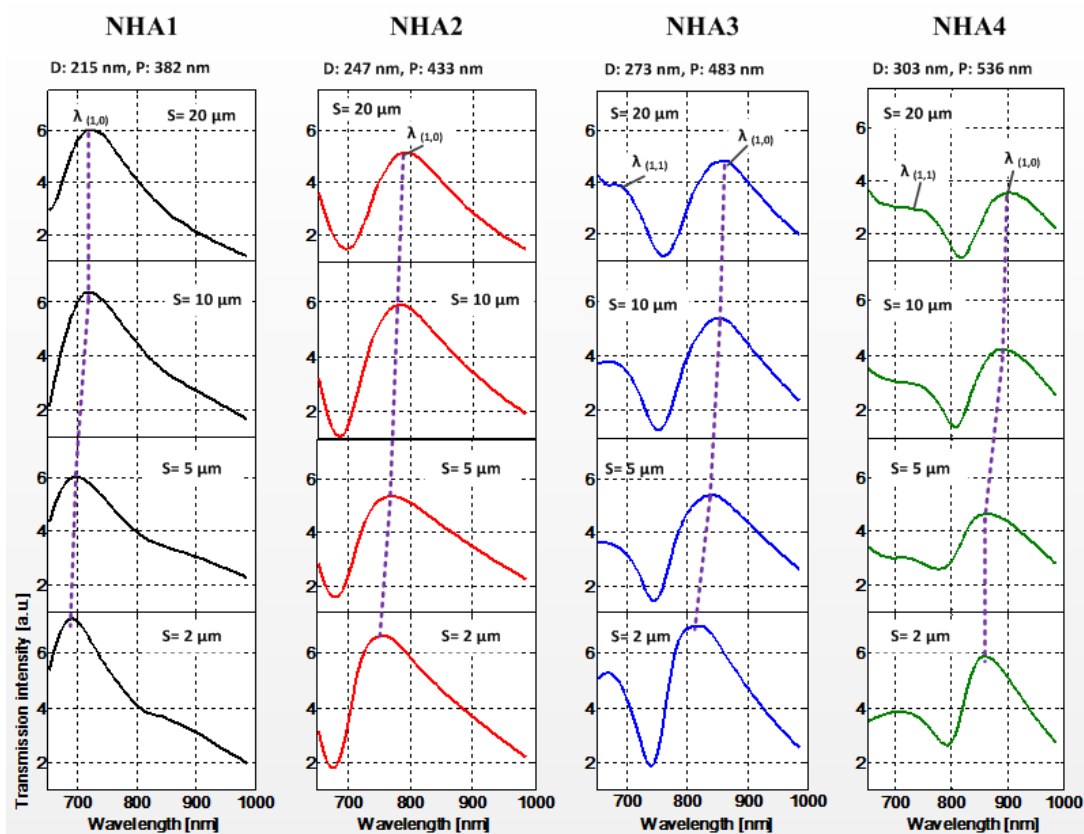


Figure D-2. Experimental transmission spectra for nano-hole arrays within a block with specific hole diameter (D), hole periodicity (P) and inter-array spacing (S). All NHAs were selected from the same central block position within the 4 × 4 grid of each device.

Analysis of Figure D-3 (a) suggested that even at an inter-array spacing of 20 μm there was cross-talk between NHAs. For example, the resonance wavelength for NHA1 was blue-shifted for blocks from the left side of the device to the right side. However, the differences in resonance wavelength were typically ≤ 20 nm and much smaller for NHA2 through NHA4. These observations lead us to conclude that larger inter-array spacings or intervening structures are required to completely prevent cross-talk effects between closely packed NHAs. In the case of 2 μm inter-array spacing (Figure D-3 (c) and D-3 (e)), cross-talk introduced blue-shifts in Pyrex-gold $\lambda_{(1,0)}$ of approximately 20 to 50 nm depending on the location and design parameters of the specific NHA being considered. For multiplexed SPR sensing applications, this systematic effect is competitive with the expected changes in resonance wavelength due to local index of refraction changes. However, if small systematic shifts in resonance wavelength are tolerable, then close packing of NHAs by reduction of the inter-array spacing may be a worthwhile approach to miniaturization of multiplexed SPR sensors.

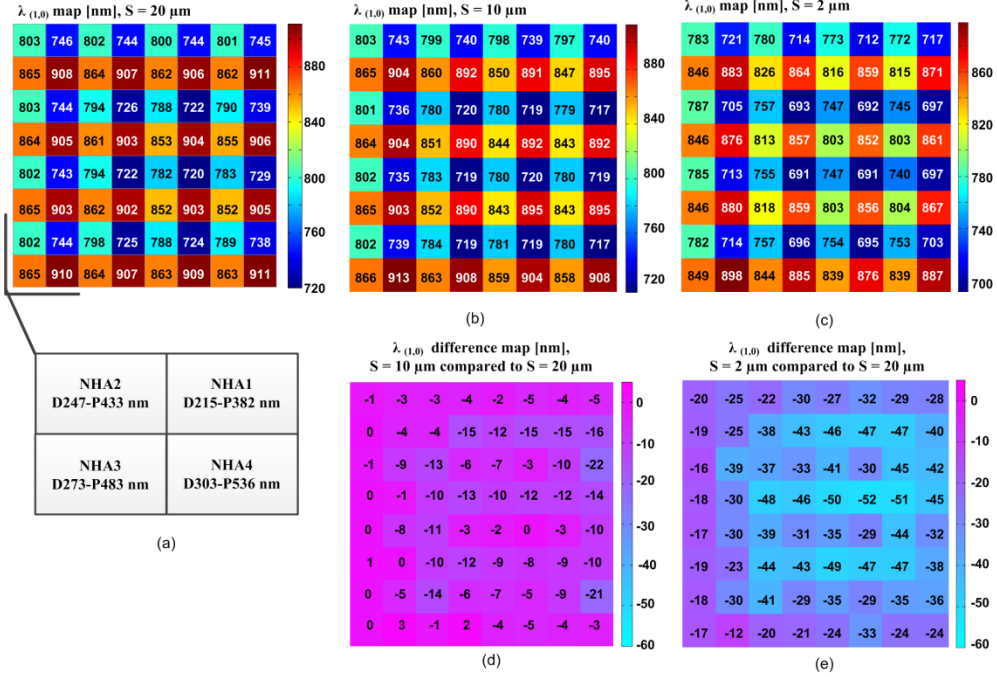


Figure D-3. Resonance wavelength maps of NHAs with (a) 20 μm inter-array spacing, (b) 10 μm inter-array spacing, and (c) 2 μm inter-array spacing. Resonance wavelength difference map of NHAs with (d) 10 μm inter-array spacing compared to 20 μm inter-array spacing, and (e) 2 μm inter-array spacing compared to 20 μm inter-array spacing.

Conclusions

The goal of this study was to evaluate the effect of SP cross-talk on the transmission spectra of closely packed NHAs. We fabricated four NHA devices, each with unique inter-array spacing. Each device contained a set of sixteen identical blocks of NHAs and each block contained 4 individual NHAs each 30 $\mu\text{m} \times 30 \mu\text{m}$ in size with unique hole diameter and periodicity. Each NHA had SP resonance peaks in the near infrared, which were related primarily to the Pyrex-gold interface. The transmission spectrum of each NHA was measured and the resonance wavelength was extracted. Experimental results revealed progressively larger changes in the resonance wavelength as the inter-array spacing decreased from 20 μm down to 2 μm . The resonance wavelength and the Wood's anomaly minima blue shifted as the inter-array spacing was decreased. No systematic behavior was observed for the optical transmission intensity of NHAs with different inter-array spacings.

Acknowledgments

This project was funded by grants from the Natural Sciences and Engineering Research Council of Canada to Dr. Bozena Kaminska and Dr. Jeffery J.L. Carson. Dr. Fartash Vasefi was supported by a London Regional Cancer Program Translational Breast Cancer Research Trainee Fellowship.

References

- D1. Ghaemi, H. F., Thio, T., Grupp, D. E., Ebbesen, T. W., & Lezec, H. J. (1998). Surface plasmons enhance optical transmission through subwavelength holes. *Physical Review B*, 58(11), 6779-6782. Retrieved from <http://link.aps.org/doi/10.1103/PhysRevB.58.6779>
- D2. De Leebeek, A., Kumar, L. K. S., de Lange, V., Sinton, D., Gordon, R., & Brolo, A. G. (2007). On-chip surface-based detection with nanohole arrays. *Analytical Chemistry*, 79(11), 4094-4100. doi:10.1021/ac070001a
- D3. Lesuffleur, A., Im, H., Lindquist, N. C., Lim, K. S., & Oh, S. (2008). Plasmonic nanohole arrays for real-time multiplex biosensing. Paper presented at the San Diego, CA, USA. , 7035(1) 703504. doi:10.1117/12.794299
- D4. Przybilla, F., Degiron, A., Genet, C., Ebbesen, T., de Léon-Pérez, F., Bravo-Abad, J., Martín-Moreno, L. (2008). Efficiency and finite size effects in enhanced transmission through subwavelength apertures. *Optics Express*, 16(13), 9571-9579. Retrieved from <http://www.opticsexpress.org/abstract.cfm?URI=oe-16-13-9571>
- D5. Lindquist, N. C., Lesuffleur, A., & Oh, S. (2007). Periodic modulation of extraordinary optical transmission through subwavelength hole arrays using surrounding bragg mirrors. *Physical Review B*, 76(15), 155109. Retrieved from <http://link.aps.org/doi/10.1103/PhysRevB.76.155109>
- D6. Lindquist, N. C., Lesuffleur, A., & Oh, S. (2007). Lateral confinement of surface plasmons and polarization-dependent optical transmission using nanohole arrays with a surrounding rectangular bragg resonator. *Applied Physics Letters*, 91(25), 253105. doi:10.1063/1.2825587
- D7. Barnes, W. L., Dereux, A., & Ebbesen, T. W. (2003). Surface plasmon subwavelength optics. *Nature*, 424(6950), 824-830. Retrieved from <http://dx.doi.org/10.1038/nature01937>
- D8. Raether, H. (1988). *Surface plasmons*. Berlin: Springer-Verlag.
- D9. Palik, E. D. (1985). *Handbook of optical constants of solids*. New York: Academic Press.
- D10. Najiminaini, M., Vasefi, F., Kaminska, B., & Carson, J. J. L. (2010). Experimental and numerical analysis on the optical resonance transmission properties of nanohole arrays. *Optics Express*, 18(21), 22255-22270. Retrieved from <http://www.opticsexpress.org/abstract.cfm?URI=oe-18-21-22255>

- D11. Najiminaini, M., Vasefi, F., Landrock, C. K., Kaminska, B., & Carson, J. J. . (2010). Experimental and numerical analysis of extraordinary optical transmission through nano-hole arrays in a thick metal film. Paper presented at the San Francisco, California, USA. , 7577(1) 75770Z. doi:10.1117/12.842727
- D12. Gordon, R., Brolo, A. G., Sinton, D., & Kavanagh, K. L.(2010). Resonant optical transmission through hole-arrays in metal films: Physics and applications. *Laser and Photonics Rev* 4(2), 311-335.
- D13. Lesuffleur, A., Im, H., Lindquist, N. C., & Oh, S. (2007). Periodic nanohole arrays with shape-enhanced plasmon resonance as real-time biosensors. *Applied Physics Letters*, 90(24), 243110-3. Retrieved from <http://link.aip.org/link/?APL/90/243110/1>
- D14. Przybilla, F., Degiron , A., Laluet, J. Y., Genet, C., Ebbesen, T.W. (2006). Optical transmission in perforated noble and transition metal films. *Journal of Optics A: Pure and Applied Optics*, 8(5) 458. Retrieved from <http://stacks.iop.org.proxy.lib.sfu.ca/1464-4258/8/i=5/a=015>
- D15. Odom, T. W., Gao, H., McMahon, J. M., Henzie, J., & Schatz, G. C. (2009). Plasmonic superlattices: Hierarchical subwavelength hole arrays. *Chemical Physics Letters*, 483(4-6), 187. doi:10.1016/j.cplett.2009.10.084.

Appendix E.

Angular domain fluorescence lifetime imaging: a tissue like phantom study¹⁰

Abstract

We describe a fluorescence lifetime imaging technique employing the collimation detection capabilities of an angular filter array (AFA). The AFA accepts minimally scattered photons emitted from fluorophores up to 2 mm deep within turbid media. The technique, referred to as Angular Domain Fluorescence Lifetime Imaging (ADFLI), is described and its performance evaluated in comparison to a conventional (lens and pinhole) system. Results from a tissue-mimicking phantom demonstrated that ADFLI provides better spatial resolution and image contrast for fluorescent probes at greater depths compared to a lens and pinhole system.

Introduction

The recent advancement of disease-targeted fluorescent markers has stimulated concurrent developments in non-invasive optical molecular imaging techniques. These advancements have made optical molecular imaging an effective alternative to positron emission tomography and magnetic resonance imaging, predominantly in drug delivery research. In particular, time-resolved fluorescence imaging offers a rich array of information, namely fluorescence localization and lifetime that can be used to interrogate local molecular and physiological processes in tissue, providing complex diagnostic and prognostic information [E1] [E2]. The combination of this technique with molecularly-targeted contrast agents having physiologically-sensitive lifetimes has obvious applications for early-stage cancer diagnostics since the distribution of fluorescence could be used to locate tumors and the lifetime of the fluorescence could be used to investigate tumor microenvironment (notable examples include pH and temperature) [E3]-[E6]. In addition, fluorescence lifetime imaging (FLI) can be used to distinguish fluorescent probe distributions more effectively than intensity mapping since lifetime can be used to separate out the auto-fluorescence signal [E7]. Fluorescent lifetime imaging can be used to spatially resolve

¹⁰ The following chapter is published in Optics Express, Vol. 18, No. 20, 23247 (2010) under the co-authorship of Fartash Vasefi, Kenneth M. Tichauer, Ting-Yim Lee, Bozena Kaminska, and Jeffery J.L. Carson. Retrieved from: <http://dx.doi.org/10.1364/OE.18.023247>

This paper was published in [Optics Express] and is made available as an electronic reprint with the permission of OSA. The paper can be found at the following URL on the OSA website: [<http://www.opticsinfobase.org/oe/fulltext.cfm?uri=oe-18-22-23247&id=206761>]. Systematic or multiple reproduction or distribution to multiple locations via electronic or other means is prohibited and is subject to penalties under law.

combinations of different fluorescent probes with single excitation wavelengths but different lifetimes [E7] [E8]. Recent progress has been made on the application of near-infrared FLI in a high resolution, wide field-of-view imaging platform that enables acquisition of quantitative optical property maps with simultaneous reconstruction of lifetime [E8]. Applications of FLI to cell imaging by microscopy have been numerous and highly successful [E9]. The use of two-photon microscopy provides the benefit of better localization of fluorescent targets in samples at deeper depths with reduced auto-fluorescence [E10] [E11]. For optically-thick, highly-turbid samples such as tissue, several approaches to FLI have been developed. One approach is to solve the inverse problem using diffuse photon density waves [E12]. The fluorescence lifetime can be extracted using time domain (TD) or frequency domain (FD) measurement techniques [E13] [E14] [E15]. Compensation for the rapid loss of spatial resolution as a function of depth has been attempted by combining finite-element light propagation models with image reconstruction algorithms [E16] [E17]. However, large depth-dependent discrepancies in signal intensity arising from embedded fluorophores make it difficult to resolve complex distributions containing both shallow and deep fluorescence populations, precipitating the need for multiple projections to be collected [E18]. Time domain techniques provide the potential advantage of direct measurement of lifetime by means of multiple exponential fits to fluorescence decays, an aspect well exploited for non-scattering thin tissue samples by fluorescence lifetime imaging microscopy (FLIM). However, in thicker samples, the diffuse propagation of light within the tissue creates asymptotic decay of the TD fluorescence temporal function, which must be corrected with reconstruction methods [E19].

Although much effort has been directed at applications of FLI to microscopy and FLI to imaging macroscopic samples (e.g. tomography), here we present a reflectance-based FLI method optimized for the mesoscopic domain (i.e. beyond the capabilities of FLIM but below the centimeter spatial scale representative of macroscopic imaging). The method is based on angular domain fluorescence imaging (ADFI), which offers a conceptually simpler technique to mitigate spatial resolution degradation with depth and minimize the loss of signal intensity [E20]. With ADFI, spatial resolution is improved by restricting the detection of scattered photons arising from the imaging medium with an angular filter array (AFA). The AFA is comprised of a parallel array of high aspect ratio micro-tunnels, micro-machined into a silicon substrate [E21]. The objective of the work reported here was to extend the capabilities of ADFI to mesoscopic fluorescent lifetime imaging. The paper builds upon our preliminary work [E22] [E23] [E24] and begins with an overview of angular domain fluorescence lifetime imaging (ADFLI) followed by a comparison of the technique to FLI with a Keplerian lens and pinhole. The comparison was achieved by successively imaging tissue-like phantoms containing two fluorescent sources with distinct lifetimes. Experiments were repeated for sources placed at various depths within the phantom.

Angular domain fluorescence imaging

In ADFI, an angular filter array is employed to reject unwanted scattered photons and accept the spatially informative quasi-ballistic photons based on acceptance angle. As shown in Figure E-1(a), the angular filter device differentiates between minimally scattered fluorescent photons from the more plentiful scattered fluorescent photons emitted from fluorophores situated in tissue. The scattered photons emitted from fluorophores have less likelihood of exiting the tissue surface with an angular deviation acceptable to the AFA. Only photons emitted from the fluorophore that have small angular deviation are accepted by the AFA. Hence, these minimally deviated photons can pass through the AFA and be detected by the camera. Since the performance of the AFA is not dependent on coherence, or the wavelength of light, and AFAs can be fabricated several centimeters in width, ADFI can be used to map fluorophores over a large field-of-view with millimeter range spatial resolution at significant depths (~2 mm) into tissue [E20].

The angular filter array consists of a parallel array of square-shaped micro-tunnels (typically 80 microns wide along a 1.5 cm long plate) to obtain a high aspect ratio of approximately 188:1 (see Figure E-1(b)). The bottom component of the AFA is fabricated by etching a silicon substrate and the walls of the bottom component can be patterned with many small features to suppress internal reflections within each micro-tunnel (Figure E-1(c)). A flat silicon wafer is used as the top component to enclose the micro-tunnels to form the AFA. Since the micro-tunnels are square in geometry, there exists an angular acceptance angle variation from 0.3° (wall to wall) to 0.42° (corner to corner). This design is known from previous work to be selective for quasi-ballistic photons and provides at least $200\ \mu\text{m}$ spatial resolution for targets embedded in homogenous turbid media [E25].

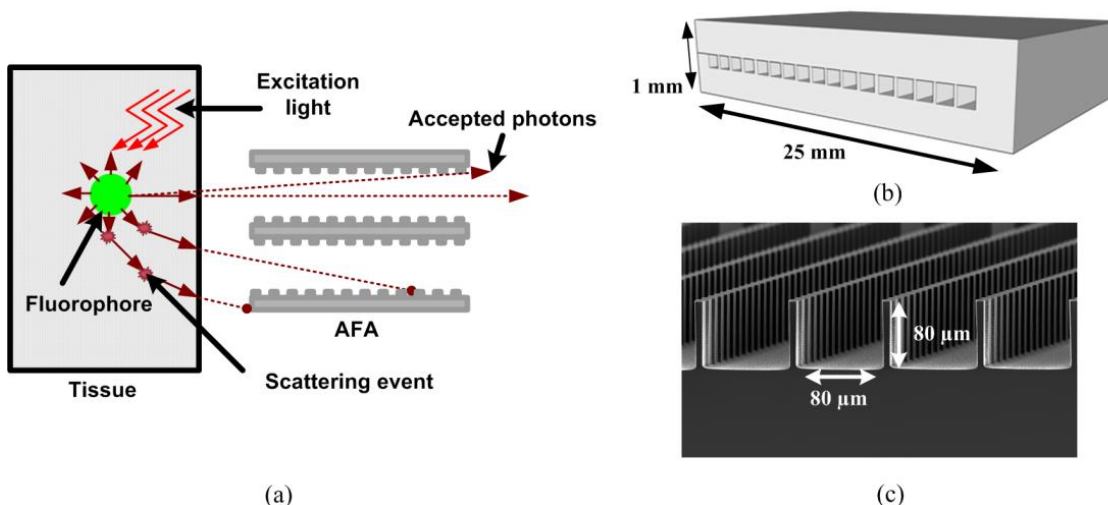


Figure E-1. (a) *Illustration of angular filtering, (b) an illustration of the full angular filter array, and (c) scanning electron microscope image of uncapped angular filter array.*

In theory, the principles of ADFI can also be applied to time-resolved photon detection to potentially improve fluorescence lifetime property extraction. Based on the improved performance of ADFI over reflective imaging, it is expected that angular-domain fluorescence lifetime imaging (ADFLI) will provide images with greater spatial resolution of embedded sources compared to conventional FLI techniques. Furthermore, ADFLI should be more resistant to the temporal lengthening effects of depth on the surface calculation of lifetime since the mean differential path-length should be shorter.

Results and discussion

System setup

The experimental setup based on the ADFLI configuration in the reflection mode is shown in Figure E-2 (a). In this mode, both the illumination source and the aligned detector system are located on the same side of the sample. In our system, a collimated beam from a pulsed-laser source was expanded to uniformly illuminate a sample containing two fluorescent targets. Then, the angular distribution of emitted photons from the embedded fluorescence targets was restricted by a Keplerian lens and pinhole system with an acceptance angle of 1.2° and, in some cases, was further restricted to 0.4° by an AFA. Finally, fluorescence emission was detected

using a gateable intensified CCD camera, where time gating of the camera was synchronized to the pulsed laser source with a programmable delay.

A high power picosecond diode laser (780 nm wavelength) was employed for all experiments (PicoTA, PicoQuant GmbH and TOPTICA Photonics). A spectral filter ($\lambda = 780 \pm 5$ nm) was used to block the background emission caused by the laser amplifier system. The diode laser had a pulse width of 100 ps (FWHM), a repetition rate of 80 MHz, and an average power of 500 mW. The laser beam (2.4 mm in diameter) was expanded into a collimated circular beam with a diameter of 1 cm. The AFA was aligned precisely at the same height as the light source to enable capture of the in-line fluorescent emission. A dichroic mirror was placed before the lenses of the Keplerian system to enable laser light delivery to the sample. The Keplerian lens and pinhole system was located between the sample and the AFA to transfer fluorescent emission from the sample to the AFA. Reflected laser light was rejected in the detection optical path by an emission bandpass filter (FL830-10, Thorlabs, NJ, USA) and a laser line long-pass filter (NT47-508, Edmund Optics Inc., NJ, USA) prior to reaching the camera.

Time-domain fluorescence was collected with a gateable intensified CCD camera (PicoStar HR, LaVision). A trigger delay unit (Delay Unit, LaVision, Germany) coupled to a synchronization signal from the laser driver was used to control a high-rate imager (HRI, Kentech Instruments, UK), which facilitated collection of CCD images from specific short-duration temporal windows. By performing a delay sweep, full fluorescence temporal point spread functions (FTPSFs) were constructed using a 500 ps gate width at 25-ps delay steps.

In all AFA optical imaging systems, including ADFLI, the light intensity at the output of the AFA is spatially modulated based on the micro-tunnel size and spacing as shown in Figure E-1 (a). The line intensity profile has a sinusoidal pattern with the same periodicity as the micro-tunnel spacing, with signal peaks corresponding spatially to the center of the micro-tunnel openings. We attempted to remove the image artifacts by locating the upper envelope for each ADI line image and smoothing the resultant 2D ADI image in-row in order to eliminate the noise at each line profile in the intensity and lifetime maps. We used the “rloess” smoothing method in MATLAB (The Mathworks, Natick, MA), which employed local regression using weighted linear least squares and a 2nd degree polynomial model. Additional detail about artifact correction in angular domain imaging systems has been presented elsewhere [E26].

The one dimensional linear array of micro-tunnels necessitated a scanning system for the capture of 2D images. We employed a computer-controlled z-axis stage to incrementally raise the sample between scans. One horizontal line image of the sample was taken through the AFA at each step and a final 2D image was assembled from the stacked line images. Hence, an entire region of the sample could be passed through the field of view of the AFA and imaged.

Phantom preparation

Three similar phantoms were constructed to explore both resolution (spatial and lifetime) and contrast (spatial and lifetime) of ADFLI. As shown in Figure E-2 (b) and (c), phantoms were created by embedding two glass capillary tubes, each containing a different fluorophore with a distinct lifetime, at depths of 0, 1, or 2 mm, and separated laterally by 3 mm. The fluorescence sources were 20 μ M solutions of 3,3-diethylthiatricarbocyanine iodide (DTTCl, lifetime \sim 1 ns) and indocyanine green (ICG, lifetime \sim 0.5 ns) embedded in a 1% Intralipid™ scattering medium (see Figure E-2 (b) and (c)). DTTCl and ICG dyes were characterized separately using a Beckman DU-640 spectrometer. The absorption peak was found to be μ a-DTTCl = 2.5 cm^{-1} at 758 nm for 20 μ M DTTCl and μ a-ICG = 3.2 cm^{-1} at 772 nm for 20 μ M ICG. The absorption range for DTTCl and ICG at the excitation wavelength ($\lambda = 780 \pm 5$ nm) was determined to be 1.8 cm^{-1} and 3 cm^{-1} , respectively. Intralipid™ has optical scattering properties similar to tissue at visible and near infrared wavelengths. In addition, it has low optical absorption in the visible and near infrared

regime [E27] [E28]. Each phantom was imaged with the ADFLI system, with and without the AFA in place to investigate the performance of the AFA. As described in [E27] [E28], considering the forward scattering property ($g = 0.75$) common in tissue-mimicking phantoms, the reduced scattering coefficient for 1% Intralipid™ is roughly 8-10 cm^{-1} in the near infrared, while the absorption coefficient is about 0.1-0.01 cm^{-1} , which is two to three orders of magnitude smaller. The reciprocal value of reduced scattering coefficients yields the reduced mean free path (MFP'). We estimate that the minimum path for a fluorescent target at a depth of 2 mm will be about 4 MFP'. That is, photons at the excitation wavelength should travel two MFP' to reach the fluorophore and the emitted photons will travel a similar path, but in reverse, to reach the phantom surface.

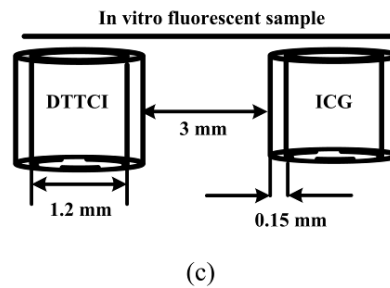
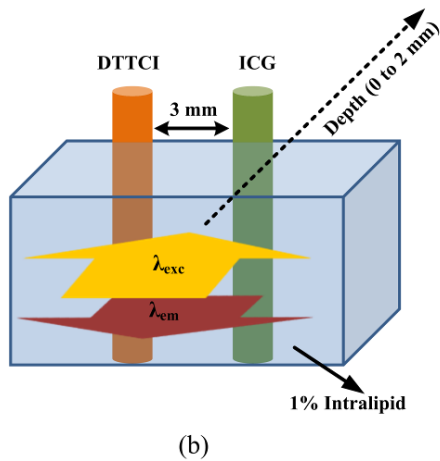
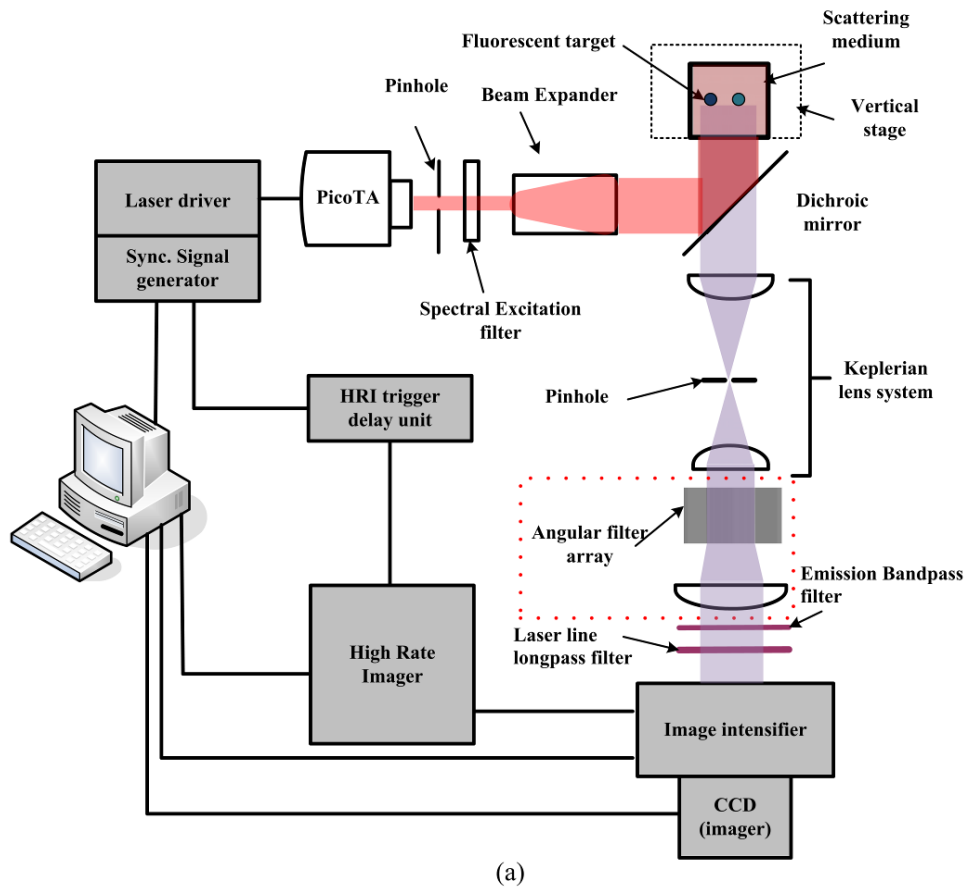


Figure E-1. (a) An illustration of the ADFLI system, (b) three-dimensional schematic of the phantom, and (c) a schematic of the tubes used to contain the fluorescent dyes showing wall thickness and tube separation distance.

Fluorescence lifetime map calculation

Fluorescence lifetime maps were created by fitting a single exponential decay,

$$\propto \exp\left(-\frac{t-t_0}{\tau}\right), \quad \text{E-1}$$

where α is a weighting factor, t is the fluorescent lifetime, and t_0 is a time shift parameter to account for delays in signal arrival (since no instrument response function was accounted for), to the down-slope of each FTPSF collected starting at 75% of the peak value of the FTPSF to the end of the collection window (typically about 30% of the peak value of the FTPSF). Fitting was performed with a Levenberg-Marquardt least squares algorithm applied in MATLAB. To avoid calculation of lifetime from pixels with minimal fluorescence signal, only FTPSFs whose sum was greater than 30% of the sum of the maximum intensity FTPSF in each image were fitted for lifetime. All other FTPSFs were assigned a lifetime of 0 ns.

Undersampling the fluorescence temporal response functions

To explore the feasibility of faster imaging times, FTPSFs from both ADFLI and lens and pinhole FLI were undersampled from 25-ps resolution to 50-, 75-, 100-, 125-, and 150-ps resolutions for all phantom images. Lifetime maps were then recalculated for each case to determine the effect of reduced temporal resolution on the lifetime estimates.

Results and discussion

Depth analysis

The intensity and lifetime maps obtained with and without the AFA from a pair of DTTCl and ICG sources at 0, 1, and 2 mm depths are shown in Figure E-3. In addition, Figure E-4 shows the horizontal line intensity and lifetime profiles computed for each intensity and lifetime image for all depths to provide a clearer comparison between results with and without the AFA. The intensity maps in Figure E-3 were normalized in order to facilitate clearer comparisons between the images. However, the intensity line profiles in the Figure E-4 represent the absolute values as measured with the experimental setup in order to facilitate comparison of the sensitivity of the two methods as depth increased. The DTTCl and ICG sources are on the left and right side of each image, respectively. The dimensions of each image are 0.75 x 20 mm (height-x-width).

The images collected with the AFA revealed less broadening for fluorescent target lifetimes as the depth increased compared to images collected without the AFA. As a result, a clear improvement was observed in the spatial resolution of the fluorescence in the AFA technique, particularly for fluorescent sources at deeper depths. Furthermore, the lifetime contrast measured between the two fluorophore sources was significantly larger for the AFA technique for all source depths. The lifetime contrast ratios for AFA and No AFA images were 2.3 and 1.8 at 0 mm, 2.2 and 1.6 at 1 mm, and 2.0 and 1.4 at 2 mm, respectively. Lifetime of both DTTCl and ICG increased with depth of the fluorescence sources equally with and without the AFA. One source of this effect could be explained by dispersion of photons through tissue (which we did not attempt to account for) that would occur to a greater extent for deeper sources and would be roughly equivalent for both techniques. Theoretical analysis using the diffusion equation of light

propagation in a homogeneous scattering media has suggested that a depth of 2 mm will result in an error in the lifetime estimate of approximately 0.01 ns [E29]. This level of error could be used to explain the increase in lifetime of the DTTCI inclusions with depth; however, the increase in ICG lifetime with depth was much larger. Therefore, the greater increase in lifetime of the ICG sources with depth may have been a phenomenon of a mixing of fluorescence signal from both sources, which would have occurred with greater propensity at deeper source positions. In other words, aside from an expected increase in measured lifetime with source depth, increasing source depth also increased the likelihood of fluorescence mixing from both tubes; wherein, the lifetime of the ICG would be expected to lengthen and the lifetime of DTTCI would be expected to shorten. However, since our procedure for estimating the lifetime used the later part of the FTPFS, the rapid signal decay from ICG may not have contributed to the shortening of the lifetime estimate for DTTCI, which is consistent with our data.

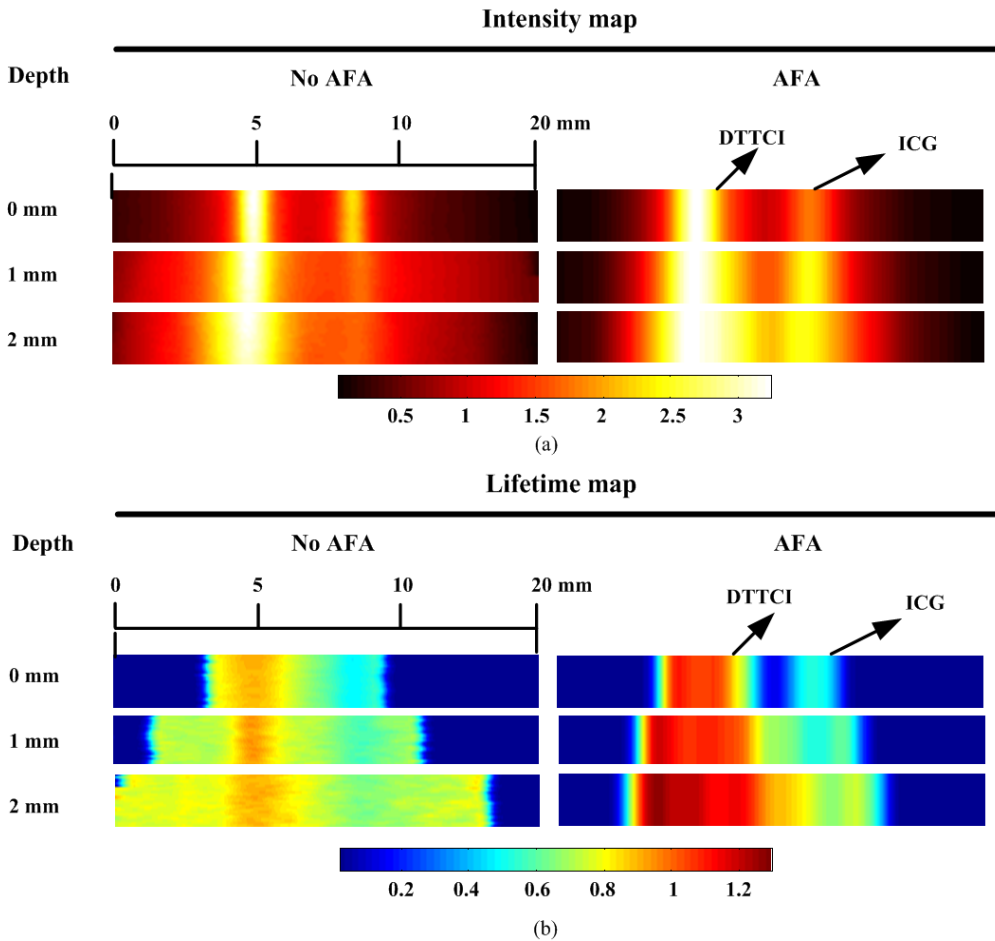


Figure E-3. (a) Intensity (hot scale; arbitrary units) normalized to facilitate comparison and (b) lifetime (colormetric; ns) maps of the three phantoms without and with AFA for three depths (0 mm, 1 mm, and 2 mm).

As shown in Figure E-4, the fluorescence emission intensity for the AFA case was approximately 5-fold lower than the No AFA case at 0 mm depth, but the ratio decreased to approximately 3-fold

at 2 mm depth. In addition, the setup with the AFA had a reduced dependence of signal intensity on depth with a signal loss of approximately 50% (0 to 2 mm), where the setup lacking the AFA experienced a 3-fold drop in signal intensity for the same change in target depth. Greater noise was observed in the fluorescence cross-sections obtained with the AFA compared to No AFA. This owed to the restricted photon acceptance angle of the AFA, which permitted fewer photons to reach the detector. Additionally, the MCP gain of the camera system was increased to compensate for loss of signal and likely resulted in increased noise in the fluorescence images. Therefore, we hypothesize that the AFA system would be better suited to brighter fluorophores with higher extinction coefficients and quantum yields. Despite the reduced signal to noise ratio of the AFA images, it is clear from Figure E-4 that the AFA provided major improvements over the No AFA method in relation to resolution, contrast, and fluorescence lifetime contrast. For instance, it was very difficult to resolve the two separate sources at a depth 2 mm using the lifetime map collected without the AFA, while a clear separation was observed for the AFA lifetime map. Even with simple thresholding, the localization of different fluorophores was qualitatively easier with the AFA in place. Also, the lateral spatial resolution of the AFA system was expected to be uniform over the entire field of view due to the geometric and photon acceptance uniformity of the angular filter array.

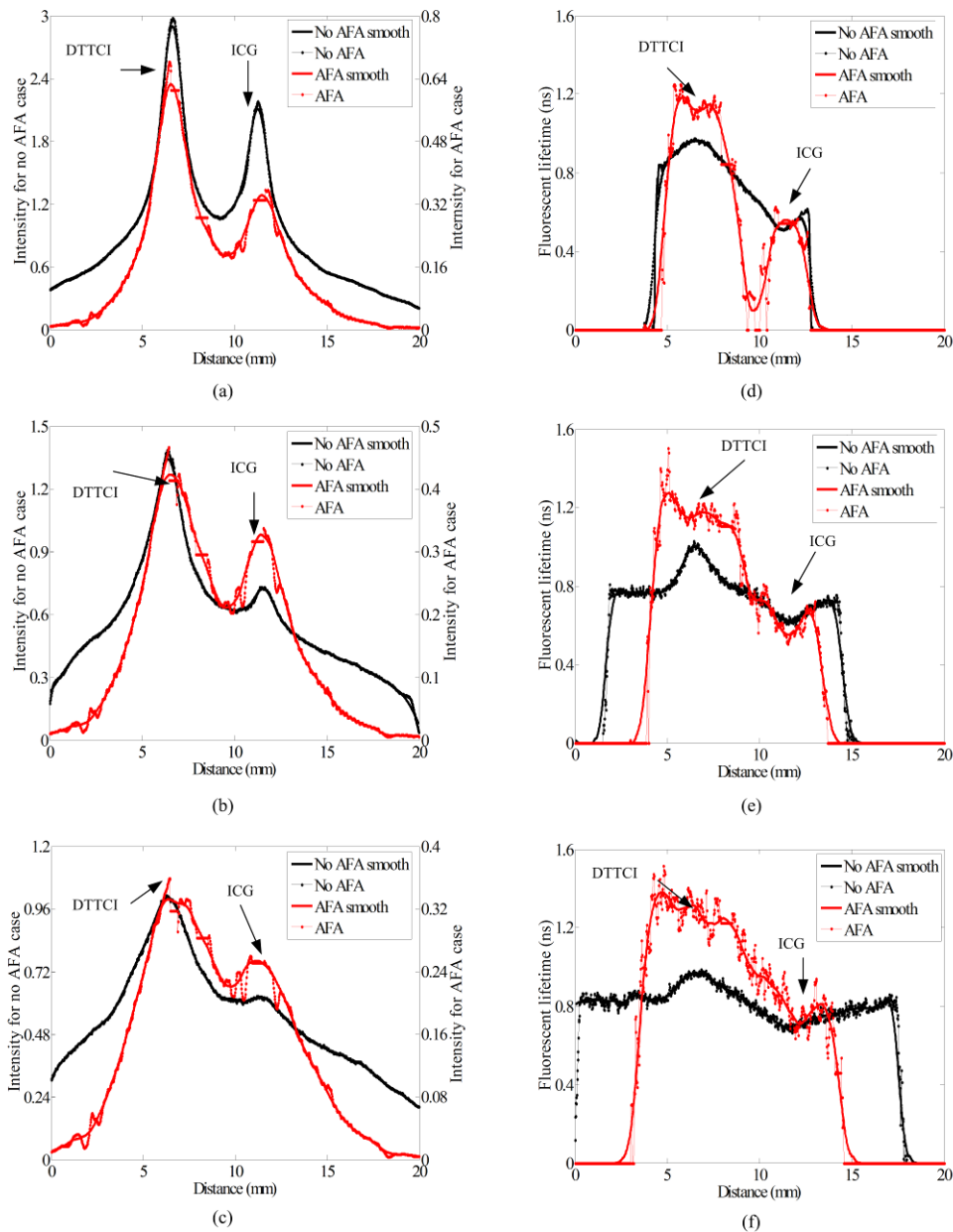


Figure E-4. Cross-sections of fluorescence intensity of (a) 0 mm, (b) 1mm, and (c) 2 mm depth phantoms and lifetime maps of (d) 0 mm, (e) 1mm, and (f) 2 mm depth phantoms. The black solid curve represents the smoothed curve while the thin line represent the measured signal of fluorescence intensity and lifetime line profile without AFA and the red curve represents with the same measure with the AFA. Arrows denote the location of each fluorophore inclusion.

The imaging results shown in Figure E-3 and Figure E-4 for the AFA system were captured when the sample was illuminated over a large area and detection was over a narrow line equivalent to

the AFA aperture size. Since the illumination was over an area and only a small portion of the beam was co-aligned with the AFA, scattered light originating out of the detection plane is expected to contribute to a decrease in contrast. It is anticipated that shrinkage of the illumination area to a narrow line of light, co-linear with the AFA, will lead to a decrease in the background fluorescent signal and improved estimates of fluorescence intensity and lifetime.

Exposure time and effect of undersampling

For each scan line in ADFLI, the FTPSF was obtained by temporally scanning over 120 delay steps in 25 ps increments. For each point of the FTPSF, the camera exposure time was set to 600 ms with four times accumulation, which resulted in 2.4 sec acquisition time at each temporal delay step. Therefore, the time needed to acquire the FTPSF data with ADFLI was 288 s per horizontal line and collection of a 2D lifetime map depended directly on the number of lines used to create the 2D stack. Significant improvements to imaging speed could be realized by reducing the time to acquire each horizontal line. Following this approach, we tested the effect of undersampling the FTPSF at each line as a potential method to reduce acquisition time. As a result, we estimated the undersampling effect on the noise level of the lifetime signal. The noise was computed as the standard deviation of the lifetime estimates for each temporal sampling resolution. Specifically, we computed

$$\sigma = \sqrt{\frac{1}{N} \sum_{i=1}^N (x_i - \mu)^2}, \quad \text{E-2}$$

where N , x , and μ were the number of spatial points, lifetime estimates, and the smoothed lifetime estimates at computed at a 25-ps temporal sampling resolution. Figure E-5 (a) displays the effect of undersampling the FTPSF on the lifetime map for a phantom with targets at a depth of 1 mm collected with and without the AFA. Figure E-5 (b) displays the relationship between the standard deviation of the lifetime estimates and the temporal resolution used to collect the FTPSF with and without the AFA for ICG and DTTCl fluorophore agents at 1 mm depth.

Undersampling the FTPSF did not affect the spatial resolution of the lifetime maps for either the AFA or non-AFA systems; however, undersampling significantly increased the noise on the lifetime estimates. This was expected, since fluorescence lifetime quantification depends on the fidelity of each FTPSF, which is related to the number of samples used to estimate each FTPSF. Higher temporal sampling of each FTPSF is expected to provide better lifetime estimates, but at the cost of longer data acquisition time. The dependence of noise on temporal resolution was much less significant for lifetimes obtained from FTPSFs collected without the AFA.

In addition to FTPSF undersampling, imaging speed could be improved by incrementing the power of the excitation light and/or increasing the intensifier gain. In either case, integration times would be reduced, but with potentially undesirable consequences such as bleaching effects and/or introduction of additional electronic noise into the measurements. Undersampling the FTPSF provided an alternative method to speed up the image acquisition by a factor of 2 to 5 without increasing either the laser power or the intensifier gain and with relatively minor impact (~2-fold increase in noise for 5-fold decrease in acquisition time) on the noise in the lifetime estimates. Undersampling of the FTPSF may be well-suited to fluorophores with longer lifetimes.

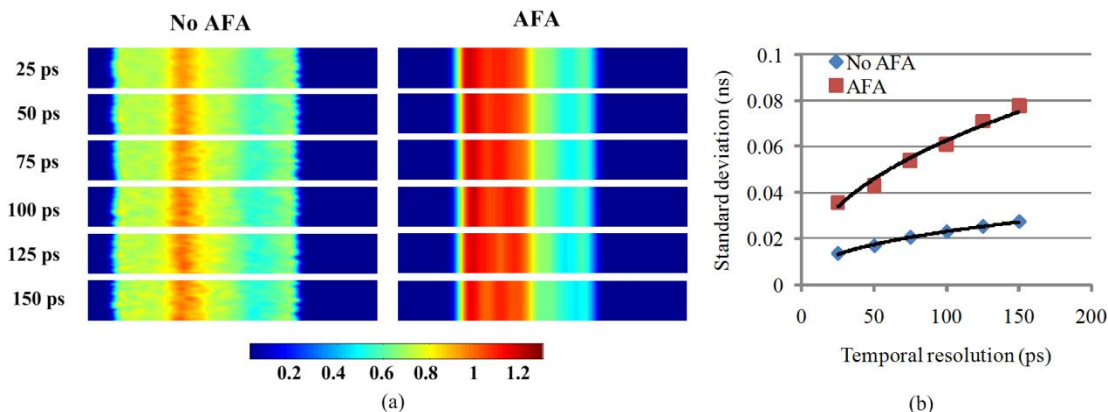


Figure E-5. (a) The lifetime maps of ICG and DTTCl tubes at 1 mm depth within 1% Intralipid™ solution quantified with different temporal resolution (from 25 ps to 150 ps). The lifetime maps show the effect of undersampling of the FTPSF on the lifetime map (DTTCl and ICG) (color map scale; ns, each fluorescent lifetime map presents a region of interest of 20 mm wide × 0.75 mm high). (b) Correlation between noise on the fluorescence lifetime estimates and the temporal sampling resolution for the AFA (red symbols) and No AFA (blue symbols) computed for images of ICG and DTTCl fluorophores at 1 mm depth.

Conclusions

In summary, phantom model tests demonstrated the usefulness of employing an angular filter array for fluorescent lifetime imaging to enhance the localization and lifetime determination of fluorescently-labeled targets. ADFLI has several advantages over other lifetime fluorescence imaging modalities, which include a larger field of view while preserving spatial image resolution, and better image contrast at tissue depths exceeding 1 mm. ADFLI could be used ultimately for the detection and sizing of tumor-targeted fluorescent agents at tissue depths significantly greater than conventional reflection-based imaging methods. Furthermore, precise and spatially-resolved fluorescent lifetime information could potentially improve quantification of the tumor microenvironment.

Acknowledgments

This project was funded by grants from the Natural Sciences and Engineering Research Council of Canada (NSERC) to Drs. Jeffery J.L. Carson and Bozena Kaminska, and the Canadian Foundation for Innovation to Jeffery J.L. Carson. In addition, partial funding was provided by the Translational Breast Cancer Fellowship to Dr. Fartash Vasefi from the London Regional Cancer Program.

References

- E1. Bambot, S. B., Lakowicz, J. R., & Rao, G. (1995). Potential applications of lifetime-based, phase-modulation fluorimetry in bioprocess and clinical monitoring. *Trends in Biotechnology*, 13(3), 106. doi:10.1016/S0167-7799(00)88915-5"
- E2. Rao, J., Dragulescu-Andrasi, A., & Yao, H. (2007). Fluorescence imaging in vivo: Recent advances. *Current Opinion in Biotechnology*, 18(1), 17. doi:10.1016/j.copbio.2007.01.003"
- E3. Godavarty, A., Sevick-Muraca, E. M., & Eppstein, M. J. (2005). Three-dimensional fluorescence lifetime tomography. *Medical Physics*, 32(4), 992-1000. doi:10.1118/1.1861160
- E4. Lakowicz, J. R., Szmacinski, H., Nowaczyk, K., & Johnson, M. L. (1992). Fluorescence lifetime imaging of free and protein-bound NADH. *Proceedings of the National Academy of Sciences*, 89(4), 1271-1275. Retrieved from <http://www.pnas.org/content/89/4/1271>.
- E5. Lakowicz, J. R., & Szmacinski, H. (1993). Fluorescence lifetime-based sensing of pH, Ca²⁺, K⁺ and glucose. *Sensors and Actuators B: Chemical*, 11(1-3), 133. doi:10.1016/0925-4005(93)85248-9"
- E6. Berezin, M. Y., Lee, H., Akers, W., & Achilefu, S. (2007). Near infrared dyes as lifetime solvatochromic probes for micropolarity measurements of biological systems. *Biophysical Journal*, 93(8), 2892. doi:10.1529/biophysj.107.111609"
- E7. May, A., Bhaumik, S., Gambhir, S. S., Zhan, C., & Yazdanfar, S. (2009). Whole-body, real-time preclinical imaging of quantum dot fluorescence with time-gated detection. *Journal of Biomedical Optics*, 14(6), 060504. doi:10.1117/1.3269675
- E8. Gioux, S., Lomnes, S. J., Choi, H. S., & Frangioni, J. V. (2010). Low-frequency wide-field fluorescence lifetime imaging using a high-power near-infrared light-emitting diode light source. *Journal of Biomedical Optics*, 15(2), 026005. doi:10.1117/1.3368997
- E9. Bastiaens, P. I. H., & Squire, A. (1999). Fluorescence lifetime imaging microscopy: Spatial resolution of biochemical processes in the cell. *Trends in Cell Biology*, 9(2), 48. doi:10.1016/S0962-8924(98)01410-X"
- E10. Piston, D. W., Kirby, M. S., Cheng, H., Lederer, W. J., & Webb, W. W. (1994). Two-photon-excitation fluorescence imaging of three-dimensional calcium-ion activity. *Appl. Opt.*, 33(4), 662-669. doi:10.1364/AO.33.000662
- E11. Diaspro, A. (2001). Confocal and two-photon microscopy: Foundations, applications and advances. In (pp. 101-125) Wiley-VCH.

- E12. O'Leary, M. A., Boas, D. A., Li, X. D., Chance, B., & Yodh, A. G. (1996). Fluorescence lifetime imaging in turbid media. *Opt.Lett.*, 21(2), 158-160. doi:10.1364/OL.21.000158
- E13. Kumar, A. T., Skoch, J., Bacskai, B. J., Boas, D. A., & Dunn, A. K. (2005). Fluorescence-lifetime-based tomography for turbid media. *Opt.Lett.*, 30(24), 3347-3349. doi:10.1364/OL.30.003347
- E14. Elson, D., Requejo-Isidro, J., Munro, I., Reavell, F., Siegel, J., Suhling, K.,... French, P. (2004). Time-domain fluorescence lifetime imaging applied to biological tissue. *Photochem.Photobiol.Sci.*, 3(8), 795-801. doi:10.1039/B316456J"
- E15. Paithankar, D. Y., Chen, A. U., Pogue, B. W., Patterson, M. S., & Sevick-Muraca, E. M. (1997). Imaging of fluorescent yield and lifetime from multiply scattered light reemitted from random media. *Appl.Opt.*, 36(10), 2260-2272. doi:10.1364/AO.36.002260
- E16. Davis, S. C., Pogue, B. W., Springett, R., Leussler, C., Mazurkewitz, P., Tuttle, S. B., . . . Paulsen, K. D. (2008). Magnetic resonance--coupled fluorescence tomography scanner for molecular imaging of tissue. *Review of Scientific Instruments*, 79(6), 064302. doi:10.1063/1.2919131
- E17. Milstein, A. B., Oh, S., Webb, K. J., Bouman, C. A., Zhang, Q., Boas, D. A., & Millane, R. P. (2003). Fluorescence optical diffusion tomography. *Appl.Opt.*, 42(16), 3081-3094. doi:10.1364/AO.42.003081
- E18. Kepshire, D. S., Davis, S. C., Dehghani, H., Paulsen, K. D., & Pogue, B. W. (2007). Subsurface diffuse optical tomography can localize absorber and fluorescent objects but recovered image sensitivity is nonlinear with depth. *Appl.Opt.*, 46(10), 1669-1678. doi:10.1364/AO.46.001669
- E19. Kumar, A. T., Skoch, J., Bacskai, B. J., Boas, D. A., & Dunn, A. K. (2005). Fluorescence-lifetime-based tomography for turbid media. *Opt.Lett.*, 30(24), 3347-3349. doi:10.1364/OL.30.003347
- E20. Vasefi, F., Belton, M., Kaminska, B., Chapman, G. H., & Carson, J. J. L. (2010). Angular domain fluorescence imaging for small animal research. *Journal of Biomedical Optics*, 15(1), 016023. doi:10.1117/1.3281670
- E21. Vasefi, F., Hung, B. S. L., Kaminska, B., Chapman, G. H., & Carson, J. J. L. (2009). Angular domain optical imaging of turbid media using enhanced micro-tunnel filter arrays. Paper presented at the Munich, Germany. , 7369(1) 73691N. doi:10.1117/12.831644
- E22. Tichauer, K. M., Najiminaini, M., Vasefi, F., Lee, T., Kaminska, B., & Carson, J. J. (2010). Improved lifetime analysis using angular-domain fluorescence imaging in a tissue-like phantom. Paper presented at the Biomedical Optics, BTuD75. Retrieved from <http://www.opticsinfobase.org/abstract.cfm?URI=BIOMED-2010-BTuD75>

- E23. Najiminaini, M., Vasefi, F., Kaminska, B., Chapman, G. H., & Carson, J. J. L. (2009). Macroscopic fluorescent lifetime imaging in turbid media using angular filter arrays. Paper presented at the Engineering in Medicine and Biology Society, 2009. EMBC 2009. Annual International Conference of the IEEE, 5364-5368. doi:10.1109/IEMBS.2009.5334594
- E24. Vasefi, F., Ng, E., Kaminska, B., Chapman, G. H., & Carson, J. J. L. (2009). Angular domain fluorescent lifetime imaging in turbid media. Paper presented at the San Jose, CA, USA. , 7183(1) 71830. doi:10.1117/12.809458
- E25. Vasefi, F., Kaminska, B., Chapman, G. H., & Carson, J. J. (2008). Image contrast enhancement in angular domain optical imaging of turbid media. *Opt.Express*, 16(26), 21492-21504. doi:10.1364/OE.16.021492
- E26. Vasefi, F., Akhbardeh, A., Najiminaini, M., Kaminska, B., Chapman, G. H., & Carson, J. J. (2010). Correction of artifacts in angular domain imaging. Paper presented at the Biomedical Optics, BSuD36. Retrieved from <http://www.opticsinfobase.org/abstract.cfm?URI=BIOMED-2010-BSuD36>
- E27. Optical properties of "Intralipid™", an aqueous suspension of lipid droplets
Retrieved from <http://omlc.ogi.edu/spectra/intralipid/index.html>
- E28. Staveren, H. J. v., Moes, C. J. M., Marie, J. v., Prahl, S. A., & Gemert, M. J. C. v. (1991). Light scattering in intralipid-10% in the wavelength range of 400-1100 nm. *Appl.Opt.*, 30(31), 4507-4514. doi:10.1364/AO.30.004507
- E29. Han, S., Farshchi-Heydari, S., & Hall, D. J. (2008). Analysis of the fluorescence temporal point-spread function in a turbid medium and its application to optical imaging. *Journal of Biomedical Optics*, 13(6), 064038. doi:10.1117/1.3042271